Creating a shallow-water experimental wave environment

David Aknin

Imperial College London

Department of Civil and Environmental Engineering

Thesis submitted in partial fulfilment of the requirements for the degree of Doctor of Philosophy in Civil Engineering of Imperial College London and the Diploma of Imperial College London

Declaration of originality

I, David Aknin, declare that this thesis is my own work and has not been submitted in any form for another degree or diploma at any university or other institute of tertiary education. Information derived from the published and unpublished work of others has been acknowledged in the text and a list of references is given in the bibliography.

Copyright declaration

The copyright of this thesis rests with the author and is made available under a Creative Commons Attribution Non-Commercial No Derivatives licence. Researchers are free to copy, distribute or transmit the thesis on the condition that they attribute it, that they do not use it for commercial purposes and that they do not alter, transform or build upon it. For any reuse or redistribution, researchers must make clear to others the licence terms of this work.

Abstract

This PhD concerns laboratory wavemaking in shallow and intermediate water conditions. Theoretical solutions and experimental evidence are presented to advance both our understanding of the wave generation process as well as its practical success. A comparison is made between two wave generation techniques, a first based on controlling the wavemaker displacement, and a second based on controlling the wavemaker force.

In deep water, a force-based approach, which includes active wave absorption, was recently shown to offer benefits in terms of wave quality. To investigate the influence of the water depth on this type of control, a range of generation scenarios is considered, including regular, bi-chromatic, focused and random waves. The work demonstrates that force-based wave generation in shallow water suffers from similar limitations as position control. This principally concerns the contamination of the testing area due to unwanted free waves, where the present focus is placed on the superharmonic range.

The main advance of the work lies in the solutions it offers to overcome this free wave contamination. The nature of the nonlinear wave solution upon which force-based generation should be based depends on the type of wave case (regular, bi-chromatic, focused or random). For each of these cases, a suitable methodology is proposed and validated. The developed methodology allows for high quality wave generation, whilst maintaining the benefit of active wave absorption.

The work is timely in the sense that is responds to two recent developments. First, the majority of wavemaking facilities are now computer controlled, and active absorption has become commonplace. The work presented offers solutions highly relevant to such installations. Second, developments particularly in offshore wind, have seen many new structures placed in relatively shallow-water depth. It is essential that the model testing of such structures adequately accounts for the issues and solutions presented herein.

Acknowledgements

A PhD is a long journey that cannot be achieved without the help and support of many people. The most important help I received came from my supervisor Dr. Johannes Spinneken, who relentlessly led and supported my work throughout. In addition to being a kind and considerate person, Johannes has exceptional teaching skills, and the feedback he regularly provided me with enabled the success of my research.

I would like to also thank Prof. Chris Swan, my second supervisor, as well as Dr. Marios Christou and Dr. Maarten Van Reeuwijk whose significant expertise in fluid mechanics was of great help to my PhD project. The Hydrodynamics Laboratory at Imperial College London hosts many talented researchers and it was a privilege for me to make the most of their knowledge during my PhD.

Other PhD students, including Marcos Rodriguez, Mark Bruggemann, Georgios Deskos, Livio de Lutio, Joseph Haley, Mohamed Latheef and Erwan Kasiman have all been very helpful for different reasons. Mark's dedication to sharing his programming skills (and political comments) with us was particularly kind, I will not forget it. Marcos has always been present to assist with all types of issues encountered during my time in the laboratory.

I would like to thank Edinburgh Designs Ltd. for providing access to their control system. Special thanks go to Douglas Rogers for many inspiring technical discussions. I also do not want to forget the extensive amount of help received from Dave de Ruyter and Paul Crudge who have always managed to find time to assist with technical and manual work whenever it was needed. Many thanks to Dr. Colin Whittaker, who kindly invited me to conduct experimental work at the School of Marine Science and Engineering at Plymouth University.

Most importantly, this thesis would never have seen the day without the continuous attention, support and love of my parents, Myriam and Alex. They made me the person I am today, and I want to dedicate this thesis to them. Also, my cousins André, Philippe and Alice are very important to me, and their presence has been very helpful during the time of my PhD research. Finally, I would like to give special thanks to my partner Aleksandra, who has always been there to support me and cheer me up during the challenging periods of my PhD.

Contents

Abstract **7**

Acknowledgements **8**

List of Figures **14**

List of Tables **19**

Nomenclature **20**

1 Introduction **23**

1.1 Motivation 23

1.2 Research strategy and scope of the work 24

1.3 Thesis layout 26

2 Background **28**

2.1 Chapter overview 28

2.2 Nonlinear wave modelling 29

2.2.1 Introduction 29

2.2.2 Analytical wave solutions 30

2.2.3 Semi-analytical wave solutions 31

2.2.4 Assessment of wave solutions 32

2.3 Laboratory wave generation 33

2.3.1 Introduction 33

2.3.2 Wavemaker theories 34

2.3.3 The wavemaking boundary value problem 36

2.3.4 Linear wavemaker theory 38
2.3.5 Second-order position-control wavemaker theory 42
2.3.6 Stream-function position-control wavemaker theory 43
2.4 Laboratory wave generation and absorption 45
2.4.1 Introduction 45
2.4.2 Position-controlled wave generation 47
2.4.3 Force-controlled wave generation and absorption 47
2.4.4 First-order force-control wavemaker theory 50
2.4.5 Second-order force-control wavemaker theory 50
2.4.6 Stream-function force-control wavemaker theory 51

3 Regular wave generation in shallow water 53
3.1 Chapter overview 53
3.2 Theoretical comparison of nonlinear wavemaking theories 54
3.2.1 Introduction 54
3.2.2 First-harmonic wavemaker displacement 55
3.2.3 Second-harmonic wavemaker displacement in position control 57
3.2.4 Second-harmonic force in force control 59
3.3 Introduction to experimental investigation 62
3.4 Experimental validation of position control 63
3.4.1 Progressive wave field coefficient 63
3.4.2 First-order and second-order control 68
3.4.3 Stream-function based correction 75
3.4.4 Alternative second-order correction 77
3.5 Experimental validation of force control 82
3.5.1 First-order control 82
3.5.2 Second-order forces 83
3.5.3 Second-order control 85
3.5.4 Stream-function control 89
3.6 Extended nonlinear set 89
3.7 Conclusions 93

4 Bi-chromatic waves **95**

4.1 Chapter overview . . . 95

4.2 Theoretical analysis . . . 96

4.2.1 Introduction . . . 96

4.2.2 Second-order position control . . . 96

4.2.3 Second-order force control . . . 100

4.3 An experimental investigation . . . 103

4.3.1 Overview . . . 103

4.3.2 Second-order position control . . . 104

4.3.3 Second-order force control . . . 112

4.3.4 Relative water depth . . . 118

4.3.5 Wave nonlinearity . . . 119

4.4 Conclusions . . . 122

5 Focused wave groups **123**

5.1 Chapter overview . . . 123

PART I: A NUMERICAL INVESTIGATION

5.2 The modelling of focused wave groups . . . 124

5.3 Wave conditions and domain definition . . . 126

5.4 Defining a minimum focus location . . . 128

5.5 Free-surface boundary condition error . . . 131

5.5.1 Introduction . . . 131

5.5.2 Quantitative description . . . 132

5.5.3 The importance of the phase angle distribution . . . 134

5.5.4 Minimum phase gradient condition . . . 135

5.5.5 The linkage of focus time and location . . . 137

5.5.6 Variations in the water depth . . . 139

5.6 A numerical wave tank study . . . 140

5.6.1 Introduction . . . 140

5.6.2 Convergence of a focused group . . . 141

5.7 Application of error criterion and conclusions . . . 144

PART II: A LABORATORY INVESTIGATION

5.8 Introduction . . . 146
5.9 Wave generation in first-order control . . . 146
5.9.1 Generation of small-amplitude focused wave groups . . . 146
5.9.2 The generation of large amplitude focused wave groups . . . 151
5.10 A surface elevation-based calibration . . . 154
5.10.1 Calibration of a small-amplitude event . . . 154
5.10.2 Generation of a large amplitude event . . . 157
5.11 A displacement-based calibration . . . 160
5.12 Wave generation in second-order control . . . 165
5.13 Conclusions . . . 167

6 Irregular waves **169**
6.1 Chapter overview . . . 169
6.2 Nonlinear control in irregular seas . . . 170
6.2.1 Second-order control . . . 170
6.2.2 Alternative nonlinear formulations . . . 171
6.3 Irregular sea laboratory testing . . . 173
6.4 Wave generation and absorption . . . 174
6.5 Small amplitude sea states . . . 178
6.6 Steep sea states in intermediate water depth . . . 180
6.7 Steep sea states in shallow water . . . 184
6.8 An alternative wave generation approach . . . 186
6.9 Conclusions . . . 192

7 Conclusions **194**
7.1 Principal achievements . . . 195
7.2 Further work . . . 198
7.2.1 Modelling viscous effects . . . 198
7.2.2 Irregular sea wave generation . . . 199
7.2.3 Multi-directional wave generation . . . 199

7.3 Final remarks 200

A Second-order wavemaker theory **201**

B Stream-function wavemaker theory **205**

C Force-control wavemaker theory **207**

D Independent confirmation of progressive wave field coefficient **211**

List of Figures

1.1 Arrangement of a sector-carrier piston-type wavemaker 25

2.1 Definition of a piston-type wavemaker. 37
2.2 Wave field coefficients showing the progressive wave mode and the evanescent wave modes 41
2.3 Normalised wavemaker velocity and horizontal fluid velocity in shallow water 41
2.4 Normalised wavemaker velocity and horizontal fluid velocity in deep water 42
2.5 Control strategy for a position-controlled wavemaker. 47
2.6 Control strategy for a force-controlled absorbing wavemaker 49

3.1 First-harmonic wavemaker displacement predicted by second-order wavemaker theory and Stream-function wavemaker theory 56
3.2 Normalised second-harmonic wavemaker displacement due to second-order theory and Stream-function theory 58
3.3 Normalised second-harmonic correction force due to second-order theory and Stream-function theory 61
3.4 Setup of wave flume for regular wave investigation 63
3.5 Water surface elevation for small-amplitude cases with experimental data and theoretical prediction 65
3.6 Progressive wave field coefficient with experimental data and theoretical prediction 67
3.7 Water surface elevation for large-amplitude cases (second-order position control) 70

3.8 Magnitude and phase of the bound wave content 71
3.9 Magnitude and phase of the free wave content 72
3.10 Spurious free wave content (second-order position control) 73
3.11 Water surface elevation for large-amplitude cases (Stream-function position control) 75
3.12 Spurious free wave content (Stream-function position control) . . . 76
3.13 Phase of the complex transfer function 79
3.14 Water surface elevation for large-amplitude cases (corrected second-order control) 80
3.15 Water surface elevation for large-amplitude cases (optimum second-order force control) 81
3.16 Spurious free wave content in position control (corrected) 82
3.17 Water surface elevation for small-amplitude force-control cases . . . 84
3.18 Second-harmonic wavemaker displacement due to the nonlinear force feedback 86
3.19 Water surface elevation for large-amplitude cases (second-order force control) 87
3.20 Spurious free wave content (second-order force control) 88
3.21 Water surface elevation for large-amplitude cases (Stream-function force control) 90
3.22 Spurious free wave content (Stream-function force control) 91
3.23 Water surface elevation for extended-nonlinear cases 92

4.1 Calculated water surface elevation for a bi-chromatic wave case . . . 97
4.2 Ratio of the cross-interaction superharmonic free to bound wave amplitude in position control 99
4.3 Ratio of the cross-interaction subharmonic free to bound wave amplitude in position control 99
4.4 Ratio of the cross-interaction superharmonic free to bound wave amplitude in force control 101

4.5 Ratio of the cross-interaction subharmonic free to bound wave amplitude in force control 102
4.6 Surface elevation for bi-chromatic wave case Bi1 (position control) . 105
4.7 Surface elevation for bi-chromatic wave case Bi2 (position control) . 107
4.8 Wave components for case Bi1 (position control) 109
4.9 Wave components for case Bi2 (position control) 111
4.10 Surface elevation for bi-chromatic wave case Bi1 (force control) . . . 113
4.11 Surface elevation for bi-chromatic wave case Bi2 (force control) . . . 114
4.12 Wave components for case Bi1 (force control) 116
4.13 Wave components for case Bi2 (force control) 117
4.14 Water surface elevation for case Bi7 120

5.1 Numerical domain and definition of notation adopted 127
5.2 Focused wave group with $k_p h = 1.56$ and $A_{\text{sum}} = 0.11$ 129
5.3 Error in KFSBC and DFSBC for wave cases with $k_p h = 1.56$ and $T_r = 45T_p$ 133
5.4 Phase angle and water surface elevation at $x = 0$ 135
5.5 Contributions to the wave component phase at $x = 0$ 137
5.6 Non-dimensional frequency kh of the component with the minimum phase at $x = 0$ 138
5.7 Error in KFSBC and DFSBC for wave case with $k_p h = 1.56$ and $T_r = 90T_p$ 139
5.8 Error in the free-surface boundary conditions for a range of wave cases 140
5.9 Convergence of a focused event generated in a NWT 143
5.10 Analysis of a focused event generated in a NWT 144
5.11 Minimum focus location based upon maximum permissible error . . 145
5.12 Water surface elevation for small-amplitude focused wave groups . . 147
5.13 Progressive wave field coefficient for a focused wave group 149

5.14 Water surface elevation for small-amplitude focused groups (corrected) . . . 151
5.15 Water surface elevation for a moderately steep focused wave group . 153
5.16 Calibration based on a small-amplitude event in position control . . 156
5.17 Water surface elevation for a moderately steep focused wave group (calibrated) . . . 158
5.18 Water surface elevation for a moderately steep focused wave group (alternative calibration) . . . 163
5.19 Water surface elevation for steep focused wave groups . . . 164
5.20 Water surface elevation for steep focused wave groups under second-order control . . . 166

6.1 Progressive wave field coefficient in an irregular sea state . . . 176
6.2 Water surface elevation recorded for successive repeat times . . . 177
6.3 Crest elevation probability of exceedance for a sea state with $k_p h = 1.4$ and $\frac{1}{2} H_s k_p = 0.03$ . . . 179
6.4 Crest elevation probability of exceedance for a sea state with $k_p h = 1.4$ and up to $\frac{1}{2} H_s k_p = 0.10$ . . . 181
6.5 Wavemaker demand amplitude spectrum for a sea state with $k_p h = 1.4$ and up to $\frac{1}{2} H_s k_p = 0.10$ . . . 183
6.6 Crest elevation probability of exceedance for a sea state with $k_p h = 0.8$ and up to $\frac{1}{2} H_s k_p = 0.08$ . . . 185
6.7 Wavemaker demand amplitude spectrum for a sea state with $k_p h = 0.8$ and up to $\frac{1}{2} H_s k_p = 0.08$ . . . 187
6.8 Time histories of surface elevation and depth-averaged velocity for *ad-hoc* approach . . . 190
6.9 Probability of exceedance of depth-averaged horizontal fluid velocity 191
6.10 Crest elevation probability of exceedance for a sea state with $k_p h = 0.8$ and $\frac{1}{2} H_s k_p = 0.08$ (*ad-hoc* approach) . . . 191

D.1 Magnitude of progressive wave field coefficient at alternative facility 212

D.2 Spurious free wave content in position control at alternative facility 212

List of Tables

2.1 Comparison of water wave theories 32

3.1 Experimental wave parameters 64
3.2 Polynomial regression of the corrected phase of the transfer function 78

4.1 Experimental wave parameters for bi-chromatic investigation 103
4.2 Experimental data for second-order control for cases Bi3 to Bi6 . . 118
4.3 Experimental data for second-order control for cases Bi7-1 to Bi7-7 121

Nomenclature

α	Wave phase or Phillips parameter
δ_{nm}	Kronecker parameter
η	Water surface elevation
Λ	Dispersion correction in the frequency domain
λ	Wavelength
λ_d	Dispersion correction term
$\mathbb{R}$	Real part
$\mathscr{F}$	Transfer function for second-order correction term
ω	Circular wave frequency
ϕ	Velocity potential
ρ	Water density
A	Wave amplitude
A_{lin}	Linear wave amplitude
A_{sum}	Wave amplitude sum
$B(\omega)$	System transfer function in force control
c	Wave phase velocity
$C(\omega)$	Wavemaker motion controller
c_f	Force-control tank transfer function
c_g	Wave group velocity
c_0	Progressive wave field coefficient
c_j	Wave field coefficient for mode j
d	Distance between bed and bottom of the wavemaker
$d(\omega)$	Radiation damping

E	Boundary condition error
f	Wave frequency
$F(\omega)$	Wavemaker force
$f(t)$	Wavemaker force in time domain
g	Acceleration due to gravity
$G(\omega)$	Drive motor torque to wavemaker velocity transfer function
$G_{jl}^{\pm}$	Nonlinear wavemaker transfer function (surface elevation)
H	Wave height
h	Water depth
H_s	Significant wave height
i	Imaginary number
K	Wavemaker buoyancy stiffness
k	Wavenumber
M	Wavemaker mass
$m(\omega)$	Added mass
p	Pressure
Q	Bernoulli constant or Probability of exceedance
S	Wave nonlinearity parameter
s	Laplace variable
$S_{\eta\eta}$	Spectral density function
T	Wave period
t	Time
T_r	Repeat time
U	Depth-averaged horizontal fluid velocity
u	Horizontal fluid velocity component
X	Wavemaker position
x	Horizontal coordinate
X_0	Wavemaker motion amplitude at the mean water level
Z	Impedance term
z	Vertical coordinate

Term	Definition of term
Bi-chromatic wave	A wave group composed of two fundamental wave components
Bound wave	A wave that is bound to its fundamental wave components
Evanescent wave	A wave that remains stationary and decays with distance from some given origin
Free wave	A wave that propagates in its own right, and satisfies the dispersion equation
Harmonic	A frequency term
Irregular wave	A sea state comprised of a number of wave components
Order	An expansion term
Progressive wave	A wave that propagates with a given celerity
Regular wave	A wave with one fundamental wave component
Spurious wave	An unwanted wave component arising at higher harmonic
Sub-harmonic	An interaction arising at the difference frequency
Super-harmonic	An interaction arising at the sum frequency

1

Introduction

1.1 Motivation

Laboratory testing is an essential step in the development of offshore and coastal structures. The past twenty years have seen a significant rise in the number of hydrodynamics laboratories equipped with modern wavemakers. In the United Kingdom, this was primarily driven by research funding associated with the development of marine renewable technology. More globally, many of the large commercial and military hydrodynamics testing facilities have upgraded their traditional hydraulic drive systems to modern electrical servo systems. All state-of-the-art systems are now computer controlled, and active wave absorption has become a key-characteristic of a modern wavemaking system.

The goal of any wavemaking system is the reproduction of the ocean at scale. To achieve this, the field of 'wavemaking theory' derives the mathematical expressions that enable the generation of high-quality ocean-like conditions in the laboratory. An appropriate theory must be formulated for each type of wavemaker geometry and for each type of control. Fortunately, only few generic wavemaker geometries exist, and the type of control is also limited to two main strategies.

The majority of installed wavemakers can be categorised as one of two types: flap-type wavemakers or piston-type wavemakers. Flap-type wavemakers are com-

monly installed if deep to intermediate water testing is undertaken. In contrast, piston-type wavemakers are best suited in shallow and intermediate water conditions. The type of control is principally determined by the way in which active wave absorption is achieved. Historically, two main types of absorption strategies were developed, a first based on controlling the wavemaker position (position control) and a second based on controlling the hydrodynamic force acting on the wave board (force control).

In addition to the wavemaker geometry and the type of control, the relative water depth is also important. In deep water using flap-type devices, a recent investigation showed that force control may offer inherent benefits in terms of wave quality. It is well known that nonlinear shallow-water wave mechanics differ significantly from deep-water formulations. In this context, it is much less clear how the type of control affects the wave quality in shallow water. For position control, it is well established that a nonlinear demand input is required to achieve high-quality shallow-water wave generation. In force control, this is presently not clear. In fact, previously reported visual observations suggest that the wave quality based on a linear force demand signal is not satisfactory. This potential deficiency of force-controlled wave generation in shallow water forms the prime motivation for the present PhD.

1.2 Research strategy and scope of the work

A significant body of work exists in the description of the nonlinear wavemaking problem in shallow water; an account of the available literature being given in Chapter 2. The vast majority of this work was undertaken in the context of position control. Indeed, nonlinear wavemaking in force control has only been considered in deep-to-intermediate water conditions, with a focus on flap-type wavemakers. In effect, the present PhD seeks to combine the existing knowledge on shallow-water wavemaking with the recent advances in nonlinear force control.

A range of nonlinear shallow-water wave generation techniques exists, and their

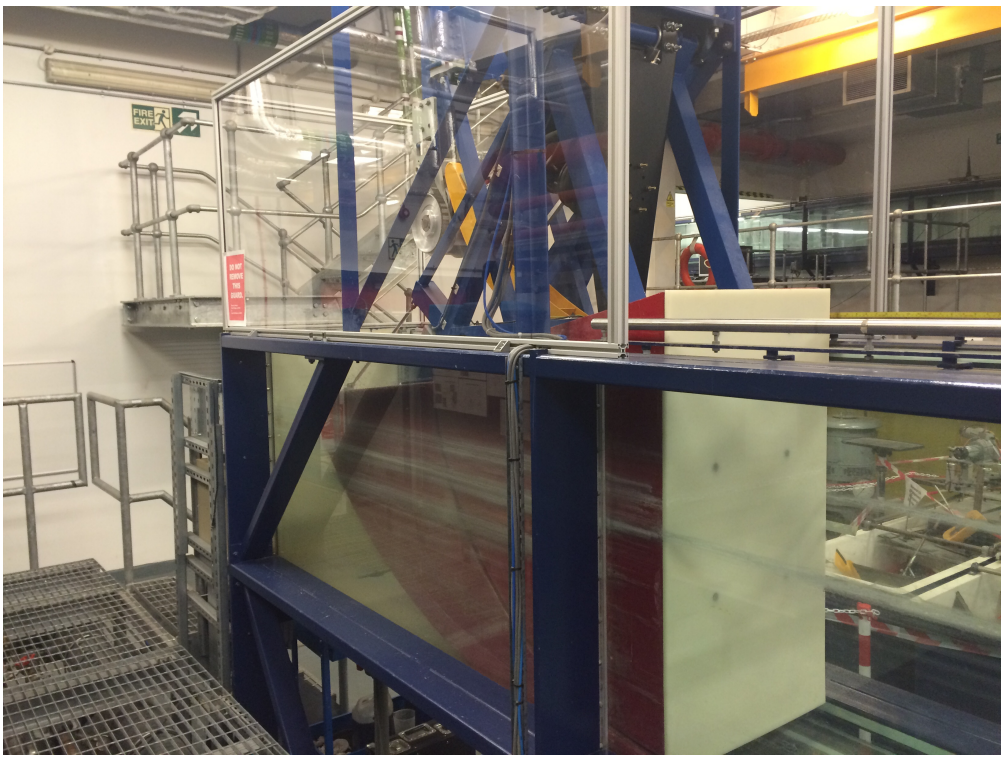


Figure 1.1: Arrangement of a sector-carrier piston-type wavemaker

application varies depending on the type of sea state to be modelled (regular or irregular; uni-directional or multi-directional). In theory, each of the techniques may also be adopted to both flap-type and piston-type wavemakers. Given this wide range of scenarios, some simplifications must be made to limit the scope of this PhD. Addressing nonlinear force control in shallow water for the first time, it was deemed appropriate to limit the scope to piston-type wavemakers and uni-directional waves. In addressing this important case, both regular and irregular waves are considered.

The wavemaker arrangement used throughout the present thesis is shown in Figure 1.1. The type of wavemaker used is referred to as a sector-carrier wavemaker, which ensures that waves are only generated on the front face of the device. The rear part of the wavemaker is curved in a way that avoids the disturbance of fluid. This is particularly important in the context of force control, where the hydrodynamic force is sought to only relate to waves generated on the front face. The white front panel was installed to ensure that fluid leakage around the sides

of the wavemaker is reduced as far as possible; further detail being provided in the relevant technical chapters. The wavemaker shown in Figure 1.1 can be operated in position control and force control.

One clear deficiency of the existing body of work is the inherent lack of experimental verification. A number of shallow-water generation theories have been formulated, but their experimental verification is usually very limited. To address this, each aspect of the work formulated here will also be demonstrated experimentally. This undoubtably is of considerable importance, particularly in a field where the experimental evidence is the only true and final purpose of the work.

1.3 Thesis layout

This thesis is divided into 7 main chapters, addressing the problem of shallow-water wave generation in increasing complexity as the work progresses.

Chapter 2 introduces the relevant background. Any new wavemaking theory inevitably builds upon advances in the underlying wave theories, and the appropriate theoretical wave mechanics are introduced first. An introduction to the wavemaking problem subsequently addresses both nonlinear wave generation and active wave absorption. The chapter also provides the mathematical descriptions required for nonlinear control in shallow water.

Chapter 3 addresses the regular wavemaking problem. This commences with a theoretical comparison between position control and force control, establishing some important differences between these two approaches. The majority of the chapter concerns a laboratory investigation, providing data for both control modes. This investigation is extensive in the sense that it covers a wide range of wave conditions, ranging from a verification of small-amplitude (linear) wavemaking theory to the generation of steep, near-breaking waves in shallow water.

Chapter 4 extends the complexity of the problem by considering the interactions arising between two fundamental wave components, the so-called bi-chromatic wave case. In contrast to much of the established wavemaking literature, this comparison primarily concerns the super-harmonic wave interaction terms. In similarity to Chapter 3, the required theoretical analysis is introduced first, followed by an experimental comparison between position control and force control.

Chapter 5 addresses focused wave groups, considering the problem in two distinct parts. Part I concerns a numerical analysis, defining the nonlinear terms involved, and providing numerical reference data. Part II provides an experimental assessment of focused wave groups, placing specific emphasis on the wave group quality that can be achieved through a range of calibration approaches. A novel calibration approach is introduced, and comparison to the numerical reference data is made.

Chapter 6 concerns the most challenging of any wave generation approaches, involving the accurate description of random seas. This includes an analysis of the wavemaker absorption performance in long-random simulations, as well as the description of nonlinear crest statistics. In defining the latter, a novel *ad-hoc* wave generation approach is introduced, which has the potential to overcome the limitations of second-order wavemaker theory in shallow water.

Chapter 7 draws overall conclusions, re-emphasises the importance of the work, states the principal achievements, and makes suggestions for further work.

2

Background

2.1 Chapter overview

This chapter introduces the relevant background required for the development of effective force-controlled wave generation and absorption in shallow water conditions. To achieve this overall research objective, three main aspects of the existing body of work must be considered:

(i) The development of wave solutions appropriate to shallow-to-intermediate water wave modelling,

(ii) Nonlinear wave generation techniques building upon (i) above and

(iii) Actively controlled wave absorption.

While wave modelling, (i) above, is essential to the correct understanding of shallow-water waves, the combination of (ii) and (iii) is essential in developing effective generation and absorption of such shallow-water waves. This chapter continues as follows. Section 2.2 provides an introduction to a number of relevant analytical wave theories and numerical wave solutions. A description of both linear and nonlinear wave generation techniques is then provided in §2.3. Finally, §2.4 introduces the concept of active absorption, and summarises the existing work on (nonlinear) force-feedback control.

2.2 Nonlinear wave modelling

2.2.1 Introduction

A wavemaker is inevitably characterised by the nature and quality of the waves it generates. Good quality waves are characterised by a surface profile and fluid kinematics that are in close agreement with field data or theoretical predictions. Therefore, a sound understanding of water wave mechanics is required to fully appreciate the operation of wavemakers; the present section providing an introduction to the relevant concepts.

In defining a nonlinear water wave, two important parameters are its steepness and its relative water depth. The steepness is often defined as the product of the wave amplitude A and the wavenumber $k = 2\pi/\lambda$, where λ is the wavelength. This product Ak characterises the wave's curvature or slope. The relative water depth may be defined as the actual depth h multiplied by the wavenumber k. Expressed in terms of kh, the water depth is commonly defined as three distinct regions:

(i) Shallow water with $kh < \pi/10$

(ii) Intermediate water with $\pi/10 \leq kh \leq \pi$

(iii) Deep water with $kh > \pi$

This PhD thesis is concerned with a relatively shallow water range of practical interest to laboratory wave generation. In terms of the above definition, most of the wave cases considered herein lie within the shallow end of the intermediate water region. For ease of description, this region is referred to as relatively shallow water or simply shallow water, even if this does not strictly satisfy the $kh < \pi/10$ condition.

Idealised linear (or sinusoidal) waves only exist in deep water conditions for waves of very low steepness. As the relative depth decreases, or the steepness increases, the wave becomes increasingly more nonlinear, and accounting for nonlinear effects is required. To describe this nonlinearity, both analytical and numerical

solutions have been developed; a brief description of the most relevant approaches being given in §2.2.2 (analytical) and §2.2.3 (numerical). The relative merits of the different approaches, along with their applicability to the present wavemaking research, are then summarised in §2.2.4.

2.2.2 Analytical wave solutions

The first original contribution to water wave mechanics was presented by Stokes (1847), providing a closed linear solution for regular waves. A Stokes-type regular wave theory valid up to fifth order was later derived by Fenton (1985); this solution being valid in most deep water conditions. An important aspect of higher-order expansions is that they lead to solutions that include a number of harmonics. For example, a linear wave solution is fully described by a single harmonic, whereas a second-order Stokes-type expansion must also include a second harmonic and a mean term.

Unfortunately, Stokes-type expansions in terms of the wave steepness have a limited range of validity in shallow water conditions. To address this, an alternative analytical model based on Cnoidal theory was derived, with a good summary of the developed concepts given in Isobe (1985). Cnoidal theory relies on the Korteweg de Vries equation, an approximation of the Boussinesq equation for the case of uni-directional wave propagation. Cnoidal theory has been derived up to fifth order (Fenton, 1979), and high-order Cnoidal theories have been shown to be valid in both shallow and intermediate water conditions. Nevertheless, its inability to model irregular waves makes it relevant only to the prediction of regular waves.

Building upon the earlier work by Longuet-Higgins and Stewart (1960), an irregular Stokes-type expansion valid up to second order was developed by Sharma and Dean (1981). Unlike regular waves, which are composed of a single wave component, irregular waves include a (large) number of components and represent ocean sea states much more realistically. One difficulty in their modelling lies in the high number of interactions that occur between the different wave components,

which makes the calculation of the wave elevation and kinematics computationally demanding. Nevertheless, the second-order wave model by Sharma and Dean (1981) is the most robust irregular wave theory presently available, and plays a significant role in the development of this research.

2.2.3 Semi-analytical wave solutions

In contrast to the above noted analytical theories, semi-analytical algorithms are commonly based on the exact description of the nonlinear free-surface boundary conditions. The perhaps most established model is based on a Stream-function formulation, where the Newton-Raphson method may be applied to derive a best fit to the free-surface boundary conditions (Chaplin (1980) and Fenton (1988)). However, due to the fact that the computation of the solution is performed in a coordinate system moving with the wave, Stream-function wave theory does not apply to the modelling of irregular waves, as a common frame of reference cannot be established.

This difficulty prompted the development of semi-analytical wave solutions based on a double Fourier formulation, which apply to both regular and irregular waves. The first double Fourier solution was devised by Lambrakos (1981). In close similarity to the Stream-function methodology, the double Fourier solution seeks to minimise the error in the nonlinear free-surface boundary conditions. A key difference of the double Fourier solution is that the water surface elevation must be known *a priori* and is used in the minimisation procedure. The double Fourier algorithm is based on a Fourier series expansion in both space and time, and ultimately provides the Fourier coefficients as well as the water wave kinematics. Baldock and Swan (1994) applied the double Fourier methodology to the case of focused wave groups, and concluded that this solution successfully predicts the crest kinematics even for highly nonlinear extreme wave events.

In contrast to double Fourier techniques, local Fourier methods are based on a single Fourier series expansion in time. Furthermore, the minimisation procedure

in local Fourier algorithms is performed only in a local window; a segmentation of the overall time window being required first. A solution is then computed for each time segment, and the local solutions are finally concatenated. Sobey (1992) developed the first local Fourier solution, and confirmed its validity for both regular waves and irregular sea states where the water surface elevation is provided by field data. Smith and Swan (2002) considered this latter solution in the context of focused wave groups. They arrived at the conclusion that the method is efficient in capturing the highly nonlinear interactions present in the crest of an extreme wave event. However, they also noted that double Fourier solutions are more effective at predicting low-frequency components characterised by a long wave period. Table 2.1 summarises several key aspects relevant to the theories introduced above.

Table 2.1: Comparison of water wave theories

	Stokes-type expansion	*Cnoidal*	*Stream-function*	*Local/Double Fourier*
Computational effort	Very low	Very low	Low	Medium to high
Nonlinearity of the solution	Partial (up to 5^{th} order)	Partial (up to 5^{th} order)	Fully nonlinear	Fully nonlinear
Validity domain	Deep to intermediate	Shallow	Deep to shallow	Deep to shallow
Irregular waves	✓	-	-	✓

2.2.4 Assessment of wave solutions

Dean (1972) conducted a comparison of Stokes, Stream-function and Cnoidal wave theories in shallow to deep water conditions and defined their success based on the error in the free-surface boundary conditions. According to Dean (1972), Stream-function theory is the best wave theory available for a wide range of deep to shallow water conditions; Stokes theory being invalid in shallow water and Cnoidal theory being invalid in deep water conditions. Stream-function theory was also shown to perform well for steep waves. This versatility makes Stream-

function theory highly relevant to the development of wave generation techniques; its only significant practical limitation being the inability to model irregular waves. Sobey et al. (1987) performed an assessment of regular wave theories based on a direct comparison of their water wave kinematics. Although this assessment was not based on a quantitative criterion such as in Dean (1972), Sobey et al. (1987) confirmed the importance of higher-order solutions when moving into more shallow water conditions.

In the context of irregular waves, Smith and Swan (2002) confirmed that an appropriate design solution must account for (i) the unsteadiness and (ii) the nonlinearity of the sea state. They also showed that irregular wave solutions based on linear wave theory and second-order wave theory are unable to predict the highly nonlinear interactions occurring in the crest of an extreme wave. In this context, Smith and Swan (2002) demonstrated that double Fourier and local Fourier methodologies bring a significant improvement in the modelling of extreme wave events. However, these wave solutions also have their limitations when applied to the wavemaking problem; this being discussed further in the context of irregular wave generation in Chapter 6.

2.3 Laboratory wave generation

2.3.1 Introduction

The derivation of any wavemaker theory involves considering the motion of the wavemaker and its influence on the surrounding fluid. An ideal approach would be to design a wavemaker geometry and motion that match the desired fluid kinematics exactly. However, for practical purposes, wavemaker geometries generally consist of flat wavemakers, having a single translational or rotational degree of freedom. The mismatch between the ideal and the practical design leads to two principal issues:

(i) The mismatch between the wavemaker velocity and the fluid (wave) kinemat-

ics throughout the water column leads to the existence of evanescent wave modes. Fortunately, these modes are only significant in the vicinity of the wavemaker and do not propagate into the testing area. However, they must be understood if considering the applied fluid load on the wavemaker.

(ii) More importantly to nonlinear wavemaking research, a combination of the geometric mismatch and a mismatch in terms of the description of the harmonic content leads to the generation of spurious or unwanted free wave components. These components may arise both at low frequencies (subharmonics) and high frequencies (superharmonics). Given that these spurious components propagate freely, they inevitably contaminate the testing area.

A complete nonlinear wavemaker theory must address both effects (i) and (ii) above. In this context, the present section provides the background necessary to an understanding of wavemaker theories in shallow water conditions. A summary of wavemaker theories is first provided in §2.3.2. The boundary value problem associated with the analytical description of laboratory wavemaking is then outlined in §2.3.3. A linear solution to this problem is provided in §2.3.4, followed by an introduction of second-order wavemaker theory, §2.3.5. Finally, an overview of Stream-function wavemaker theory is given in §2.3.6. All theories are introduced in the context of position control; an extension to force control being provided in §2.4.

2.3.2 Wavemaker theories

At least three nonlinear shallow-water wavemaking approaches have been considered in the past: (i) Stokes-type expansions up to second order, (ii) Stream-function based theories and (iii) Cnoidal based theories. In close similarity to the underlying wave theories, (i) has been extended to irregular sea states, whereas (ii) and (iii) are limited to regular waves.

Stokes-type wavemaker theories rely on a perturbation expansion of the relevant boundary conditions. In addition to expanding the free-surface boundary

conditions about the mean water level, the wavemaker displacement must be expanded about its mean position. A first-order Stokes-type solution to the wavemaking problem was presented by Havelock (1929). This solution gives an explicit relation between the wavemaker motion amplitude and the generated progressive wave amplitude, and was validated experimentally by Ursell et al. (1960).

At second order, wave-wave interactions give rise to both self-interactions and cross-interactions. These second-order interaction terms can occur as superharmonics and subharmonics. Ottesen-Hansen et al. (1980) and Sand and Donslund (1985) established that a second-order correction is required for the successful generation of long waves, particularly due to the importance of subharmonics. Sulisz and Hudspeth (1993) developed a complete second-order solution for regular waves based on a matched eigenfunction methodology. The second-order formulation used within the present thesis originates from the framework established by Schäffer (1996), who combined much of the earlier work in a single consistent analytical formulation. A brief description of this theory is provided in §2.3.5; a full account of the solution being given in Appendix A.

Goring and Raichlen (1980) suggested that effective generation of long waves requires a different approach. Unlike Stokes-type expansions of the wavemaker displacement about its mean position, Goring and Raichlen (1980) established a methodology where the wavemaker motion is considered relative to the generated wave kinematics. This approach was also demonstrated in the related development of several nonlinear wavemaker theories, including the Cnoidal approach by Goring (1979).

Zhang and Schäffer (2007) devised a Stream-function wavemaker theory appropriate to both shallow and intermediate water conditions. This approach inherits from Stream-function wave theory its high performance for a wide range of conditions. In particular, Stream-function wavemaker theory was shown to offer benefits over Cnoidal wavemaker theory in intermediate water, and to be more accurate than Stokes second-order wavemaker theory in deep water (Zhang and Schäffer, 2007). A brief overview of Stream-function wavemaker theory is given in §2.3.6; a

full description being provided in Appendix B.

Unfortunately, Stream-function wavemaker theory suffers from the same limitations as Stream-function wave theory, most importantly its inability to model irregular waves. An alternative wave generation approach for irregular waves will hence be introduced in the relevant Chapter 6.

2.3.3 The wavemaking boundary value problem

The majority of wavemaker solutions have in common that they rely on a potential flow formulation. Formulations exist for a variety of wavemaker geometries, including flap-, piston- and plunger-type wavemakers. In shallow-to-intermediate water conditions, piston-type wavemakers have emerged as the most common geometry. This choice of wavemaker is driven by a number of practical constraints, not least its ability to generate large amplitude waves. For long wave or shallow water generation, large volumes of fluid must be displaced, and piston-type wavemakers are best suited to this purpose. As a result, the present mathematical formulation focuses on piston-type geometries.

Figure 2.1 illustrates a piston-type wavemaker located in a two-dimensional wave flume. A Cartesian coordinate system (x, z) is aligned such that $x = 0$ defines the mean position of the wavemaker, and $z = 0$ defines the still water level in water of depth h. Waves generated by the wavemaker propagate into the positive $x-$direction and the instantaneous surface elevation is defined by $\eta(x, t)$, where t denotes time. The wavemaker is defined by the distance d between the bed and the bottom of the wavemaker, with the horizontal time-varying position of the wavemaker being denoted as $X(t)$.

Assuming the flow to be inviscid and irrotational, a velocity potential ϕ may be introduced. This velocity potential must satisfy mass continuity throughout the fluid domain, which is commonly expressed through Laplace's equation as

$$\frac{\partial^2 \phi}{\partial x^2} + \frac{\partial^2 \phi}{\partial z^2} = 0. \tag{2.1}$$

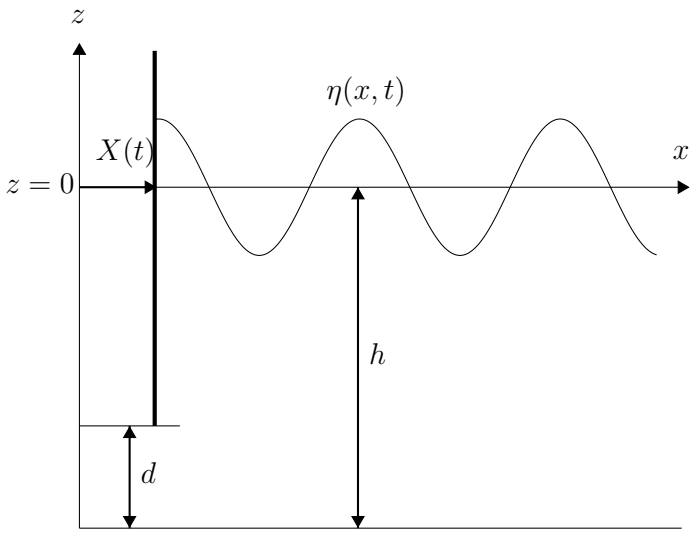


Figure 2.1: Definition of a piston-type wavemaker.

Furthermore, the wavemaking problem defined in Figure 2.1 can be fully specified by the following boundary conditions:

(a) A bed boundary condition, whereby the vertical fluid velocity on the horizontal and impermeable bed must be equal to zero.

(b) A lateral boundary condition, whereby the horizontal fluid velocity on the vertical and impermeable wavemaker must be equal to the wavemaker velocity.

(c) The Kinematic Free-Surface Boundary Condition (KFSBC), whereby the water surface profile is assumed to be a streamline.

(d) The Dynamic Free-Surface Boundary Condition (DFSBC), whereby the pressure on the instantaneous water surface is constant and equal to the atmospheric pressure.

Expressing these boundary conditions as a set of nonlinear equations yields

$$\frac{\partial \phi}{\partial z} = 0 \quad \text{at} \quad z = -h, \tag{2.2a}$$

$$\frac{\partial \phi}{\partial x} = \begin{cases} \frac{dX}{dt} & \text{at } x = X(t) \text{ for } -(h-d) \leq z \leq \eta(X(t),t) \\ 0 & \text{at } x = 0 \text{ for } -h \leq z < -(h-d), \end{cases} \tag{2.2b}$$

$$\frac{\partial \eta}{\partial t} = \frac{\partial \phi}{\partial z} - \frac{\partial \phi}{\partial x}\frac{\partial \eta}{\partial x} \text{ at } z = \eta(x,t) \text{ and} \tag{2.2c}$$

$$\frac{\partial \phi}{\partial t} = -g\eta - \frac{1}{2}\left\{\left(\frac{\partial \phi}{\partial x}\right)^2 + \left(\frac{\partial \phi}{\partial z}\right)^2\right\} \text{ at } z = \eta(x,t), \tag{2.2d}$$

where equations (2.2a) - (2.2d) correspond to conditions (a)-(d) respectively.

2.3.4 Linear wavemaker theory

Linear wavemaker theory relies on a Taylor series expansion of equations (2.2a) to (2.2d), retaining only expansion terms up to the first order of wave steepness $O(Ak)$. Performing this expansion provides the linearised boundary conditions as

$$\frac{\partial \phi^{(1)}}{\partial z} = 0 \text{ at } z = -h, \tag{2.3a}$$

$$\frac{\partial \phi^{(1)}}{\partial x} = \begin{cases} \frac{dX^{(1)}}{dt} & \text{at } x = 0 \text{ for } -(h-d) \leq z \leq 0 \\ 0 & \text{at } x = 0 \text{ for } -h \leq z < -(h-d), \end{cases} \tag{2.3b}$$

$$\frac{\partial \eta^{(1)}}{\partial t} = \frac{\partial \phi^{(1)}}{\partial z} \text{ at } z = 0 \text{ and} \tag{2.3c}$$

$$\frac{\partial \phi^{(1)}}{\partial t} = -g\eta^{(1)} \text{ at } z = 0, \tag{2.3d}$$

where the superscript $^{(1)}$ indicates the first-order solution. If N wave components of frequencies ω_n are considered, the first-order wavemaker motion is defined as

$$X^{(1)}(t) = \mathbb{R}\left\{-i\sum_{n=1}^{N} X_n e^{i\omega_n t}\right\}, \tag{2.4}$$

where X_n represents the complex amplitude of the wavemaker motion for wave component n, $\mathbb{R}$ denotes real part and $i = \sqrt{-1}$. Subject to this wavemaker displacement, equations (2.3a)-(2.3d) can be solved to obtain the first-order velocity potential (Schäffer, 1996) as

$$\phi^{(1)}(x,z,t) = \mathbb{R}\left\{\sum_{n=1}^{N} \frac{igX_n}{\omega_n} \sum_{j=0}^{\infty} c_{jn} \frac{\cosh k_{jn}(z+h)}{\cosh k_{jn}h} e^{i(\omega_n t - k_{jn}x)}\right\}, \tag{2.5}$$

and the first-order water surface elevation as

$$\eta^{(1)}(x,t) = \mathbb{R}\left\{\sum_{n=1}^{N} X_n \sum_{j=0}^{\infty} c_{jn} e^{i(\omega_n t - k_{jn}x)}\right\}. \tag{2.6}$$

The wavenumbers k_{jn} are the solutions to the dispersion equation

$$\omega_n^2 = g k_{jn} \tanh\left(k_{jn}h\right), \tag{2.7}$$

where g denotes acceleration due to gravity. This overall solution is composed of a single progressive wave mode for $j = 0$ and an infinite series of evanescent components for $j \geq 1$. For the progressive mode, the wavenumber k_{0n} is real, whereas k_{jn} are imaginary with $ik_{jn} > 0$.

In defining the velocity potential (equation (2.5)), a so-called wave field coefficient c_{jn} is introduced. Adopting a series of orthogonal functions (Schäffer, 1996), this coefficient may be obtained analytically. For piston-type wavemakers, this analytic solution is given by

$$c_{jn} = \frac{2\sinh(k_{jn}h)(\sinh(k_{jn}h) - \sinh(k_{jn}d))}{k_{jn}h + \sinh(k_{jn}h)\cosh(k_{jn}h)}, \tag{2.8}$$

where $j = 0$ again concerns the progressive wave mode and c_{0n} is real. In contrast, c_{jn} for $j \geq 1$ is imaginary and describes the evanescent modes with $ic_{jn} > 0$.

Comparison of equations (2.4) and (2.6), relates the magnitude of the first-order wavemaker displacement X_n to first-order progressive wave amplitude A_{0n}

as

$$|A_{0n}| = c_{0n}|X_n|. \tag{2.9}$$

For brevity, the progressive wave field coefficient c_{0n} for wave component n will simply be referred to as c_0 hereafter. It is important to note that the phase shift between the wavemaker displacement and the progressive wave on the wavemaker front face is 90°. This ensures that the first-order progressive wave elevation is in phase with the first-order wavemaker velocity.

Figure 2.2 illustrates the wave field coefficient for both the progressive wave mode, c_{0n}, and the evanescent wave modes; the latter being expressed by the sum $\sum_{j=1}^{\infty} ic_{jn}$. The figure concerns a very wide range of relative water depth kh. Observing Figure 2.2, both coefficients c_{0n} and $\sum_{j=1}^{\infty} ic_{jn}$ increase with increasing kh; the coefficient c_{0n} reaching a limiting value of 2 for $kh > 5$. Furthermore the evanescent wave modes are seen to be negligible in shallow water conditions ($kh < 0.5$).

The latter observation is readily explained by the properties of the horizontal fluid particle velocity in shallow water, where the velocity profile becomes near-uniform over depth. This is confirmed by Figure 2.3, which shows the normalised horizontal fluid velocity profile in the range $-1 \leq z/h \leq 0$ for a shallow-water wave with $kh = 0.5$ (dashed line). Figure 2.3(a) only considers the progressive wave kinematics, whereas 10 and 100 evanescent modes are added in Figures 2.3(b) and 2.3(c) respectively. The figure also shows the normalised wavemaker velocity profile (solid line). Indeed, the good match between the horizontal fluid velocity and the wavemaker velocity in all cases (a)-(c) confirms the small influence of the evanescent modes in shallow water. In contrast, Figure 2.4 considers a deep water case with $kh = 5$. In this case, a good match between the horizontal fluid velocity and wavemaker velocity requires at least 100 evanescent modes.

The above observations are of upmost importance in the context of the present research, indicating that evanescent wave modes may potentially be neglected when developing a shallow-water wavemaking technique.

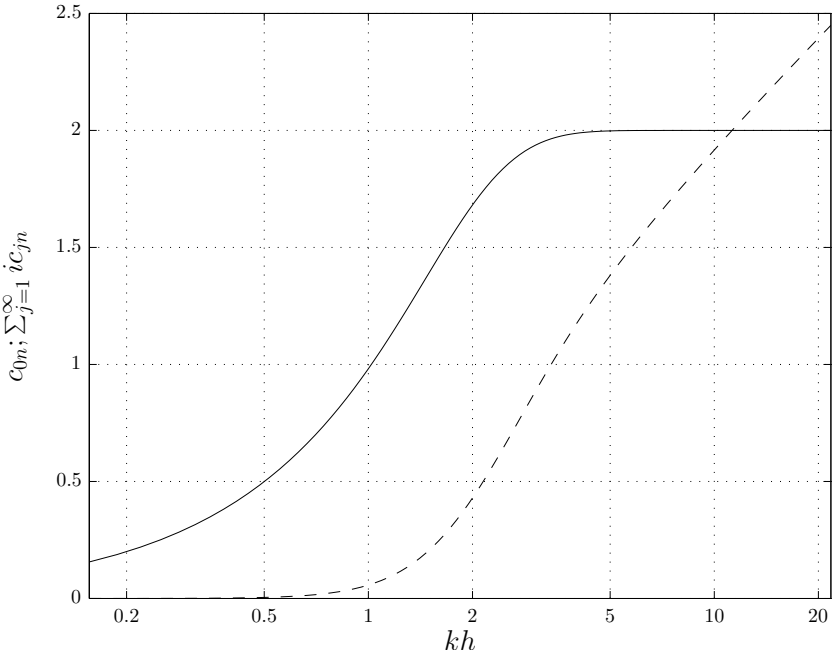


Figure 2.2: Wave field coefficients showing ——— the progressive wave mode and – – – the evanescent wave modes.

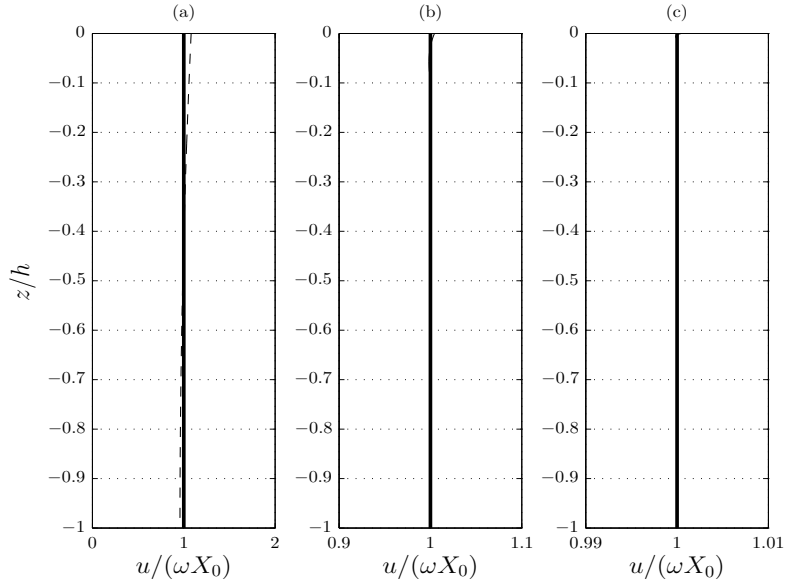


Figure 2.3: Normalised ——— wavemaker velocity and – – – horizontal fluid velocity in water of depth $kh = 0.5$ considering (a) no evanescent wave modes, (b) 10 evanescent wave modes and (c) 100 evanescent wave modes.

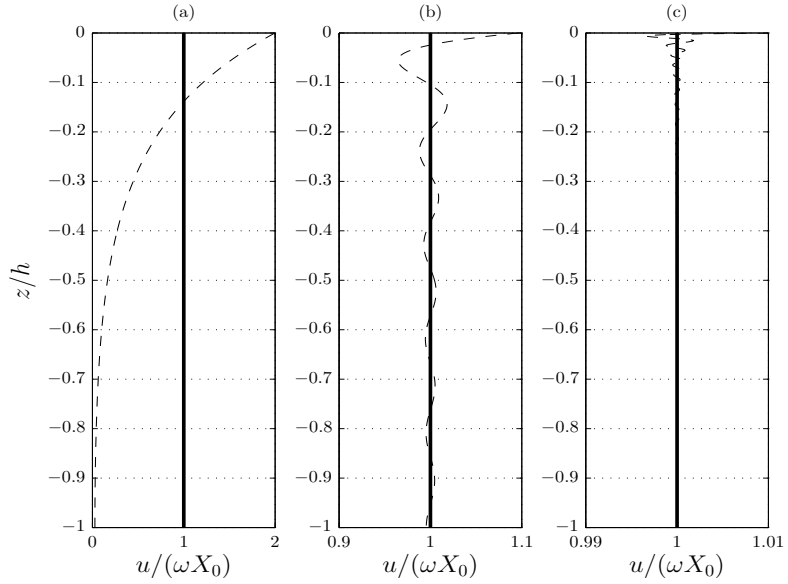


Figure 2.4: Normalised ——— wavemaker velocity and – – – horizontal fluid velocity in water of depth $kh = 5$ considering (a) no evanescent wave modes, (b) 10 evanescent wave modes and (c) 100 evanescent wave modes.

2.3.5 Second-order position-control wavemaker theory

Introducing the second-order potential as $\phi^{(2)}$, an expansion of the boundary conditions (2.2a) to (2.2d) up to second order yields

$$\frac{\partial \phi^{(2)}}{\partial z} = 0 \quad \text{at} \quad z = -h, \tag{2.10a}$$

$$\frac{\partial \phi^{(2)}}{\partial x} = \begin{cases} \frac{dX^{(2)}}{dt} - X^{(1)} \frac{\partial^2 \phi^{(1)}}{\partial x^2} & \text{at} \quad x = 0 \quad \text{for} \quad -(h-d) \leq z \leq 0 \\ 0 & \text{at} \quad x = 0 \quad \text{for} \quad -h \leq z < -(h-d), \end{cases} \tag{2.10b}$$

$$\frac{\partial \eta^{(2)}}{\partial t} = \frac{\partial \phi^{(2)}}{\partial z} - \frac{\partial \phi^{(1)}}{\partial t}\frac{\partial \eta^{(1)}}{\partial x} + \eta^{(1)} \frac{\partial^2 \phi^{(1)}}{\partial z^2} \quad \text{at} \quad z = 0 \quad \text{and} \tag{2.10c}$$

$$\frac{\partial \phi^{(2)}}{\partial t} = -g\eta^{(2)} - \frac{1}{2}\left\{ \left(\frac{\partial \phi^{(1)}}{\partial x} \right)^2 + \left(\frac{\partial \phi^{(1)}}{\partial z} \right)^2 \right\} - \eta^{(1)} \frac{\partial^2 \phi^{(1)}}{\partial z \partial t} \quad \text{at} \quad z = 0, \tag{2.10d}$$

where equations (2.10a) - (2.10d) again correspond to boundary conditions (a) - (d).

A full analytical solution to this second-order problem was reported by Schäffer (1996); a complete description of the terms involved being provided in Appendix A. At this stage, a brief discussion concerning the key solution properties is instructive. For ease of analytical treatment, the full second-order potential $\phi^{(2)}$ is separated into three distinct contributions:

(i) A potential $\phi^{(21)\pm}$, defining the second-order wave-wave interaction arising in the absence of the wavemaker; this part being equivalent to the potential derived in Sharma and Dean (1981).

(ii) A potential $\phi^{(22)\pm}$, defining the spurious or unwanted free wave arising due to the presence of the wavemaker; the purpose of any nonlinear wavemaker theory being to suppress this unwanted potential.

(iii) A potential $\phi^{(23)\pm}$, defining the additional free-wave correction due to a prescribed second-order motion of the wavemaker.

Throughout the solution presented by Schäffer (1996), the superscript $\pm$ indicates that interactions between the wave components arise both as superharmonics ($+$ or sum terms) and subharmonics ($-$ or difference terms). Most importantly, Schäffer (1996) derived a correction signal to the wavemaker displacement, that eliminates the spurious or unwanted term due to $\phi^{(22)\pm}$ given by

$$X_{nm}^{(2)\pm} = \mathscr{F}^{\pm} \frac{A_n A_m^{-*}}{h}, \tag{2.11}$$

where (A_n, A_m) are the amplitudes of the generated progressive waves for a pair of wave components (n, m), the superscript $^{-*}$ refers to the complex conjugate for subharmonics, and a full expression for $\mathscr{F}^{\pm}$ is provided in Appendix A. This second-order wavemaker displacement produces an additional free wave $\eta^{(23)\pm}$, which is equal in magnitude but of opposite sign to $\eta^{(22)\pm}$ (Appendix A).

2.3.6 Stream-function position-control wavemaker theory

Zhang and Schäffer (2007) first derived a Stream-function wavemaker theory, re-

lying on an *ad-hoc* combination of linear fully dispersive wavemaker theory and nonlinear wave generation. Mathematically, this theory is developed in two steps as follows:

(i) In a first step, the wavemaker displacement required for this shallow water theory, $X^{sw}(t)$, is obtained excluding the effect of wave dispersion. This displacement is obtained from the numerical solution of

$$\frac{dX^{sw}(t)}{dt} + \omega_c X^{sw}(t) = U(X^{sw}(t), t), \tag{2.12}$$

which describes the required velocity boundary condition at the wavemaker. Indeed, equation (2.12) ensures that the wavemaker velocity, $dX^{sw}(t)/dt$, and the nonlinear depth-averaged horizontal fluid velocity, $U(X^{sw}(t), t)$, match. The additional proportional term, $\omega_c X^{sw}(t)$, describes a first-order high-pass filter of characteristic angular frequency ω_c. The sole purpose of this filter is to avoid any small low-frequency drift of the wavemaker. The depth-averaged horizontal fluid velocity required in equation (2.12) may be obtained by considering continuity expressed as

$$U(x,t) = \frac{c\eta(x,t)}{h + \eta(x,t)}, \tag{2.13}$$

from which it is evident that the solution relies on an *a priori* knowledge of the water surface elevation $\eta(x,t)$. In the context of Stream-function wavemaker theory, the phase velocity c and the surface elevation $\eta(x,t)$ are provided by Stream-function wave theory. However, this methodology is universal in that it can be based on a water surface elevation predicted by any regular wave theory.

(ii) In a second step, a correction term is applied to account for wave dispersion,

providing the wavemaker displacement as the convolution product

$$X_{0s}(t) = \int_{-t_0}^{t_0} X^{sw}(t-\tau)\lambda_d(\tau)d\tau, \tag{2.14}$$

where t_0 represents the width of the convolution window and $\lambda_d(t)$ is the inverse Fourier transform of the dispersion correction term in the frequency domain; further details concerning this convolution integral being given in Appendix B. The signal $X_{0s}(t)$ provides the desired time-domain demand applied to the wavemaker.

2.4 Laboratory wave generation and absorption

2.4.1 Introduction

All of the wavemaking theories discussed in §2.3 are not directly applicable where active wave absorption is sought. However, active absorption is essential to any modern wavemaking apparatus. Wave energy is generally reflected from downstream beaches, and any test model placed within a laboratory wave flume or wave basin also reflects some wave energy back towards the wavemaker. The purpose of an absorbing wavemaker is to remove this unwanted reflected wave energy, hence maintaining an incident wave field of consistent quality. Research on active laboratory wave absorption led to a number of strategies, most importantly: (i) position-controlled absorption techniques and (ii) force-controlled absorption techniques.

Position-controlled absorption was the first strategy to be developed, and is most commonly based on the water surface elevation recorded on the front face of the wavemaker feeding back into the system (Milgram, 1970). One drawback of this absorption strategy are the difficulties related to high-frequency position control. For example, any spike or rapid change in the demand signal or the feedback signal will lead to abrupt changes in the control quantity (the position), which may lead to instabilities in the wavemaker motion. Another practical limitation is

the accurate determination of the water surface elevation at the wavemaker front face. Inaccuracies may arise, for example, due to the influence of chemicals present in the fluid. Difficulties of this type have perhaps hindered the development of nonlinear position-controlled wavemaker theories in the presence of active absorption. To the author's best knowledge, this type of control is currently limited to the work by Schäffer and Jakobsen (2003).

In seeking to devise a more robust approach, Salter (1982) developed a force-controlled absorption technique, based upon the applied hydrodynamic force feeding back into the system. Given that the force demand determines the acceleration of the wavemaker rather than its position, any noise or rapid change will be integrated twice (from acceleration to position), hence resulting in smooth wavemaker displacements. Salter (1982) argued that a methodology based on force feedback allows for the determination of the average water conditions across the wavemaker front. In this context, it is also of critical importance that force sensors are not affected by the chemical conditions of the fluid and can be considered calibration free.

In defining the most suitable absorption strategy, laboratory techniques greatly benefited from research undertaken in the field of wave energy conversion. Evans (1976) and Falnes (1993) pioneered this research and presented theories concerning optimum absorption. Building upon these theoretical developments, Spinneken and Swan (2009*a*) derived an analytical second-order theory for actively absorbing force-controlled wavemakers; an accompanying experimental verification being presented in Spinneken and Swan (2009*b*). Spinneken and Swan (2009*a*,*b*) also provided a correction force to cancel the spurious wave content at second order. However, they demonstrated that in many practical wave conditions a first-order force demand signal suffices, eliminating the need for a second-order demand.

This latter work focused on flap-type wavemakers in deep-to-intermediate water conditions. In contrast, the present PhD concerns the shallow-to-intermediate water range adopting piston-type wavemakers. As the present thesis directly builds upon Spinneken and Swan (2009*a*), an account of the relevant theory is presented

in §2.4.5. Given the difficulties associated with position-controlled absorption, the remainder of this thesis only addresses absorption techniques based on force control.

2.4.2 Position-controlled wave generation

For all experiments undertaken in position control, a simple controller as shown in Figure 2.5 was adopted. Absorption was not considered in position control, such that the only feedback quantity is the wavemaker position. The corrector, C, ensures that the desired wavemaker position, X, and the position demand, X_d, match closely. The wavemaker transfer function in position control, P, relates the motor torque to the wavemaker position. An exact treatment of either C or P is outside the scope of the present work, but these can be readily defined from a knowledge of the wavemaker dynamics.

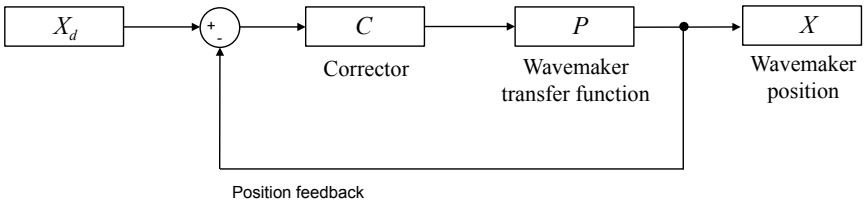


Figure 2.5: Control strategy for a position-controlled wavemaker.

2.4.3 Force-controlled wave generation and absorption

A force-control strategy fundamentally relies on the measurement of both the wavemaker velocity and the wavemaker force; the product of these two quantities being directly related to the absorbed power. Falnes (1980) showed that two conditions must be met to maximise this power, a phase condition and a magnitude condition. To achieve these two conditions in practice, a real-time absorption controller is commonly adopted, continuously monitoring both the force and the velocity, and acting upon changes in the incident wave field to maintain optimum absorption at all times. A number of alternative methodologies exist for the

implementation of this absorption controller:

(a) a discrete frequency implementation, utilising a frequency estimator (Chatry et al., 1998).

(b) a Finite Impulse Response filter (FIR); this having been investigated by Frigaard and Christensen (1994).

(c) a multiplication factor applied to the position and velocity feedback signals (Naito, 2006).

(d) an Infinite Impulse Response filter (IIR), approximating the ideal transfer function (Salter, 1982).

Spinneken and Swan (2009*c*) provide a direct comparison between the methodologies outlined above, and conclude that (d) provides the most effective and robust control strategy. As a result, this IIR methodology is also applied throughout the present study. Generally speaking, the IIR filter methodologies are based upon an impedance matching procedure, ensuring that the two aforementioned conditions of optimum absorption are met. The advantage of using an IIR filter approach lies in the inherent causality of the resulting digital filter (Spinneken and Swan, 2009*c*). The overall control strategy is outlined in Figure 2.6, where the absorption controller (or filter) $Z_f(\omega)$ is applied to the wavemaker's velocity signal. If $Z_d(\omega)$ is the impedance characterising the dynamics of the wavemaker, Falnes (1980) demonstrated that optimum absorption occurs if

$$Z_f = Z_d^*, \tag{2.15}$$

where $*$ denotes the complex conjugate. Following Spinneken and Swan (2009*a*), the dynamic wavemaker impedance Z_d is readily shown to be

$$Z_d(\omega) = i\omega\left[M + m(\omega)\right] + d(\omega) + \frac{K}{i\omega}, \tag{2.16}$$

where M is the mass of the wavemaker and K is the wavemaker buoyancy stiffness due the immersed part of the sector-carrier wavemaker. The added mass $m(\omega)$ and the radiation damping $d(\omega)$ are directly related to the radiation force arising as a consequence of the generated wave; their analytic expressions for a piston-type wavemaker being provided in Appendix C.

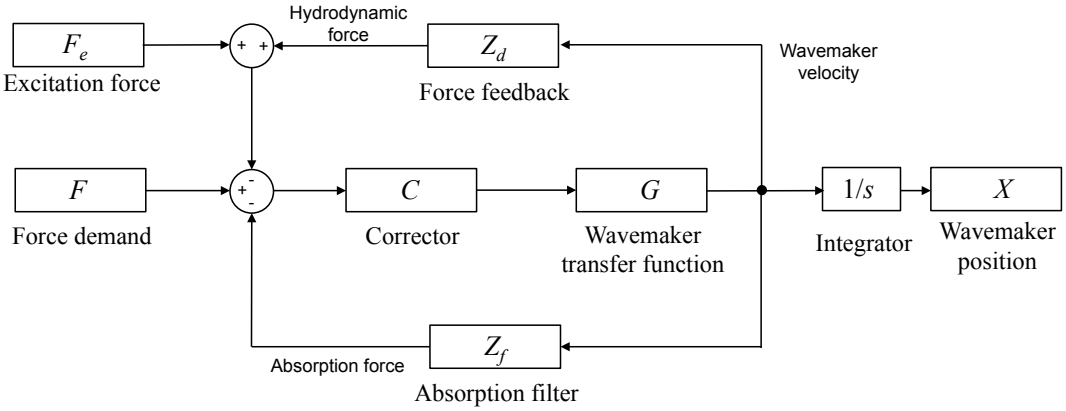


Figure 2.6: Control strategy for a force-controlled absorbing wavemaker.

If $C(\omega)$ expresses the wavemaker motion controller, and $G(\omega)$ relates the drive motor torque to the wavemaker velocity, the block diagram shown in Figure 2.6 can be expressed as the following transfer function

$$B(\omega) = \frac{X(\omega)}{F(\omega)} = \frac{1}{i\omega} \frac{C(\omega)G(\omega)}{1 + C(\omega)G(\omega)(Z_f(\omega) + Z_d(\omega))}, \tag{2.17}$$

where $B(\omega)$ relates the force demand signal $F(\omega)$ to the wavemaker position $X(\omega)$. A similar transfer function may also be derived for the wave excitation force. Assuming a sufficiently high feedback correction through the controller $C(\omega)$, the transfer function $B(\omega)$ may be approximated by

$$B(\omega) \approx \frac{1}{i\omega} \frac{1}{Z_f(\omega) + Z_d(\omega)}, \tag{2.18}$$

which avoids the need for an explicit formulation of $C(\omega)$ and $G(\omega)$.

2.4.4 First-order force-control wavemaker theory

In the context of position control, §2.3.4 introduced the progressive wave field coefficient c_0, relating the magnitude of the first-order wavemaker displacement, X_n, to the first-order progressive wave amplitude, A_{0n}. In contrast, force control concerns the demand force F_n, and the relation to the first-order progressive wave amplitude A_{0n} may be introduced as

$$A_{0n} = c_f F_n, \tag{2.19}$$

where the coefficient c_f is defined as

$$c_f = B(\omega)c_0. \tag{2.20}$$

It is important to note that the force coefficient or transfer function c_f contains both real and imaginary components. As a result, the phase relation between the wavemaker demand (now the force F_n) and the progressive wave amplitude is not as straightforward as in position control. Furthermore, the transfer function c_f does not only depend on the wavemaker geometry, but also on the parameters of the absorption filter $Z_f(\omega)$ and the dynamic transfer function $Z_d(\omega)$.

2.4.5 Second-order force-control wavemaker theory

In the context of force-controlled wave generation, an effective correction of the spurious free wave requires accounting for the force feedback at second order. Indeed, even a linear or sinusoidal wavemaker displacement induces a second-order hydrodynamic force. This force, in turn, feeds back into the system and leads to the generation of an additional spurious wave. In some cases, particularly for flap-type wavemakers, this additional spurious free wave has been shown to (partially) cancel the unwanted free wave due to $\phi^{(22)\pm}$ (Spinneken and Swan, 2009*b*). However, this may not always be the case, so that an expression for the additional correction term in force control must be sought.

First, the force required to achieve a spurious wave compensation in the absence of the nonlinear force-feedback component is

$$F_{c,0}^{(2)\pm} = \mathscr{F}^{\pm}\frac{A_n A_m^{-*}}{hB(\omega_n \pm \omega_m)}. \tag{2.21}$$

This equation directly arises from equation (2.11), and would lead to the desired second-order wavemaker displacement $X_{nm}^{(2)\pm}$ if the nonlinear force-feedback was neglected. However, the nonlinear force-feedback, introduced as $F_{\phi}^{(2)\pm}$, must also be taken into consideration as noted above; a full expression for $F_{\phi}^{(2)\pm}$ being provided in Appendix C.2. A correct cancellation of the spurious free wave in force control can now be performed by imposing a combined correction of both the spurious free wave due to the velocity potential $\phi^{(22)\pm}$, and the spurious free wave caused by the second-order force feedback $F_{\phi}^{(2)\pm}$. This combined force correction is given by

$$F_{c}^{(2)\pm} = \mathscr{F}^{\pm}\frac{A_n A_m^{-*}}{hB(\omega_n \pm \omega_m)} + F_{\phi}^{(2)\pm} = F_{c,0}^{(2)\pm} + F_{\phi}^{(2)\pm} \tag{2.22}$$

which is consistent with the formulation provided by Spinneken and Swan (2009*a*). Spinneken and Swan (2009*a*) showed that this force correction is relatively small, as the two terms shown in equation (2.22) approximately cancel over a wide range of practical wavemaking frequencies. Unfortunately this is not the case for piston-type wavemakers; a detailed discussion of this effect being provided in §3.2.

2.4.6 Stream-function force-control wavemaker theory

Prior to this PhD thesis, a force-control Stream-function wavemaking theory did not exist; the purpose of the present section being to derive a suitable mathematical expression for this type of control. Building upon the Stream-function based wavemaker displacement $X_{0s}(t)$ introduced in §2.3.6, the implementation of Stream-function wavemaker theory in force control concerns the force demand required to achieve $X_{0s}(t)$. As noted in the context of second-order force control, this must take into account the nonlinear forces introduced through the force feed-

back path. In contrast to the second-order discussion, the Stream-function force correction is not limited to harmonics arising at the second order. Indeed, the time-domain force demand, $f(t)$, is defined as

$$f(t) = \int_{-h}^{\eta(X_{0s}(t),t)} p(X_{0s}(t), z)dz, \tag{2.23}$$

where the pressure $p(x, z)$ is given by the unsteady form of Bernoulli's equation as

$$p(x, z) = -\rho g z - \rho \frac{\partial \phi}{\partial t} - \frac{1}{2}\rho \left[\left(\frac{\partial \phi}{\partial x} \right)^2 + \left(\frac{\partial \phi}{\partial z} \right)^2 \right], \tag{2.24}$$

with ρ denoting the water density and g the acceleration due to gravity. Within this latter expression for pressure, the velocity potential ϕ must be derived directly from Stream-function wave theory; a detailed account of the practical application of equations (2.23) and (2.24) being given in Chapter 3. In considering the force in equation (2.23), it is important to note that this concerns the hydrodynamic force only. To obtain the overall demand force, the absorption feedback must also be taken into consideration (§2.4.5).

3

Regular wave generation in shallow water

3.1 Chapter overview

Chapter 2 established the relevant background for wave generation in shallow water, and introduced a number of important mathematical expressions. In a regular wave context, this primarily concerned second-order and Stream-function based theories. The aim of the present chapter is to demonstrate the suitability of each of these approaches, particularly where this concerns force-controlled or absorbing wavemaking. As outlined in Chapter 2, this demonstration can ultimately only be achieved through experimental evidence. To provide a base for this experimental work, §3.2 presents a number of supporting calculations. The experimental investigation is then structured as follows:

(i) An introduction to the experimental test conditions is provided in §3.3

(ii) Position-controlled wave generation is considered in §3.4, addressing the following key quantities:

   (a) An experimental assessment of the first-order wave field coefficient c_0 is presented in §3.4.1. All subsequent hydrodynamic quantities (surface elevation, velocity potential, forces) rely on this fundamental coefficient.

Crucially, at second order, the coefficient c_0 is being squared, and any first-order inaccuracies are further amplified.

(b) An assessment of the spurious free wave content $A^{(22)+}/A^{(21)+}$ and the second-order correction term $X^{(2)+}$ is presented in §3.4.2.

(c) The spurious wave content established under (b) is compared to the Stream-function approach in §3.4.3.

(iii) An equivalent series of steps (ii) (a)-(c), but incorporating force-feedback control, is presented in §3.5 and §3.6.

A set of conclusions, summarising the key benefits of each type of control, is finally provided in §3.7.

3.2 Theoretical comparison of nonlinear wavemaking theories

3.2.1 Introduction

This section concerns a theoretical comparison of second-order and Stream-function wavemaker theory. The second-order wavemaker theory by Schäffer (1996) directly provides the first-order and second-order wavemaker displacements. In contrast, Stream-function wavemaker theory provides the time-history of the wavemaker position, where all frequency components (first harmonic, second harmonic and higher harmonics) are represented in a single signal. In this context, it is important to emphasise that Stream-function wavemaker theory is a fully-nonlinear wavemaker theory, and therefore not restricted to second order.

For such a fully-nonlinear theory, it is important to distinguish between orders and harmonics, as a particular harmonic may arise at several orders. For example, the second harmonic may arise due to interactions at the second and the fourth order. However, if it can be assumed that fourth-order interactions are small, the

influence of the fourth order on the second harmonic may also be assumed to be small. Nevertheless, to be entirely clear, all comparisons to follow are based upon the harmonic rather than the order.

A direct comparison of the first- and second-harmonic quantities required by Stream-function and second-order wavemaker theories is instructive, particularly for shallow water waves where Stream-function wavemaker theory is expected to provide more accurate predictions. The first-harmonic wavemaker displacement is addressed in §3.2.2. The second-harmonic displacement is first considered in position control (§3.2.3), with an extended discussion relating to force control presented in §3.2.4.

3.2.2 First-harmonic wavemaker displacement

Figure 3.1 shows the normalised first-harmonic wavemaker displacement, $X^{(1)}/X_0$, predicted by both second-order and Stream-function wavemaker theories, where X_0 defines the linear wavemaker demand. In the context of the second-order theory, the first-harmonic wavemaker motion is not affected; this case being represented by the horizontal line at unity in Figure 3.1. In contrast, Stream-function wavemaker theory contains terms beyond second order, which may give rise to changes at the first harmonic. This is demonstrated by the four steepness cases considered with (i) $Ak = 0.05$ (solid black line), (ii) $Ak = 0.15$ (dark grey line), (iii) $Ak = 0.25$ (light grey line) and (iv) $S = 1$ (dashed line). The parameter S relevant to case (iv) was introduced by Schäffer (1996) as

$$S = 4A \mid G^{+}_{0000} \mid \tag{3.1}$$

with $G^{\pm}_{jnlm}$ provided in Appendix A. The purpose of this parameter is to define the range of applicability of second-order wavemaker theory, where $S = 1$ defines the extreme upper limit.

In considering Figure 3.1, it is apparent that $S = 1$ corresponds to a very small wave steepness Ak in shallow water conditions. To be entirely clear, the

points at which the solid lines intersect with the dashed line defines the smallest kh at which second-order theory may be applied for a given wave steepness. For example, the black line ($Ak = 0.05$) and the dashed line cross at $kh \approx 0.58$, so that second-order theory may not be applied for $kh < 0.58$ if $Ak = 0.05$. For $Ak = 0.15$ (dark grey line) the relative depth is limited to $kh > 0.9$, which increases further to $kh = 1.18$ for $Ak = 0.25$. Perhaps more importantly, Figure 3.1 also indicates that the first-harmonic motion is significantly affected when adopting a Stream-function based theory. For a steepness of $Ak = 0.15$ (dark grey line), the first-harmonic wavemaker motion is reduced by more than 15% for $kh \leq 0.6$. This clearly emphasises the importance of higher-order terms in shallow water, which will be assessed further as part of the experimental investigation.

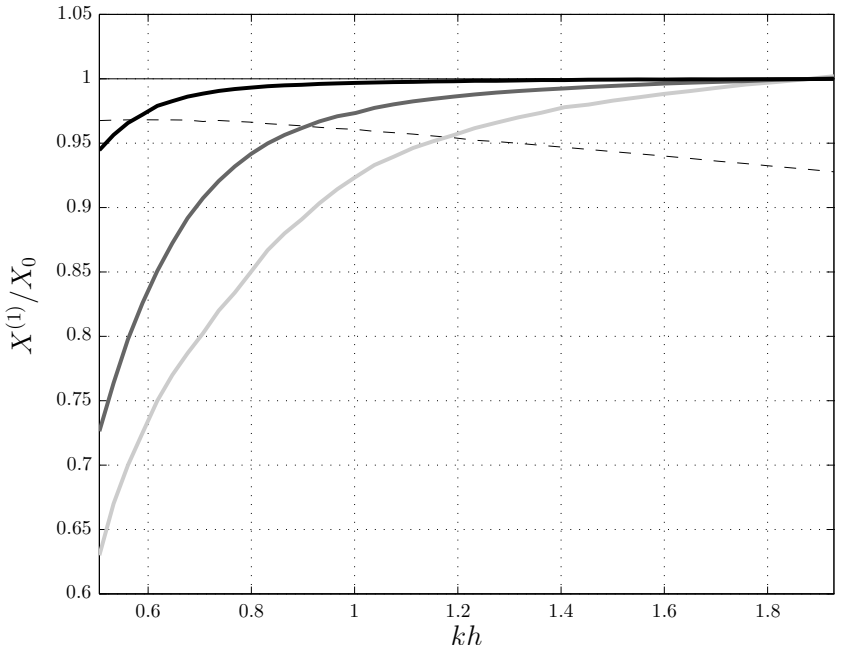


Figure 3.1: First-harmonic wavemaker displacement predicted by —— second-order wavemaker theory, and Stream-function wavemaker theory with —— $Ak = 0.05$, —— $Ak = 0.15$, —— $Ak = 0.25$ and — — $S = 1$.

3.2.3 Second-harmonic wavemaker displacement in position control

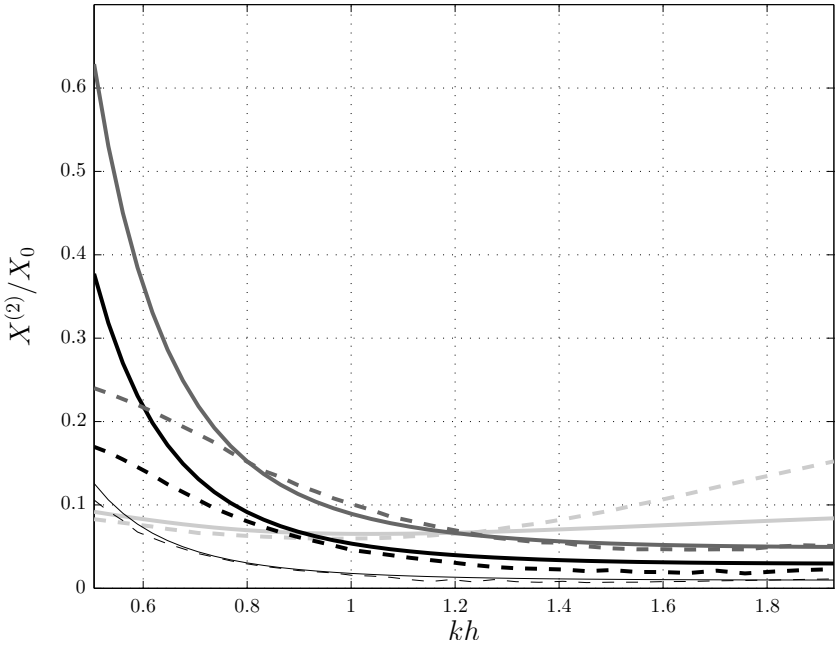
Figure 3.2 concerns both the magnitude (part (a)) and the phase (part (b)) of the normalised second-harmonic wavemaker displacement, $X^{(2)}/X_0$, required to eliminate the spurious free wave content (Chapter 2, §2.3.5). Within Figure 3.2, all solid lines refer to second-order calculations, whilst the dashed lines represent Stream-function theory. A number of distinct wave steepness cases are considered, including $Ak = 0.05$, $Ak = 0.15$, $Ak = 0.25$ and $S = 1$. The similarities and differences in the magnitude of $X^{(2)}/X_0$, Figure 3.2(a), based upon the two theories are as follows:

(i) For the range $0.8 \leq kh \leq 1.4$, second-order theory and Stream-function theory lead to very similar results.

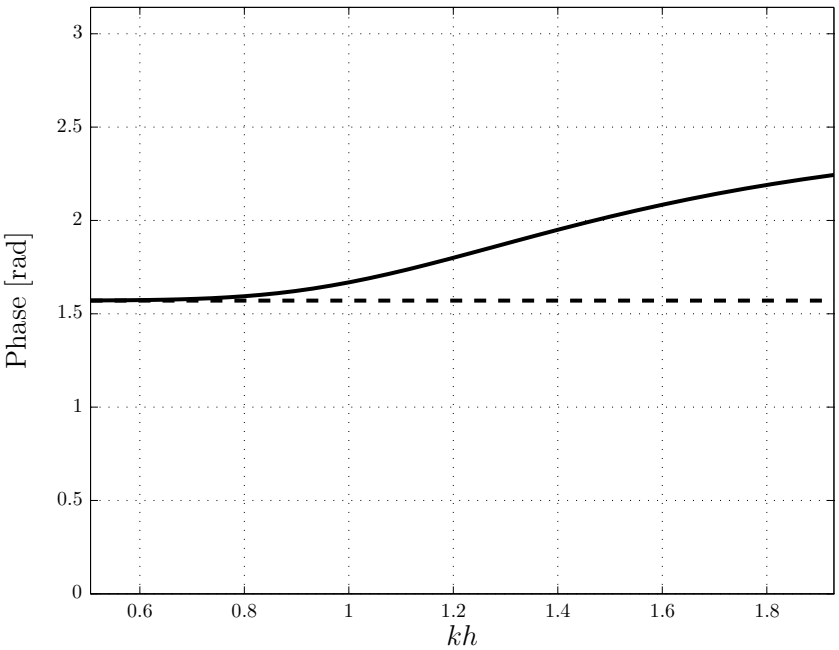
(ii) As kh increases beyond 1.4, some discrepancies arise between the two theories. In this context, it is important to note that Stream-function wavemaker theory also includes terms beyond second order. For example, at fourth order, additional second-harmonic wave components arise. In deep water and with $S = 1$, the steepness of the wave cases is such that second-harmonic, fourth-order terms become important, which explains the difference between the two theories for $kh > 1.4$ and $S = 1$.

(iii) For $kh < 0.8$, the second-harmonic wavemaker displacement predicted by second-order theory increases rapidly. It is well known that second-order theory leads to over predictions for combinations of small kh and large Ak. This over prediction is particularly evident for $Ak = 0.15$ and $Ak = 0.25$. As a result, Stream-function theory is likely to be more reliable for $kh < 0.8$, particularly as S exceeds unity.

(iv) For $S = 1$ (light grey line), the calculations by the two theories are very similar for $kh < 1.4$. This is as expected, given that $S = 1$ defines the limit



(a) Magnitude



(b) Phase

Figure 3.2: Normalised second-harmonic wavemaker displacement with (a) magnitude of $X^{(2)}/X_0$ and (b) phase of $X^{(2)}$. All solid lines correspond to second-order theory, and all dashed lines correspond to Stream-function theory. In both cases, the colours represent: —— $Ak = 0.05$, —— $Ak = 0.15$, —— $Ak = 0.25$ and —— $S = 1$.

of validity for second-order theory. Indeed, the close match between the two light grey lines provides an independent measure of the range of applicability of second-order wavemaker theory in shallow water conditions.

The phase of $X^{(2)}$, Figure 3.2(b), is readily explained. First, the phase information does not depend upon the wave steepness Ak, so that only two lines are shown. As before, the solid line corresponds to second-order theory, and the dashed line corresponds to Stream-function theory. In the case of Stream-function wavemaker theory, evanescent modes are not taken into consideration, so that the phase of $X^{(2)}$ is constant at $\pi/2$. In contrast, the increasing significance of the evanescent wave field with kh leads to a phase shift in $X^{(2)}$ if based upon second-order theory. The phase shift between the two theories becomes apparent from $kh \approx 0.8$, and increases to as much as 0.6 rad for $kh = 1.8$. This indicates that Stream-function wavemaker theory may not be effective in deeper water, where the evanescent wave field must be taken into consideration.

3.2.4 Second-harmonic force in force control

Figure 3.3 concerns the comparison of the two wavemaking theories under force control. The second-harmonic wavemaker displacement required to compensate for the spurious wave field is identical to that presented in Figure 3.2 and as discussed in Chapter 2 and Spinneken and Swan (2009*a*). However, in the force-control case, the demand quantity is a second-harmonic force. The normalised magnitude of this force, $F_c^{(2+)}/F^{(1)}$, is shown in Figure 3.3(a), with the phase information provided in Figure 3.3(b). The overall comparison between second-order theory and Stream-function theory is very similar to that observed in the context of the wavemaker displacement (Figure 3.2). The key difference between position control and force control is that the latter must take into account the nonlinear hydrodynamic feedback force. This is perhaps best observed in the phase of $F_c^{(2+)}$, Figure 3.3(b), as follows:

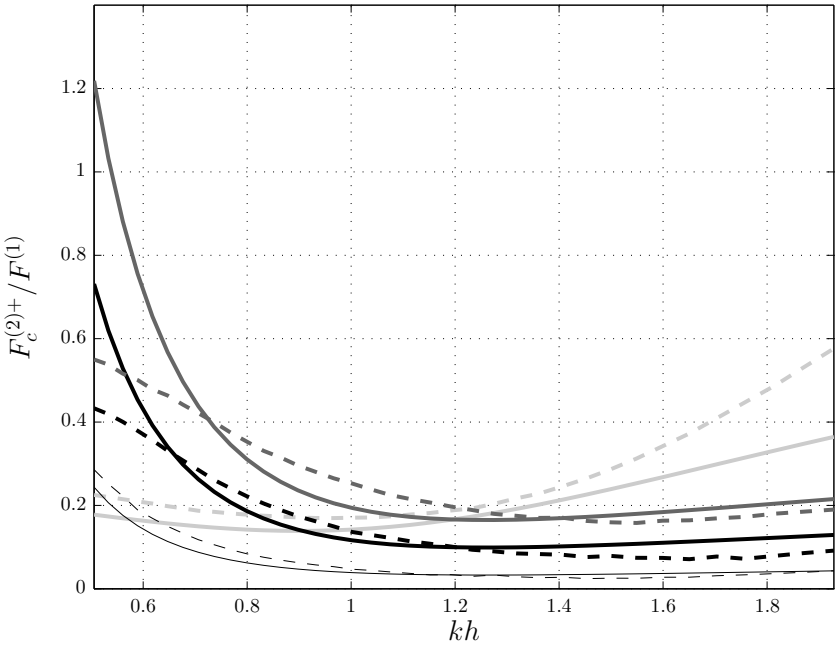
(i) The phase in Figure 3.3(b) is quite different from the phase observed on Fig-

ure 3.2(b). The phase difference between position control and force control is approximately $\pi/2$ in shallow water ($kh < 0.6$). The wave field in shallow water is dominated by the progressive wave field, and the evanescent modes are relatively small. As a result, the wavemaker force in shallow water is dominated by the associated radiation damping, which is in phase with the wavemaker velocity. The phase difference between the wavemaker displacement and the wavemaker velocity explains the phase shift of approximately $\pi/2$ for $kh < 0.6$.

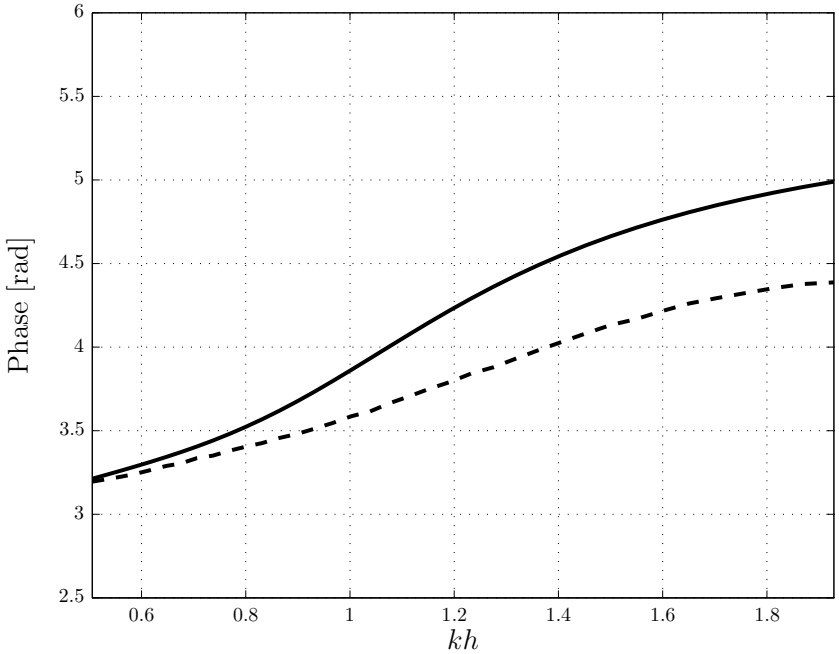
(ii) The phase for both theories increases with kh. Given that Stream-function wavemaker theory does not account for the evanescent wave field, this cannot be due to the evanescent modes. In fact, the observed phase shift in part relates to the wavemaker inertia (an additional force) and in part to the nonlinear hydrodynamic feedback.

(iii) The increasing phase difference between the two theories (solid line and dashed lines in Figure 3.3(b)) is once again attributed to the increasing importance of the evanescent wave field with increasing kh.

In summary, the above discussion highlighted that both second-order and Stream-function wavemaker theories have common ranges of applicability, but also exhibit distinct limitations. Stream-function wavemaker theory may offer some advances in shallow water; this being demonstrated experimentally in the following section.



(a) Magnitude



(b) Phase

Figure 3.3: Normalised second-harmonic correction force with (a) magnitude of $F_c^{(2+)}/F^{(1)}$ and (b) phase of $F_c^{(2+)}$. All solid lines correspond to second-order theory, and all dashed lines correspond to Stream-function theory. In both cases, the colours represent: —— $Ak = 0.05$, —— $Ak = 0.15$, —— $Ak = 0.25$ and —— $S = 1$.

3.3 Introduction to experimental investigation

All experiments shown herein were conducted in the Coastal Wave Flume located in the Hydrodynamic Laboratory at Imperial College London. This wave flume is equipped with a 0.6m wide sector-carrier piston-type wavemaker, as well as a highly optimised parabolic beach located 23m downstream of the wavemaker. For the purpose of the present work, the water depth was held constant at $h = 0.6$m throughout the flume. A schematic of the wave flume setup is provided in Figure 3.4.

The experimental investigation concerns the wave cases noted in Table 3.1. This includes three experimental sets with (i) a small-amplitude set, (ii) a base nonlinear set and (iii) an extended nonlinear set. For each case considered, Table 3.1 provides the non-dimensional water depth kh, the wave frequency $f = \omega/(2\pi)$, the nonlinearity parameter S, the steepness Ak and the actual wave amplitude A.

The small-amplitude set is included for comparison to linear wavemaker theory, particularly the wave field coefficient c_0 (§3.4.1). The nonlinear part of the investigation concerns cases in the range $0.5 < kh < 2$. In addition, the small-amplitude comparison also addresses wave cases that lie at the second harmonic of this range. This extended range is important in the generation of the second-harmonic correction wave, $\eta^{(23)+}$, as c_0 directly contributes to this latter expression (Appendix A). For the small-amplitude set, the wave nonlinearity is adjusted to $Ak = 0.05$ or $S = 0.33$, whichever is more restrictive. Within the base nonlinear set, the steepness is adjusted such that $Ak = 0.15$ for $kh > 0.9$ and $S = 1$ for $kh < 0.9$. As a result, these cases lie within the range of validity of second-order theory. In contrast, S is close to or in excess of unity for the extended nonlinear set; these cases are included to highlight the limitations of second-order theory (§3.6).

Given the nature of the relatively small quantities involved at higher orders, it is important that all instrumentation is of the upmost precision. The water surface elevation was recorded by seven tensioned resistive wire gauges, with the first wave gauge located at $x_g = 3.5h$ (Figure 3.4). This distance was considered

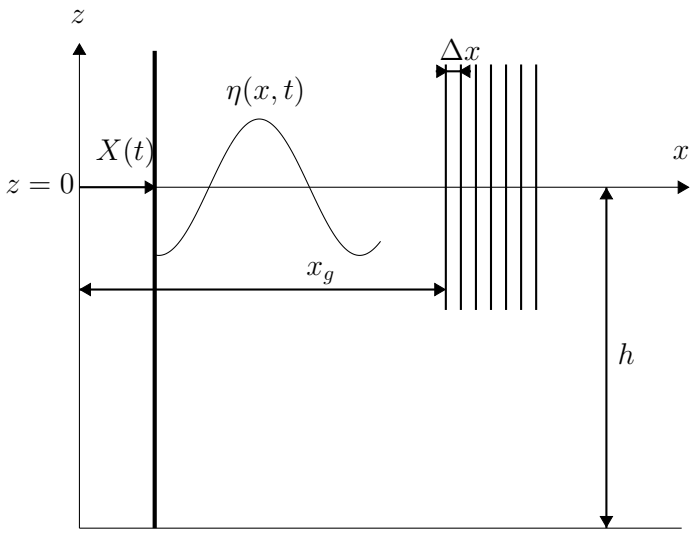


Figure 3.4: Setup of wave flume for regular wave investigation.

sufficiently far downstream of the wavemaker to neglect the effect of any evanescent modes. Subsequent wave gauges were located with a spacing of $\Delta x = h/3$. The wavemaker position was recorded using a high-precision laser displacement sensor directed towards the wavemaker front face.

3.4 Experimental validation of position control

3.4.1 Progressive wave field coefficient

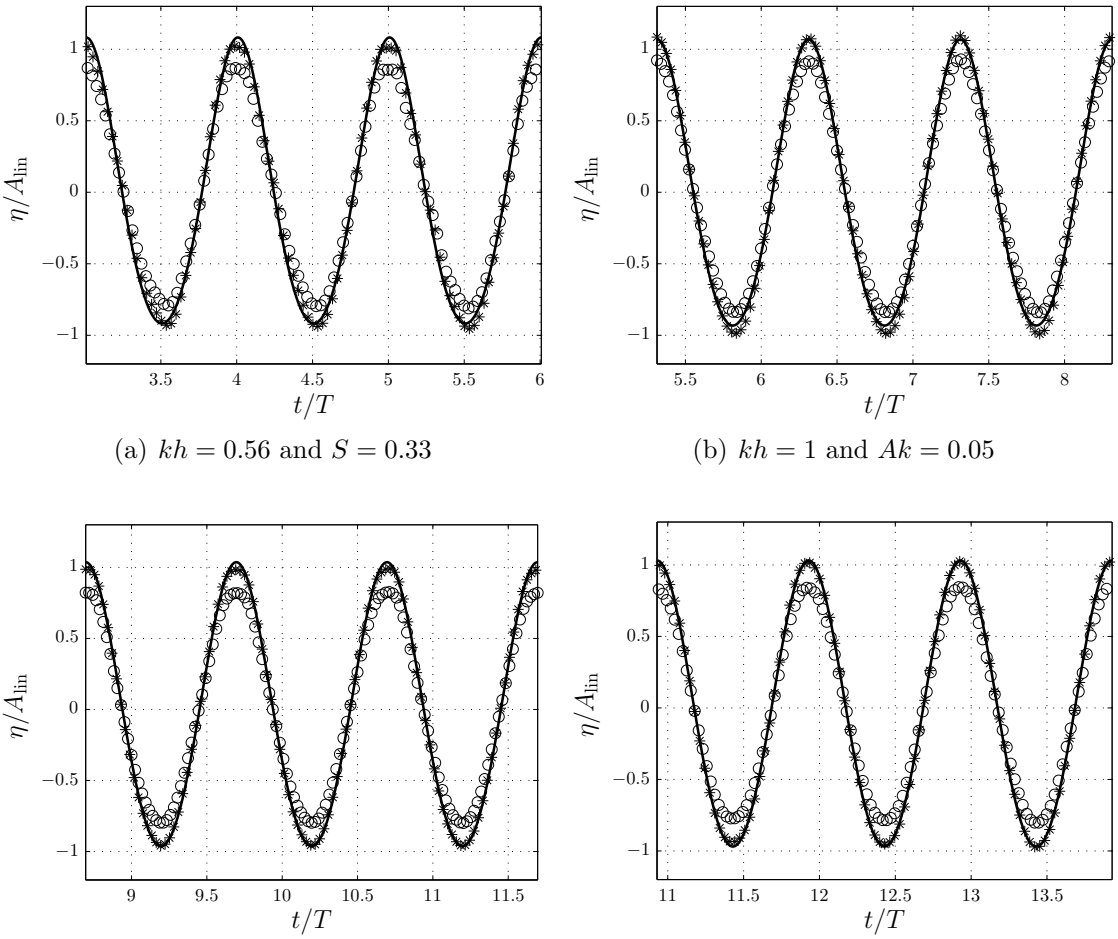
The progressive wave field coefficient c_0 relates, at first order, the wavemaker displacement to the produce progressive wave amplitude. The accuracy of the coefficient c_0 is crucial in operating a wavemaker as it provides the wavemaker displacement required to generate a wave at a specific amplitude. Within the second-order potentials ($\phi^{(21)+}$ and $\phi^{(22)+}$, Appendix A) the coefficient c_0 is squared, and the success of any second-order correction relies on an accurate knowledge of c_0. Therefore, an experimental assessment of the magnitude and phase of c_0 was conducted first.

Figure 3.5 shows four sample surface elevations, $\eta(t)/A_{\text{lin}}$, corresponding to

Table 3.1: Experimental wave parameters.

		Small amplitude			Base nonlinear			Extended nonlinear		
kh	f	S	Ak	A	S	Ak	A	S	Ak	A
[−]	[Hz]	[−]	[−]	[mm]	[-]	[-]	[mm]	[-]	[-]	[mm]
0.50	20/64	0.33	0.012	14	1	0.036	43			
0.56	22/64	0.33	0.016	17	1	0.048	51			
0.62	24/64	0.33	0.021	20	1	0.061	60	1.5	0.092	90
0.68	26/64	0.33	0.026	23	1	0.077	68			
0.74	28/64	0.33	0.032	26	1	0.095	77			
0.80	30/64	0.33	0.038	29	1	0.114	86			
0.86	32/64	0.33	0.045	31	1	0.136	94			
0.93	34/64	0.32	0.050	32	0.945	0.150	97			
1.00	36/64	0.27	0.050	30	0.819	0.150	90			
1.07	38/64	0.24	0.050	28	0.718	0.150	84			
1.15	40/64	0.21	0.050	26	0.637	0.150	78			
1.23	42/64	0.19	0.050	24	0.572	0.150	73	0.858	0.225	109
1.32	44/64	0.17	0.050	23	0.519	0.150	68			
1.40	46/64	0.16	0.050	21	0.476	0.150	64			
1.50	48/64	0.15	0.050	20	0.441	0.150	60			
1.60	50/64	0.14	0.050	19	0.412	0.150	56			
1.70	52/64	0.13	0.050	18	0.389	0.150	53			
1.81	54/64	0.12	0.050	17	0.370	0.150	50			
1.93	56/64	0.12	0.050	16	0.354	0.150	47			
2.18	60/64	0.11	0.050	14						
2.45	64/64	0.11	0.050	12						
2.75	68/64	0.10	0.050	11						
3.07	72/64	0.10	0.050	10						
3.41	76/64	0.10	0.050	9						
3.78	80/64	0.10	0.050	8						
4.16	84/64	0.10	0.050	7						
4.57	88/64	0.10	0.050	7						
4.99	92/64	0.10	0.050	6						
5.43	96/64	0.10	0.050	6						
5.89	100/64	0.10	0.050	5						
6.38	104/64	0.10	0.050	5						
6.88	108/64	0.10	0.050	4						

a subset of the small amplitude cases noted in Table 3.1. For the avoidance of any doubt, the normalisation is undertaken by A_{lin}, corresponding to the linearly calculated wave amplitude A. The figure is presented as four parts, with (a) $kh = 0.56$, (b) $kh = 1$, (c) $kh = 1.4$ and (d) $kh = 1.8$. In each case, the experimental data due to a wavemaking demand of $X_0 = A/c_0$ is shown by the discrete symbols $\circ$. The black solid line provides a theoretical comparison evaluated using Stream-



(a) $kh = 0.56$ and $S = 0.33$

(b) $kh = 1$ and $Ak = 0.05$

(c) $kh = 1.4$ and $Ak = 0.05$

(d) $kh = 1.8$ and $Ak = 0.05$

Figure 3.5: Water surface elevation $\eta(t)/A$ with $\circ$ experimental data corresponding to c_0, $*$ experimental data corresponding to $c_0{}'$ and ━━ theoretical prediction by Stream-function wave theory for a wave of linear amplitude A.

function theory, where the amplitude of this wave was computed from first-order wavemaker theory ($A = c_0 X_0$). In considering the data in Figure 3.5, it is clear that the experimentally achieved surface profiles are consistently smaller than those predicted by first-order wavemaker theory.

To investigate this further, Figure 3.6 shows the magnitude (part (a)) and the phase (part (b)) of the experimentally observed coefficient c_0, where the data corresponds to the full set of the small-amplitude cases (Table 3.1). The first-harmonic wavemaker displacement X_0 and the wave amplitude A were obtained by applying a Discrete Fourier Transform (DFT) to the respective experimental

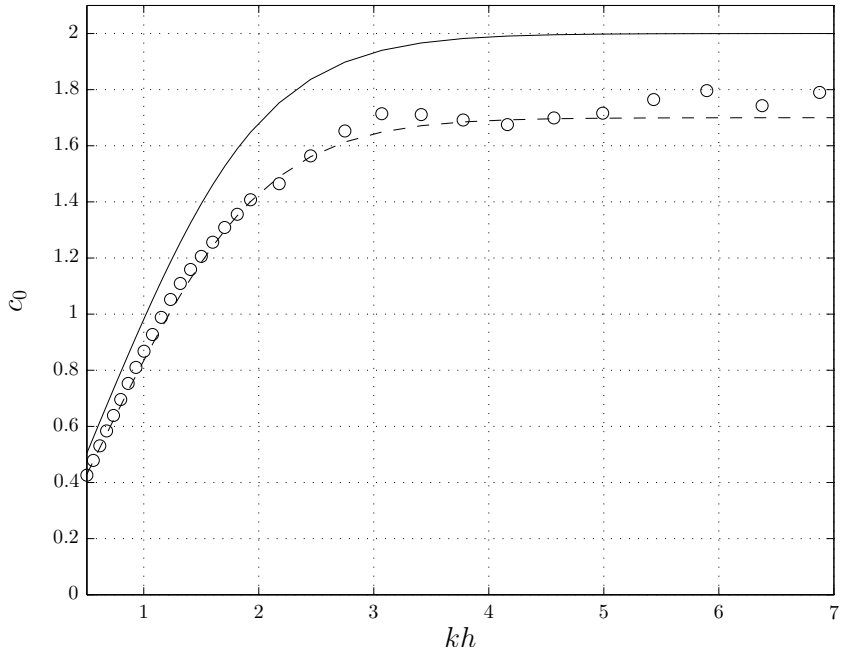
recordings, retaining the first-harmonic information only. The magnitude of the experimentally observed coefficient c_0 was then calculated as the magnitude ratio of $|A|$ and $|X_0|$; the phase being obtained by subtracting the respective phases $\arg(A)$ and $\arg(X_0)$.

In considering the phase of c_0 in Figure 3.6(b), a good agreement between the theoretical prediction and the experimentally observed data is found throughout. The theoretical phase of the first-order wavemaker displacement is $\pi/2$ rad. This constant phase is a direct consequence of the progressive wave being in phase with the wavemaker's velocity, and this constant phase relationship is matched well by the experimental data. The maximum departure between the theoretical prediction and the experimental observation is 0.22 rad (Figure 3.6(b)).

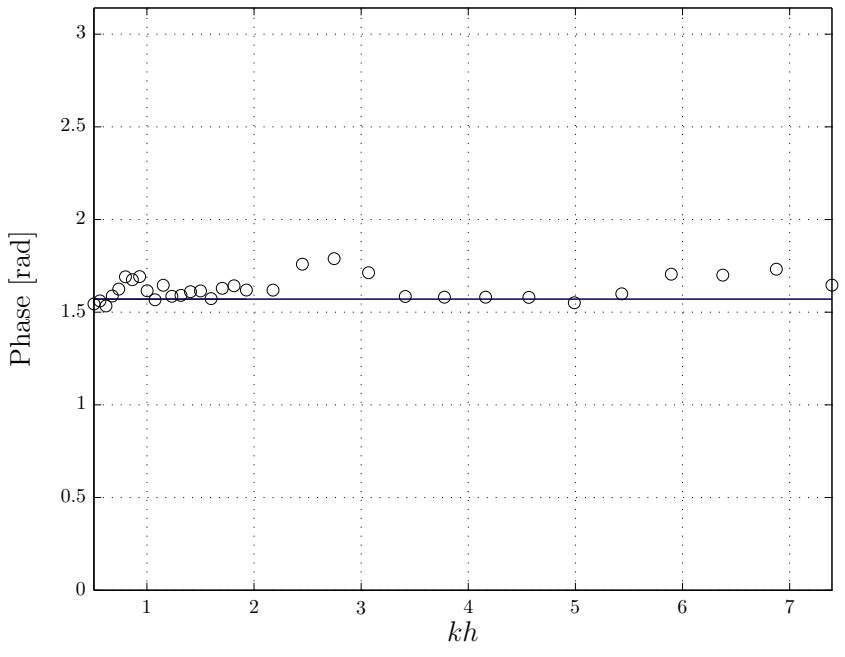
In contrast to the phase information, significant departures arise in the magnitude of c_0 as shown in Figure 3.6(a). Within Figure 3.6(a), the solid line represents the theoretical magnitude of c_0 based on equation (2.8). The discrete points (symbol $\circ$) represent the experimental data, which are consistently lower than the predicted values. Indeed, the maximum departure is 16%, the average departure is 15%, and the theoretical coefficient consistently over predicts the amplitude of the generated wave field. A similar trend was reported by Ursell et al. (1960) who obtained an estimation of c_0 that was 10% lower than the theoretical prediction. According to Ursell et al. (1960) such a discrepancy may be due to:

(i) Fluid leakage past the wavemaker due to the gaps between the flume and the wavemaker edges. In the context of the present experimental investigation, an optimisation of the wavemaker geometry was carried out by reducing all side gaps from approximately 20mm to less than 5mm. As a result, fluid leakage is expected to only have a very minor role in explaining the observed departures. The reduction in the wavemaker gap led to a small improvement in c_0, from an average departure of 17% to the average departure of 15% observed in Figure 3.6.

(ii) Finite-amplitude effects. To address this, the experimental comparison was



(a) Magnitude of c_0



(b) Phase of c_0

Figure 3.6: Progressive wave field coefficient with (a) magnitude and (b) phase showing ∘ experimental data —— theoretical prediction of c_0 and — — adjusted coefficient $c_0{}' = 0.85c_0$.

also undertaken for the base nonlinear set noted in Table 3.4. No marked difference between the small-amplitude set and the base nonlinear set could be observed; the departure of c_0 being 15% in average in both cases.

It is suspected that the experimentally observed departures are associated with viscous effects. In part, this may be due to skin-friction as the fluid moves vertically along the front of the wavemaker. A second contribution is likely to be due to small vortices being shed at the base of the wavemaker. The wavemaker side gaps were reduced to 5mm, and the gap underneath the wavemaker is also approximately 5mm when the wavemaker is in its mean position. However, over the full stroke of the wavemaker, this bottom gap increases up to 15mm, as the sector-carrier motion describes an arc of finite radius.

These effects lead to a dissipation of a part of the wavemaker-induced energy. Nevertheless, a detailed investigation of non-potential wavemaker effects lies outside the scope of the present PhD. For the purpose of the experimental investigations to follow, a corrected progressive wave field coefficient $c_0{}'$ was taken as the reference for the application of linear wavemaking theory. This coefficient $c_0{}'$ is represented by the dashed line in Figure 3.6(a) and was designed to be both proportional to the theoretical magnitude of c_0, and to match the experimental magnitude of c_0. These two conditions provide a coefficient $c_0{}'$ which is given by $c_0{}' = 0.85c_0$. Figure 3.5 demonstrates the applicability of this modified wave field coefficient, where the experimental data with symbol $*$ is due to a wavemaker demand of $X_0 = A/c_0{}'$.

3.4.2 First-order and second-order control

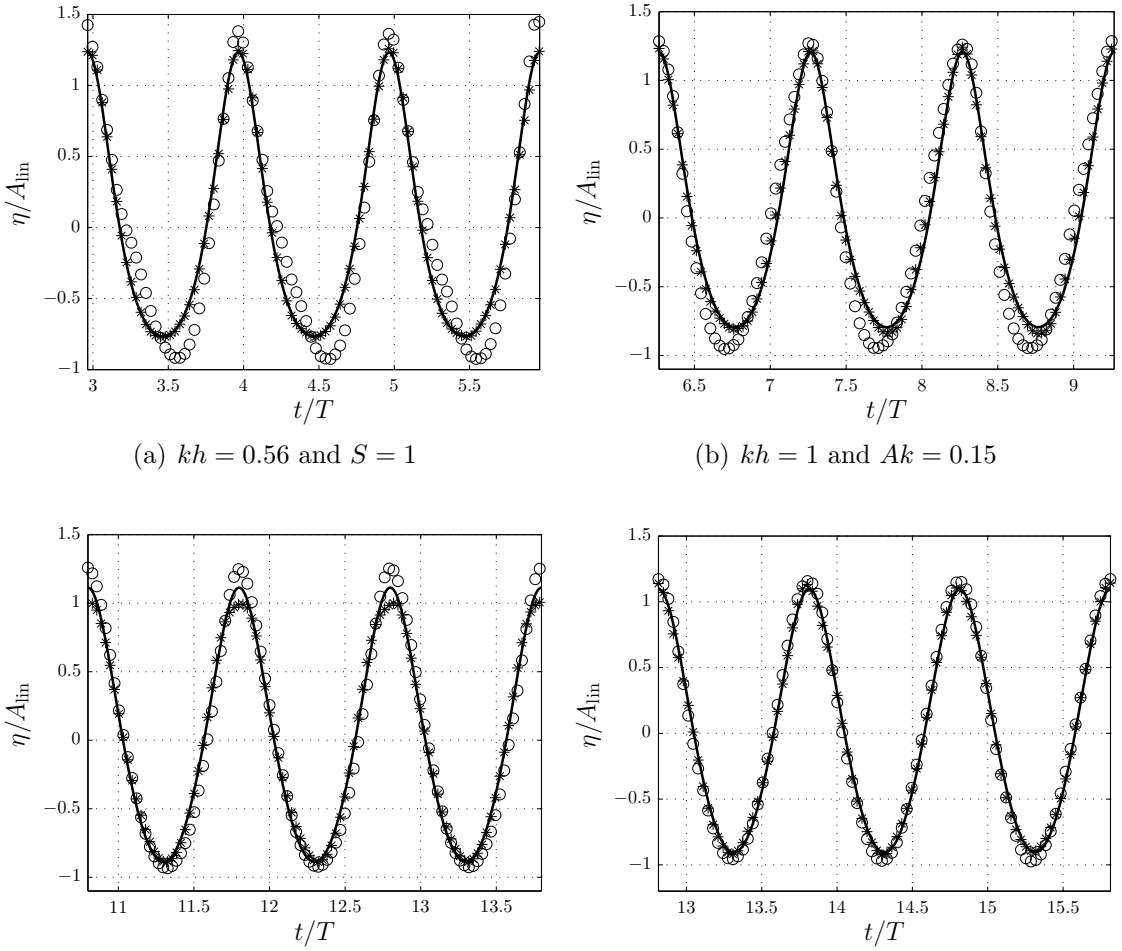
Adopting the modified coefficient $c_0{}'$, the base nonlinear test cases described in Table 3.1 were produced. The test cases were generated twice, first based upon a first-order control signal and, subsequently, based upon a second-order control signal. Figure 3.7 concerns a comparison of the generated surface elevations, recorded at $x = 3.5h$, with (a) $kh = 0.56$, (b) $kh = 1$, (c) $kh = 1.4$ and (d)

$kh = 1.8$. Within Figure 3.7, the data with symbol $\circ$ correspond to first-order control, and the data with symbol $*$ relate to second-order control. In addition, the black solid line indicates the theoretical Stream-function solution for comparison.

Considering the case with $kh = 0.56$ first (Figure 3.7(a)), it is clear that first-order control leads to a significant departure from the theoretically predicted surface elevation; this being due to the presence of a pronounced spurious free wave. In contrast, the second-order control case is in close agreement with the theoretical prediction, providing evidence for the successful suppression of the spurious free wave content. Similar arguments apply to the case with $kh = 1$ in Figure 3.7(b). For $kh = 1.4$, Figure 3.7(c), the second-order control case is markedly different from first-order control, but it is difficult to argue which of these two represents a better match to the theoretical prediction. In the final case, Figure 3.7(d) with $kh = 1.8$, it is difficult to distinguish between the two cases based upon a visual comparison alone.

To provide further evidence of the success of second-order control, an extended analysis was undertaken on the recordings at all seven wave gauges (Figure 3.4). The second harmonic of the surface elevation recorded at each of the seven wave gauges contains information about both the bound and the free wave content. To separate these two contributions, the methodology introduced by Lin and Huang (2004) was applied to each of the wave cases. Within this analysis, a DFT is applied to the recorded water surface elevation, and a least-square method leads to the separation of the free and bound components; full detail being provided in Lin and Huang (2004).

Figure 3.8 shows the amplitude and the phase of the bound wave component, $A^{(21)+}$, under first-order position control. In considering this data, it should first be noted that the discontinuity at $kh \approx 0.9$ relates to the change from $Ak = 0.15$ to $S = 1$ (Table 3.1). Taken as a whole, the bound wave content illustrated in Figure 3.8 matches the theoretical prediction well. The bound wave amplitude is in average 13% higher than the prediction by Schäffer (1996), with a largest departure of 48%. However, it should be noted that this largest departure arises



(a) $kh = 0.56$ and $S = 1$

(b) $kh = 1$ and $Ak = 0.15$

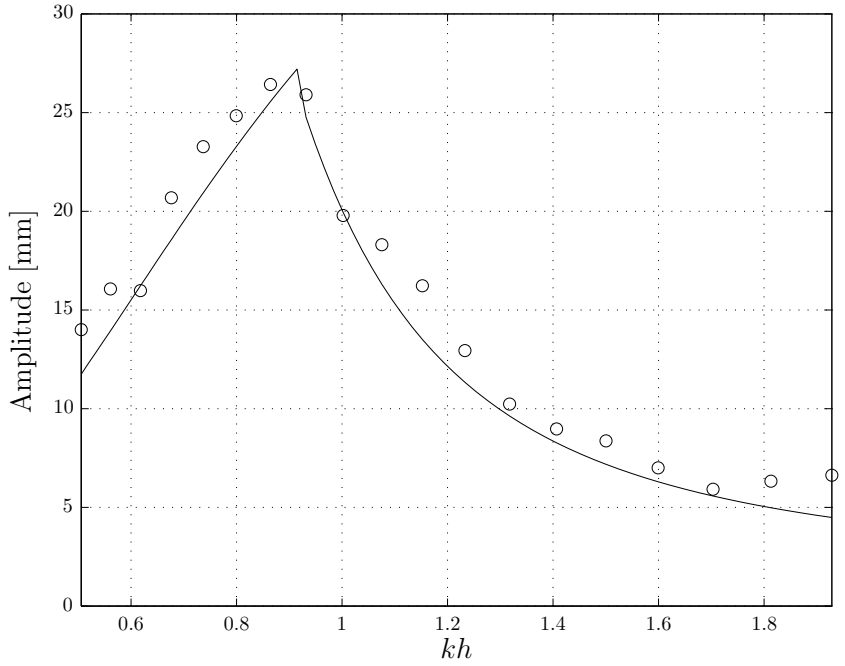
(c) $kh = 1.4$ and $Ak = 0.15$

(d) $kh = 1.8$ and $Ak = 0.15$

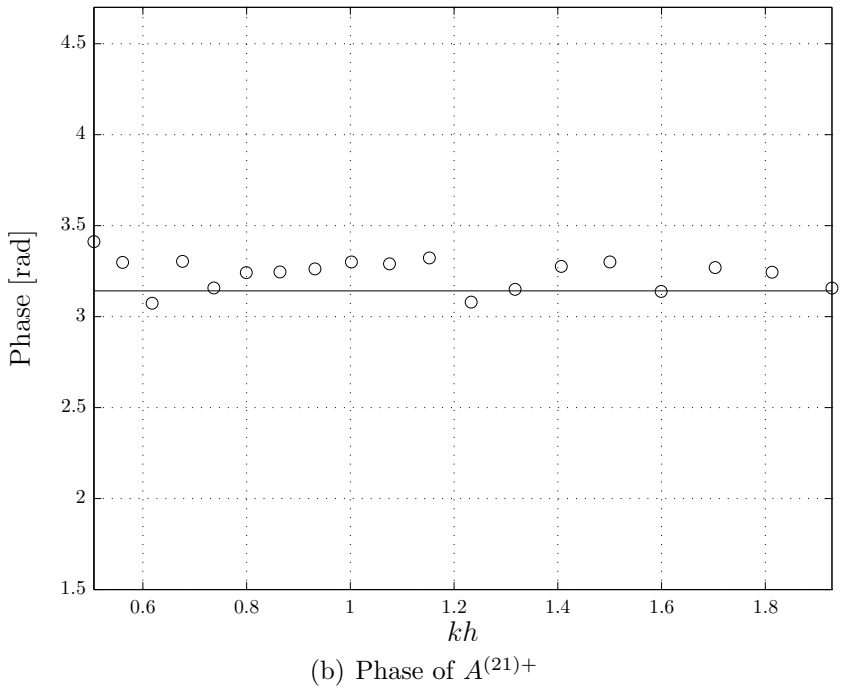
Figure 3.7: Water surface elevation $\eta(t)/A$ with ——— Theoretical Stream-function solution and experimental data based upon ∘ first-order position control and ∗ second-order position control.

for the shortest wave case ($kh \approx 2$), where the absolute magnitude of the bound wave content is relatively small. A good match can also be observed between the measured bound wave phase and the prediction by Schäffer (1996), Figure 3.8(b). The predicted wave phase is π rad, and the experimentally observed phase closely matches this prediction, with a maximum departure of 8.6%.

The free wave amplitude, $A^{(22)+}$, under first-order position control is shown in Figure 3.9(a), and is seen to be consistently lower than the theoretical prediction by Schäffer (1996). On average, the spurious free wave content is 24% lower than expected. Perhaps more importantly, some very large departures can be observed

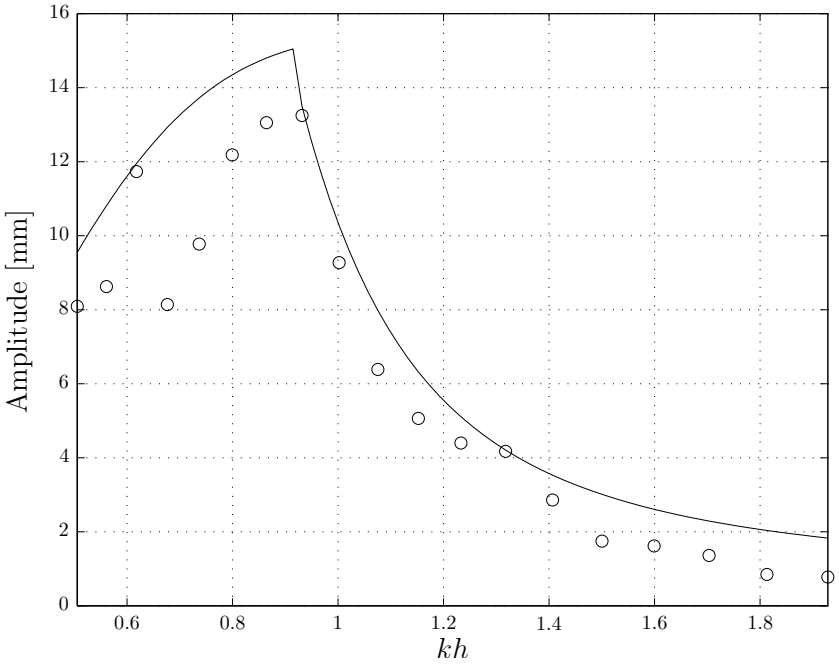


(a) Magnitude of $A^{(21)+}$

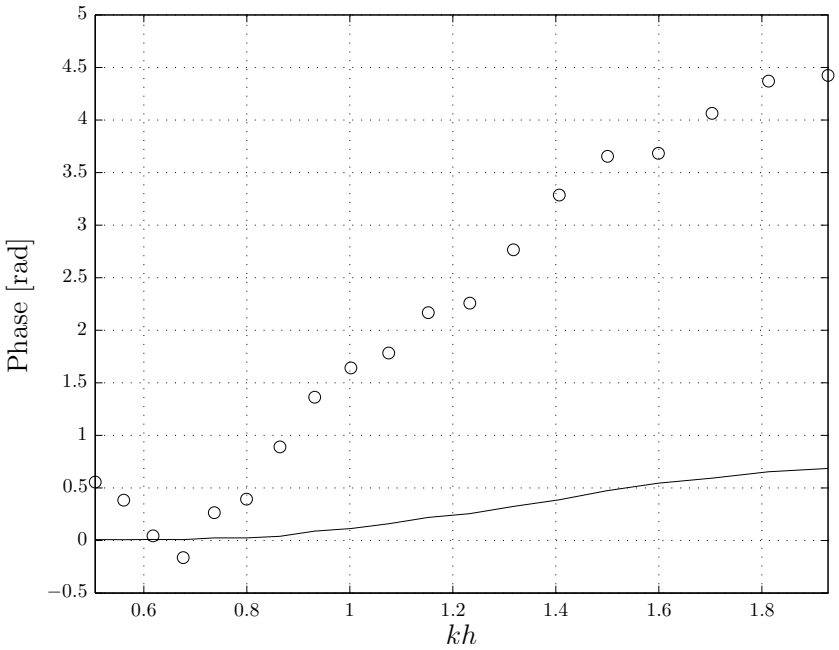


(b) Phase of $A^{(21)+}$

Figure 3.8: Magnitude and phase of the bound wave content $A^{(21)+}$ with —— theoretical calculation and ∘ experimental observation.



(a) Magnitude of $A^{(22)+}$



(b) Phase of $A^{(22)+}$

Figure 3.9: Magnitude and phase of the free wave content $A^{(22)+}$ with —— theoretical calculation and ∘ experimental observation.

in the spurious free wave phasing, Figure 3.9(b). Indeed, the measured spurious free wave phase only matches the prediction in shallow water, where its value is

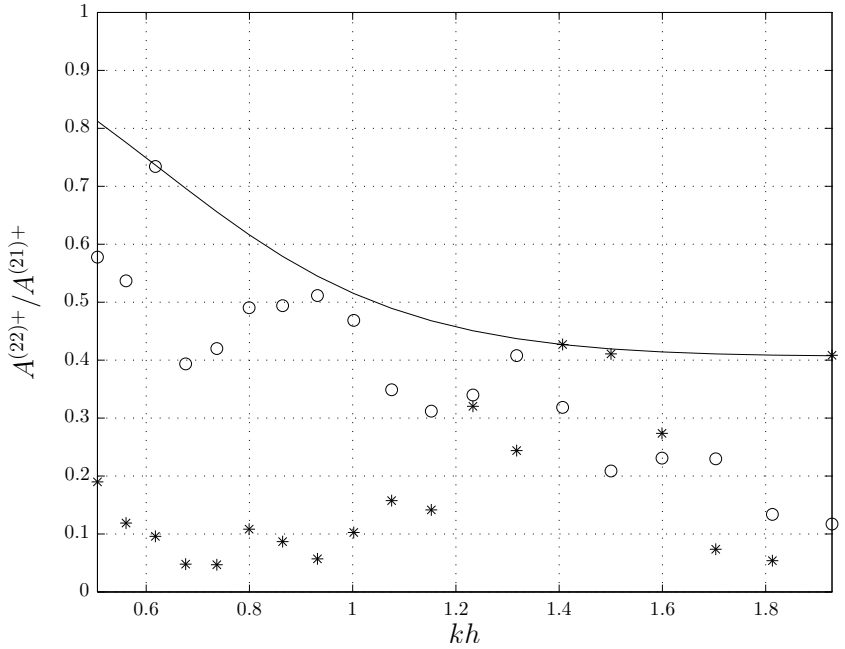


Figure 3.10: Spurious free wave content in position control with —— theoretical content under first-order control and experimental data based on ∘ linear and ∗ second-order wavemaker theory.

approximately zero. In deeper water conditions (larger kh), the experimentally observed phase increases significantly more rapid than expected from the theoretical prediction, reaching a phase in excess of 4 rad for $kh = 2$. In contrast, the theoretically predicted phase for $kh = 2$ doest not exceed 1 rad.

This experimentally observed phase shift has important implications on the spurious free wave correction. Figure 3.10 shows the non-dimensional spurious wave content $A^{(22)+}/A^{(21)+}$ for both a linear position-control demand (symbol ∘, based upon $X^{(1)}$) and a second-order position-control demand (symbol ∗, based upon $X^{(1)} + X^{(2)}$). The first-order case, based on $X^{(1)}$ alone, directly corresponds to the ratio of the magnitude data shown in Figures 3.8(a) and 3.9(a), and any departures observed in Figure 3.10 are directly attributed to the departures observed in Figures 3.8(a) and 3.9(a).

In considering the second-order control case (symbol ∗), the approach presented is successful in cancelling out the spurious free wave content for most of the cases with $kh < 1.2$. To be entirely clear, a spurious wave content of $A^{(22)+}/A^{(21)+} = 0$ corresponds to the absence of any spurious free wave ($\eta^{(22)+} = 0$), which is the

desired condition. For $0.5 < kh < 1.2$, the average remaining spurious content is approximately 10%, so that the spurious free wave only corresponds to one tenth of the bound content.

In contrast, the cancellation of the spurious free wave is not entirely successful beyond $kh = 1.2$. This may be due to two different effects:

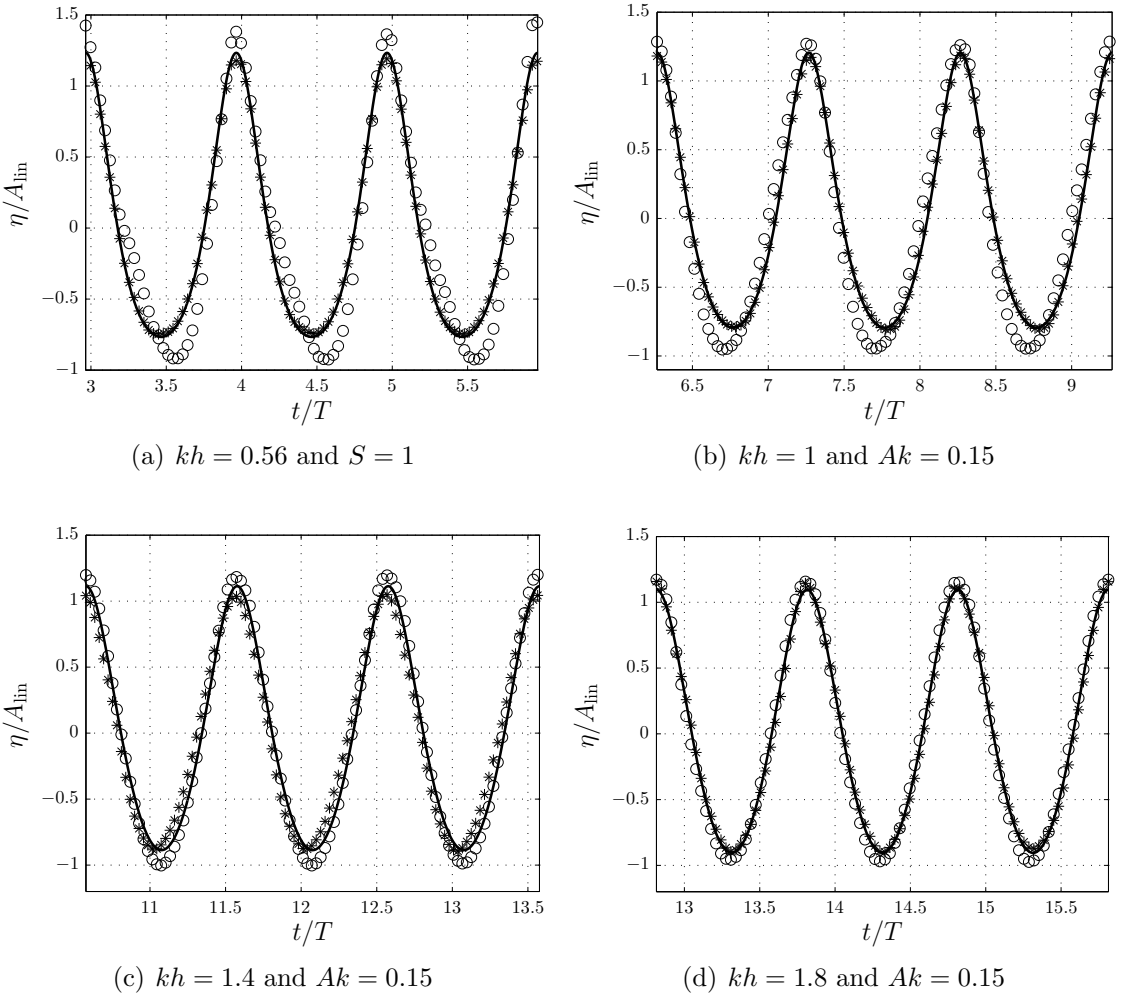
(i) The phase of the correction term $\eta^{(23)+}$ is derived from the phase of the theoretical spurious free wave $\eta^{(22)+}$. Given the large discrepancies in the phase of the spurious free wave observed in Figure 3.9(b), it is likely that the theory is unable to provide for a complete spurious wave suppression in intermediate water depth conditions due to a phase mismatch.

(ii) The wavemaker may be unable to correctly reproduce the desired correction term $\eta^{(23)+}$ due to limitations in the control. In this context, it is important to highlight that the required second-harmonic wavemaker displacement $X^{(2)+}$ is a small quantity at relatively high frequency.

To identify the primary cause of the departures in intermediate water ($kh > 1.2$), an additional set of test cases was considered. Within this additional test series, the desired correction term was produced in the absence of the first-harmonic wave; the wavemaker displacement being equal to $X^{(2)+}$ only. The results of this verification (not shown herein) provided an excellent agreement between the predicted values and the experimental data, confirming that the wavemaker is indeed capable of producing the desired correction term. This confirms that (ii) above is not responsible for the unsuccessful cancellation of the spurious free wave in intermediate water. As a consequence, the inability to correctly predict the phase of the second-order free wave, (i) above, is the most probable reason for the failure of the second-order wavemaker theory in intermediate water conditions. An experimentally derived solution to this issue will be presented in §3.4.4.

3.4.3 Stream-function based correction

The present section highlights the differences that arise when the nonlinear position-control demand is based upon the Stream-function wavemaker theory by Zhang and Schäffer (2007). Figure 3.11 provides the water surface elevation for four cases, where the selection of cases ($kh = 0.56$, $kh = 1$, $kh = 1.4$ and $kh = 1.8$) and the data representation is very similar to that adopted in the context of Figure 3.7. In contrast to Figure 3.7, the data with symbol $*$ in Figure 3.11 relate to a Stream-function demand. However, despite this different type of control, the



(a) $kh = 0.56$ and $S = 1$

(b) $kh = 1$ and $Ak = 0.15$

(c) $kh = 1.4$ and $Ak = 0.15$

(d) $kh = 1.8$ and $Ak = 0.15$

Figure 3.11: Water surface elevation $\eta(t)/A$ with ——— Theoretical Stream-function solution and experimental data based upon $\circ$ first-order position control and $*$ Stream-function position control.

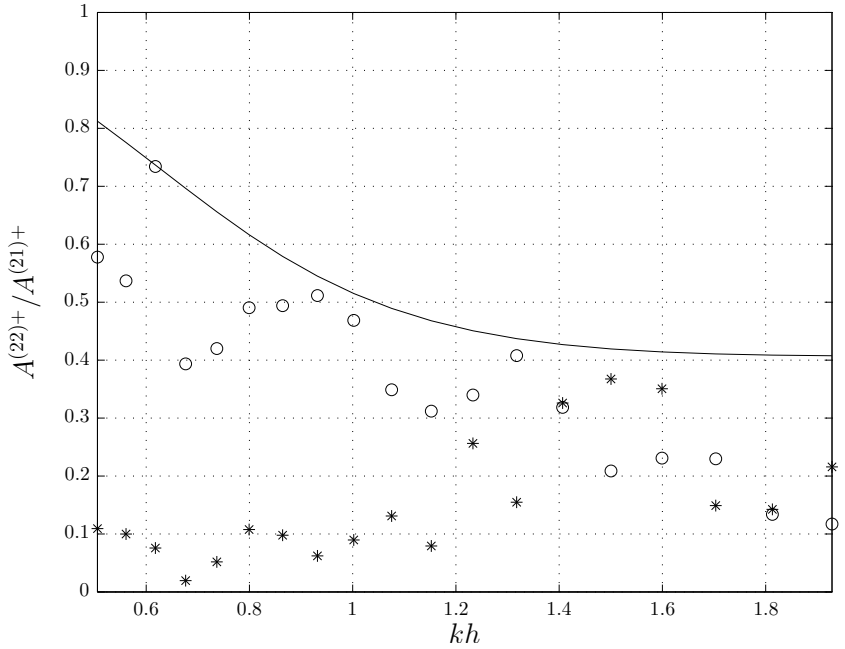


Figure 3.12: Spurious free wave content in position control with —— theoretical content under first-order control and experimental data based on ∘ first-order control and ∗ Stream-function control.

comments made in the context of Figure 3.7 largely apply to Figure 3.11. For $kh = 0.56$ and $kh = 1$ (Figure 3.11 (a) and (b)), the nonlinear Stream-function input clearly leads to an improvement over first-order control; this being less clear for $kh = 1.4$ and $kh = 1.8$ (Figure 3.11 (c) and (d)).

Figure 3.12 shows the non-dimensional superharmonic spurious free wave content $A^{(22)+}/A^{(21)+}$, making a direct comparison between (i) the theoretically expected content under first-order control (black line), (ii) the experimental data relating to a first-order demand signal (symbol ∘) and (iii) the experimental data relating to the Stream-function demand (symbol ∗). Observing the data in Figure 3.12, it is evident that the spurious free wave content based upon the Stream-function demand is similar to the spurious free wave content based on the second-order theory (Figure 3.10). In close similarity to the second-order demand, the Stream-function wavemaker theory succeeds in cancelling the spurious free wave content for $kh < 1.2$, but is unable to provide a full compensation beyond $kh = 1.2$. The causes for this discrepancy may be two-fold:

(i) The data provides further evidence for the effects discussed in §3.4.2. Indeed, the experimental data confirms that the unsuccessful cancellation of the spurious free wave for $kh > 1.2$ is not specific to second-order wavemaker theory. As a result, this phenomenon is not directly related to the type of theoretical expansion, but is likely to be caused by the underlying assumption of potential flow theory.

(ii) In considering the development of Stream-function wavemaker theory (§2.3.6), it is important to note that all evanescent mode interactions are neglected. With the evanescent modes becoming more relevant for increasing kh, the departures observed in Figure 3.12 may also be attributed to this latter cause.

3.4.4 Alternative second-order correction

Sections §3.4.2 and §3.4.3 demonstrated that both second-order control and Stream-function control are unable to fully eliminate the spurious free wave for $kh > 1.2$; this being due a phase shift in the underlying free wave $\eta^{(22)+}$ (Figure 3.9(b)). To resolve this, an adequate phase correction in the second-order wavemaker displacement must be introduced. Two methodologies were considered:

(i) The corrected phase of the transfer function $\mathscr{F}^+$ is directly based upon the experimentally obtained phase of the spurious free wave $\eta^{(22)+}$ as shown in Figure 3.9(b).

(ii) The corrected phase of the transfer function $\mathscr{F}^+$ is obtained through an approach that seeks to minimise the spurious free wave content at each frequency. To achieve this, the spurious wave content was minimised experimentally for the cases of frequency $kh = 0.5$, $kh = 1$ and and $kh = 1.6$; a polynomial regression giving the corrected phase for the remaining frequencies of interest.

In both approaches (i) and (ii) the magnitude of $\mathscr{F}^+$ remains unchanged. A polynomial regression provided a sixth- and a fourth-order polynomial ap-

Table 3.2: Polynomial regression of the corrected phase of the transfer function $\mathscr{F}^+$ based on the measured phase of the spurious free wave (Method (i)) and an experimental optimisation approach (Method (ii)).

Order	Method (i)	Method (ii)
0	58.882	0.924
1	−315.047	4.943
2	666.139	−9.283
3	−719.058	7.062
4	424.855	−1.658
5	−130.559	
6	16.312	

proximation for approach (i) and (ii) respectively (Table 3.2). These polynomials were subsequently used to determine the phase for any case in the range $0.504 \leq kh \leq 1.926$. Figure 3.13 shows the phase of the transfer function $\mathscr{F}^+$ as provided by Schäffer (1996) (solid line), the phase according to method (i) (line $-\cdot-$) and the phase according to method (ii) (line $--$). Method (i) effectively describes the phase shift observed previously in Figure 3.9(b). In contrast, method (ii) leads to a substantially reduced phase shift, which lies much closer to the analytical prediction by Schäffer (1996).

Figures 3.14 and 3.15 show sample surface elevations for method (i) and (ii) respectively; the data representation and selection of case being as discussed previously. For $kh = 0.56$ (Figure 3.14(a) and Figure 3.15(a)) the two methods yield very similar results. This is as expected, given the phase of approximately zero in Figure 3.13.

Figure 3.14(b), with $kh = 1$, clearly demonstrates that method (i) fails to successfully correct for the spurious wave content. Indeed, this method leads to a significantly larger spurious wave than the uncorrected second-order compensation (Figure 3.7(b)). In contrast, method (ii) achieves an excellent spurious wave suppression for $kh = 1$, as evident by the surface elevation shown in Figure 3.15(b). Furthermore, this method is also successful for $kh = 1.4$ and $kh = 1.8$ (Figures 3.15(c) and 3.15(d)), and delivers the most consistent results of all method considered thus far.

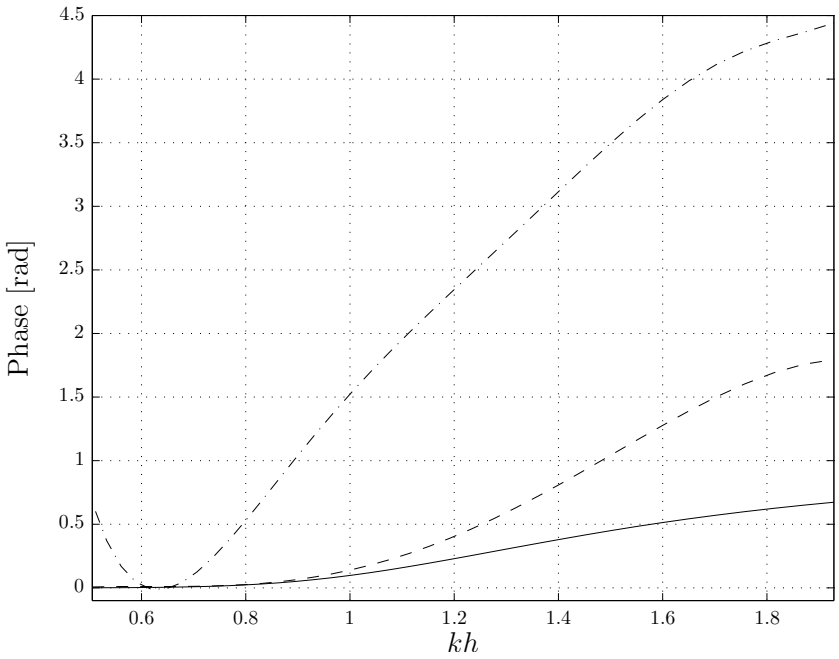
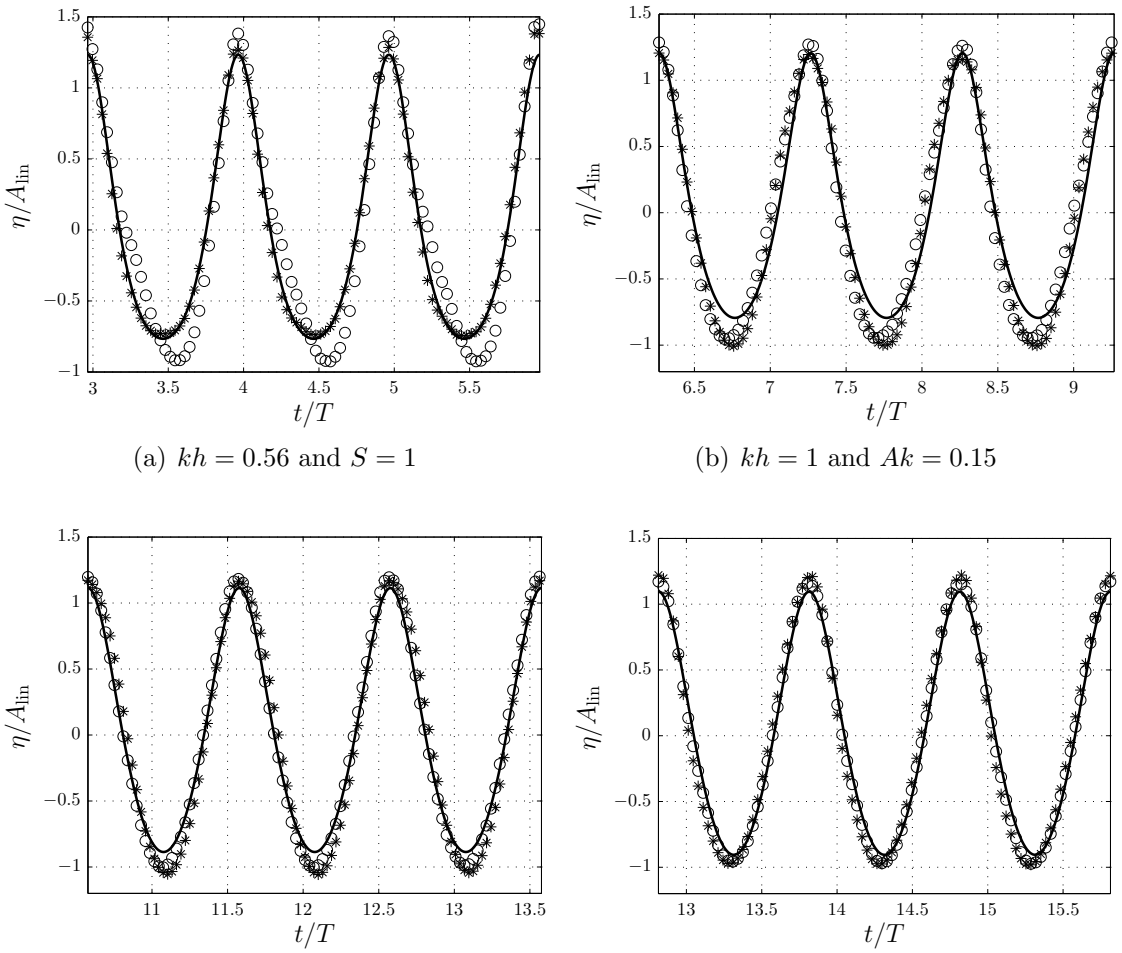


Figure 3.13: Phase of the complex transfer function $\mathscr{F}^+$ based on —— theory by Schäffer (1996), – · – the measured phase of the spurious free wave at first order (method (i)), and – – an experimental optimisation approach (method (ii)).

This is confirmed in Figure 3.16, showing the spurious free wave content for the corrected phase methods (i) (symbol +) and (ii) (symbol $*$). The spurious free wave content based upon the experimental optimisation approach remains very small for all kh, with a maximum free wave content of 20%. In contrast, method (i) provides a very poor second-order correction, and does not eliminate the spurious free wave.

In considering the above evidence, it is surprising that the optimal phase of the transfer function $\mathscr{F}^+$ does not correspond to the phase of the spurious free wave observed in Figure 3.9(b). The term $\mathscr{F}^+$ is derived such that the correction wave $\eta^{(23)+}$ is exactly out of phase (180 degrees phase shift) with the spurious free wave $\eta^{(22)+}$. As a result, any phase shift in $\eta^{(22)+}$ should also apply to $\eta^{(23)+}$ and therefore $\mathscr{F}^+$. This phenomenon remains unexplained. Nevertheless, method (ii) provides an alternative means of obtaining the optimum phase of $\mathscr{F}^+$.



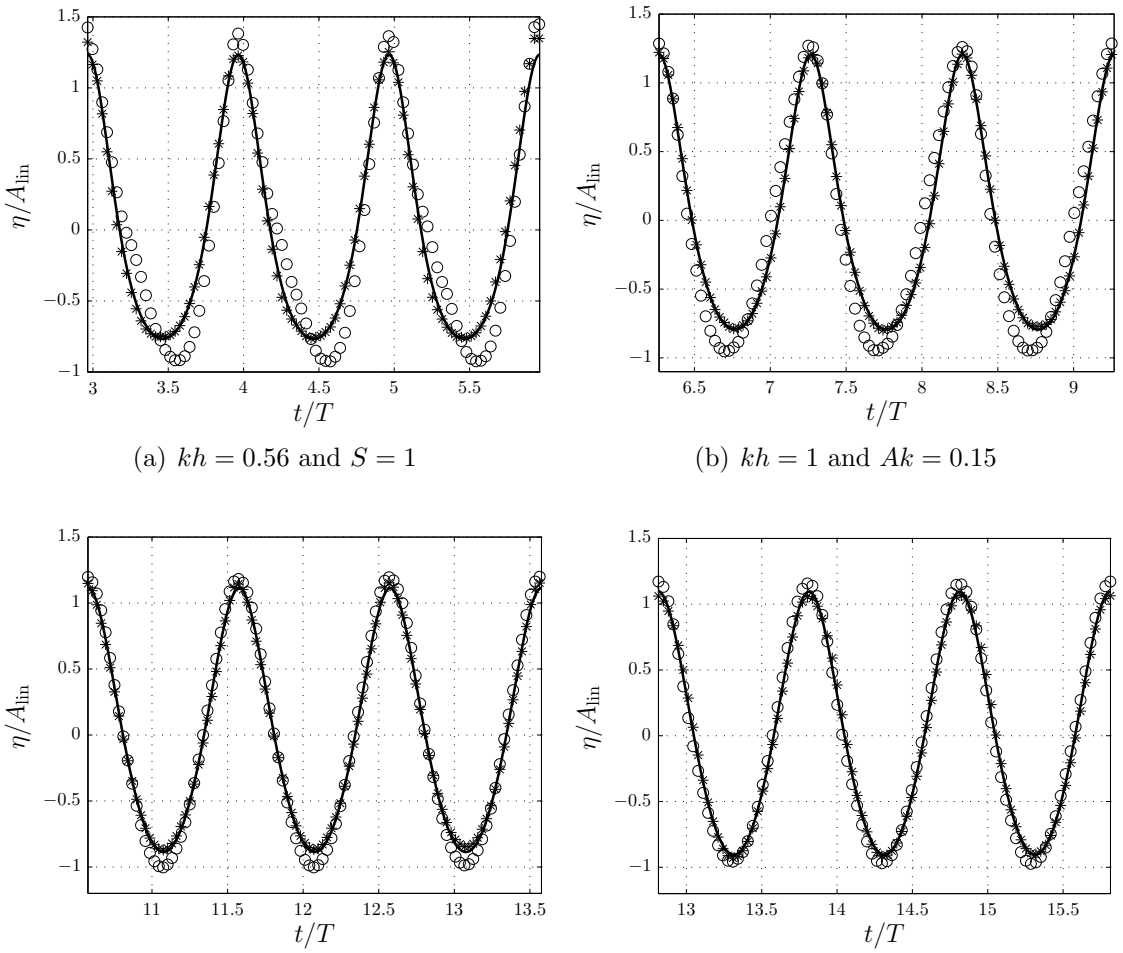
(a) $kh = 0.56$ and $S = 1$

(b) $kh = 1$ and $Ak = 0.15$

(c) $kh = 1.4$ and $Ak = 0.15$

(d) $kh = 1.8$ and $Ak = 0.15$

Figure 3.14: Water surface elevation $\eta(t)/A$ with ——— Theoretical Stream-function solution and experimental data based upon ∘ first-order position control and ∗ Second-order correction with experimentally obtained phasing of $\eta^{(22)+}$.



(a) $kh = 0.56$ and $S = 1$

(b) $kh = 1$ and $Ak = 0.15$

(c) $kh = 1.4$ and $Ak = 0.15$

(d) $kh = 1.8$ and $Ak = 0.15$

Figure 3.15: Water surface elevation $\eta(t)/A$ with ——— Theoretical Stream-function solution and experimental data based upon ∘ first-order position control and ∗ second-order correction with experimental phase optimisation.

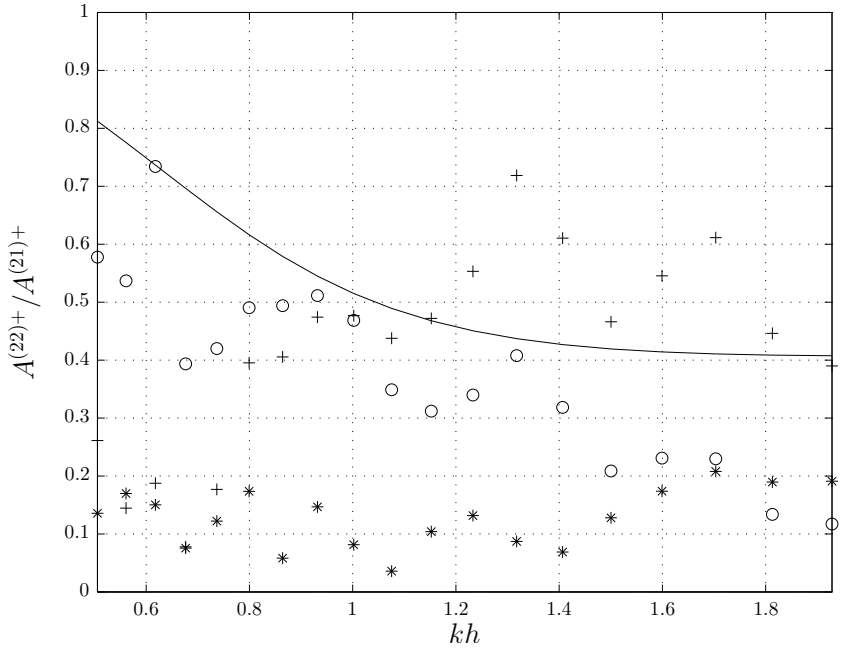


Figure 3.16: Spurious free wave content in position control with —— theoretical content under first-order control and experimental data based on ∘ first-order control and second-order control with phase correction using + Method (i) and ∗ Method (ii).

3.5 Experimental validation of force control

3.5.1 First-order control

Under force control, the demand to the wavemaker is represented by a force rather than a position. To achieve a particular (desired) wave amplitude in the wave flume, the force transfer function must be pre-computed. This transfer function incorporates the following components: (i) the wavemaker mass or inertia, (ii) the wavemaker spring stiffness, (iii) the wavemaker radiation damping and (iv) the wavemaker added mass. Further details of this transfer function were previously discussed in Spinneken and Swan (2011), and the analytic expressions for the wavemaker hydrodynamic coefficients are provided in Appendix C.1.

From the expressions in Appendix C.1 (equations C.2 and C.3) it is clear that the progressive wave field coefficient c_0 directly affects the wavemaker's hydrodynamic coefficients. As a result, any inaccuracy in c_0 is also reflected in an inaccurate prediction of the wavemaker force. To overcome this, the modified

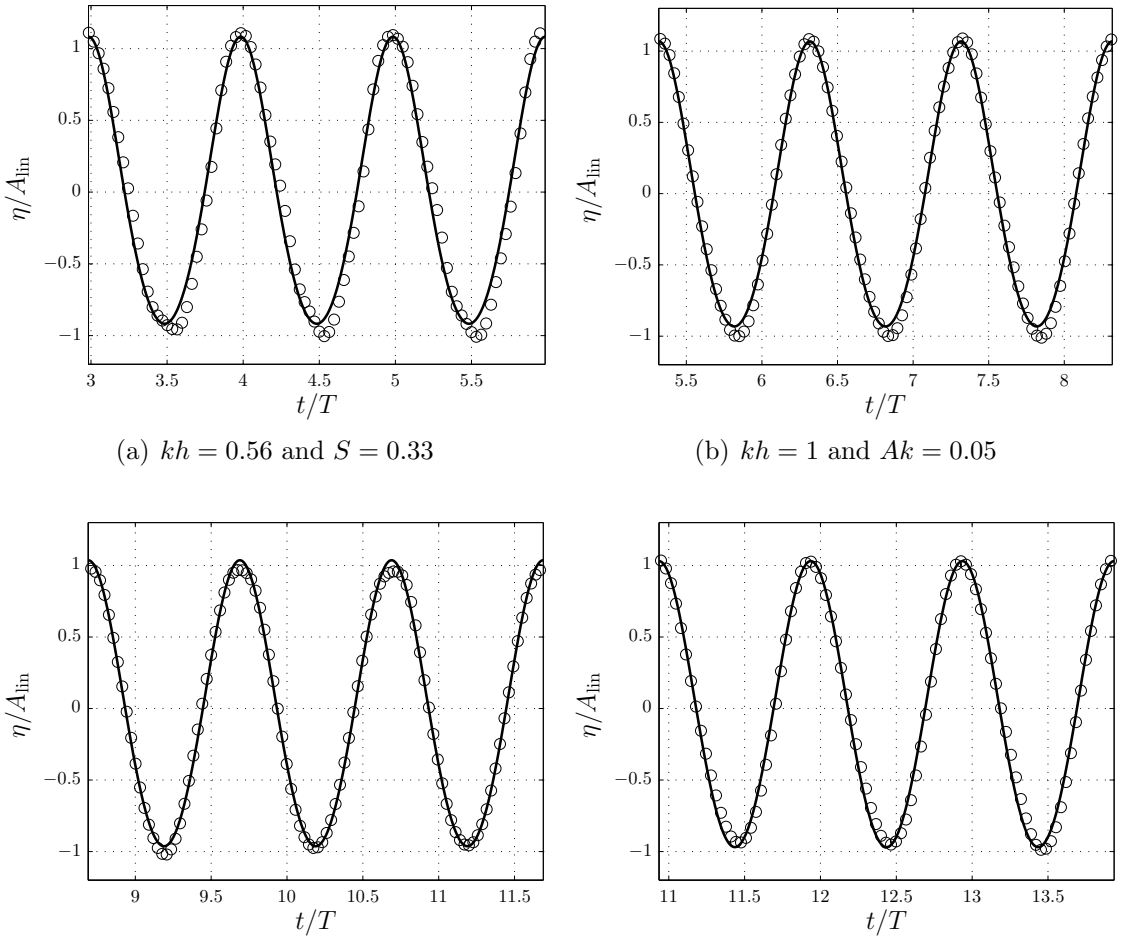
coefficient $c_0{}'$ was once again adopted. Based upon $c_0{}'$, the force demand was calculated entirely analytically, without any further modifications.

Figure 3.17 shows the surface elevations generated from a first-order force demand, concerning a subset of the small-amplitude wave cases with (a) $kh = 0.56$, (b) $kh = 1$, (c) $kh = 1.4$ and (d) $kh = 1.8$. As before, the theoretical Stream-function solution is provided for reference, and the agreement between the experimental data and the analytical expression is evident. As a result, Figure 3.17 confirms that the analytical expressions provided for the hydrodynamic coefficients are indeed correct. However, these expressions must take into consideration the reduction in c_0; the modified coefficient $c_0{}'$ being adopted for all force-control experiments shown herein. Additional experiments for the small-amplitude cases noted in Table 3.1 confirmed that the generated wave amplitudes in first-order force-control were consistently within 5% of the theoretical prediction.

3.5.2 Second-order forces

If the wavemaker operates under force control, the additional nonlinear force feedback must be taken into consideration (§2.4.5 and §3.2.4). This additional force feedback arises due to second-harmonic forces acting on the wavemaker, even when the wavemaker motion is entirely sinusoidal. To provide a full compensation of the spurious free wave content, both the phasing and the magnitude of this additional nonlinear force feedback must be predicted accurately; the purpose of the present section being to validate the theoretical expressions derived in §2.4.5.

The second-harmonic force feedback can be determined by (i) measuring the force applied to the wavemaker load cell or by (ii) evaluating the (nonlinear) wavemaker displacement. For the purpose of the present investigation, the latter approach was chosen due to the high accuracy of the laser displacement sensor. Figure 3.18 concerns the second-harmonic of the wavemaker displacement operated using a *first-order* or sinusoidal force demand. As outlined above, this second-harmonic displacement arises due to the second-harmonic forcing on the



(a) $kh = 0.56$ and $S = 0.33$

(b) $kh = 1$ and $Ak = 0.05$

(c) $kh = 1.4$ and $Ak = 0.05$

(d) $kh = 1.8$ and $Ak = 0.05$

Figure 3.17: Water surface elevation $\eta(t)/A$ with $\circ$ experimental data corresponding to first-order force control based on $c_0{}'$ and ━━ theoretical prediction by Stream-function wave theory for a wave of linear amplitude A.

wavemaker. Both the experimentally obtained magnitude (Figure 3.18(a)) and the phase (Figure 3.18(b)) are shown (symbol $\circ$), and a direct comparison is made to the theoretical expressions derived in §2.4.5 (solid lines).

Taken as a whole, the trends predicted analytically match the data relatively well. However, the magnitude is over-predicted for $kh < 1.1$ and under-predicted for $kh > 1.1$. The observed discrepancies are relatively significant in terms of their percentage departure, but actually corresponds to a maximum absolute difference of only 1.1mm; this maximum departure being observed for $kh = 0.8$. This difference is believed to have an insignificant impact on the wave quality as it is

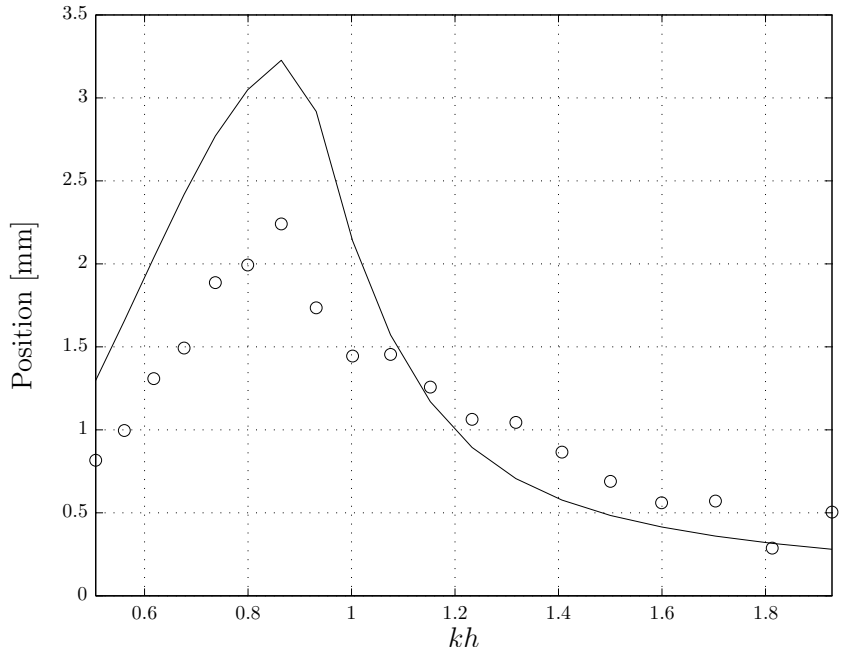
small when compared to the wavemaker stroke (108 mm for $kh = 0.8$) and also small when compared to the second-order wavemaker correction term (7.5 mm for $kh = 0.8$). The phasing of the additional second-harmonic displacement is predicted well, with a maximum difference of 0.5 rad.

At this stage it should also be noted that the data in Figure 3.18 provide the first direct evidence of the occurrence of second-harmonic wavemaker displacements under first-order force control. Spinneken and Swan (2009*a*) derived the theoretical model to explain this additional second-harmonic displacement. However, the experimental data by Spinneken and Swan (2009*b*) did not provide an explicit confirmation of the nonlinear displacement. Indeed, the discussion in Spinneken and Swan (2009*b*) focused on the observed surface elevation, and did not address the wavemaker displacement. While the wavemaker displacement may not be of primary concern, it acts as a useful indicator of the overall system response. As a result, the data in Figure 3.18 provide additional evidence of the general force-feedback model developed by Spinneken and Swan (2009*a*).

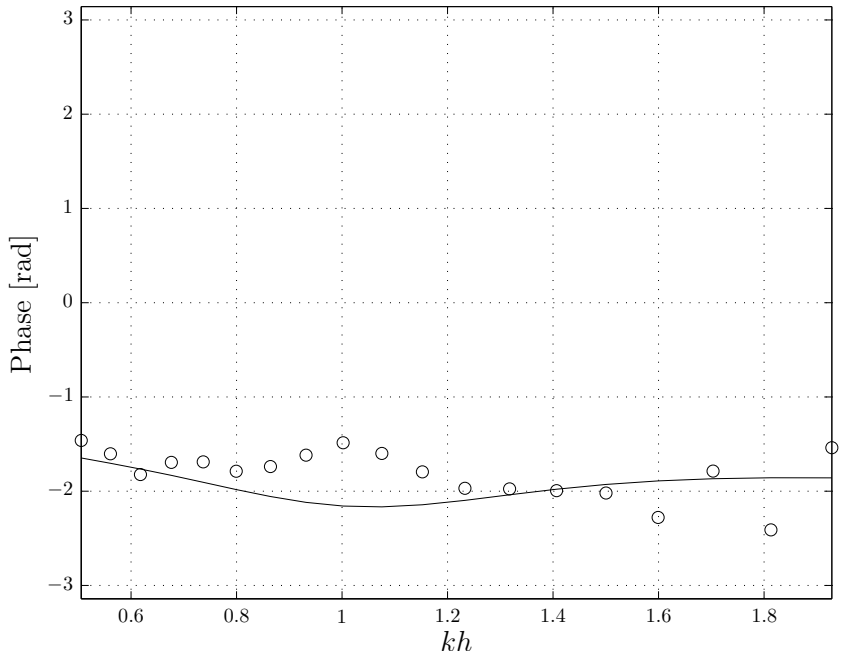
3.5.3 Second-order control

To achieve effective second-order force control, the effects noted in the context of second-order position control must be taken into consideration. Specifically, §3.4.4 demonstrated that a phase correction must be applied to the transfer function $\mathscr{F}^+$. This phase correction, based on the experimental optimisation approach (method (ii) in §3.4.4), was once again adopted for the purpose of the present experiments. To be entirely clear, no further modifications to this phase correction were made, and $\mathscr{F}^+$ was identical to that adopted in the context of position control. This function was then used in the expression for the second-order correction term, equation (2.22).

Adopting this methodology, Figure 3.19 illustrates the water surface elevations for the four select cases as before; the equivalent data in second-order position control being presented in Figure 3.15. Within Figure 3.19, the first-order con-



(a) Magnitude

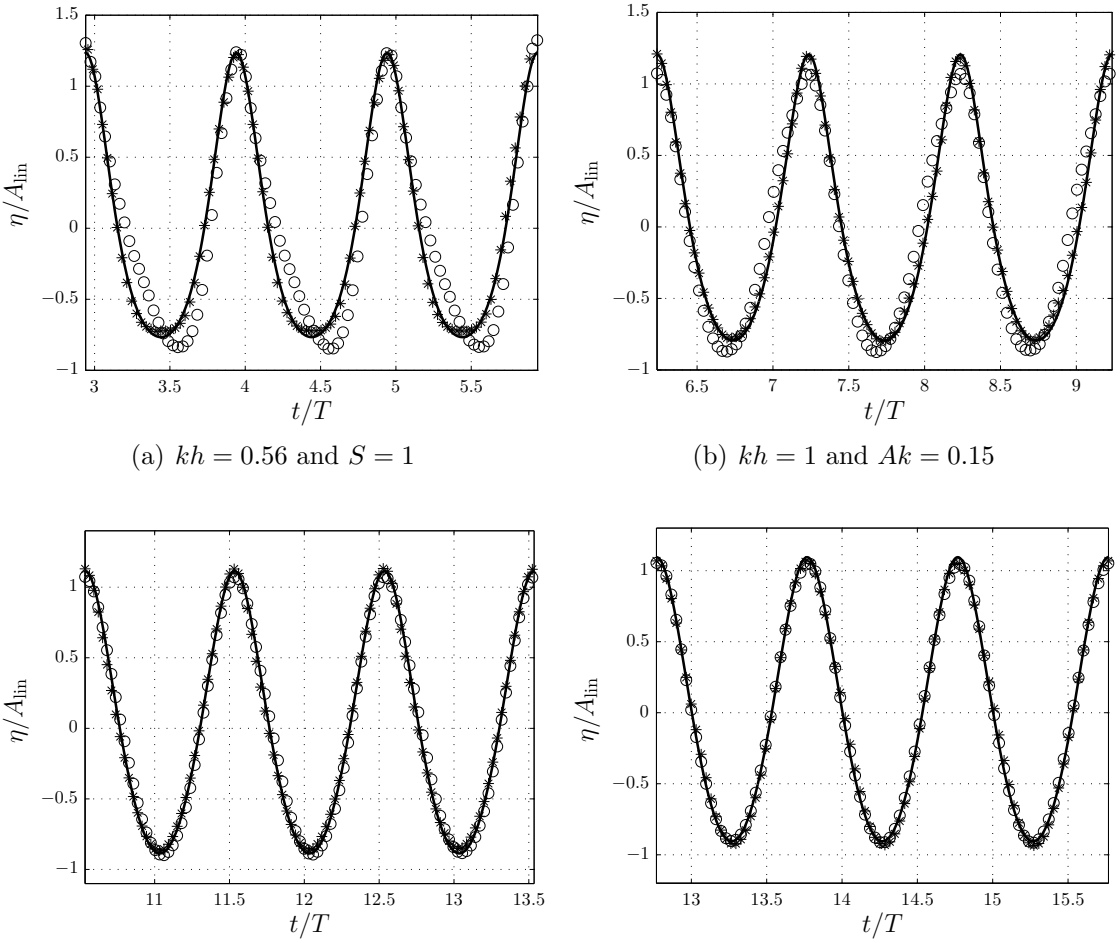


(b) Phase

Figure 3.18: Second-harmonic wavemaker displacement due to the nonlinear force feedback with —— theoretical prediction and ∘ experimental observation.

trol case is included as the data with symbol ∘, and second-order force control is represented by the data points ∗. For all four cases shown, the experimentally observed surface elevations under second-order control closely match the theoretical Stream-function prediction (solid line).

In making a direct comparison between Figures 3.19 and 3.15, it can also be observed that the data based upon first-order control differ slightly; this being particularly evident in parts (a) and (b). This difference is simply due to the added nonlinear wavemaker motion under force control, as outlined in §3.5.2. Nevertheless, adopting second-order control leads to a very comparable wave quality in



(a) $kh = 0.56$ and $S = 1$

(b) $kh = 1$ and $Ak = 0.15$

(c) $kh = 1.4$ and $Ak = 0.15$

(d) $kh = 1.8$ and $Ak = 0.15$

Figure 3.19: Water surface elevation $\eta(t)/A$ with ——— Theoretical Stream-function solution and experimental data based upon ∘ first-order force control and ∗ second-order force control.

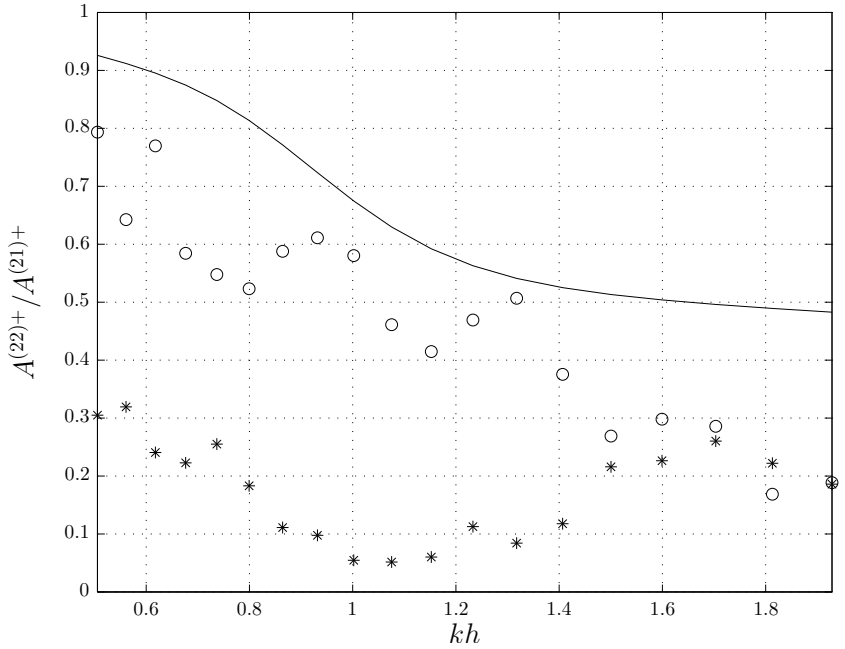


Figure 3.20: Spurious free wave content in force control for —— theoretical content under first-order control and experimental data based on ∘ linear and ∗ second-order wavemaker theory.

both types of control (force and position).

Figure 3.20 shows the spurious free wave content for the full set of nonlinear base cases, and includes both first- and second-order force control. In close similarity to position control, the theoretical prediction (solid line) over-estimates the spurious free wave content. Nevertheless, the second-order correction is successful in eliminating a significant part of the spurious free wave content for most cases. Second-order control is particularly effective in the range $0.8 \leq kh \leq 1.4$, where the remaining free wave content may be as low as 5%. The free wave content of up to 30% for $kh < 0.8$ is most probably caused by an over-prediction of the second-order wavemaker displacement due to the nonlinear force feedback (Figure 3.18). Indeed, this implies that the second-order force feedback is slightly over-corrected for $kh < 0.8$. For $kh > 1.5$, the small remaining spurious content is likely to be caused by an under-prediction of the second-order wavemaker displacement (Figure 3.18). Setting aside these two small issues, the wave quality under second-order force control is considered very good.

3.5.4 Stream-function control

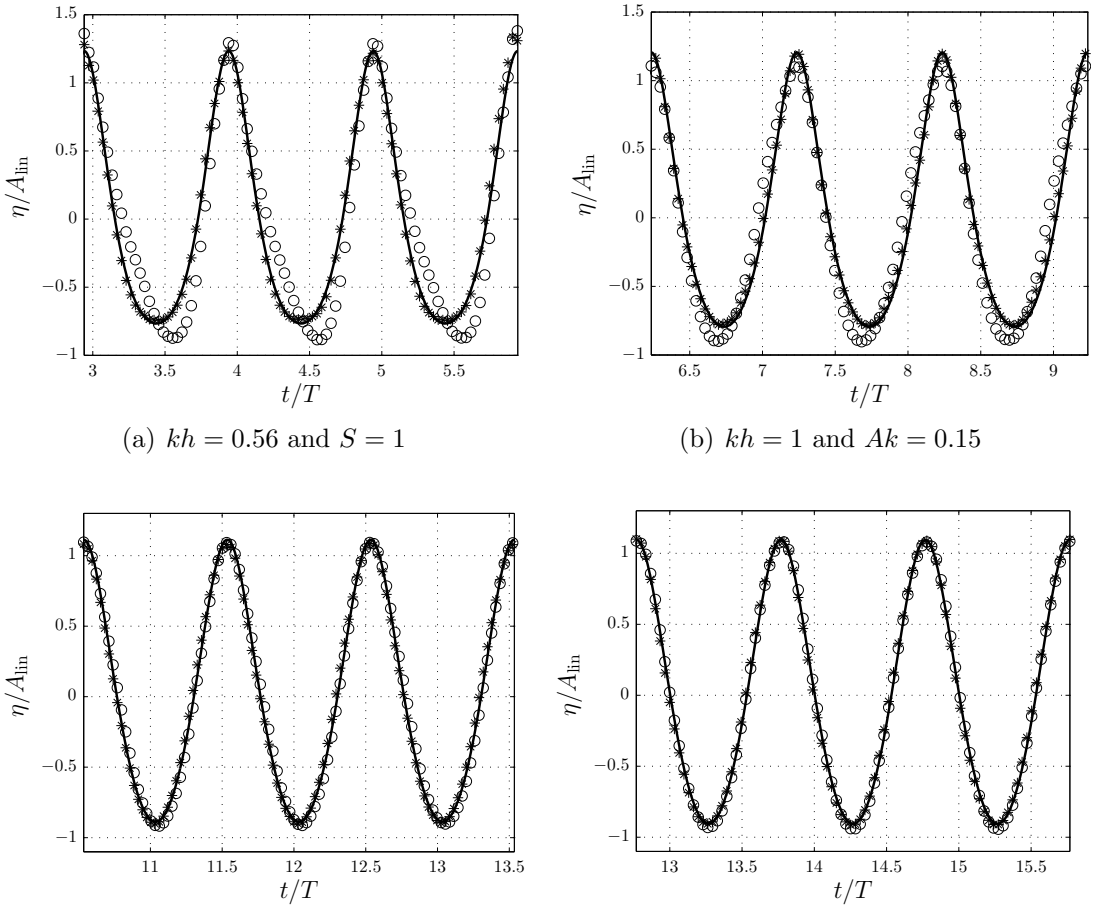
Figure 3.21 illustrates the surface elevation relating to force-controlled Stream-function wavemaking (symbol $*$). As before, the theoretical Stream-function wave solution (solid line) and the first-order force-control data (symbol $\circ$) are also shown. In all four cases, the experimental data relating to the Stream-function demand is in excellent agreement with the theoretical prediction, with little or no spurious wave content noticeable. In considering this data, it should be stressed that the only empirical correction relates to the wave field coefficient $c_0{}'$, with no further phase modification at second harmonic.

Indeed, the excellent match of the data in Figure 3.21 is somewhat surprising, given that position-control Stream-function wavemaking exhibited some small remaining departures (Figure 3.11). Whilst the comparison between these two cases (Figure 3.21 and Figure 3.11) highlights some variability in the application of nonlinear wavemaking theories, the data on Figure 3.21 nonetheless provides evidence of the success of nonlinear force-feedback control. This is also confirmed in Figure 3.22, where the remaining free wave content is $< 30\%$ for all cases considered, with an average content of approximately 15%.

3.6 Extended nonlinear set

The above discussion highlighted that both second-order control and Stream-function control are suitable for the generation of mildly-nonlinear waves in relatively shallow water. To ensure that the range of validity of second-order control was maintained, all of the previous wave cases remained within the bounds of $S \leq 1$ (Table 3.1). A nonlinearity parameter of $S > 1$ indicates that the underlying second-order theory no longer applies.

To examine the influence of both large S and Ak, an extended set of wave cases was considered. This concerns two cases, as noted in Table 3.1, characterised by (i) $kh = 0.61$ and $S = 1.5$ (or $Ak = 0.092$) and (ii) $kh = 1.23$ and $Ak = 0.225$ (or



(a) $kh = 0.56$ and $S = 1$

(b) $kh = 1$ and $Ak = 0.15$

(c) $kh = 1.4$ and $Ak = 0.15$

(d) $kh = 1.8$ and $Ak = 0.15$

Figure 3.21: Water surface elevation $\eta(t)/A$ with ——— Theoretical Stream-function solution and experimental data based upon ∘ first-order force control and ∗ Stream-function force control.

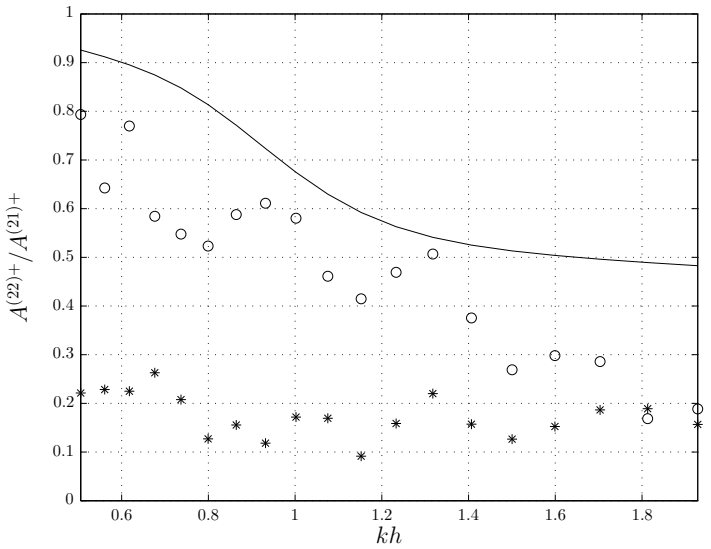
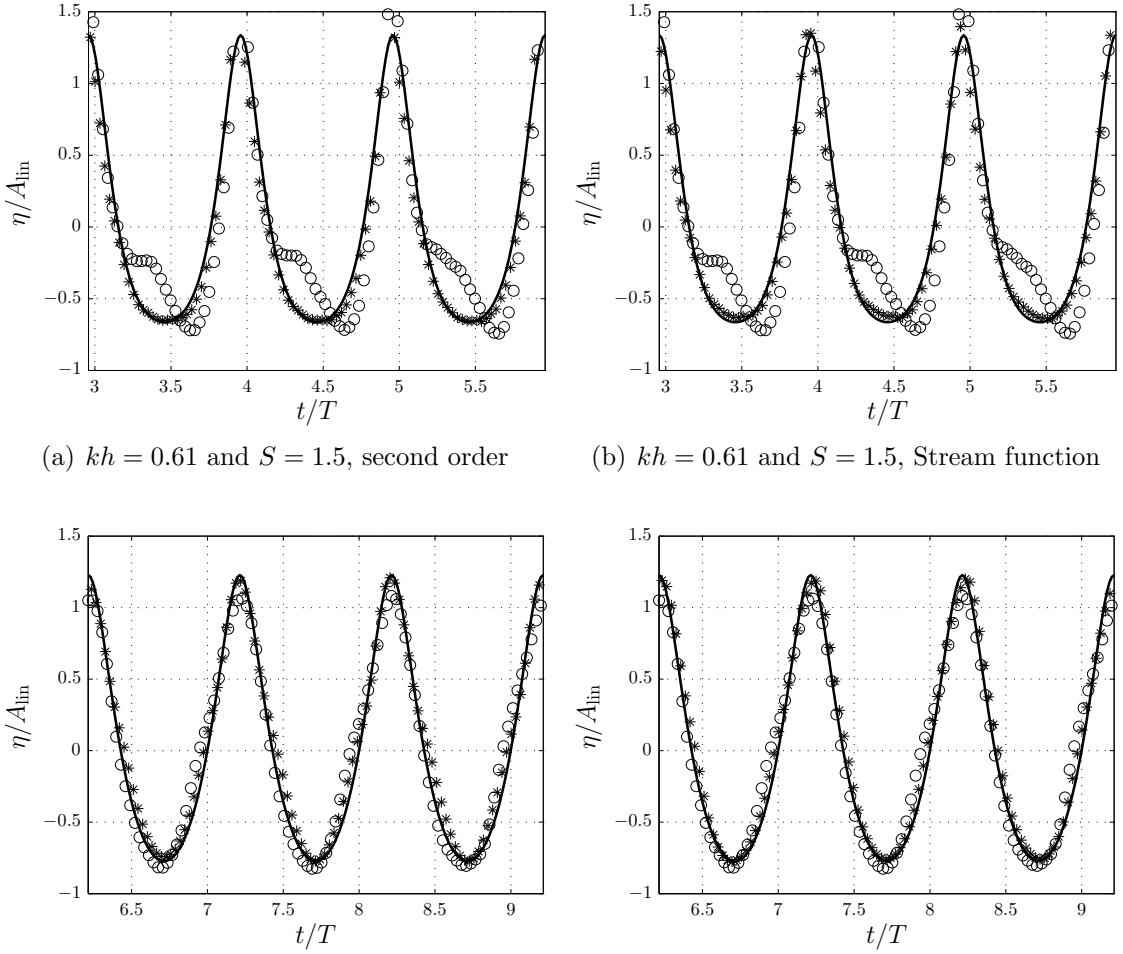


Figure 3.22: Spurious free wave content in force control with —— theoretical content under first-order control and experimental data based on ∘ first-order control and ∗ Stream-function control.

$S = 0.858$). These reasons for choosing these two cases are as follows. Case (i) presents a case with $S > 1$, where the maximum wave steepness was limited by the available Stroke of the wavemaker. In effect, this case is the steepest shallow-water case than can be produced in the Coastal Wave Flume. Case (ii), with $kh = 1.23$, lies in the intermediate water depth regime. For $Ak = 0.225$, the onset of wave breaking was observed, which limits the steepness for this particular case.

Both cases were produced in position control and force control. With the findings being very similar, only the force control data are reported here. Figure 3.23 concerns the water surface elevation for both cases (i) and (ii), and relates to (a, c) second-order force control and (b, d) Stream-function force control. Considering case (i) in Figures 3.23 (a) and (b), it is clear that first-order control (symbol ∘) leads to a very pronounced free wave content. Expressed in terms of the ratio of free and bound second-harmonic wave, first-order control leads to a spurious wave content of $A^{(22)+}/A^{(21)+} = 0.61$.

This spurious free wave content reduces to $A^{(22)+}/A^{(21)+} = 0.24$ under second-order control (Figure 3.23(a)) and $A^{(22)+}/A^{(21)+} = 0.11$ under Stream-function control (Figure 3.23(b)). Given that $S = 1.5$, the difference between the two con-



(a) $kh = 0.61$ and $S = 1.5$, second order

(b) $kh = 0.61$ and $S = 1.5$, Stream function

(c) $kh = 1.23$ and $Ak = 0.225$, second order

(d) $kh = 1.23$ and $Ak = 0.225$, Stream function

Figure 3.23: Water surface elevation $\eta(t)/A$ based on (a, c) second-order force control and (b, d) Stream-function force control showing ——— theoretical Stream-function solution ∘ experimental first-order control and ∗ experimental nonlinear control.

trol modes is surprisingly small, indicating that second-order control may perhaps be stretched beyond $S = 1$. It is also important to re-emphasise that this wave case relates to the largest wave possible within the stroke limitation of the wavemaker. As a result, it may be argued that second-order control is adequate for the large majority of the regular wave generation range in a medium-sized coastal wave facility. However, for facilities with increased stroke capabilities, this may not apply.

Case (ii) with $Ak = 0.225$ (but $S < 1$) in Figure 3.23 (c) and (d) relates to a steep near breaking case. A first-order control signal leads to $A^{(22)+}/A^{(21)+} = 0.31$,

which is approximately 15% less than theoretically predicted (Figure 3.22). Both second-order control and Stream-function control lead to a small yet significant improvement, with $A^{(22)+}/A^{(21)+} = 0.24$ and $A^{(22)+}/A^{(21)+} = 0.17$ respectively. The difference between the two control methods is again relatively small, and it may be argued that second-order control is sufficiently accurate (Figure 3.23(c)).

3.7 Conclusions

The present chapter investigated the generation of nonlinear regular waves in shallow and intermediate water conditions. Ultimately, the main advance lies in the development and validation of nonlinear generation techniques under force control. However, due to a lack of existing high-quality experimental data in position control, this case was examined first. In considering nonlinear position control, two empirical correction factors were found to be necessary. First, a magnitude correction of 15% was required in the first-order progressive wave field coefficient; this correction factor being constant over a wide range of water depths and wave steepnesses. Second, a phase correction proved crucial in the formulation of the second-order control signal. This phase shift was found to be negligible in shallow water conditions, but plays an important role in the generation of high-quality waves in intermediate water depths. The methodology developed herein, combining theoretical predictions with small empirical corrections, enables the successful compensation of the spurious free wave content in position control.

Based upon the position-control findings, high-quality force-controlled wave generation can also be achieved in both shallow and intermediate water. In this context, an important difference between flap-type and piston-type wavemakers was established. Previous work demonstrated that flap-type wavemakers may often rely on a linear force-demand signal. This is not the case for piston-type wavemakers. In the flap-type case, a nonlinear force-feedback term was previously shown to lead to an inherent self-correction of the spurious free wave content. In contrast, the nonlinear force-feedback arising in the piston wavemaker case is

relatively small, and self-correction was not observed. As a result, piston-type force-controlled wavemakers exhibit a spurious free wave content similar to that observed under position control. Given this relatively large free wave content, a nonlinear correction force is required.

To address this, both second-order and Stream-function correction terms were derived and experimentally verified. These nonlinear approaches enable force-controlled generation of comparable wave quality to position control. Furthermore, the work also demonstrated that second-order control may indeed be adequate for the large majority of the practical wave generation range in a typical coastal wave facility; the improvement due to Stream-function control generally being relatively minor.

4

Bi-chromatic waves

4.1 Chapter overview

In any realistic sea state, most commonly represented by an underlying spectral density function, a large number of wave components interact. In the presence of the wavemaker boundary condition, this gives rise to a large number of spurious subharmonic and superharmonic wave components. To simplify this very complex problem, it is often instructive to consider a bi-chromatic wave case first, where the analysis is limited to two fundamental wave components. The present chapter concerns a detailed analysis of this bi-chromatic wave case, addressing both position control and force control.

It is important to note, at this stage, that Stream-function wavemaker theory, which provided consistently good results in the context of regular waves (Chapter 3), cannot be extended to the bi-chromatic case. As a result, bi-chromatic wavemaker theories are limited to first-order and second-order theories. Section §4.2 reviews the existing second-order theory, and sets this theoretical knowledge into the context of force control. The practical success of the nonlinear generation of bi-chromatic waves, involving both position control and force control, is then considered experimentally in §4.3. A set of overall conclusions is finally presented in §4.4.

4.2 Theoretical analysis

4.2.1 Introduction

At second order, the interaction between two fundamental wave components gives rise to both self- and cross-interaction terms. In the context of laboratory wavemaker theory, each interaction also gives rise to bound and free wave components; the former being due to wave-wave interactions and the latter being due to the presence of the wavemaker. For two fundamental wave components (n, m) of wave frequency (f_n, f_m), wave amplitude (A_n, A_m) and wavenumber (k_n, k_m), the above noted interactions give rise to the following terms:

(i) two bound superharmonic wave components at $2f_n$ and $2f_m$, denoted as $A_n^{(21)+}$ and $A_m^{(21)+}$;

(ii) two bound cross-interaction wave components at $f_n \pm f_m$, denoted as $A_{nm}^{(21)\pm}$;

(iii) two free spurious wave components at $2f_n$ and $2f_m$, each satisfying the free wave dispersion equation, denoted as $A_n^{(22)+}$ and $A_m^{(22)+}$;

(iv) two free spurious wave components at $f_n \pm f_m$, again satisfying the dispersion equation, denoted as $A_{nm}^{(22)\pm}$.

As a result, the interactions of two wave components in the presence of a wavemaker give rise to eight distinct interaction terms, occurring at four frequencies ($2f_n$, $2f_m$ and $f_n \pm f_m$).

The self interaction terms ($2f_n$ and $2f_m$) have been discussed previously in the context of regular wave generation, Chapter 3, and the present theoretical analysis focuses on the cross-interaction terms. The more established position-control case is discussed first, §4.2.2. Building upon this case, an assessment of the influence of the nonlinear force-feedback on the cross-interaction terms is provided in §4.2.3.

4.2.2 Second-order position control

At this stage, it is instructive to introduce the bi-chromatic wave problem by way of an example. Figure 4.1 shows the normalised water surface elevation,

$\eta(t)/A_{\mathrm{sum}}$, for a wave case with $A_{\mathrm{sum}} = A_n + A_m$. This case is characterised by $A_n k_n = 0.045$, $k_n h = 0.68$, $A_m k_m = 0.049$ and $k_m h = 0.74$; these parameters being equivalent to one of the experimental cases considered in §4.3. In a linear sense, the superposition of these two wave components would yield a maximum surface elevation of $\eta_{\mathrm{max}}/A_{\mathrm{sum}} = 1$. Furthermore, the horizontal axis was normalised by the wave period of component n, denoted as T_n.

All data included in Figure 4.1 are based on theoretical second-order calculations, following the equations given in Chapter 2, and showing two sets of approaches. The two grey lines indicate the desired surface elevation in the absence of any spurious free wave, calculated at $x = 3h$ (solid line) and $x = 4h$ (dashed line). In contrast, the black lines also include the predicted spurious free wave content due to first-order position control, again presented at $x = 3h$ (solid line) and $x = 4h$ (dashed line).

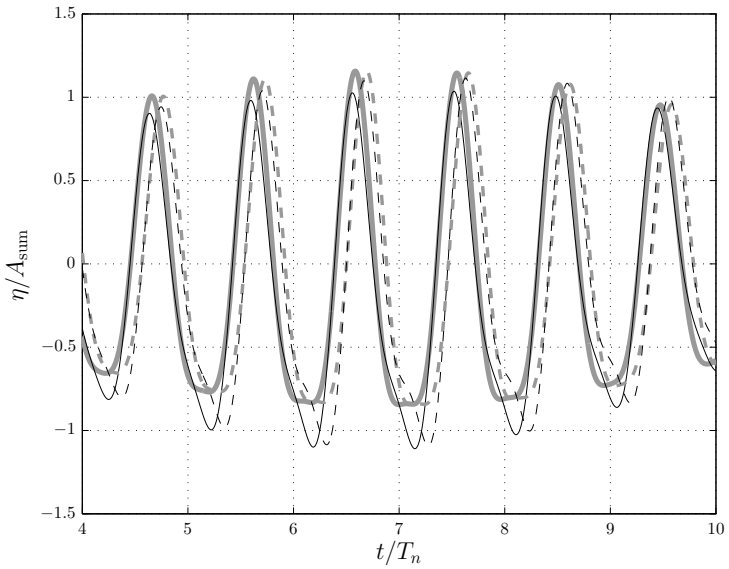


Figure 4.1: Calculated water surface elevation $\eta(t)/A_{\mathrm{sum}}$ for a bi-chromatic wave case showing the desired surface elevation at $x = 3h$ and $x = 4h$ and the surface elevation in the presence of spurious waves at $x = 3h$ and $x = 4h$.

A first observation of the desired surface elevation (grey lines) in Figure 4.1 confirms that the evolution of $\eta(t)$ is unsteady in both space and time. Given that k_n and k_m are similar, the spatial evolution of the wave group is limited, and the surface elevation at $x = 4h$ closely resembles that at $x = 3h$. The occurrence

of spurious free waves (black lines) leads to an additional undesired unsteadiness, again in both space and time. The purpose of nonlinear control is to eliminate this spurious free wave content, achieving a solution that closely resembles the desired surface elevation (grey lines). In contrast to the regular wave solution, this can no longer be confirmed by simply considering the steadiness of the wave profile, as an unsteady evolution now forms an important part of the desired solution.

For each combination of k_n and k_m, the spurious cross-interaction term differs. The magnitude of this cross-interaction term is best illustrated as shown in Figure 4.2, providing the ratio of the free and bound wave component amplitudes, $A_{nm}^{(22)+}/A_{nm}^{(21)+}$. It should be noted that this ratio is steepness independent, as it expresses the ratio of two second-order quantities. In close similarity to the regular wave case, the spurious free wave content increases with decreasing water depth (lower kh). Furthermore, the spurious free wave content also becomes more significant as the spacing between k_n and k_m is reduced. As a result, the spurious cross-interaction terms are most pronounced if

(i) both fundamental wave components have low kh values and

(ii) the frequencies of these two wave components are closely spaced.

To provide an example, the superharmonic cross-interaction between two wave components with $k_nh = 1.2$ and $k_mh = 1.3$ gives rise to a spurious wave content of $A_{nm}^{(22)+}/A_{nm}^{(21)+} = 44.7\%$. In contrast, with $k_nh = 0.5$ and $k_mh = 2$, the spurious free wave content reduces to 41.1%. This reduction takes place despite the fact that the sum $k_nh + k_mh = 2.5$ is identical in both cases.

Similar arguments apply to the spurious subharmonic cross-interaction term, $A_{nm}^{(22)-}/\ A_{nm}^{(21)-}$, illustrated in Figure 4.3. The cross interaction is most pronounced for low kh and relatively closely spaced wave frequencies. However, in the subharmonic case, the interaction of two closely spaced wave components $(f_n - f_m)$ gives rise to a subharmonic at very low frequency f or wavenumber k. With the wavelength being defined as $\lambda = 2\pi/k$, this would lead to a very long free wave. It is questionable whether such a free wave would actually develop within a wave

tank of finite length; this being assessed as part of the experimental investigation (§4.3).

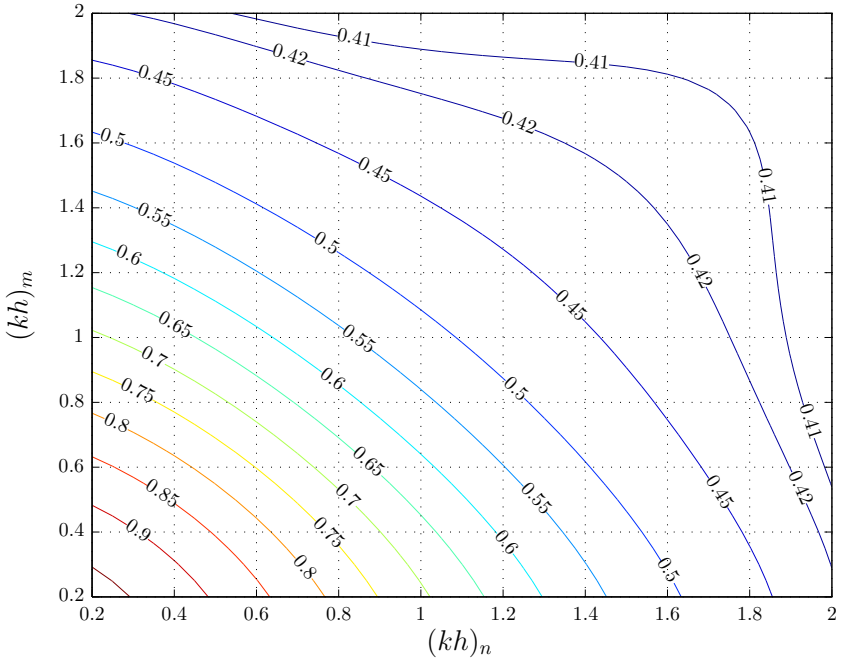


Figure 4.2: Ratio of the cross-interaction superharmonic free to bound wave amplitude, $A_{nm}^{(22)+}/A_{nm}^{(21)+}$, due to first-order position control.

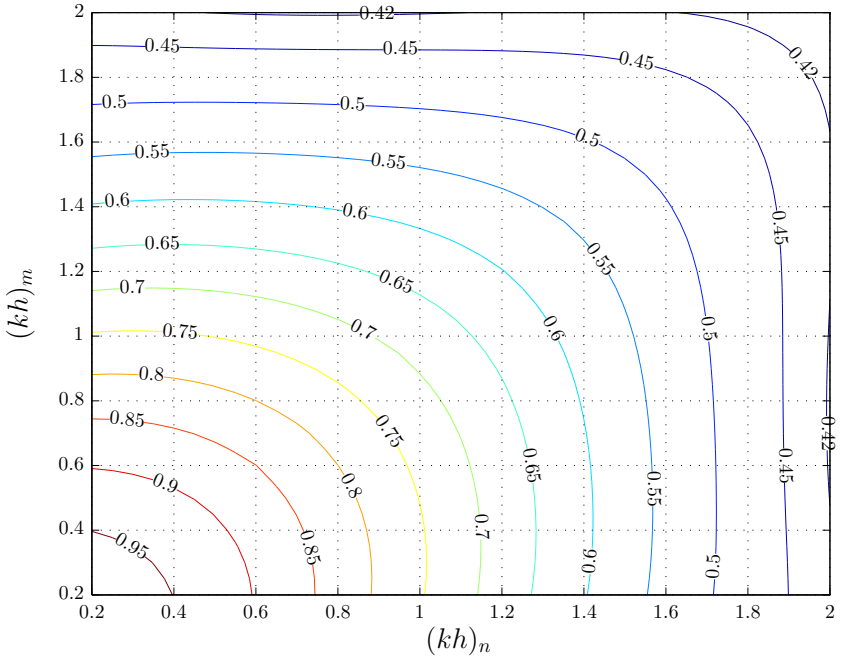


Figure 4.3: Ratio of the cross-interaction subharmonic free to bound wave amplitude, $A_{nm}^{(22)-}/A_{nm}^{(21)-}$, due to first-order position control.

4.2.3 Second-order force control

In position control, the wavemaker motion based on a first-order demand signal was assumed to be entirely sinusoidal for each wave component. In contrast, the force-control calculations must also include the effect of the nonlinear force feedback. As discussed in the context of regular wave generation, this nonlinear force feedback leads to additional harmonics in the wavemaker motion, even under first-order force control. The superharmonic cross-interactions due to a first-order force-control signal are shown in Figure 4.4, which confirms that

(i) the spurious wave content increases with decreasing kh,

(ii) the free wave content is more pronounced for closely spaced wave components,

(iii) the spurious content in force control is 15 to 20% larger than that under first-order position control (Figure 4.2).

The explanation for (iii) above lies in the presence of the nonlinear force feedback, responsible for the generation of an additional spurious free wave through the nonlinear wavemaker motion. A very similar observation was made for regular waves, §3.5, and the associated discussion also applies here. Indeed, the increase in the spurious cross-interaction content due to the force feedback is similar to that for the self-interaction terms (Figure 3.20), accounting for an increase of approximately 15 to 20%. Given the importance of this term, an adequate second-order compensation must be provided; this being addressed as part of the experimental investigation in §4.3.

The subharmonic cross-interaction term in first-order force control is considered in Figure 4.5. In this case, significant departures are seen compared to position control (Figure 4.3); the main difference being that the spurious content is no longer symmetrical about the diagonal $k_n h = k_m h$. To explain this difference, it is instructive to consider the magnitude of the spurious subharmonic in position

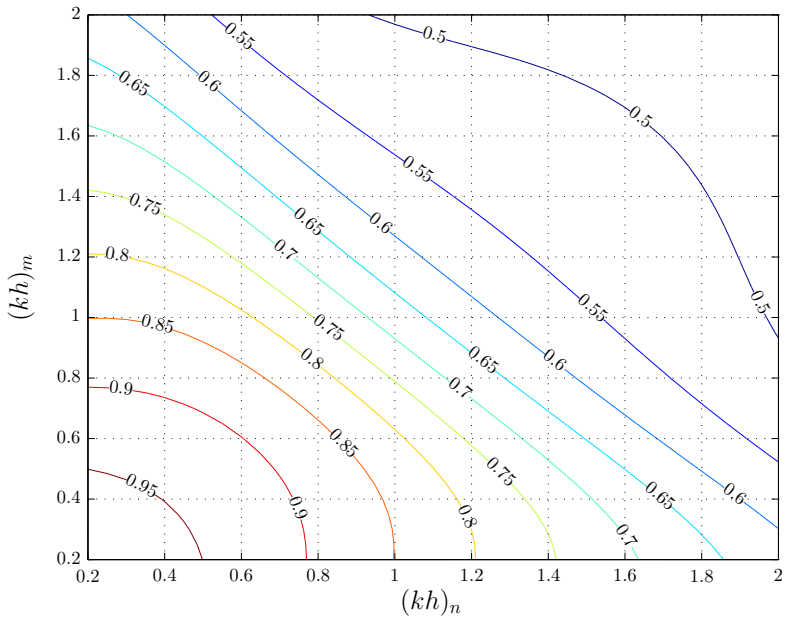


Figure 4.4: Ratio of the cross-interaction superharmonic free to bound wave amplitude, $A_{nm}^{(22)+}/A_{nm}^{(21)+}$, due to first-order force control.

control, given by

$$A_{nm}^{(22)-} = \left| \frac{c_{0n} X_n c_{0m} X_m^*}{h} c_0^{(22)-} \right|. \tag{4.1}$$

In considering this latter term, Schäffer and Steenberg (2003) highlighted the antisymmetry of the real part of $c_0^{(22)-}$; this antisymmetry only being observed in the case of subharmonic interactions. In the context of the present discussion, the term *antisymmetric* refers to a term that is symmetric in magnitude, but of opposite sign. Given that the spurious free wave amplitude $A_{nm}^{(22)-}$ is expressed through the magnitude of $c_0^{(22)-}$, the antisymmetry was not observed in discussing the position-control case. Furthermore, this antisymmetry does not appear in the spurious subharmonic content (Figure 4.3) as this is expressed by the ratio

$$\frac{A_{nm}^{(22)-}}{A_{nm}^{(21)-}} = \frac{\left| c_0^{(22)-} \right|}{h \left| G_{0n0m}^{-} \right|}. \tag{4.2}$$

In contrast, the subharmonic free wave in force control is given by

$$A_{nm}^{(22)-} = \left| \frac{c_{0n} X_n c_{0m} X_m^*}{h} c_0^{(22)-} - F_{nm}^{(2)-} B(\omega_n - \omega_m) c_0^{(23)-} \right|, \tag{4.3}$$

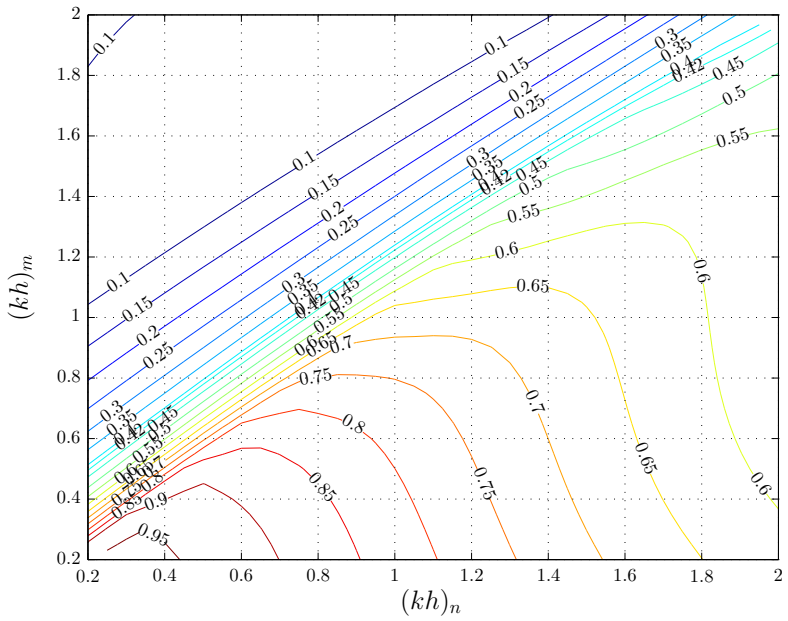


Figure 4.5: Ratio of the cross-interaction subharmonic free to bound wave amplitude, $A_{nm}^{(22)-}/A_{nm}^{(21)-}$, due to first-order force control.

which arises due to the combination of (i) the free wave in position control and (ii) the second-order force feedback. The subharmonic force feedback term $F_{nm}^{(2)-}$ includes the contribution of six force components (Appendix C.2) with

$$F_{nm}^{(2)-} = F_{\phi^{(1)}}^{(2)-} + F_{hydro}^{(2)-} + F_{u^2}^{(2)-} + F_{w^2}^{(2)-} + F_{\phi^{(21)}}^{(2)-} + F_{\phi^{(22)}}^{(2)-}. \tag{4.4}$$

Within these second-order force contributions, the imaginary part of $F_{\phi^{(1)}}^{(2)-}$, $F_{hydro}^{(2)-}$ and $F_{\phi^{(21)}}^{(2)-}$, and the real part of $F_{\phi^{(22)}}^{(2)-}$ are antisymmetrical. This causes the global second-order force $F_{nm}^{(2)-}$ to be asymmetrical. The combination of the asymmetrical force $F_{nm}^{(2)-}$ and the antisymmetrical coefficient $c_0^{(22)-}$ leads to an asymmetrical spurious free wave content $A_{nm}^{(22)-}/A_{nm}^{(21)-}$ (Figure 4.5). From Figure 4.5, it is also clear that the force-feedback leads to a partial cancellation of the free wave content in the subharmonic range. However, the practical consequences of this are believed to be very limited, as these cases correspond to very long waves which are unlikely to exist in practice.

4.3 An experimental investigation

4.3.1 Overview

For the purpose of the present experimental investigation, bi-chromatic waves were considered in both position control and force control. All experiments were again undertaken in the Coastal Wave Flume (Chapter 3) with a constant depth of $h = 0.6$m. The water surface elevation was recorded by seven tensioned wire gauges, with the first gauge located at $x = 4h$, where $x = 0$ defines the position of the wavemaker. Subsequent gauges were spaced equidistantly with a spacing of $\Delta x = h/3$.

Table 4.1: Experimental wave parameters for bi-chromatic investigation.

Case	k_nh	A_nk_n	S_n	k_mh	A_mk_m	S_m
Bi1	0.68	0.045	0.58	0.74	0.049	0.52
Bi2	0.80	0.053	0.46	0.86	0.058	0.43
Bi3	0.50	0.018	0.50	0.62	0.031	0.50
Bi4	0.62	0.031	0.50	0.74	0.047	0.50
Bi5	0.74	0.047	0.50	0.86	0.068	0.50
Bi6	0.86	0.068	0.50	1.00	0.091	0.50
Bi7-1	0.62	0.012	0.20	0.74	0.019	0.20
Bi7-2	0.62	0.018	0.30	0.74	0.028	0.30
Bi7-3	0.62	0.025	0.40	0.74	0.038	0.40
Bi7-4	0.62	0.031	0.50	0.74	0.047	0.50
Bi7-5	0.62	0.037	0.60	0.74	0.057	0.60
Bi7-6	0.62	0.043	0.70	0.74	0.066	0.70
Bi7-7	0.62	0.049	0.80	0.74	0.076	0.80

The set of experimental cases considered is outlined in Table 4.1. This set can be categorised into (i) two base cases Bi1 and Bi2, (ii) a variation of k_n and k_m at constant wave nonlinearity $S_n = S_m = 0.5$, cases Bi3, Bi4, Bi5 and Bi6, and (iii) a variation of S_n and S_m at constant k_n and k_m, cases Bi7-1 to Bi7-7. A detailed analysis of the two base cases is presented in §4.3.2 (position control) and §4.3.3 (force control). The effect of the relative water depth and wave nonlinearity are then addressed in §4.3.4 and §4.3.5 respectively. At this stage, it is important to re-emphasise that the subharmonics are not considered further. To give an

example, cases Bi-1 and Bi-2 are predicted to have a subharmonic wavelength of approximately 39m, which is not expected to exist in a wave flume of 23m length.

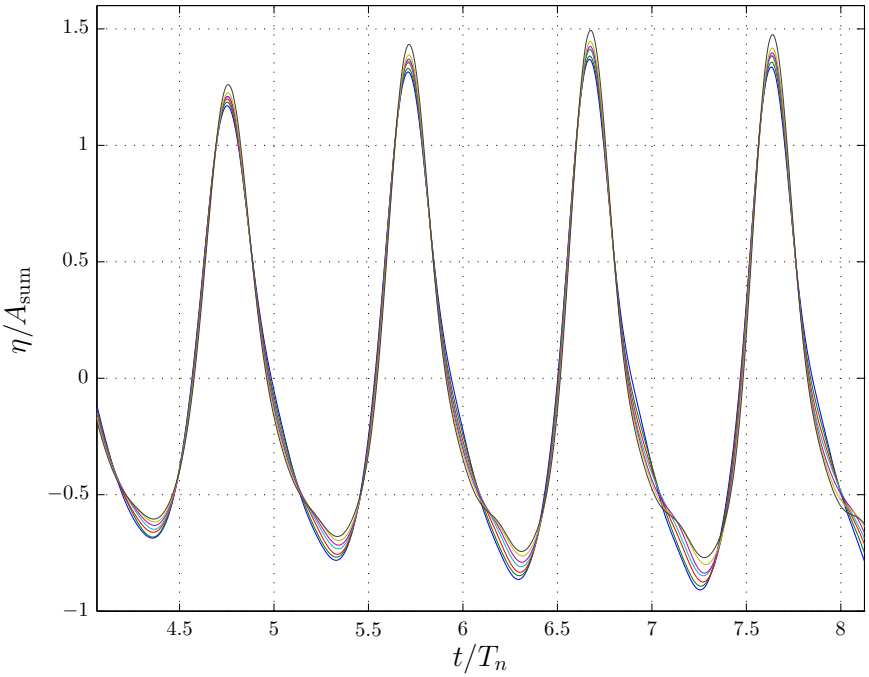
4.3.2 Second-order position control

For cases Bi1 and Bi2, the wave steepness was chosen to meet two conditions. First, the steepness was chosen to ensure that the resulting case lies approximately within the range of validity of second-order wave theory. While no exact description of this condition is available for bi-chromatic waves, the nonlinearity parameter was expressed as $S_{\mathrm{nm}} = S_n + S_m$. Second, the overall steepness must be limited due to the stroke limitations of the piston-type wavemaker.

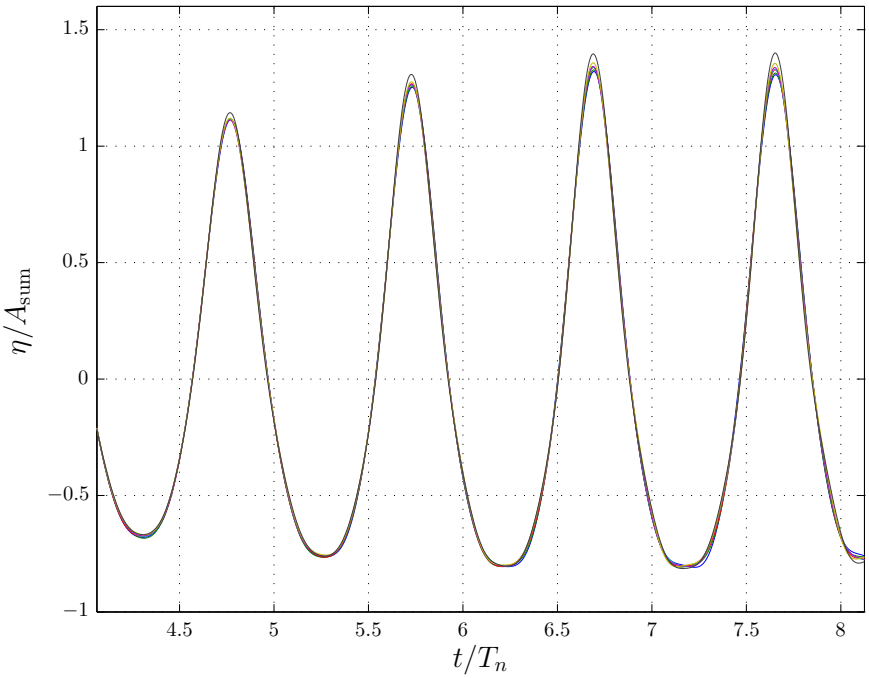
Considering both conditions led to a wave steepness $A_n k_n = 0.045$ and $A_m k_m = 0.049$ for case Bi1, and $A_n k_n = 0.053$ and $A_m k_m = 0.058$ for case Bi2. To ensure that significant wave interactions take place at the beginning of the experimental run, prior to any wave reflections contaminating the experimental data, requires an appropriate selection of the phase information for each of the two wave components. For both cases Bi1 and Bi2, the phasing of the two wave components was set to $\alpha_n = -\pi/2$ and $\alpha_m = +\pi/2$, where the phase angle α relates to the phasing of the wave component at $t = 0$ and $x = 0$.

Figure 4.6(a) shows the surface profile recorded by the seven wave probes for case Bi1 with the wavemaker being operated in first-order position control. The data recorded by gauges 2...7 was time-shifted to overlap with the surface profile measured by the first gauge. For the purpose of this time-shifting, a phase velocity corresponding to the average phase velocity of the wave components k_n and k_m was assumed. This is justified by the very small difference between the phase velocities of the two wave components, corresponding to only 1.1% for wave case Bi1.

Given the small difference in phase velocity between k_n and k_m, as well as the relatively small distance between gauge 1 and gauge 7, the wave form observed in Figure 4.6(a) is expected to be approximately steady between adjacent wave



(a) First-order position control



(b) Second-order position control

Figure 4.6: Surface elevation for bi-chromatic wave case Bi1 as described in Table 4.1. Note: The individual time histories relate to recordings at seven spatial locations, where the time histories at subsequent gauges have been shifted to overlap with the time history at the first gauge.

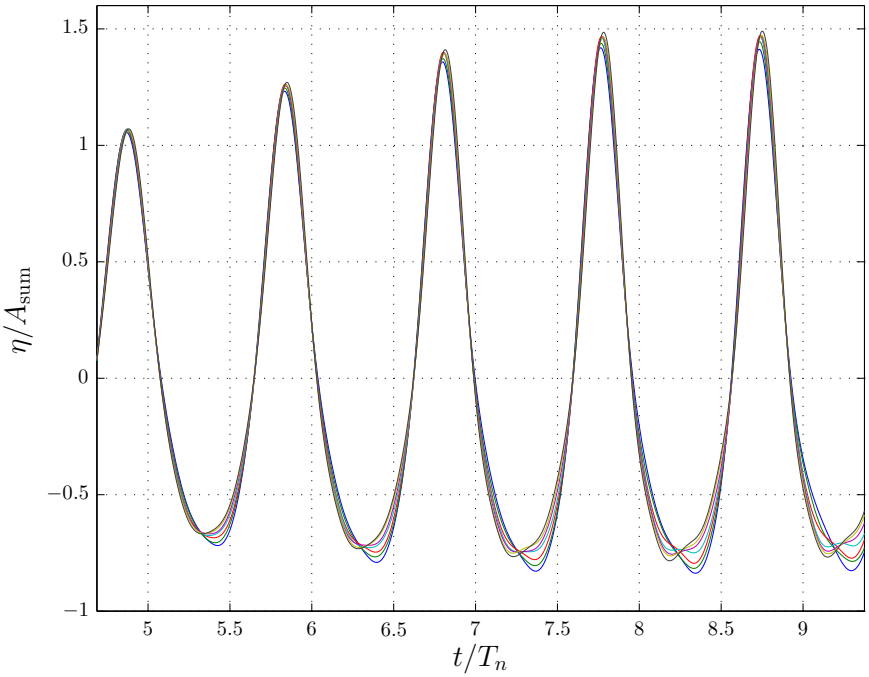
probes; any non-steadiness being associated with the presence of spurious free wave components. As a result, the data representation chosen for Figure 4.6(a) serves as a first qualitative measure for the presence of spurious free wave components.

Wave case Bi1 was generated once again, with the wavemaker now being subjected to second-order position control. The corresponding surface elevation measurement, subjected the same time-shifting as before, is shown in Figure 4.6(b). In applying this second-order control, the magnitude and phase correction factors identified in Chapter 3 were once again adopted. In this context, it is important to note that the second-order phase correction is very close to zero for the frequencies associated with cases Bi1 and Bi2. As a result, only the empirical correction factor $c_0{}'$ has an influence on the bi-chromatic data shown here. Considering Figure 4.6(b), it is clear that the nonlinear control signal is very effective at suppressing the undesired spurious free wave components; evidence of this being provided by the close match between the surface profile at the seven adjacent wave probes.

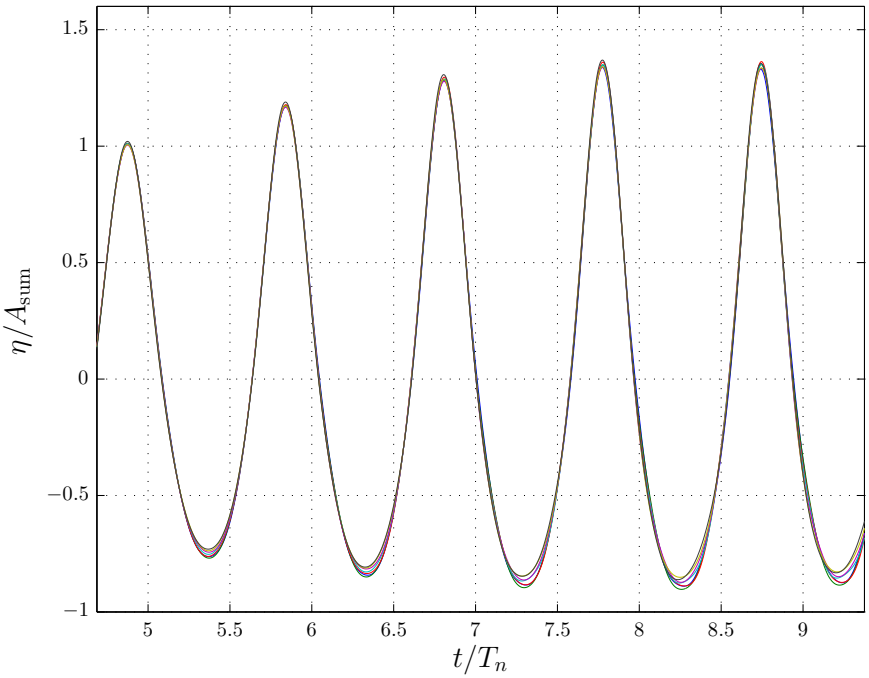
Figure 4.7 concerns wave case Bi2, once again illustrating first-order position control in part (a) and second-order position control in part (b). The data representation, including the time-shifting of the surface elevation at the seven gauge locations, is identical to the analysis applied to case Bi1, and very similar arguments apply to the experimental data. In first-order control (Figure 4.7(a)), substantial departures arise between the seven gauge locations, indicating the occurrence of spurious free wave components. This latter departure is significantly reduced when considering the second-order control case in Figure 4.7(b).

To quantify the relative merits of second-order control, a separation into free and bound components at each of the distinct sub- and superharmonic frequencies must be undertaken. This may be achieved by applying a frequency decomposition technique based on an extended version of the methodology introduced by Lin and Huang (2004). In summary, this separation technique requires the following steps:

(i) A Discrete Fourier Transform (DFT) is applied to the surface elevation data recorded at each of the seven wave probes.



(a) First-order position control



(b) Second-order position control

Figure 4.7: Surface elevation for bi-chromatic wave case Bi2 as described in Table 4.1. Note: The individual time histories shown relate to recordings at seven spatial locations, where the time histories at subsequent gauges have been shifted to overlap with the time history at the first gauge.

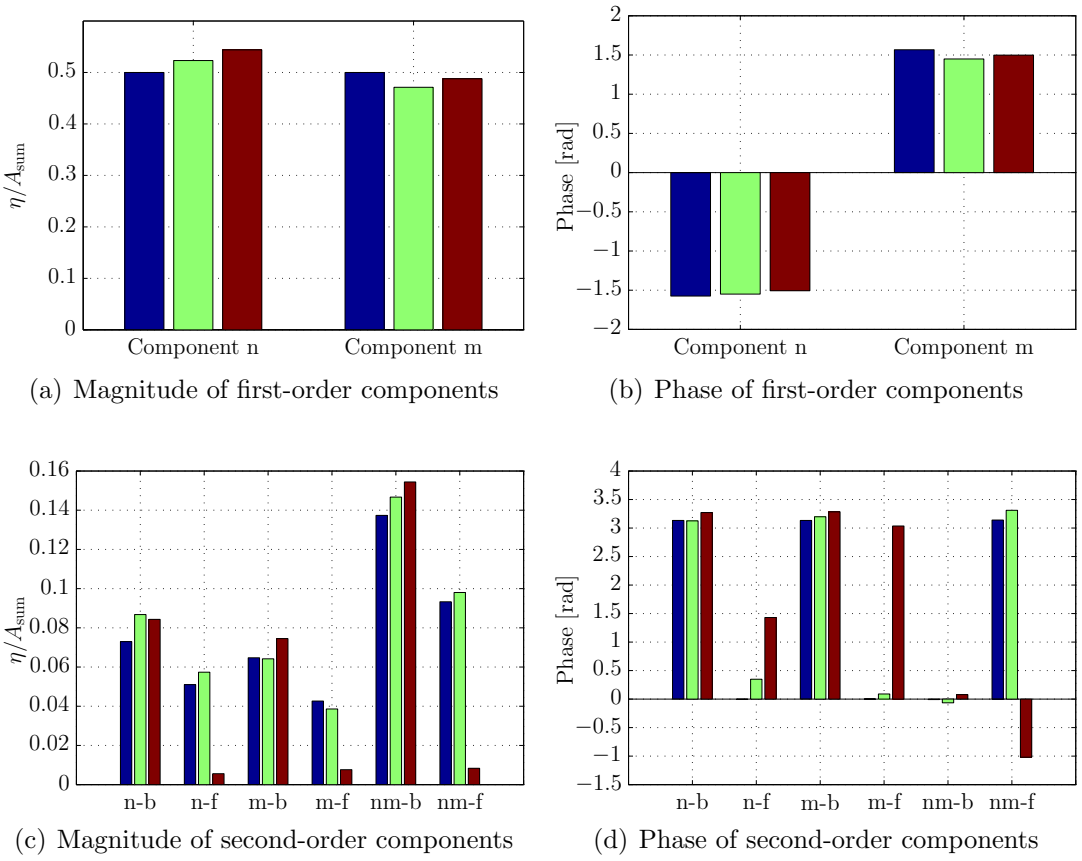
(ii) Neglecting any interactions beyond second order, the complex magnitude of the first-order wave components is directly provided by the first-harmonic DFT amplitudes.

(iii) In contrast, the second-order wave components must first be separated into free and bound components. The data resulting from the DFT analysis includes, at the same frequency, bound wave components and free wave components. A single wave gauge is thus not sufficient to extract all required information.

(iv) Lin and Huang (2004) developed a methodology to separate the second-order bound and free wave components of a regular wave. This methodology was extended to the analysis of a bi-chromatic wave, whereby it was applied separately to each second-order interaction component. This is justified by the fact that in a bi-chromatic wave each second-order interaction component arises at a different frequency. As noted before, the self-interaction terms arise at twice the fundamental frequencies, and the cross-interaction terms arise at the sum and difference frequencies of the fundamental wave components.

Adopting the above analysis yields the data illustrated in Figure 4.8 (case Bi1) and Figure 4.9 (case Bi2). Each of these two figures consists of four parts, providing (a) the magnitude of the first-order wave components, (b) the phase of the first-order wave components, (c) the magnitude of the second-order wave components and (d) the phase of the second-order wave components. For each component, the colour information relates to the type of control, where (i) blue corresponds to the theoretical predictions assuming first-order position control, (ii) green corresponds to the experimental data under first-order position control, and (iii) red corresponds to the experimental data under second-order position control.

Considering the first-order components of case Bi1 (Figure 4.8(a)), it is clear that the desired (or theoretical) magnitude of both fundamental components is



(a) Magnitude of first-order components

(b) Phase of first-order components

(c) Magnitude of second-order components

(d) Phase of second-order components

Figure 4.8: Wave components for case Bi1 providing (i) the theoretical predictions assuming first-order position control (blue), (ii) the experimental results based on first-order position control (green), and (iii) the experimental results based on second-order position control (red).

$A_n/A_{\text{sum}} = A_m/A_{\text{sum}} = 0.5$. In practice, some small departures from this desired wave amplitude arise in the experimental investigation. Based on a direct theoretical transfer function, this departure may be in the order of 15% (Chapter 3). However, the magnitude correction factor $c_0{}'$ was once again applied, leading to relatively close agreement between the desired and the achieved first-order amplitude.

The measured amplitude of wave component n is $A_n/A_{\text{sum}} = 0.52$ in first-order control (green line in Figure 4.8(a)) and $A_n/A_{\text{sum}} = 0.54$ in second-order control (red line in Figure 4.8(a)). For wave component m, the recorded first-order magnitudes are $A_m/A_{\text{sum}} = 0.47$ and $A_m/A_{\text{sum}} = 0.49$ for first-order and second-order control respectively. It should be noted once again, that these first-

order quantities are obtained directly from the DFT; the information presented in Figure 4.8(a) providing the averaged magnitude over the seven wave probe locations.

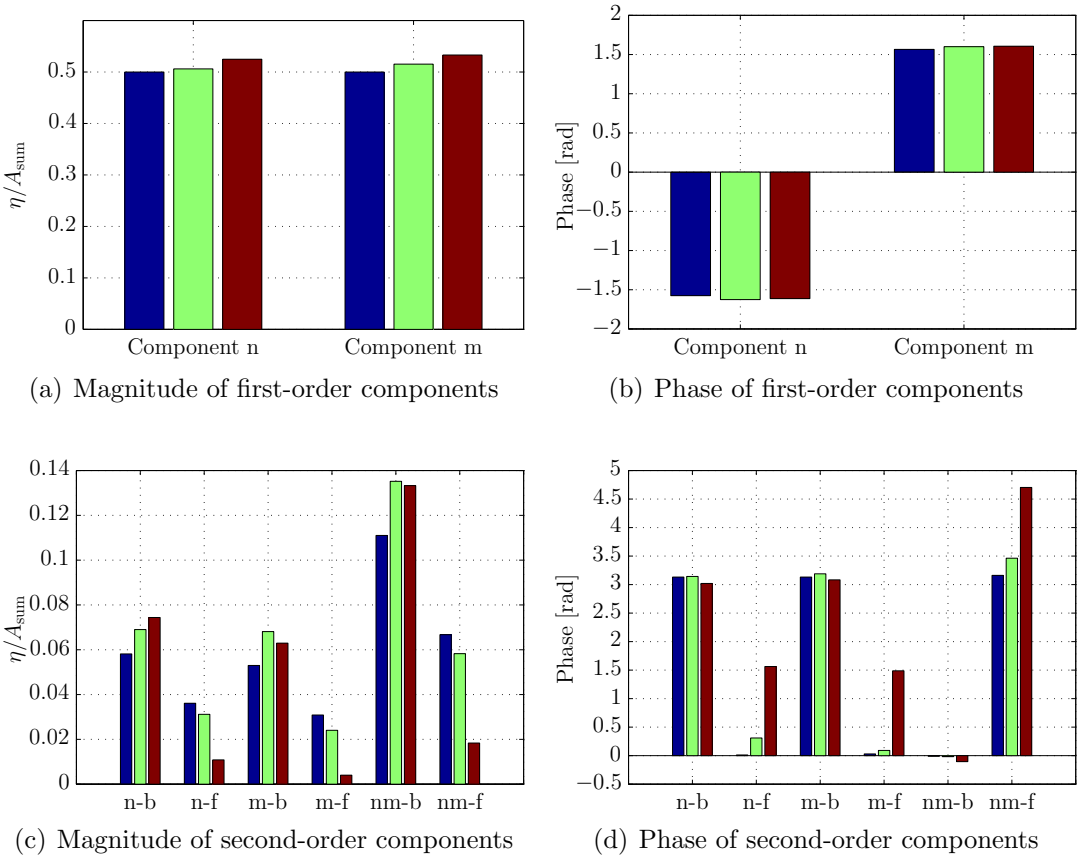
As noted above, the phases were adjusted to $\alpha_n = -\pi/2$ and $\alpha_m = +\pi/2$. The phasing achieved in the experimental cases is very similar for both first- and second-order control, with a maximum departure from the desired value of 0.12rad for α_m (Figure 4.8(b)).

The magnitude data corresponding to the second-order analysis contains a total of six terms (Figure 4.8(c)). Considering the data entries from left to right, this includes the bound self-interaction term of wave component k_n (n-b), the spurious free superharmonic due to k_n (n-f), the bound self-interaction term of component k_m (m-b), the spurious free wave due to k_m (m-f), the bound cross-interaction term between k_n and k_m (nm-b) and the corresponding spurious free component (nm-f).

The three bound terms are the desired wave components, and these should not be affected by the type of control (force or position) or the order of the demand signal (first or second). The agreement between the desired or theoretical bound components (blue lines in Figure 4.8(c)), and the bound components in first-order control (green lines) and second-order control (red lines) is indeed good. Any small departures in the bound wave content are likely to be due to the small departures in the first-order wave amplitudes noted above.

The success of nonlinear control may now be evaluated by comparing the magnitudes of the free wave components between first- and second-order control. Considering wave component n first, the self-interaction component n-free reduces from $A_n^{(22)+}/A_{\text{sum}} = 0.058$ (first-order control) to $A_n^{(22)+}/A_{\text{sum}} = 0.005$ (second-order control) providing clear evidence that the control methodology is effective. Similarly, the self-interaction term m-free reduces from 0.039 to 0.008 and the cross-interaction term nm-free reduces from 0.098 to 0.009. Indeed, the remaining spurious content for case Bi1 is very small, and is comparable to the accuracy of the data acquisition and post processing.

The phase information illustrated in Figure 4.8(d) provides additional evidence of the accuracy of the theoretical potential flow predictions. It should be noted, however, that the phase information for the free components under second-order control does not provide a reliable measure, as this relates to very small quantities within the DFT analysis.



(a) Magnitude of first-order components

(b) Phase of first-order components

(c) Magnitude of second-order components

(d) Phase of second-order components

Figure 4.9: Wave components for case Bi2 providing (i) the theoretical predictions assuming first-order position control (blue), (ii) the experimental data based on first-order position control (green), and (iii) the experimental data based on second-order position control (red).

Figure 4.9 concerns case Bi2, with the data representation being identical to that adopted for case Bi1 (Figure 4.8). As before, good agreement may be observed between the theoretical and experimental first-order quantities, with a maximum first-order magnitude departure of $\approx 6\%$ (Figure 4.9(a)), and a maximum first-order phase departure of 0.04rad (Figure 4.9(b)). Concerning the second-order amplitudes (Figure 4.9(c)) and phases (Figure 4.9(d)), conclusion similar to the

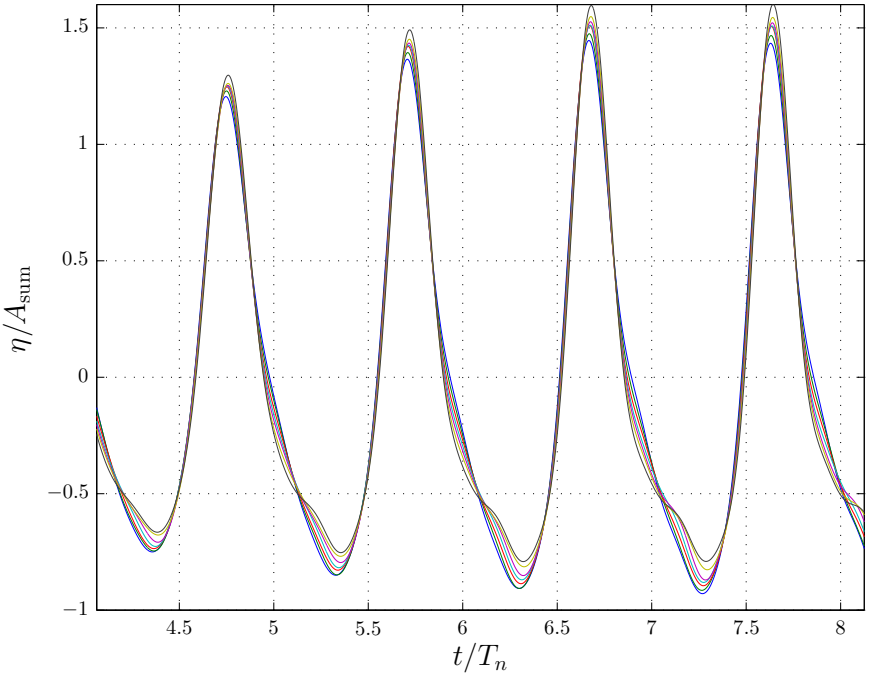
above may be drawn.

Firstly, relatively good agreement is observed between the theoretical and the experimental bound waves amplitudes. The departures observed are somewhat higher than in case Bi1, and this is likely to be attributed to overly large first-order wave amplitudes for both components n and m. Secondly, a relatively close match is observed between the free waves amplitudes provided by Schäffer (1996) and those obtained experimentally using a first-order control signal. Adopting the second-order control signal, a significant reduction is once again achieved in the spurious free wave amplitudes, leading to a maximum spurious wave nm-free of $0.018A_{\text{sum}}$. To set this into an absolute context, the remaining free wave only corresponds to 1.5mm. A very good agreement can also be observed in the second-order phases; a maximum departure of 0.3rad appearing for the superharmonic free wave associated with wave component n.

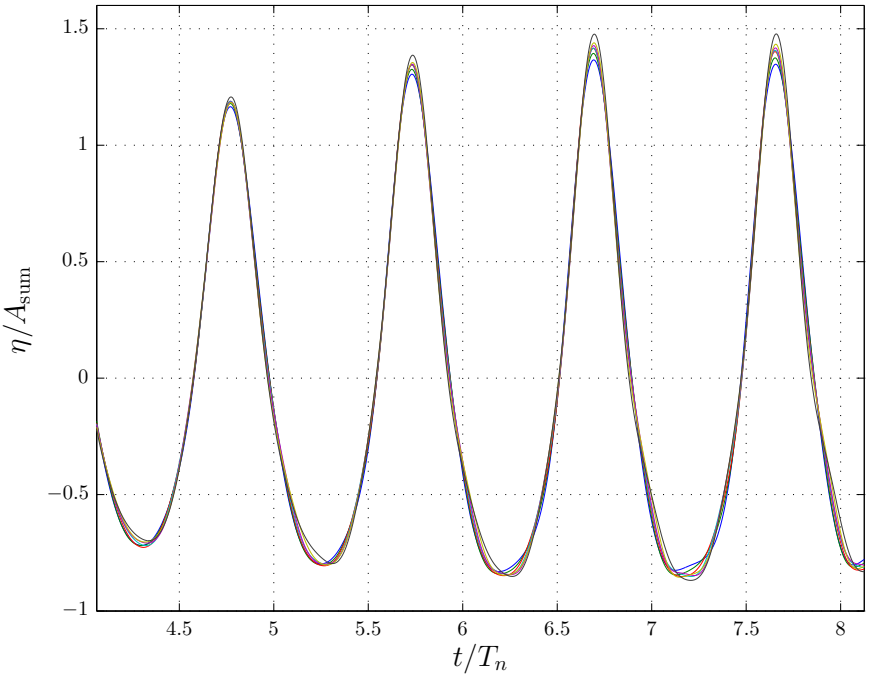
4.3.3 Second-order force control

Having established the success of the second-order correction in position control, the present section concerns cases Bi1 and Bi2 in force control. As discussed in §4.2.3, this must also take into consideration the additional nonlinear force feedback. Figure 4.10 shows the surface profiles recorded by the seven wave probes for wave case Bi1. As before, the data recorded by gauges 2...7 was time-shifted to overlap with the recording at gauge 1.

The data corresponding to a first-order control signal, Figure 4.10(a), provide clear evidence of the existence of significant spurious free wave content. Whilst this is consistent with the findings in the context of regular waves (Chapter 3), it is important to stress that the present findings are in marked contrast to the conclusions drawn for force-controlled flap-type machines (Spinneken and Swan, 2009*a*,*b*). In the flap-type case, the additional nonlinear force feedback led to a (partial) cancellation of the spurious free wave content. This is not the case for piston-type wavemakers, as evident from the data in Figure 4.10(a).

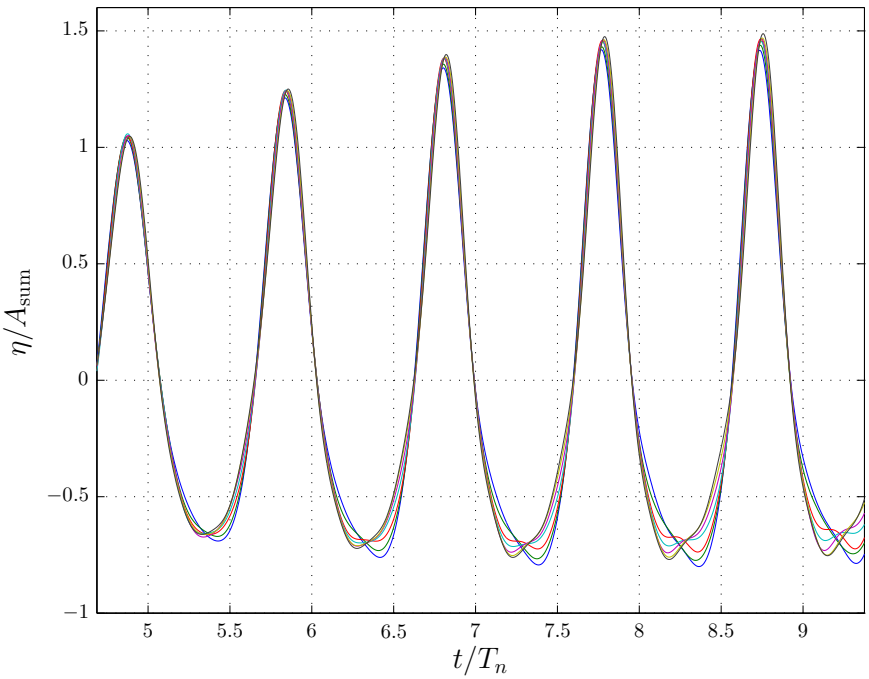


(a) First-order force control

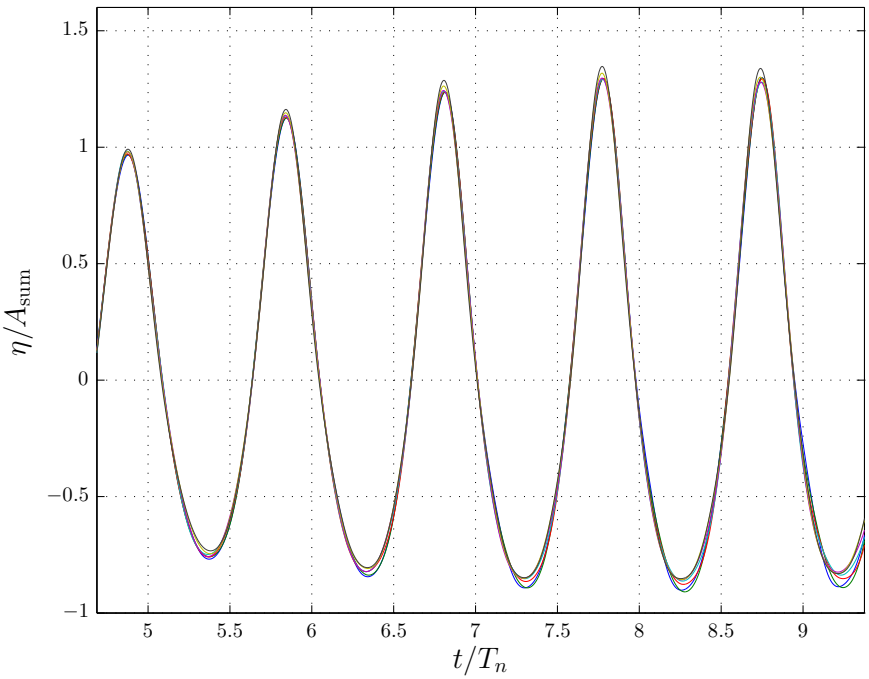


(b) Second-order force control

Figure 4.10: Surface elevation for bi-chromatic wave case Bi1 as described in Table 4.1. Note: The individual time histories relate to recordings at seven spatial locations, where the time histories at subsequent gauges have been shifted to overlap with the time history at the first gauge.



(a) First-order force control



(b) Second-order force control

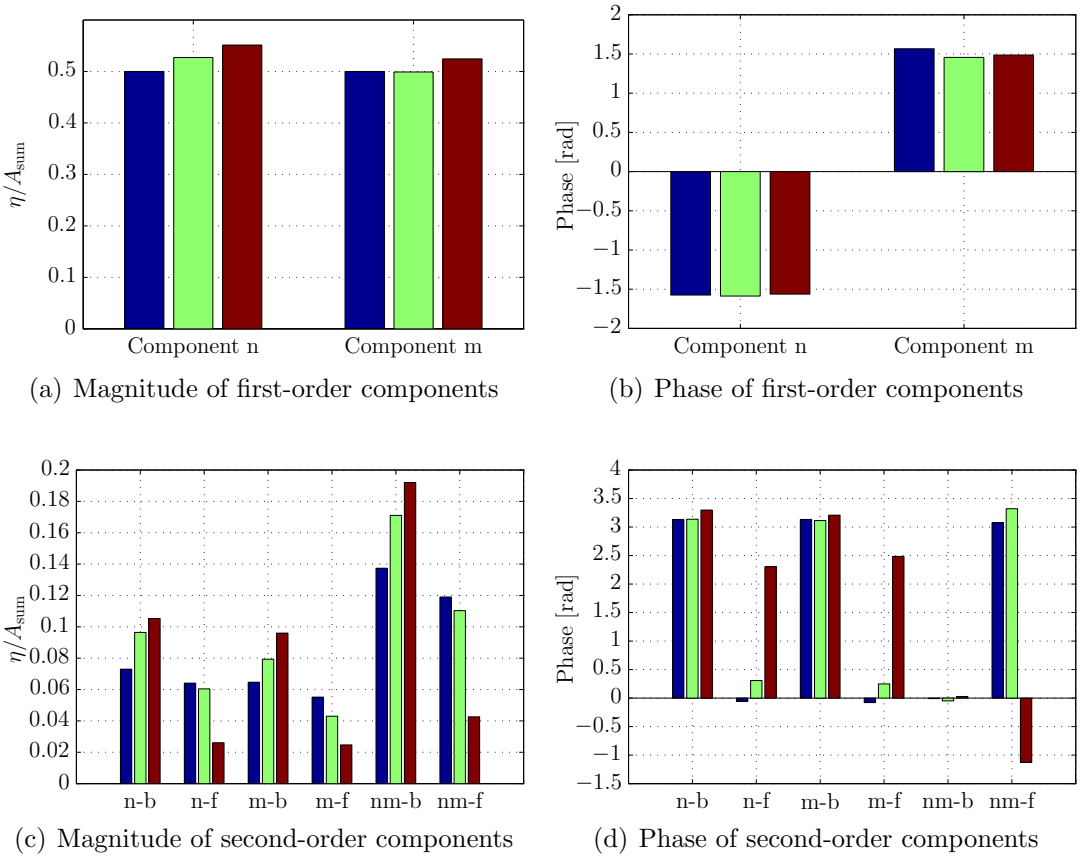
Figure 4.11: Surface elevation for bi-chromatic wave case Bi2 as described in Table 4.1. Note: The individual time histories relate to recordings at seven spatial locations, where the time histories at subsequent gauges have been shifted to overlap with the time history at the first gauge.

A significant improvement in the wave quality is observed when adopting a second-order force-control signal, Figure 4.10(b). In comparing Figures 4.10(a) and 4.10(b), the second-order control signal eliminates a large part of the spurious free wave content. From a qualitative perspective, the second-order compensation in force control is perhaps slightly less effective than in position control (Figure 4.6(b)). For case Bi2, Figure 4.11, a significant improvement in the wave quality can again be observed if a second-order force-control signal is applied. For this case, the wave quality under second-order force control (Figure 4.11(b)) appears comparable to second-order position control (Figure 4.7(b)).

To provide a more quantitative analysis, a harmonic decomposition of the wave field was once again undertaken. Adopting the same series of analysis steps as outlined in §4.3.2, the first-order and second-order quantities were extracted from the experimental data recorded at gauges 1 through 7; the corresponding results being shown in Figure 4.12 (case Bi1) and Figure 4.13 (case Bi2).

For case Bi1, relatively good agreement can be observed between the theoretically predicted and the experimentally observed first-order wave quantities. In terms of the wave phasing (Figure 4.12(b)), the maximum difference from the prediction is only 0.11rad. The maximum magnitude departure arises for $A_n/A_{\text{sum}} = 0.55$ (Figure 4.12(a)), compared to the desired amplitude of $A_n/A_{\text{sum}} = 0.5$. It is surprising, however, that the first-order wave amplitude increases slightly under second-order control; this being observed for both components n and m. To be entirely clear, the first-harmonic of the force demand signal is identical between first-order and second-order control. The first-harmonic amplitude for both components n and m increases by approximately 5% when adopting second-order control. In terms of the real-time force controller adopted, a change in the second-harmonic demand quantities should not affect the behaviour of the fundamental wave components. The observation that a small cross-coupling seems to exist indicates that either the controller or the mechanical system (the physical wavemaker) exhibit nonlinearities that are not captured by the present theoretical model.

Considering the second-order bound wave amplitudes (Figure 4.12(c)), the



(a) Magnitude of first-order components

(b) Phase of first-order components

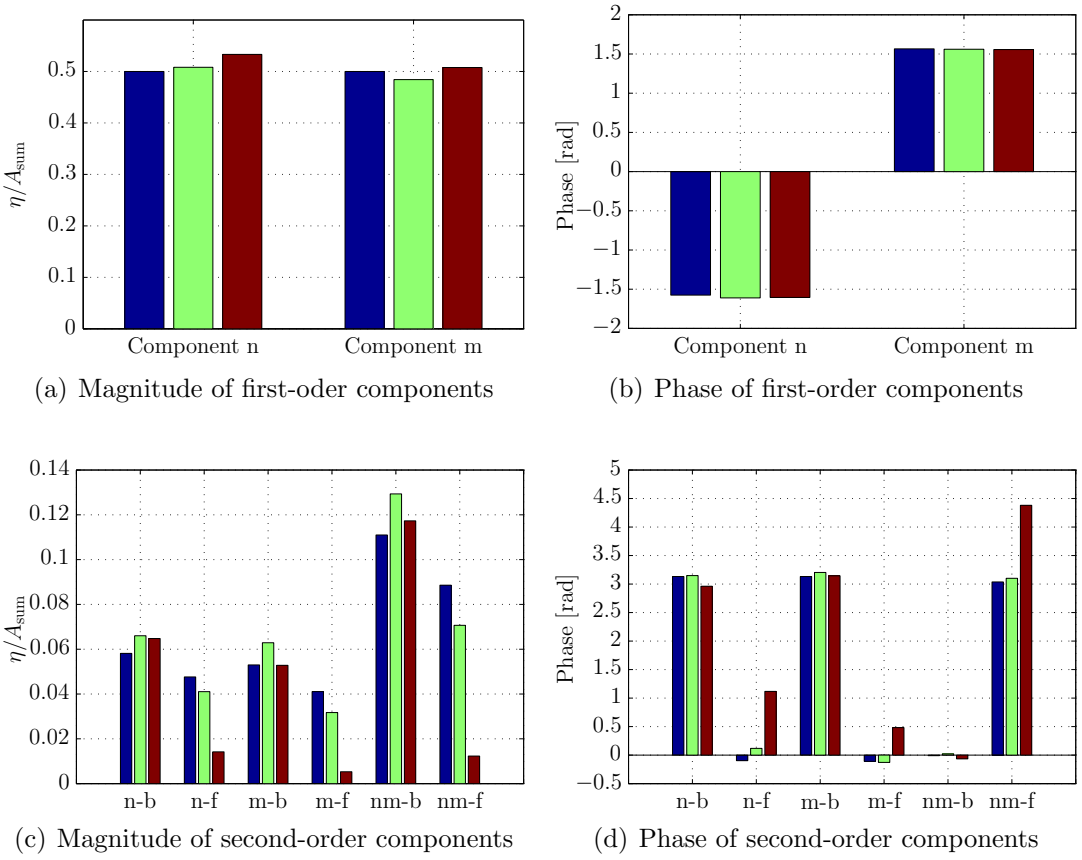
(c) Magnitude of second-order components

(d) Phase of second-order components

Figure 4.12: Wave components for case Bi1 providing (i) the theoretical predictions assuming first-order force control (blue), (ii) the experimental data based on first-order force control (green), and (iii) the experimental data based on second-order force control (red).

experimental data for both first-order and a second-order control agree reasonably well to the theoretical predictions. However, the departures between theory and experiments are more pronounced than in position control (Figure 4.8(c)); the maximum departure being $0.05A_{\text{sum}}$ for nm-bound. The most likely explanation for this again lies in the mismatch of the first-order wave amplitudes noted above. A partial compensation of the spurious free wave content is achieved, but this compensation for case Bi1 is less effective than in position control. The largest remaining free wave content arises for nm-free as $A_{nm}^{(22)+}/A_{\text{sum}} = 0.042$, which compares to a corresponding value of only 0.009 in position control. This supports the qualitative observation made in Figure 4.10.

Fortunately, these observations do not apply to all wave cases considered.



(a) Magnitude of first-oder components

(b) Phase of first-order components

(c) Magnitude of second-order components

(d) Phase of second-order components

Figure 4.13: Wave components for case Bi2 providing (i) the theoretical predictions assuming first-order force control (blue), (ii) the experimental results based on first-order force control (green), and (iii) the experimental results based on second-order force control (red).

Second-order force control for case Bi2 is considered in Figure 4.13. First, a close match is noted in the first-order amplitudes (Figure 4.13(a)) and phases (Figure 4.13(b)), with maximum departures of $0.03A_{\text{sum}}$ and 0.04rad respectively. The slight increase of the first-order wave amplitudes under second-order control is once again observed. Considering the second-order amplitudes in Figure 4.13(c) it is noted that (i) a good agreement between theoretical predictions and experimental observations is achieved in the bound wave content and (ii) the reduction of the free waves amplitude is as effective as in second-order position control (Figure 4.9(c)). For case Bi2, the largest remaining free wave is n-free with $A_n^{(22)+}/A_{\text{sum}} = 0.013$, which is comparable to position control. This agrees with the previously noted observations concerning the corresponding surface profiles,

and confirms the success of nonlinear force control for this particular case.

4.3.4 Relative water depth

The spurious wave suppression for case Bi1 was found to be less effective in force control. For case Bi2, position control and force control achieved comparable results. The purpose of the present section is to provide extended experimental evidence concerning the benefits of nonlinear control. For this purpose, the non-dimensional water depth kh is varied, whilst retaining a constant wave nonlinearity parameter S.

A wave nonlinearity of $S = 0.5$ is adopted for each of the two components n and m. If the two components are entirely in phase, they produce a linear amplitude sum equivalent to a regular wave of $S_{\mathrm{nm}} = S_n + S_m = 1.0$; this latter value defining the range of validity of second-order theory. In the absence of a consistent measure defining the validity range of second-order theory for bi-chromatic waves, the measure of S_{nm} provides a means of quantifying the nonlinearity involved. The water depth is kept constant at $h = 0.6$m, and the wave frequencies for the cases considered are as noted in Table 4.1.

Table 4.2: Experimental data for second-order control concerning cases Bi3-Bi6.

Case	$A_n^{(22)+}/A_n^{(21)+}$		$A_m^{(22)+}/A_m^{(21+)}$		$A_{nm}^{(22)+}/A_{nm}^{(21)+}$	
	P/C	F/C	P/C	F/C	P/C	F/C
Bi3	0.48	0.54	0.26	0.08	0.34	0.20
Bi4	0.10	0.23	0.13	0.30	0.17	0.33
Bi5	0.15	0.37	0.07	0.15	0.16	0.25
Bi6	0.20	0.14	0.07	0.09	0.09	0.04
Average	0.23	0.32	0.13	0.15	0.19	0.20

The results of the experimental data analysis are presented in Table 4.2. This includes the spurious superharmonic interaction terms of components n and m ($A_n^{(22)+}/A_n^{(21)+}$ and $A_m^{(22)+}/A_m^{(21+)}$) as well as the cross interaction term $A_{nm}^{(22)+}/A_{nm}^{(21)+}$. Under first-order control, these ratios lie in the order of 0.7 to 0.9. For ideal second-order correction, each of these ratios would be zero. All data

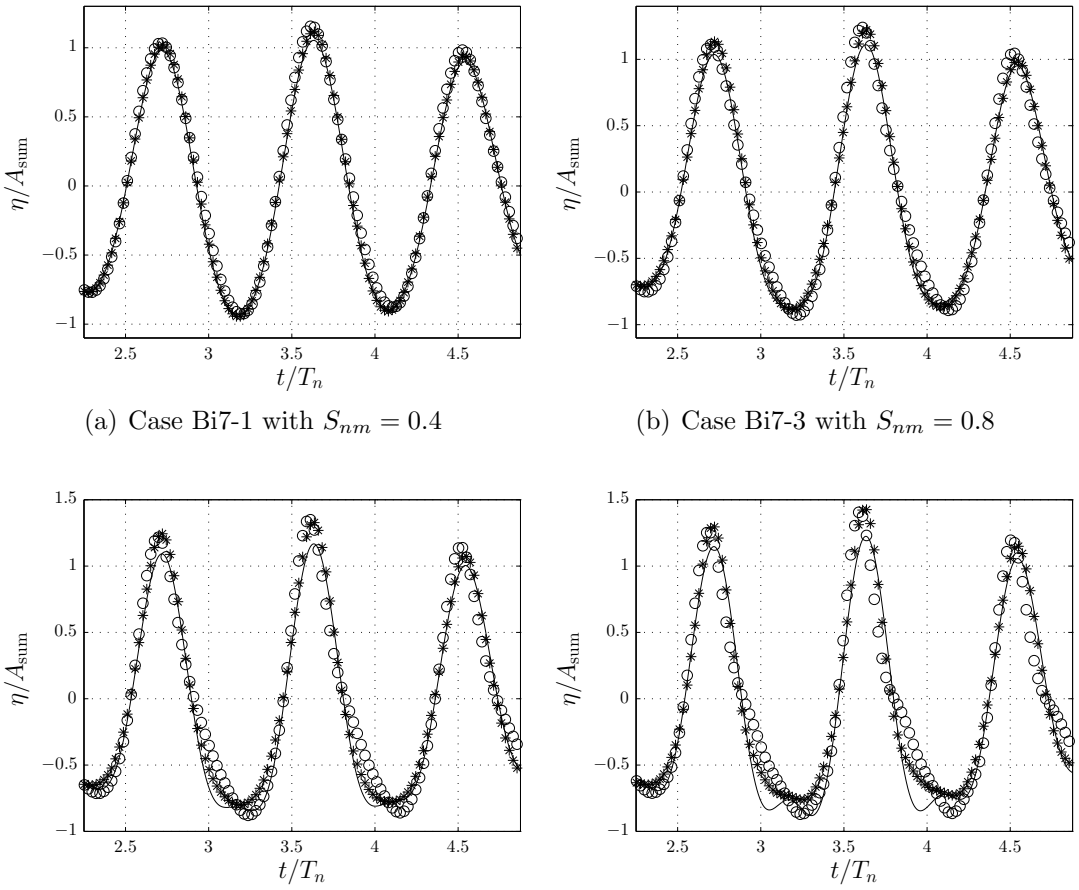
shown in Table 4.2 relate to second-order control. The position-control cases are denoted as P/C, with force control denoted as F/C.

In considering Table 4.2, the success of second-order control is evident for most conditions. The largest free wave content arises for the self-interaction term of component n in case Bi3. With $k_n h = 0.5$, this case corresponds to the most shallow water condition considered, and second-order theory may no longer be applicable. From the data shown in Table 4.2 it is difficult to make any firm recommendations as to which control mode (position or force) is more effective. On balance, the spurious free wave content in position control is slightly lower than that in force control. This is best observed by considering the average values given in the final row of Table 4.2. The average remaining free wave content for the self-interaction term of component n is 23% in position control and 32% in force control. Similarly, the free wave content for component m is marginally higher in force control (15%), compared to 13% in position control. The average remaining cross-interaction term is approximately 20% in both control modes. For the present test cases, the free wave suppression is more effective in position control, albeit the difference to force control is relatively small.

4.3.5 Wave nonlinearity

The investigation of the wave nonlinearity parameter S concerns cases Bi7-1 through Bi7-7 (Table 4.1). Within this set of cases, the two fundamental wave components remain constant at $k_n h = 0.62$ and $k_m h = 0.74$. The parameter S is varied in the range $0.2 \leq S_n \leq 0.8$ and equivalently $0.2 \leq S_m \leq 0.8$. As a result, the sum of these two wave components yields $0.4 \leq S_{nm} \leq 1.6$. As noted earlier, $S_{nm} \leq 1$ is believed to be a suitable measure to define the range of applicability of second-order theory. Applying this measure, cases Bi7-5, Bi7-6 and Bi7-7 exceed this limit.

Figure 4.14 provides an example set of surface elevations, relating to (a) case Bi7-1 with $S_{nm} = 0.4$, (b) case Bi7-3 with $S_{nm} = 0.8$, (c) case Bi7-5 with $S_{nm} =$



(a) Case Bi7-1 with $S_{nm} = 0.4$

(b) Case Bi7-3 with $S_{nm} = 0.8$

(c) Case Bi7-5 with $S_{nm} = 1.2$

(d) Case Bi7-7 with $S_{nm} = 1.6$

Figure 4.14: Water surface elevation for case Bi7 showing —— Second-order prediction in the absence of spurious wave content, ∘ Experimental data under first-order force control and ∗ Experimental data under second-order force control.

1.2, and (d) case Bi7-7 with $S_{nm} = 1.6$. The figure includes the theoretical (ideal) second-order predictions in the absence of any spurious free waves (solid line). The experimental data shown relate to first-order force control (symbol ∘) and second-order force control (symbol ∗).

For the two cases in Figures 4.14 (a) and (b) with $S_{nm} < 1$, the experimental data confirms that second-order control provides an improved match to the theoretical prediction. For cases (c) and (d) with $S_{nm} > 1$, significant departures exist between the theoretical second-order surface elevation and the experimental data under second-order control; this being particularly evident in Figure 4.14(d). From this latter figure is can also be observed that a secondary 'bump' arises in

the two lowest throughs of the bi-chromatic wave group. The occurrence of such a wave feature is known to be non-physical, and is often used to define the breakdown of second-order theory. This secondary 'bump' is not observed in any of the experimental data sets, providing further evidence that this is a non-physical condition. As a direct consequence, any comparisons between the predicted free wave content and the experimental data for $S_{nm} > 1$ (Cases Bi7-5, Bi7-6 and Bi7-7) should be considered with caution.

The result of the data analysis for the full set of test cases is summarised in Table 4.3, which is presented in the same form as Table 4.2. In close similarity to the earlier discussion, the spurious free wave content in force control is slightly higher than that in position control. The average value noted in Table 4.3 only concerns cases with $S_{nm} < 1$. For the self-interaction term of component n, second-order force control and position control achieve similar free wave contents, with 19% and 20% respectively. The difference between the two types of control is more pronounced for $A_m^{(22)+}$ and $A_{nm}^{(22)+}$, where force control leads to approximately 16% larger free wave content.

Table 4.3: Experimental data for second-order control for cases Bi7-1 to Bi7-7.

Case	$A_n^{(22)+}/A_n^{(21)+}$		$A_m^{(22)+}/A_m^{(21+)}$		$A_{nm}^{(22)+}/A_{nm}^{(21)+}$	
	P/C	F/C	P/C	F/C	P/C	F/C
Bi7-1	0.35	0.28	0.11	0.30	0.29	0.42
Bi7-2	0.18	0.18	0.08	0.26	0.18	0.38
Bi7-3	0.19	0.10	0.10	0.24	0.20	0.31
Bi7-4	0.10	0.21	0.12	0.30	0.18	0.32
Average	0.20	0.19	0.10	0.28	0.20	0.36
Bi7-5	0.19	0.55	0.12	0.29	0.12	0.27
Bi7-6	0.40	1.30	0.14	0.31	0.06	0.27
Bi7-7	0.90	1.23	0.13	0.38	0.19	0.27

As the nonlinearity parameter S_{nm} exceeds unity, the term $A_n^{(22)+}/A_n^{(21)+}$ increases rapidly. This is unsurprising, given that wave component n relates to the more shallow water component, where the applicability of second-order theory is severely limited. For cases Bi7-6 and Bi7-7 it may even be argued that second-order control is detrimental to the overall wave quality. However, this is difficult

to assert, as a reference wave theory no longer exists under these conditions.

4.4 Conclusions

In making an important step towards the modelling of random sea states, the present chapter concerned a bi-chromatic wave investigation, where only two fundamental wave components exist. A theoretical description of the nonlinear wavemaking problem established that the spurious free wave content under first-order force control is comparable to first-order position control, and may even be slightly larger. Experimental data confirmed the occurrence of significant free wave content in both position and force control. Whilst this is well established in position control, the present force control findings are novel.

Indeed, these findings are in marked contrast to a previous body of work concerning the operation of flap-type wavemakers in force control. In the flap-type case, a nonlinear force-feedback term was previously found to be beneficial to the wave quality. This is not the case for the generation of bi-chromatic waves using a piston-type wavemaker. In effect, whilst the nonlinear force-feedback term also exists in the piston-type case, it is relatively small compared to other forcing components. As a result, the bi-chromatic wave quality under first-order force control is, at best, comparable to position control.

A second-order force-control signal leads to an effective suppression of this free wave content. This suppression was demonstrated for a range of wave cases, varying both the relative water depth and the wave nonlinearity. Second-order force control leads to comparable wave quality as second-order position control, although the latter may lead to marginally better free wave suppression. The success of either control mode is limited by the applicability of the underlying second-order theory, which generally prevents a combination of shallow water and steep waves.

5

Focused wave groups

5.1 Chapter overview

Focused wave groups are often adopted to model some of the most extreme ocean wave events. Nonlinear interactions within focused wave groups can lead to significant amplifications in both the crest elevations and the crest kinematics; the correct laboratory reproduction of such extreme wave events being highly relevant to the design of offshore structures. A key practical advantage of focused wave groups is their relatively short duration, often enabling testing without contaminations by undesired reflections from a downstream beach. Nevertheless, active absorption remains important in ensuring a short tank settling time between experimental runs.

The present chapter concerns the wavemaking techniques required for the successful generation of focused wave groups in shallow water conditions. In so doing, a suitable reference model for the description of focused wave events is required first. To achieve this, Part I (§5.3 - §5.7) presents an investigation concerning the generation of focused wave groups in a numerical wave tank, defining a set of reference wave conditions. Part II (§5.8 - §5.13) subsequently presents an experimental assessment of focused wave events, addressing both position control and force control.

Part I: A numerical investigation

5.2 The modelling of focused wave groups

In seeking to develop a model that closely reproduces extreme wave events, Tromans et al. (1991) developed a methodology that predicts the most probable extreme wave in a particular sea state. Based on an extreme value analysis, the model provides a deterministic solution, effectively avoiding the statistical analysis of long and repetitive simulations of random sea states. However, the model by Tromans et al. (1991) is based on a linear spectrum, and is unable to predict the influence of nonlinearities in the evolution of a wave group.

Johannessen and Swan (2001, 2003) demonstrated that a focused wave group is associated with a nonlinear evolution that includes interaction terms beyond second order. Indeed, an important part of the wave group evolution is governed by the widening of the free-wave regime, characterised by energy transfers to the high frequencies and low frequencies. Johannessen and Swan (2003) demonstrated that departures between experimental observations and second-order wave theory are primarily due to these energy transfers. They also suggested that an improved prediction can be obtained by applying second-order wave theory to a linear spectrum that includes the widening of the free-wave regime.

However, second-order wave theory is likely to be limited in the case of highly-nonlinear focused wave groups. To obtain an improved description of highly-nonlinear focused waves, Baldock and Swan (1994) developed a numerical model for extreme waves based on a double Fourier series expansion in both space and time. The approach is based on the minimisation of the error in the free-surface boundary conditions for a given surface profile, and provides a Fourier decomposition of the sea state as well as the wave kinematics. Individual wave components in the sea state are modelled as Fourier components, which enables the formulation of a nonlinear wave model. This method is robust in the sense that it accounts for both the nonlinearities in the wave group and the unsteadiness of

the sea state. The solution includes a realistic group of bound waves and free waves that allows for the correct reproduction of extreme wave kinematics. The main drawback of the method is that it relies on a pre-defined or measured surface elevation throughout the spatial and temporal domains.

To overcome this limitation, Bateman et al. (2001) (also Bateman et al. (2003)) developed a Fourier-based methodology whereby the solution may be time marched from a set of initial conditions. If these initial conditions are representative for a relatively dispersed sea state, it can be argued that nonlinear interactions beyond the order of the initial wave solution (which could be first order or second order) may be neglected in the initial fluid state. The time marching of the fully-nonlinear free-surface boundary conditions subsequently ensures that the full nonlinearity of the problem is taken into account.

Similar arguments apply to the Numerical Wave Tank (NWT) model developed by Hague and Swan (2009), which is again based on a time marching of the fully-nonlinear free-surface boundary conditions. In contrast to Bateman et al. (2001), the NWT by Hague and Swan (2009) operates within a closed physical domain, and may be considered analogous to a physical wave tank. In making a comparison to the wavemaking BVP described in Chapter 2, §2.3.3, it is important to note that the NWT implements the governing equation (2.1), and conditions (2.2a), (2.2c) and (2.2d) in their fully-nonlinear form. In contrast, the lateral input boundary condition (equation (2.2b) in the context of the wavemaking BVP) relies on a pre-defined description of the fluid kinematics. In close similarity to the second-order wavemaker BVP, the main limitation of the NWT lies in the assumption of potential flow. Nevertheless, given the ability to capture the nonlinearity of the problem, the NWT by Hague and Swan (2009) is considered the most suitable reference model for the present comparison; this approach simply being referred to as NWT hereafter.

In the context of this NWT, the description of the initial conditions concerns the fluid kinematics at the input boundary. It has often been argued that a focused wave group can be accurately reproduced if this input boundary is located

sufficiently far upstream from the focus location; this condition ensuring a dispersed sea state at the input boundary. Similar arguments have often been noted in the context of laboratory wave group generation. To the best of the author's knowledge, a firm quantification of this effect does not exist, particularly in shallow water where the effect of dispersion is more limited than in deep water. In this context, the purpose of this Part I is two-fold:

(i) to obtain a quantitative description of the minimum distance required between the input boundary and the focused wave location and

(ii) to obtain a numerical reference description of the surface elevation at the focus location.

To achieve this, Part I of this chapter is structured as follows. The wave conditions and domain adopted for the present comparison are outlined in §5.3. The procedures by which the minimum distance to the focus location, (i) above, may be quantified are outlined in §5.4. An analysis of the errors arising in the free-surface boundary conditions is presented in §5.5. To further establish the importance of this error measure, a NWT study is then presented in §5.6. A set of Part I conclusions is finally presented in §5.7.

5.3 Wave conditions and domain definition

Figure 5.1 provides a schematic of the numerical domain adopted and defines the notation used. A cartesian coordinate system (x, z) is considered, where $z = 0$ represents the still water level and $z = -h$ corresponds to the bed. Furthermore, the location $x = 0$ defines the input of the domain, and $x = x_f$ defines the location where the wave group focuses. For the purpose of the present comparisons, the location x_f is calculated according to a linear soution. Focused events are characterised by the constructive superposition of the underlying wave components at x_f. As a consequence, the majority of the nonlinear wave-wave interactions also take place in the vicinity of this focus location. Due to wave dispersion, the

wave group becomes dispersed with increasing distance (upstream or downstream) from x_f. Provided that x_f is sufficiently far downstream from the input boundary ($x = 0$), this allows for the use of a relatively low-order theory to calculate the fluid kinematics at the input. A second-order or even linear wave theory may be sufficient, where the associated error depends on both the nonlinearity of the wave event and the distance x_f.

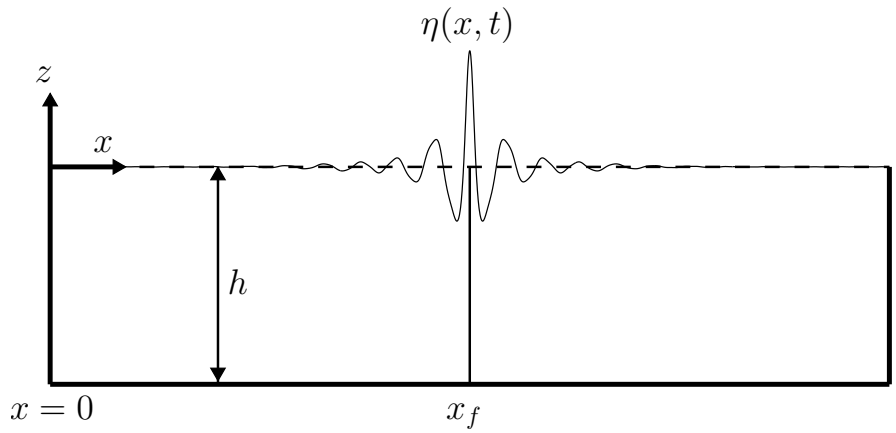


Figure 5.1: Numerical domain and definition of notation adopted.

To demonstrate this effect, the present work adopts a wave group with an underlying JONSWAP spectral density function

$$S_{\eta\eta}(\omega) = \frac{\alpha g^2}{\omega^5} \exp^{-\frac{5}{4}\frac{\omega_p^4}{\omega^4}} \gamma^{\beta}, \tag{5.1}$$

where

$$\beta = \exp\left\{-\frac{(\omega - \omega_p)^2}{2\omega_p^2\sigma^2}\right\} \tag{5.2}$$

and

$$\sigma = \begin{cases} 0.07 & \text{if} \quad \omega \leq \omega_p \quad \text{and} \\ 0.09 & \text{if} \quad \omega > \omega_p. \end{cases} \tag{5.3}$$

Furthermore, γ defines the peak enhancement factor, $\omega_p = 2\pi/T_p$ defines the peak frequency, T_p is the peak period and α is the Phillips parameter. For the purpose of the focused wave analysis, the relative water depth is expressed as $k_p h$, where

the wavenumber k_p is the solution to the dispersion equation for the period T_p and the water depth h.

A focused wave group of surface elevation $\eta(x,t)$ may now be defined by the wave amplitude sum A_{sum}, which is obtained through the linear superposition of all wave components within the spectrum. In both numerical and laboratory wave generation, the spectral representation $S_{\eta\eta}(\omega)$ must first be discretised appropriately. This can be achieved by introducing a set of discrete frequencies f_i (or angular frequencies $\omega_i = 2\pi f_i$), where f_i is an integer multiple of the fundamental frequency $df = d\omega/2\pi = 1/T_r$, and T_r is the repeat time of the spectrum. In a linear sense the amplitude of a wave component of frequency ω_i is given by

$$A_i = \sqrt{2S_{\eta\eta}(\omega_i)d\omega}, \tag{5.4}$$

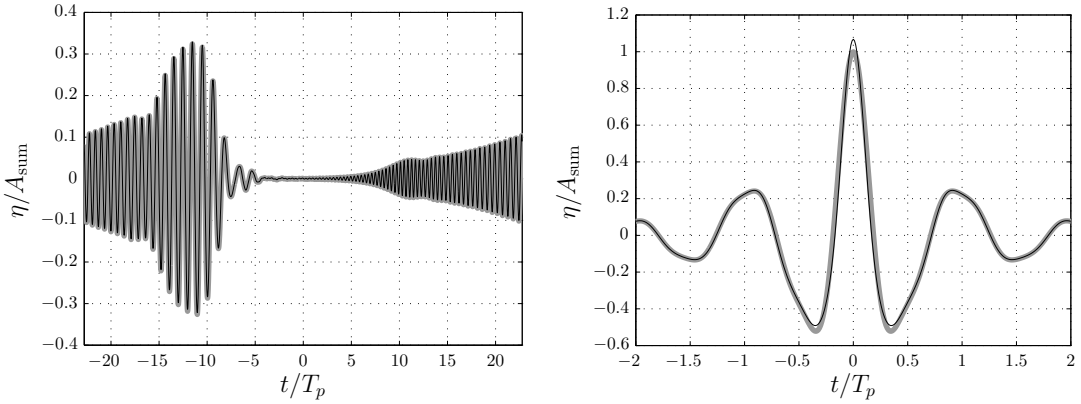
so that the linear amplitude sum may now be defined as

$$A_{\text{sum}} = \sum_i A_i. \tag{5.5}$$

5.4 Defining a minimum focus location

Figure 5.2 illustrates the water surface elevation of a wave group with $k_p h = 1.56$, $A_{\text{sum}} k_p = 0.11$ and $x_f = 30h$, showing the event at (a) the input boundary, $x = 0$, and (b) the linearly calculated focus location, $x = x_f$. In each case, both a linear (grey line) and second-order (black line) calculation are shown, where the latter is calculated after Sharma and Dean (1981). The figure clearly demonstrates the problem at hand. At $x = 0$, the two surface elevations are virtually identical, indicating that nonlinear wave-wave interactions are small. In contrast, some marked differences arise at the focus location. To quantify this, the maximum surface elevation at x_f (Figure 5.2(b)) is $\eta_{\max} = A_{\text{sum}}$ for the linear calculation and $\eta_{\max} = 1.08 A_{\text{sum}}$ for the second-order calculation. This maximum surface elevation reduces to approximately $0.32 A_{\text{sum}}$ at $x = 0$ (Figure 5.2(a)); the depar-

ture between the linear and the second-order calculation only being 0.48%. As a result, it may be argued that linear input kinematics would be sufficient for this particular combination of wave parameters ($k_p h = 1.56$ and $A_{\text{sum}} k_p = 0.11$) and focus location ($x_f = 30h$).



(a) Surface elevation at $x = 0$ (b) Surface elevation at $x = 30h$

Figure 5.2: Focused wave group with $k_p h = 1.56$ and $A_{\text{sum}} = 0.11$ showing ——— linear calculation and ——— second-order calculation.

To quantify this for a wide range of conditions, a detailed evaluation of second-order input kinematics may be undertaken. In terms of the order involved, this approach is comparable with a second-order laboratory wavemaking theory. In specifying the input kinematics directly, the occurrence of any evanescent modes adjacent to the boundary is avoided. As a result, these kinematics may be computed directly from Sharma and Dean (1981). However, in terms of the second-order formulation involved, this is entirely consistent with a second-order wavemaking theory. Indeed, the expressions in Schäffer (1996) (Appendix A) reduce to the expressions in Sharma and Dean (1981) if all evanescent modes are neglected ($j = l = 0$).

To evaluate the error associated with the specification of the second-order input kinematics, a quantitative measure must be defined. In close similarity to the regular wave analysis by Dean (1972), the measure adopted here is based upon the error in the free-surface boundary conditions. For this purpose, the surface elevation, the velocity potential and the fluid velocities are computed using the second-

order analytical expressions given in Sharma and Dean (1981). This second-order solution is subsequently substituted into the fully-nonlinear free-surface boundary conditions.

If the second-order expansion sufficiently describes the solution, then the error in satisfying the exact free-surface boundary conditions is small. To verify this boundary condition approach, the second-order solution was substituted into the second-order expansion of the free-surface boundary conditions (equations (2.10c) and (2.10d)), which is expected to yield zero. In all cases considered the error in this latter comparison was in the order of 10^{-18}, which can be attributed to numerical precision.

In defining the suitability of the input kinematics, the influence of three key parameters is considered: (i) the wave amplitude sum, A_{sum}, (ii) the distance between the input boundary and the focus location, x_f and (iii) the water depth h. In the regular wave comparison by Dean (1972), the error for a number of wave theories was evaluated over a range of wave conditions, and the theory associated with the lowest error (or best fit) in the free-surface boundary conditions was considered to be the most suitable wave theory for a given set of conditions. In the context of the present work, second-order theory is the only existing analytical nonlinear irregular wave theory, and a comparison to other mildly-nonlinear solutions is hence not possible.

To overcome this issue, the evaluation here relies on a combination of methodologies. First, §5.5 concerns the absolute error in the free-surface boundary conditions at the input boundary. A more practical and quantitative error criterion is developed by comparing this free-surface boundary error to a set of convergence criteria defined through a NWT study, §5.6.

5.5 Free-surface boundary condition error

5.5.1 Introduction

This approach relies on the absolute error in both the KFSBC (kinematic free-surface boundary condition) and the DFSBC (dynamic free-surface boundary condition). In defining the ultimate error limit in §5.6, the combined (KFSBC and DFSBC) error is considered. However, to identify their relative contributions, the DFSBC and KFSBC errors are considered separately at this stage. If the surface elevation and the velocity potential are computed at time steps t_i, $1 \leq i \leq N$, then the error in the KFSBC is given by

$$E_{K_i} = \frac{k_p}{\omega_p}\left[\frac{\partial \eta}{\partial t} + \frac{\partial \phi}{\partial x}\frac{\partial \eta}{\partial x} - \frac{\partial \phi}{\partial z}\right] \quad \text{at} \quad z = \eta \quad \text{and} \quad t = t_i, \tag{5.6}$$

and the error in the DFSBC is given by

$$E_{D_i} = \left(\frac{k_p}{\omega_p}\right)^2\left[\frac{\partial \phi}{\partial t} + g\eta + \frac{1}{2}\left\{\left(\frac{\partial \phi}{\partial x}\right)^2 + \left(\frac{\partial \phi}{\partial z}\right)^2\right\}\right] \quad \text{at} \quad z = \eta \quad \text{and} \quad t = t_i. \tag{5.7}$$

Based upon these errors at time t_i, the total errors are

$$E_K = \sqrt{\frac{1}{N}\sum_{i=1}^{N} {E_{K_i}}^2}, \tag{5.8}$$

and

$$E_D = \sqrt{\frac{1}{N}\sum_{i=1}^{N} {E_{D_i}}^2}. \tag{5.9}$$

In the context of regular waves, Dean (1972) normalised the error in the KFSBC by the horizontal fluid velocity $\partial\phi/\partial x$. The error in the DFSBC was normalised by gH, where H represents the height of a regular wave. In contrast, the present study concerns focused wave groups, and the error should be normalised by quantities that are specific to the considered input spectrum. To achieve this, the normalisation was undertaken by k_p and ω_p. For dimensional

consistency, the errors in the KFSBC and DFSBC are normalised by k_p/ω_p and $(k_p/\omega_p)^2$ in equations (5.6) and (5.7) respectively.

5.5.2 Quantitative description

Figure 5.3 concerns the error arising in (a) the KFSBC and (b) the DFSBC if based upon a second-order calculation. In all cases, a spectrum with $k_p h = 1.56$ was considered, and the event was focused at $t_f/T_r = 0.5$, where $T_r = 45T_p$. The steepness of the event is varied in the range $0.03 \leq A_{\text{sum}} k_p \leq 0.15$ and the focus location ranges from $3 \leq x_f/h \leq 90$.[1]

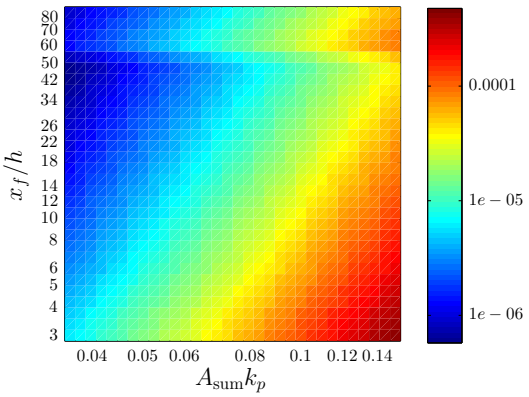
First, and perhaps most importantly, the error in both the KFSBC and DFSBC generally decreases with x_f/h but increases with $A_{\text{sum}} k_p$; this being evident in the contour plots in Figures 5.3(a) and 5.3(b). Both of these observations are as expected. As x_f/h increases, the wave conditions at the input boundary become progressively more dispersed, reducing the nonlinearity of the problem at the input boundary. In contrast, the nonlinearity of the problem increases with $A_{\text{sum}} k_p$, leading to increased boundary condition errors.

Figure 5.3(c) illustrates a subset of the data for $A_{\text{sum}} k_p = 0.11$. For this case, the error in the KFSBC is in excess of 10^{-4} for $x_f/h < 6$. For $x_f/h = 45$, this initial error reduces by almost one order of magnitude to $< 2 \cdot 10^{-5}$. Similar arguments apply to the error in the DFSBC, which reduces by approximately one order of magnitude over the same range. Concerning the actual quality of the focused wave group, it is difficult to draw any firm conclusions based on the absolute value of the error, which highlights the need for introducing a more practical error criterion, as discussed in §5.6.

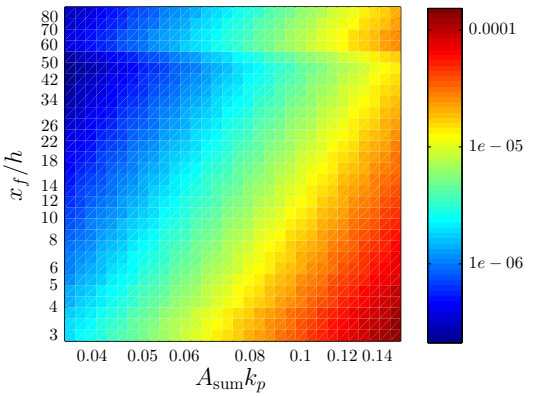
Surprisingly, beyond $x_f/h = 45$, the error in the free-surface boundary conditions increases rapidly, and decreases again after $x_f/h = 57$. Figures 5.3(a) and

[1]Note: A focus location as large as $x_f = 90h$ with $T_r = 45T_p$ would be difficult to achieve in practice, as the high-frequency tail of the spectrum would not have sufficient time to propagate to the focus location at $t_f/T_r = 0.5$. Within the second-order calculations, this effect is not considered, as the solution only concerns the steady state without any transient. Nevertheless, focus locations as large as $x_f = 90h$ are included to demonstrate an important aspect noted later on.

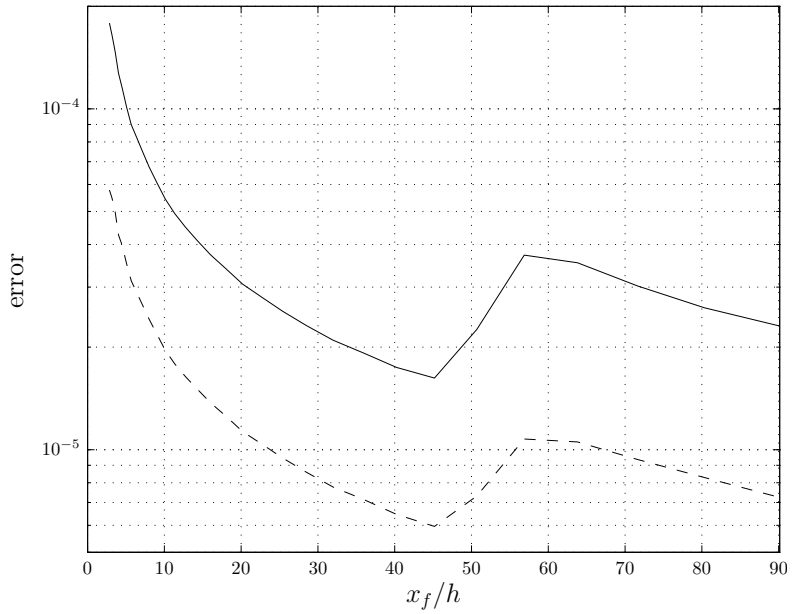
5.3(b) confirm that this rise is independent of the amplitude sum $A_{\text{sum}}k_p$, so that it is not a function of the nonlinearity of the problem. This effect is considered in detail as follows.



(a) E_K for $0.03 \leq A_{\text{sum}}k_p \leq 0.15$



(b) E_D for $0.03 \leq A_{\text{sum}}k_p \leq 0.15$



(c) —— E_K and – – E_D for $A_{\text{sum}}k_p = 0.11$

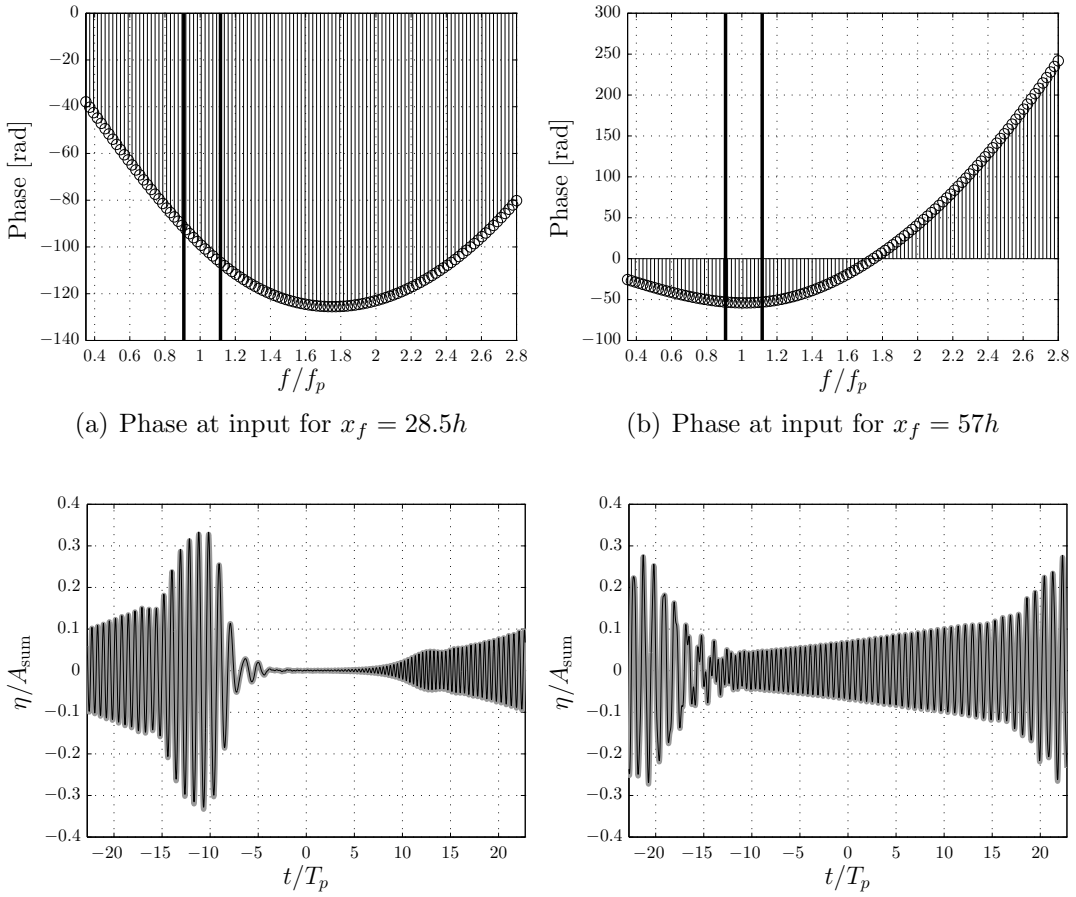
Figure 5.3: Error in KFSBC (E_K) and DFSBC (E_D) for wave cases with $k_p h = 1.56$ and $T_r = 45T_p$

5.5.3 The importance of the phase angle distribution

To investigate the origin of the error increase for $x_f/h > 45$, the phase of the wave components at $x = 0$ is considered for two cases: (i) a wave case with $x_f/h = 28.5$ (Figure 5.4(a)) and (ii) a wave case with $x_f/h = 57$ (Figure 5.4(b)). To aid this comparison, the two vertical lines in each figure represent the frequency band where the wave amplitude A_i is larger than 2/3 of the wave amplitude corresponding to the spectral peak, A_p. As a result, a large part of the total wave energy is contained within the two vertical lines.

In comparing Figures 5.4(a) and 5.4(b), it is clear that the phase gradient at $x = 0$ is very different between the two cases. In Figure 5.4(b), the phase distribution reaches a minimum that coincides with the frequency band of high energy content. In the vicinity of this minimum, the gradient of the phases is very small. As a result, the frequency components within this band are approximately in phase at $x = 0$, so that wave-wave interactions are likely to take place at this location. In contrast, the gradient of the phases around the spectral peak in Figure 5.4(a) is very steep, so that these components are not in phase at $x = 0$. This reduces the potential for wave-wave interaction between closely spaced frequencies at the spectral peak, and leads to a reduction in the error within the free-surface boundary condition (Figure 5.3).

The corresponding surface elevations at $x = 0$, Figure 5.4(c) ($x_f/h = 28.5$) and 5.4(d) ($x_f/h = 57$) further illustrate the problem. These figures also highlight an additional issue associated with large x_f. In Figure 5.4(d) the generation of the highest frequency components of the spectrum is seen to reach significantly beyond $t = 0$, effectively 'wrapping over' into the following repeat time. This indicates that any wave components 'wrapped over' this time would not actually reach the focus wave location in time for $t = t_f$, making $x_f/h = 57$ impractical. However, to be entirely clear, the 'wrapping over' does not directly lead to an error in the free-surface boundary conditions, as the second-order calculations are of steady-state nature.



(a) Phase at input for $x_f = 28.5h$

(b) Phase at input for $x_f = 57h$

(c) $\eta(t)$ at input for $x_f = 28.5h$

(d) $\eta(t)$ at input for $x_f = 57h$

Figure 5.4: Phase angle and water surface elevation at $x = 0$.

5.5.4 Minimum phase gradient condition

The above discussion highlighted that an increase in the focus location x_f is not always beneficial. The 'wrapping over' effect is well known, and may be readily calculated based upon the wave components' group velocity. The issue related to the minimum phase gradient has not been reported before, and may be explained by considering the different contributions to the phase angle. In a focused wave group, the phase α at location x is given by

$$\alpha(x, \omega) = -\omega t_f + k(x_f - x), \tag{5.10}$$

which yields the phase at $x = 0$ as

$$\alpha(0, \omega) = -\omega t_f + k x_f. \tag{5.11}$$

The minimum observed in Figure 5.4 is related to the behaviour of the two phase contributions, $-\omega t_f$ and $k x_f$, which are illustrated separately in Figure 5.5. For very low frequencies the absolute value of the phase contribution $-\omega t_f$ increases more rapidly than $k x_f$. However, for large frequencies the contribution $k x_f$ increases more rapidly. This may be explained as follows. In shallow water conditions the dispersion equation

$$\omega^2 = gk \tanh kh \tag{5.12}$$

may be approximated by

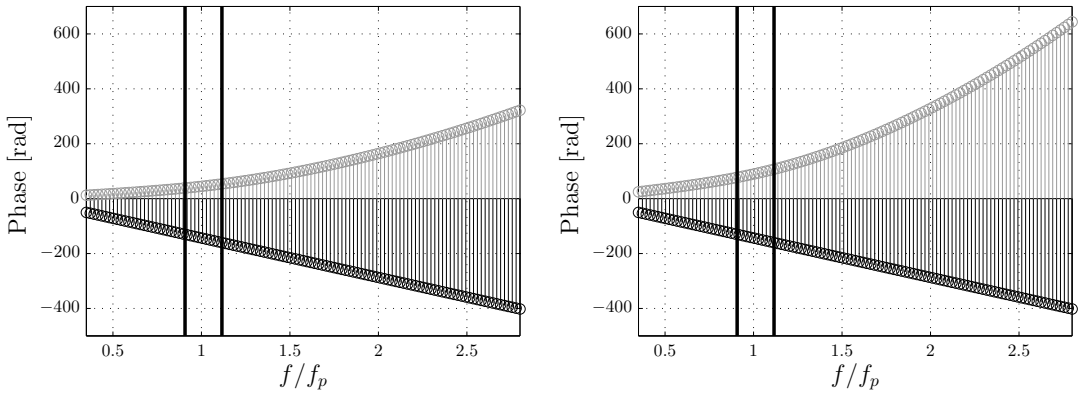
$$\omega^2 = gk^2 h, \tag{5.13}$$

where the wavenumber is proportional to the wave frequency. In contrast, the deep water dispersion equation approximates to

$$\omega^2 = gk, \tag{5.14}$$

where the wavenumber is proportional to the square of the wave frequency.

For increasing x_f, the contribution due to $k x_f$ increases, and may become equal in gradient to the contribution due to $-\omega t_f$ in the vicinity of $f/f_p = 1$ (Figure 5.5(b)). With $k_p h = 1.56$ relating to relatively shallow water, both contributions scale approximately linearly with f, and cancel in the proximity of $f/f_p = 1$. When this occurs, the largest amplitude frequency components are almost in phase and form a region of higher amplitude and higher error in the free-surface boundary conditions.



(a) Contributions for $x_f = 28.5h$ (b) Contributions for $x_f = 57h$

Figure 5.5: Contributions to the wave component phase at $x = 0$ with $-\omega t_f$ (black) and kx_f (grey).

5.5.5 The linkage of focus time and location

Having established the causes for the rise in the error at the input boundary, a method that mitigates this issue may be devised. The minimum phase for a wave component of frequency ω_n occurs if the following condition is met

$$\frac{d\alpha}{d\omega}(\omega_m) = 0. \tag{5.15}$$

Substituting equation (5.10) for α and rearranging yields

$$\frac{d\omega}{dk}(\omega_m) = \frac{x_f - x}{t_f}. \tag{5.16}$$

Consequently, the component with a minimum phase at $x = 0$ corresponds to a component with group velocity ($c_g = d\omega/dk$) equal to x_f/t_f. Using this definition, Figure 5.6 illustrates the frequency kh of the component with the minimum phase at $x = 0$, considering the range $7 \leq x_f/h \leq 71$ and $18 \leq t_f/T_p \leq 47$. The rise in the error at the input boundary was shown to be related to a phase condition associated with the high-amplitude frequency band. Considering Figure 5.6, the present case with $k_p h = 1.56$ and $t_f = 22.5T_p$ gives $x_f/h = 57$, which is indicated by the red circle at the corresponding location.

In considering Figure 5.6, it may be argued that an increase in t_f is expected to also increase the error critical location of the focus position. For the purpose of the present investigation, a focus time $t_f/T_p = 45$ is now considered, an increase by a factor of two from the previous focus time. For this value of t_f/T_p, the rise in error is expected to occur beyond $x_f/h = 100$. The repeat time is also increased by a factor of two so that $T_r/T_p = 90$.

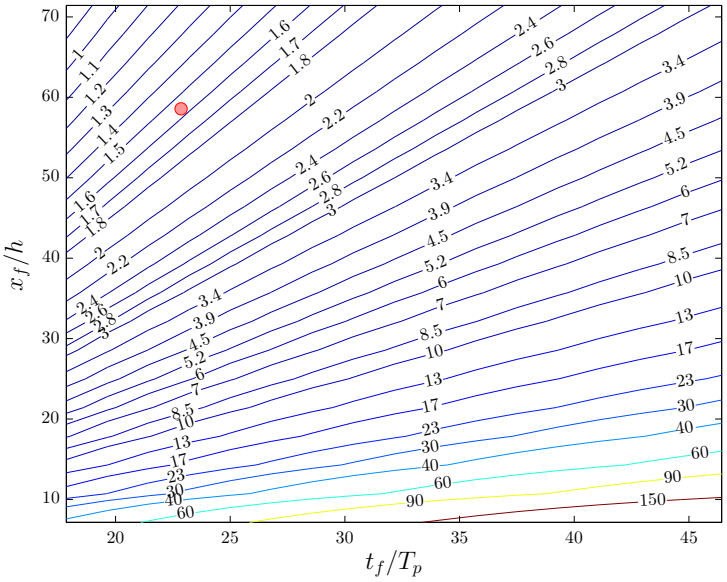
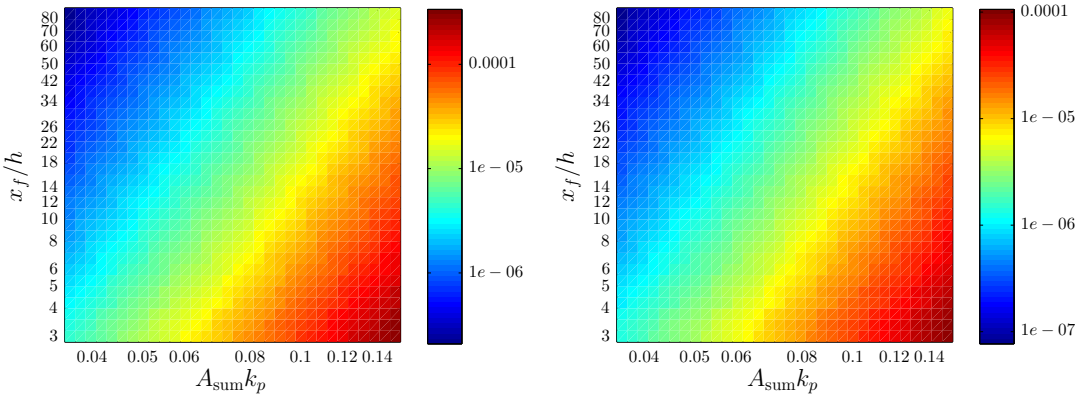
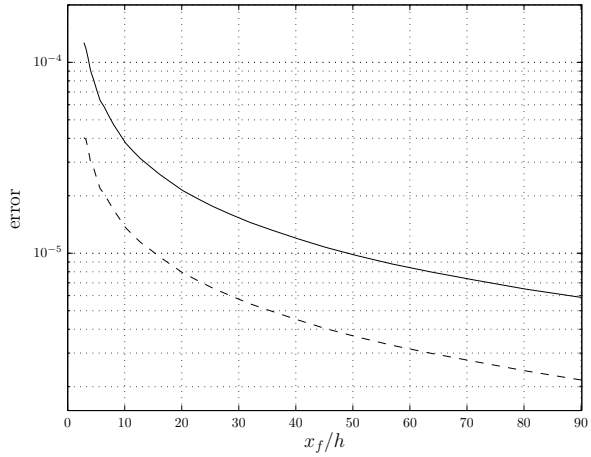


Figure 5.6: Non-dimensional frequency kh of the component with the minimum phase at $x = 0$

Figure 5.7 shows the error in the DFSBC and the KFSBC for $k_p h = 1.56$, $t_f/T_p = 45$ and $T_r/T_p = 90$. These errors are computed using equations (5.6) - (5.9). In contrast to Figure 5.3, a rise in the error within the boundary conditions cannot be observed. This rise is now expected to occur beyond $x_f/h = 100$, which is outside the boundaries of Figure 5.7.



(a) E_K for $0.03 \leq A_{\text{sum}}k_p \leq 0.15$ (b) E_D for $0.03 \leq A_{\text{sum}}k_p \leq 0.15$

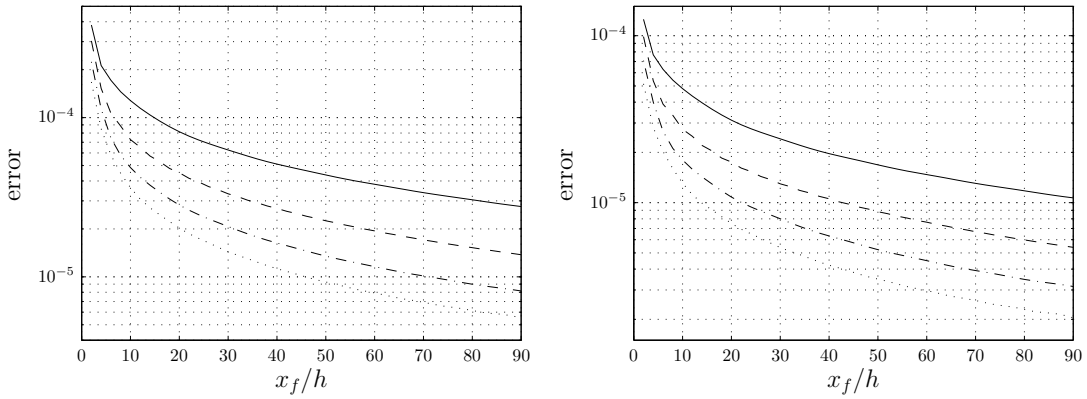


(c) —— E_K and – – E_D for $A_{\text{sum}}k_p = 0.11$

Figure 5.7: Error in KFSBC (E_K) and DFSBC (E_D) for wave case with $k_ph = 1.56$ and $T_r = 90T_p$

5.5.6 Variations in the water depth

Figure 5.8 shows the error in the free-surface boundary conditions for a water depth range $1.0 \leq k_ph \leq 1.56$. A first observation confirms that the error follows a very similar trend for all water depths. However, the overall magnitude of the error increases as the water condition becomes more shallow. The explanation for this is twofold: (i) wave dispersion is reduced in shallow water conditions, so that the wave group becomes less dispersed at $x = 0$, and (ii) the validity of second-order wave theory is more limited in shallow water conditions.



(a) KFSBC (b) DFSBC

Figure 5.8: Error in the free-surface boundary conditions for —— $k_ph = 1.0$, – – $k_ph = 1.2$, – · – $k_ph = 1.4$, · · · · $k_ph = 1.56$, $A_{\text{sum}}k_p = 0.11$ and $t_f/T_p = 45$.

5.6 A numerical wave tank study

5.6.1 Introduction

Unfortunately, the error criterion based upon the free-surface boundary conditions does not enable a practical assessment of the quality of the focused wave group. To overcome this limitation, the purpose of the present section is to link the criteria E_K and E_D to a more practical measure. The combined error E is first defined as $E = \sqrt{E_D^2 + E_K^2}$. A maximum permissible error, linked to the quality of the focused group, is then defined as $E_{\max}$. To determine $E_{\max}$, a numerical wave flume study is undertaken; the methodology adopted being as follows. Focused wave groups are computed numerically at various increasing locations x_f. A maximum error in real physical terms may then be introduced by comparing successive events in terms of:

(i) the relative difference in the maximum crest elevation, $\eta_{\max}$ and

(ii) the RMS error between the surface profiles when the wave group is focused.

The NWT adopted is based upon the multiple-flux boundary element scheme introduced by Hague and Swan (2009). In fact, the numerical scheme is identical

to that described in Hague and Swan (2009), and a description of the mathematical detail is omitted here for brevity. In the context of these computations, the input kinematics are calculated using the second-order model by Sharma and Dean (1981). To be entirely clear, the NWT input boundary reproduces the realistic velocity distribution as a function of depth, and does not rely on an actual wavemaker.

The numerical study is undertaken in a rectangular NWT (Figure 5.1) of actual water depth 0.5m $\leq h \leq$ 0.7m. The spacing of individual computational nodes within the NWT is 0.025m, with a constant time step of 0.0025s; these parameters having been shown to lead to both stable and accurate computational results (Spinneken et al., 2013). The focus location is defined as the location where the water surface elevation reaches its maximum, which may be downstream of the linearly calculated x_f (Johannessen and Swan, 2001, 2003). Both convergence criteria (i) and (ii) are based upon a water surface profile extracted at that focus location.

5.6.2 Convergence of a focused group

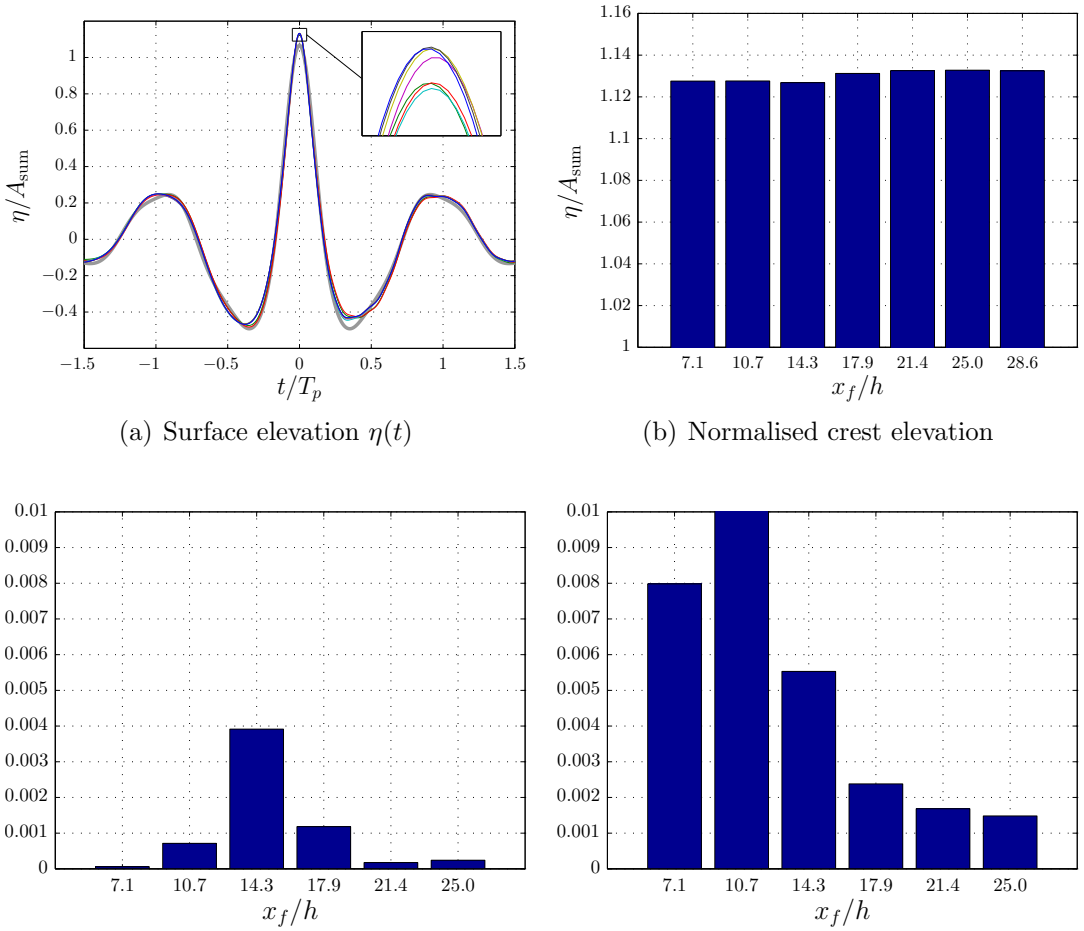
The convergence study is performed for an event of steepness $A_{\text{sum}}k_p = 0.11$ and relative depth $k_p h = 1.56$. Taking into consideration the issues associated with short repeat times, the computations are undertaken for $T_r = 90T_p$ and $t_f = 0.5T_r$. Figure 5.9 illustrates a number of comparisons for this focused group, where the subsequent focus locations were chosen as x_f/h = 7.1, 10.7, 14.3, 17.9, 21.4, 25 and 28.6. The first part of this figure, Figure 5.9(a), concerns the water surface elevation at the focus location. To enable a comparison between successive events, the time axis is shifted so that the maximum crest elevation takes place at $t = 0$ in all cases. A second-order calculation of the wave group (Sharma and Dean, 1981) is included as the grey line, and the various coloured lines relate to the numerical computations. The difference between the second-order calculation and the numerical computations highlights that wave interactions beyond second order

are important within this wave group.

In considering the computations with varying x_f, some small but important departures may be observed. This is clarified in Figure 5.9(b), showing the normalised crest amplitude $\eta_{\max}/A_{\text{sum}}$ for a variation in x_f. The data in Figure 5.9(b) confirms that the normalised crest elevation varies noticeably with x_f/h, particularly for $x_f/h < 17.9$. At locations $x_f > 17.9$, the maximum surface elevation appears to converge to a constant value. The validity of the second-order input kinematics may now be assessed by considering the convergence in the crest elevation, criterion (i) above. This may be achieved by calculating the relative difference between the crest elevations at successive values of x_f. This relative difference is shown in Figure 5.9(c), where convergence is observed as x_f increases. Indeed, the relative difference between successive focus locations is small with a maximum difference of only 0.4%.

Similar observations can be made in Figure 5.9(d), showing the normalised RMS error in $\eta(t)$ for successive values of x_f, criterion (ii) above. It can be seen in Figure 5.9(d) that convergence is also observed in the RMS error. Additional comparisons showed that the RMS error provides a more robust quantification of the wave group convergence. If convergence is defined as a maximum error of 0.5% in the RMS error between the surface profiles, then convergence is achieved for $x_f/h = 17.9$; this being confirmed by the data in Figure 5.9(d). A different bound for the RMS error could be taken here, which would affect the results noted below. However, an RMS error of 0.5% is believed to be sufficiently stringent. Relating this to the error in the free-surface boundary condition, Figure 5.8, a focused event with $k_p h = 1.56$ and $x_f/h = 17.9$ is hence associated with a maximum error $E_{\max} = 2.5 \cdot 10^{-5}$.

This quantitative value of $E_{\max}$ allows, for the first time, a definition of the range of validity of second-order input kinematics for a focused wave group. To confirm the present approach for a wider range of wave conditions, the focused wave group with $A_{\text{sum}} k_p = 0.11$ was also produced in water of reduced depth. Figure 5.10 shows the RMS error for (a) $k_p h = 1.22$ and (b) $k_p h = 1.39$. As



(a) Surface elevation $\eta(t)$

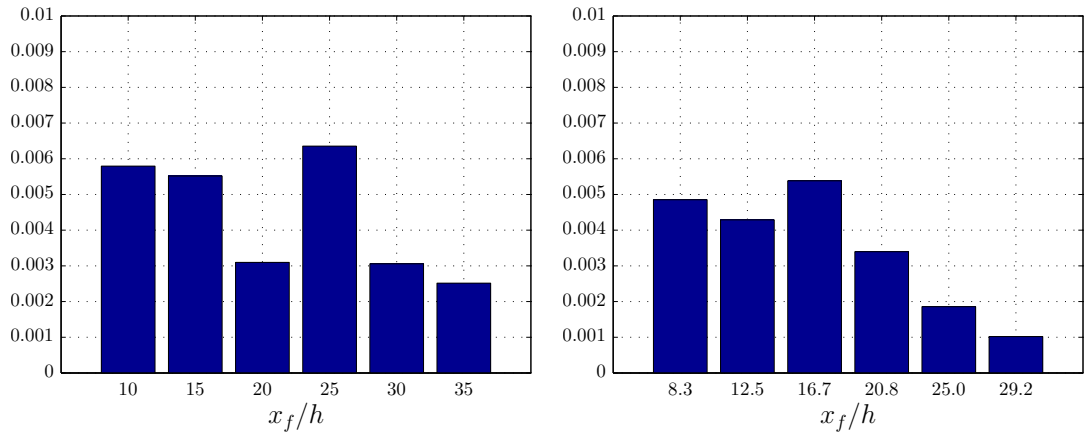
(b) Normalised crest elevation

(c) Relative difference in crest elevation

(d) Normalised RMS error

Figure 5.9: Convergence of a focused event generated in a NWT with $k_p h = 1.56$ and $A_{\text{sum}} k_p = 0.11$. Note: The time traces presented in part (a) relate to a number of different focus locations.

before, convergence in the RMS value can be observed as x_f increases, albeit with a less clear overall trend. Based upon the previous definition of a maximum error of 0.5% in the RMS, convergence is observed for larger relative focus locations as the water depth decreases. This highlights the challenge associated with the generation of focused groups in shallow water, as noted in the discussion of the free-surface boundary conditions (Figure 5.8). Nevertheless, the definition of 0.5% maximum RMS error once again allows for a definition of a corresponding error E_{max}. Based upon Figure 5.10, this error corresponds to $E_{\text{max}} = 3.6 \cdot 10^{-5}$ for $k_p h = 1.22$ and $E_{\text{max}} = 2.9 \cdot 10^{-5}$ for $k_p h = 1.39$.



(a) Normalised RMS error for $k_p h = 1.22$ (b) Normalised RMS error for $k_p h = 1.39$

Figure 5.10: Analysis of a focused event generated in a NWT with $A_{\text{sum}} k_p = 0.11$ as a function of focus location

5.7 Application of error criterion and conclusions

Having established a practical upper bound for $E_{\max}$, the calculation of the error in free-surface boundary conditions (based on second-order theory) may be adopted to define a minimum focus location. This is demonstrated in Figure 5.11 considering three relative depths ($k_p h = 1.22$, 1.39 and 1.56) and wave steepnesses of $0.04 \leq A_{\text{sum}} k_p \leq 0.11$. As expected, this minimum location $x_{f\,\min}$ increases with $A_{\text{sum}} k_p$. Furthermore, it can also be observed that $x_{f\,\min}$ increases as the relative depth decreases; this being consistent with the observations in Figure 5.8.

Part I of this chapter established a set of conditions for which second-order input kinematics may be applied. These conditions are based upon the error in the free-surface boundary conditions, and ultimately provide a minimum distance $x_{f\,\min}$ between the wave input boundary and the focus location. The specification of second-order input kinematics in a numerical scheme is entirely consistent with the application of a second-order wavemaking theory in a laboratory context; the former effectively being a special case of the latter. As a result, the conclusions drawn here are directly relevant to the physical wave flume study to follow. Fur-

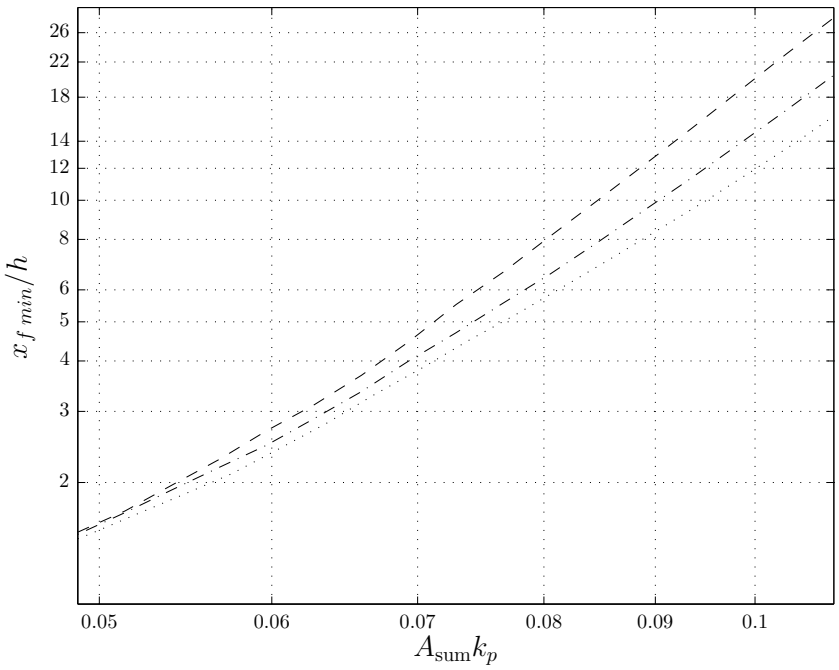


Figure 5.11: Minimum focus location $x_{f\,\mathrm{min}}$ based upon E_{max} for ▬▬ $k_ph = 1.22$, ▬·▬ $k_ph = 1.39$ and ····· $k_ph = 1.56$.

thermore, converged water surface elevations for focused wave groups were also generated, which may now be used as benchmark cases.

Part II: A laboratory investigation

5.8 Introduction

Part II concerns the laboratory generation of focused wave groups. The arguments developed numerically in Part I may equally apply in a laboratory context, where wave dispersion limits the nonlinearity of the problem in the vicinity of the wavemaker. As a result, a wavemaking technique limited to a low-order theory is likely to be sufficiently accurate; this assumption being assessed experimentally in the course of Part II. The experimental work was undertaken in the Coastal Wave Flume at Imperial College London, where the water depth was held constant at $h = 0.6$m. For additional detail concerning this wave flume, the reader is referred to Chapter 3, §3.3.

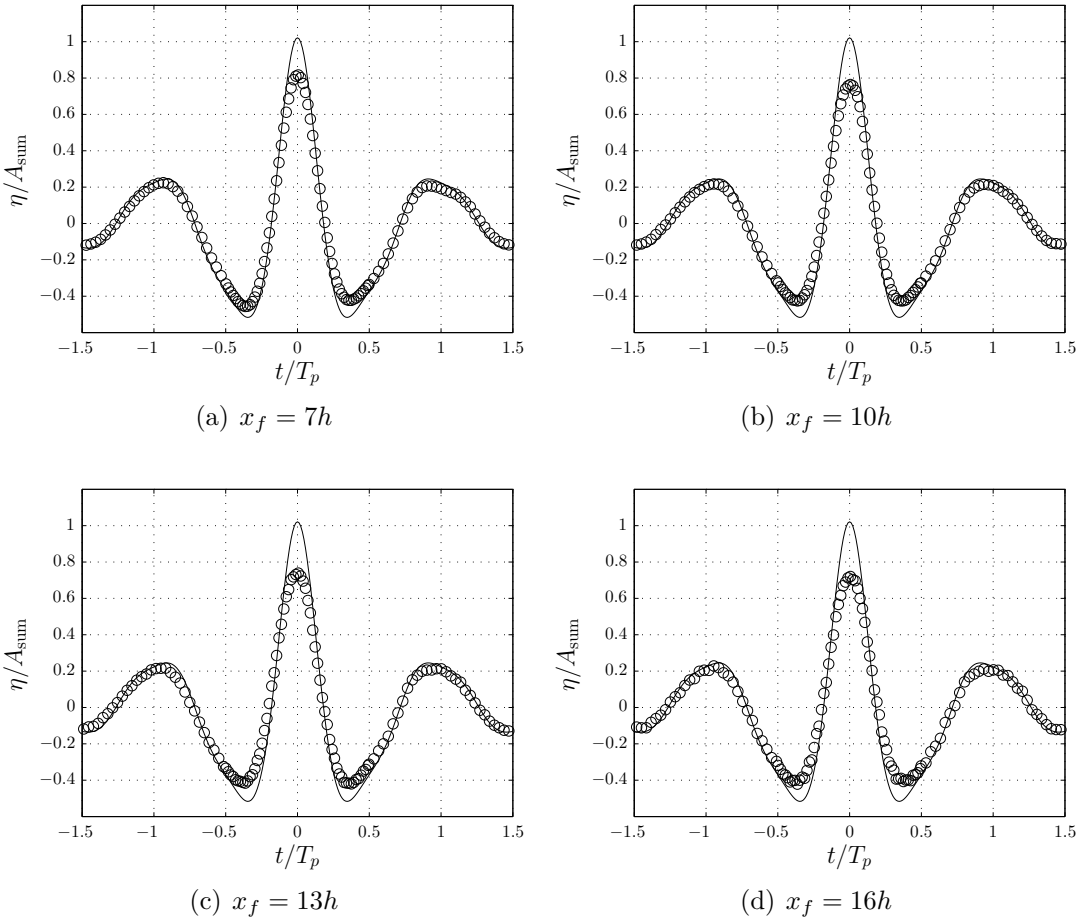
In the development of the present laboratory investigation, a wave generation approach based on a theoretical transfer function is considered first, §5.9. The benefits of two empirical correction methodologies, both relying on first-order control, are then considered in §5.10 and §5.11. Section §5.12 assesses the improvement in wave quality under second-order control. A set of overall conclusions is finally presented in §5.13.

5.9 Wave generation in first-order control

5.9.1 Generation of small-amplitude focused wave groups

A set of small-amplitude wave groups is considered first, where the wavemaker demand is based on a first-order position control signal. In defining the nonlinearity associated with a focused wave group, the product $A_{\text{sum}}k_p$ is again adopted. To ensure that the small-amplitude condition is satisfied, this initial experimental assessment was undertaken for events of steepness $A_{\text{sum}}k_p = 0.035$ with $k_p h = 1.4$. In a linear sense, the location of the focused wave group should not affect its qual-

ity. Nevertheless, to ascertain any potential influence of x_f, focused wave groups were generated and recorded at four locations $x_f = 7h$, $10h$, $13h$, and $16h$. To be entirely clear, the surface elevation was recorded by a single wave probe located at $x = x_f$; any nonlinear downstream shift in the focus location being assumed negligible. In all cases, the focus time was kept constant at $t_f = 32$s corresponding to $t_f/T_p = 22.5$.



(a) $x_f = 7h$ (b) $x_f = 10h$

(c) $x_f = 13h$ (d) $x_f = 16h$

Figure 5.12: Normalised water surface elevation $\eta(t)/A_{\text{sum}}$ at x_f with $A_{\text{sum}}k_p = 0.035$, $k_ph = 1.4$ and based on c_0, showing ——— second-order wave theory and ∘ experimental data.

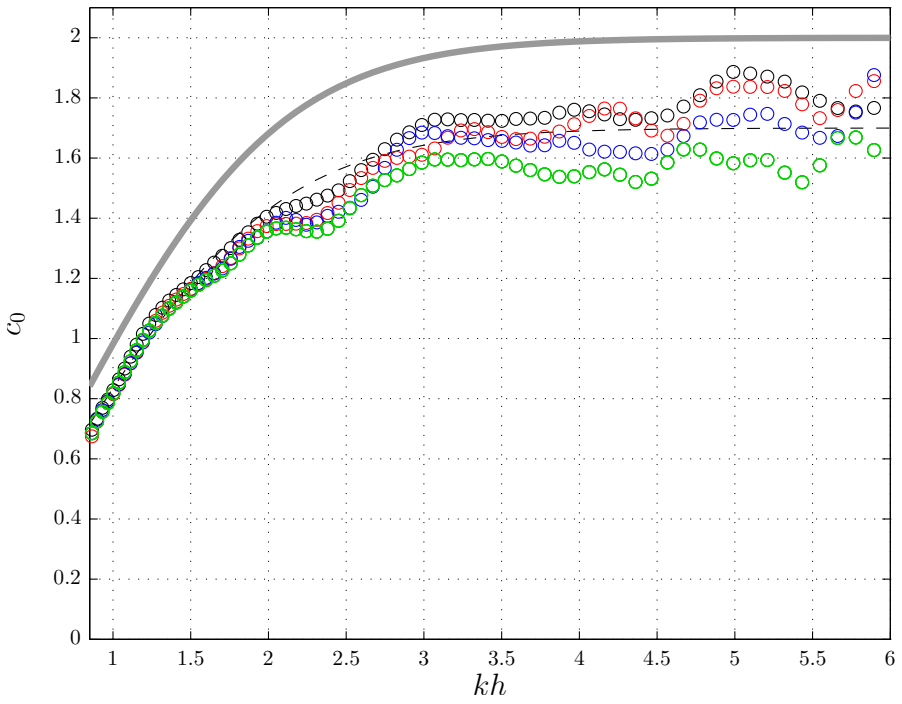
Figure 5.12 shows the normalised water surface elevation, $\eta(t)/A_{\text{sum}}$, at each of the four locations x_f. The time axis was shifted by t_f so that $t_f/T_p = 0$ corresponds to the focus time; a similar time shifting being adopted for all figures to follow. A second-order calculation of the focused wave group, shown by the black line,

is included for reference, and the experimental data are shown by the discrete points. The maximum calculated second-order surface elevation for this event is $\eta_{\max}/A_{\text{sum}} = 1.01$, which confirms the linearity of the event. Considering the experimental data, it is clear that the surface elevation is significantly lower than predicted. Furthermore, the events at increasing x_f, particularly at $x_f = 16h$ in Figure 5.12(d), show a larger departure from the analytical prediction than those focused in closer proximity to the wavemaker. To quantify this, the maximum recorded surface elevation at the four locations (a)-(d) is $\eta_{\max}/A_{\text{sum}} = 0.83$, 0.78, 0.75 and 0.74 respectively.

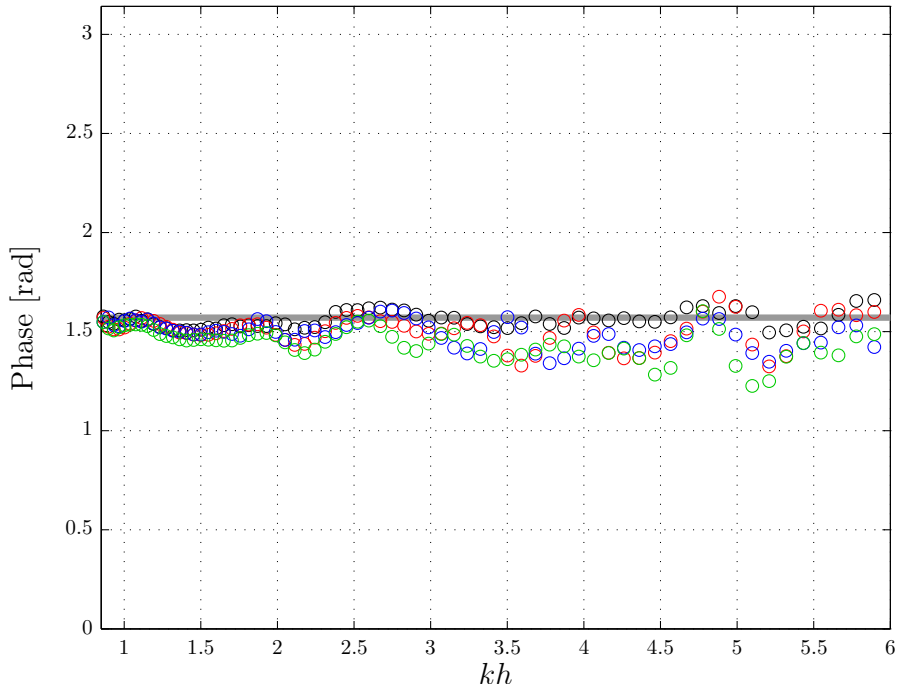
At first order, the wavemaker transfer function is described through the progressive wave field coefficient c_0; this coefficient having been considered in detail in the context of regular waves, §3.4.1. The regular wave comparison established that the measured phase of the coefficient c_0 closely matches the analytical prediction of $\pi/2$ (Figure 3.6(b)). In contrast, a departure of 15% was noted between the experimentally observed and the analytically predicted magnitude of c_0 (Figure 3.6(a)).

In the context of a small-amplitude focused wave group, the progressive wave field coefficient c_0 may be evaluated through a harmonic decomposition of the surface elevation, as each of the wave components is assumed to be freely propagating. This is achieved by applying a DFT to a time-window equivalent to the repeat time of the wave group, T_r. Applying this analysis to the four small-amplitude events yields that data in Figures 5.13(a) and 5.13(b), showing the magnitude and the phase of c_0 respectively. The analytical prediction of c_0, equation (2.8), is included as the grey line.

Figure 5.13(b) confirms that the phase match in the focused wave case is very good, and remains comparable to the regular wave observations. A small phase lag can be observed for the two furthest focus locations, $x_f = 13h$ and $x_f = 16h$; this phase lag being particularly pronounced for the highest frequencies. All locations also exhibit an increased data scatter towards the higher frequencies. In this context, it should be noted that the high frequency components in the spectrum relate



(a) Magnitude



(b) Phase

Figure 5.13: Progressive wave field coefficient for a focused wave group with ——— theoretical coefficient c_0 — — adjusted coefficient $c_0{}' = 0.85c_0$ and experimental data for ∘ $x_f = 7h$ ∘ $x_f = 10h$ ∘ $x_f = 13h$ ∘ $x_f = 16h$.

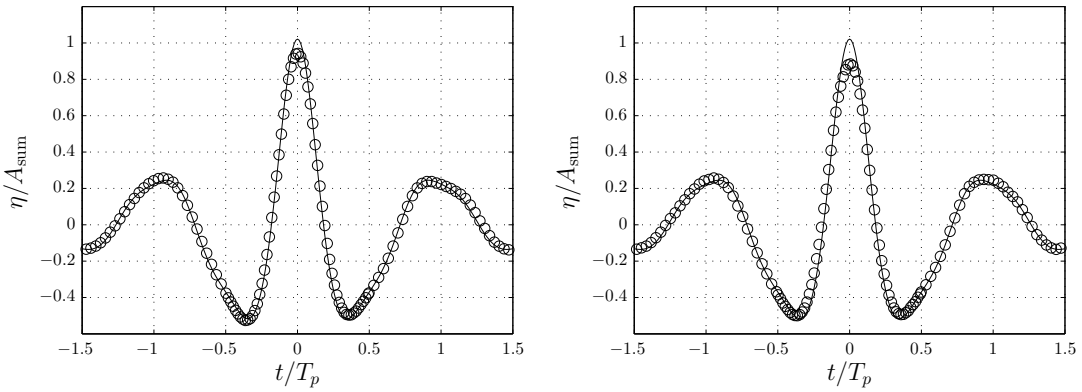
to relatively small absolute quantities, so that any errors associated with the measurement (wave gauge amplitude and location) and data post-processing (DFT) lead to some level of uncertainty. Setting aside this issue, the phase agreement is considered good.

Significant departures are observed in the magnitude of c_0, Figure 5.13(a). In an average sense, an error of approximately 15% may again serve as a reasonable description of the observed departures. The slight oscillation of the experimentally observed coefficient is believed to be due to ripples associated with the DFT process applied to a relatively short non-zero data sequence (the focused event). Perhaps more importantly, for $kh > 2$ the experimentally observed coefficients reduce as a function of the focus location x_f. This latter decrease is believed to be due to viscous effects along the flume's glass side walls, leading to errors in c_0 as large as 25% as x_f increases.

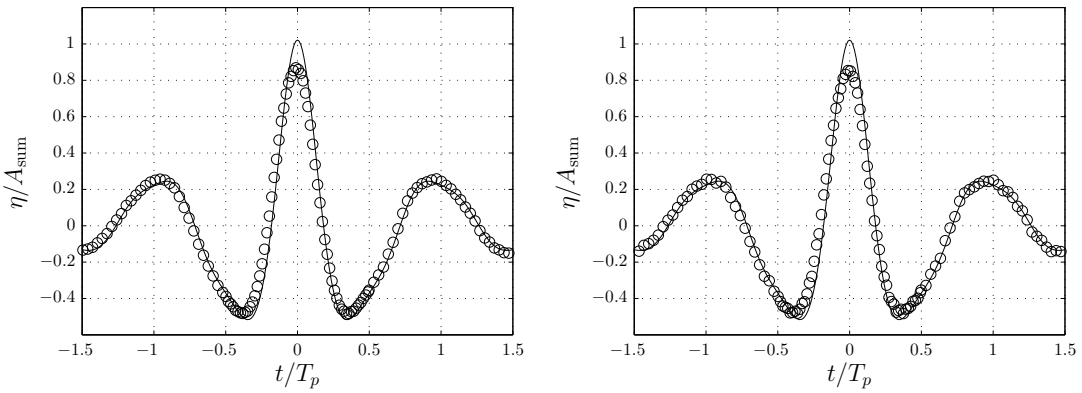
The highest frequency (largest kh) wave components are most affected by the additional viscous decay, which is due to their short wavelength relative to x_f. To provide an example for $x_f = 16h$, a wave component with $kh = 1$ corresponds to approximately 3 wavelengths in the range $0 \leq x \leq x_f$. In contrast, a component with $kh = 6$ corresponds to 15 wavelengths in that same interval. Assuming that a certain amount of energy is dissipated in each oscillation, the shorter wave components (larger kh) are more susceptible to viscous damping. As a result, a distant focus location might prove to be an obstacle to good quality wave group generation if based upon a theoretical transfer function.

The modified coefficient $c_0' = 0.85c_0$ introduced in the context of regular waves is shown by the dashed black line in Figure 5.13(a). Whilst this coefficient does not give an exact fit to all cases shown in Figure 5.13(a), it once again provides a convenient means of accounting for the average departure of c_0. Adopting this modified coefficient, the wave cases shown in Figure 5.12 were reproduced, with no further correction being made to either the wave phasing or the wave amplitude. These new cases are shown in Figure 5.14, and may be considered as a significant improvement over the data presented in Figure 5.12.

Based on Figure 5.14 (a)-(d), the maximum surface elevation is $\eta_{\max}/A_{\text{sum}} =$ 0.95, 0.9, 0.88 and 0.85 respectively. Indeed, these revised magnitudes present an improvement of approximately 15% over the previous conditions (0.83, 0.78, 0.75 and 0.74). Furthermore, the symmetry of the focused events shown in Figure 5.14 indicates that the phase condition at the focus location is largely met. Nevertheless, some departures in the maximum crest elevation remain.



(a) $x_f = 7h$ (b) $x_f = 10h$



(c) $x_f = 13h$ (d) $x_f = 16h$

Figure 5.14: Normalised water surface elevation $\eta(t)/A_{\text{sum}}$ at x_f with $A_{\text{sum}}k_p = 0.035$, $k_p h = 1.4$ and based on $c_0{}'$, showing ——— second-order wave theory and ∘ experimental data

5.9.2 The generation of large amplitude focused wave groups

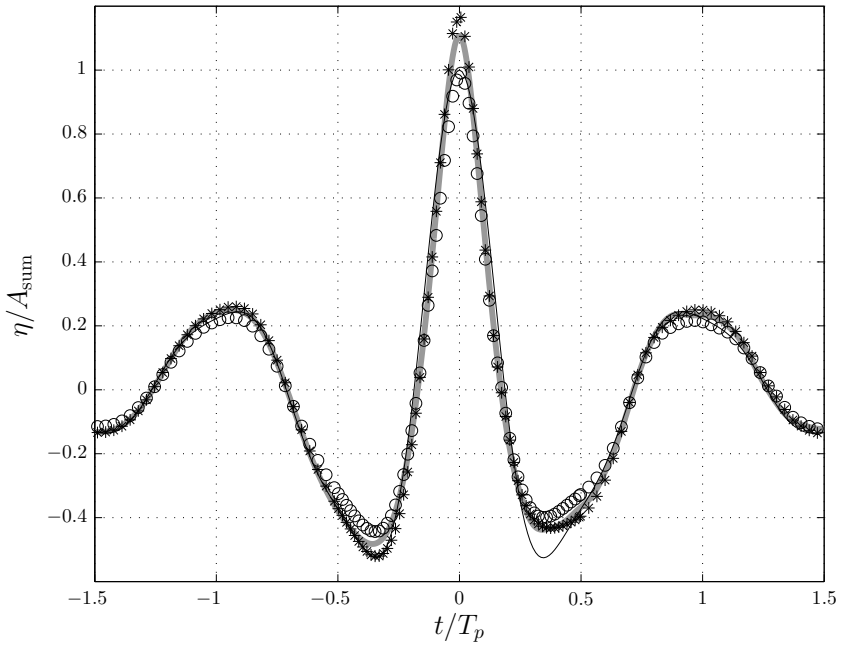
Having established the progressive wave field coefficient in small-amplitude waves, the generation of a large amplitude wave event is considered next. For this purpose,

the steepness of the event is increased to $A_{\text{sum}}k_p = 0.10$. Part I demonstrated that an increase in the focus location x_f is beneficial to the generation of large-amplitude events. Unfortunately, an extended location is also associated with additional viscous decay, so that a compromise between these two criteria must be found. Based on the above discussion, a location of $x_f = 7h$ is considered herein, as the effect of viscous decay appears to outweigh the benefits achieved by a distant focus location.

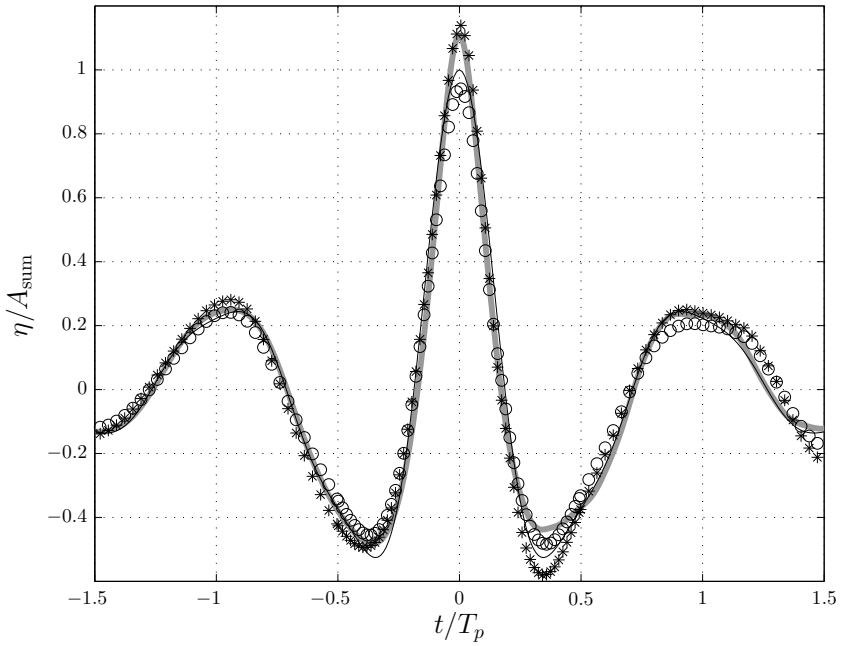
As discussed in Part I, interactions beyond second order lead to a downstream shift of the focused event. To account for this effect, the location of the wave gauge was adjusted until the maximum surface elevation for each wave event was recorded. As a result, the data considered hereafter is not necessarily recorded at $x_f = 7h$, but often slightly downstream of this location.

Figure 5.15 illustrates the water surface elevation for a focused wave group with $A_{\text{sum}}k_p = 0.10$ and $k_p h = 1.4$, showing first-order position control in part (a) and first-order force control in part (b). In both cases, the data shown was generated using two methods with: (i) a wavemaker demand based upon c_0 (symbol $\circ$) and (ii) a wavemaker demand based upon $c_0{}'$ (symbol $*$). If based on c_0, Figure 5.15 confirms that the experimental data significantly under-predicts the maximum crest elevation. For the avoidance of any doubt, the linear wave profile shown by the black line is known to significantly under-predict the surface elevation in steep wave groups. In contrast, the fully-nonlinear BEM solution, shown by the grey line, may be considered as an accurate reference solution as demonstrated in Part I of the present chapter. The maximum surface elevation predicted by the BEM computation is $\eta_{\max}/A_{\text{sum}} = 1.12$. The experimental data based on c_0 leads to $\eta_{\max}/A_{\text{sum}} = 0.98$ in position control (Figure 5.15(a)) and $\eta_{\max}/A_{\text{sum}} = 0.95$ in force control (Figure 5.15(b)), corresponding to under-predictions of 14% and 18% respectively.

The modified coefficient $c_0{}'$ (data with symbol $*$) leads to a considerable improvement in the match of the maximum crest elevation. Indeed, the match is such that it questions the results observed for the corresponding small amplitude event



(a) Position control



(b) Force control

Figure 5.15: Normalised water surface elevation η/A_{sum} for a focused wave group with $A_{\mathrm{sum}}k_p = 0.10$ and $k_p h = 1.4$, showing —— linear wave theory ═══ BEM computation and experimental data based upon $\circ$ c_0 and $*$ $c_0{}'$.

shown in Figure 5.14(a). However, reconsidering the initial small-amplitude wave coefficient c_0 in Figure 5.13(a), it can be observed that a correction of $c_0{}' = 0.85c_0$ over-compensates for the highest frequency wave components, particularly for $kh > 4.5$. These high frequency components lead to a steepening of the wave event, and subsequently increased crest elevations in the nonlinear case. In position control (Figure 5.15(a)) this gives $\eta_{\max}/A_{\text{sum}} = 1.19$, which is considered 6% too large if compared to the BEM computation. In force control, the over-prediction reduces to $\eta_{\max}/A_{\text{sum}} = 1.17$ or 4.5%. Furthermore, both control modes also show some additional departures from the BEM computation, particularly for the wave trough at $t/T_p = 0.35$ in Figure 5.15(b).

Taken as a whole, the description based on $c_0{}'$ is satisfactory. However, the desired quality of focused wave groups is often based on very stringent criteria, and an alternative calibration-based approach is considered next.

5.10 A surface elevation-based calibration

5.10.1 Calibration of a small-amplitude event

The above discussion highlighted that some inaccuracies remain in the laboratory generation of both small and large amplitude focused wave groups. To overcome this, it is established practice to undertake a calibration based upon small-amplitude wave groups; a possible calibration approach having been discussed in Masterton and Swan (2008). The calibration is often based on the recorded water surface elevation at the focus location, and derives a correction term for each frequency component. Based on these correction terms, an empirical transfer function is derived through an iterative procedure (Masterton and Swan, 2008).

The purpose of the present section is to contrast such a calibration-based approach to the theoretical wave generation described in §5.9. The calibration method adopted here is similar to that by Masterton and Swan (2008) and may be outlined as follows:

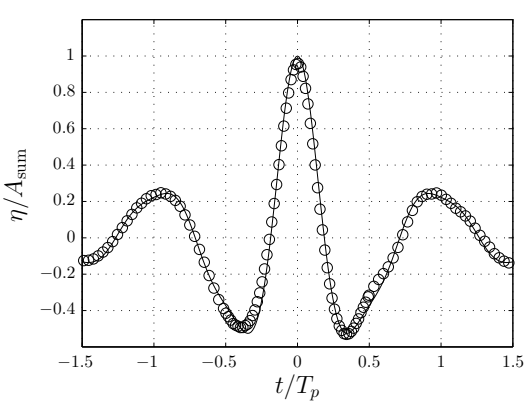
(i) A single wave gauge is located at the linearly calculated focus location, x_f.

(ii) A small-amplitude event of steepness $A_{\text{sum}}k_p = 0.035$ is produced at this location.

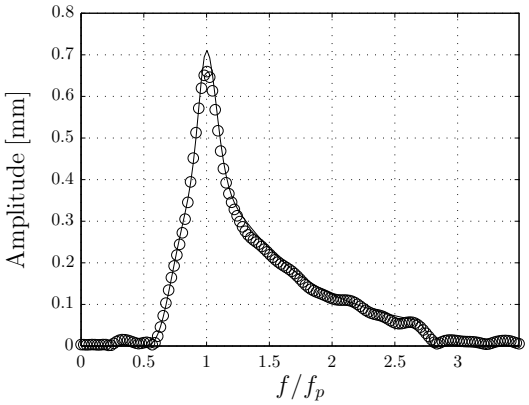
(iii) The recorded surface elevation is post-processed through a DFT, so that the amplitude and phase information for each wave component is obtained. The amplitude is compared to the demand amplitude, and a correction factor is derived as the ratio of the demanded and the measured amplitude. The phase is corrected such that all wave component phases are sought to be zero at the focus location. Masterton and Swan (2008) described a method of windowing and zero padding their data, which was primarily driven by the need to eliminate the influence of small reflections from their downstream beach. The present method only requires some minor zero padding towards the very end of the repeat time, as the wave flume used is significantly longer than the wave basin described in Masterton and Swan (2008).

(iv) A new wave event is produced using the adjusted amplitude and phase information. This process is repeated until both the recorded surface elevation and the spectral content are found satisfactory.

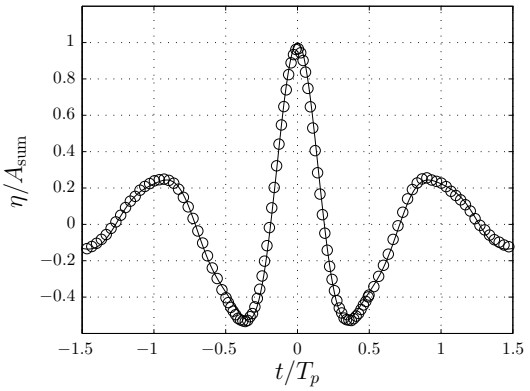
Adopting steps (i) - (iv) above, Figure 5.16 shows both the surface elevation (parts (a), (c) and (e)) and the spectral content (parts (b), (d) and (f)) for iterations 1, 3 and 5, describing an event with $A_{\text{sum}}k_p = 0.035$ and $k_ph = 1.4$ focused at $x_f = 7h$. The correction term $c_0{}' = 0.85c_0$ was adopted as an initial transfer function; this initial event having been considered previously in Figure 5.14(a). Iteration 1 (Figure 5.16(a) and 5.16(b)) refers to the wave event after a single iteration. Following this first iteration, the maximum crest elevation has increased to $\eta_{\max}/A_{\text{sum}} = 0.98$. However, a small departure in the energy content in the proximity of the spectral peak may still be observed (Figure 5.16(b)). Furthermore, an average phase departure of 0.17 rad remains, which explains the asymmetry in the surface elevation (Figure 5.16(a)).



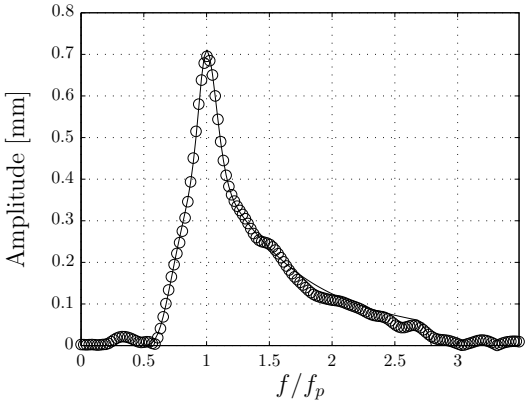
(a) $\eta(t)$ for iteration 1



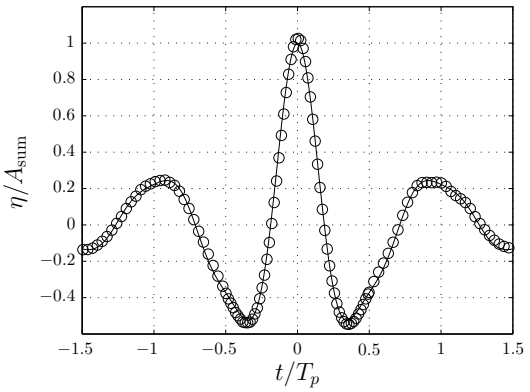
(b) Amplitude content for iteration 1



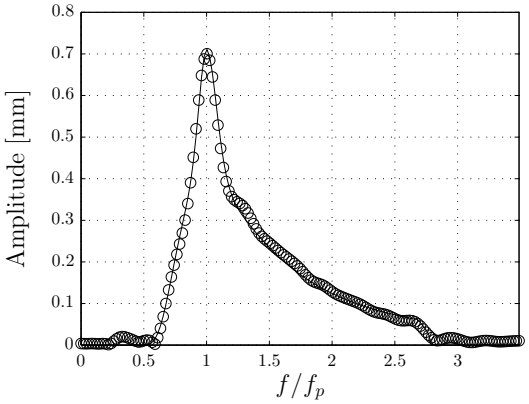
(c) $\eta(t)$ for iteration 3



(d) Amplitude content for iteration 3



(e) $\eta(t)$ for iteration 5



(f) Amplitude content for iteration 5

Figure 5.16: Calibration based on a small-amplitude event in position control for a wave group with $A_{\text{sum}}k_p = 0.035$, $k_p h = 1.4$ and $x_f = 7h$, showing —— linear wave theory and ∘ experimental data

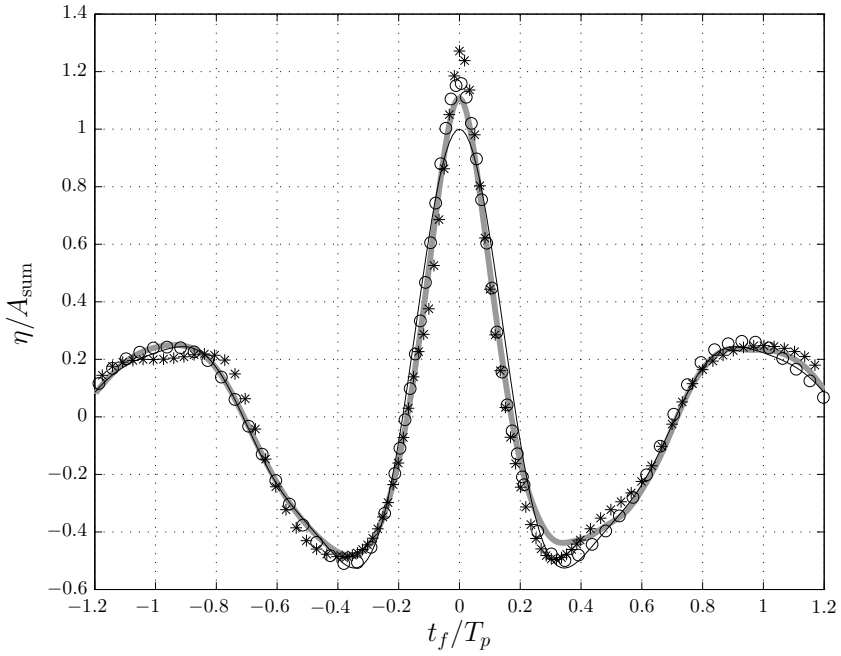
For this particular wave group, 5 iterations were considered satisfactory, so that Figures 5.16(e) and 5.16(f) illustrate the surface elevation and spectral content for the final calibrated wave event. Within this final event, the departure in the maximum surface elevation is only 0.2 % (Figure 5.16(e)). Furthermore, the average phase departure is reduced to 0.05 rad, leading to a highly symmetric wave event.

5.10.2 Generation of a large amplitude event

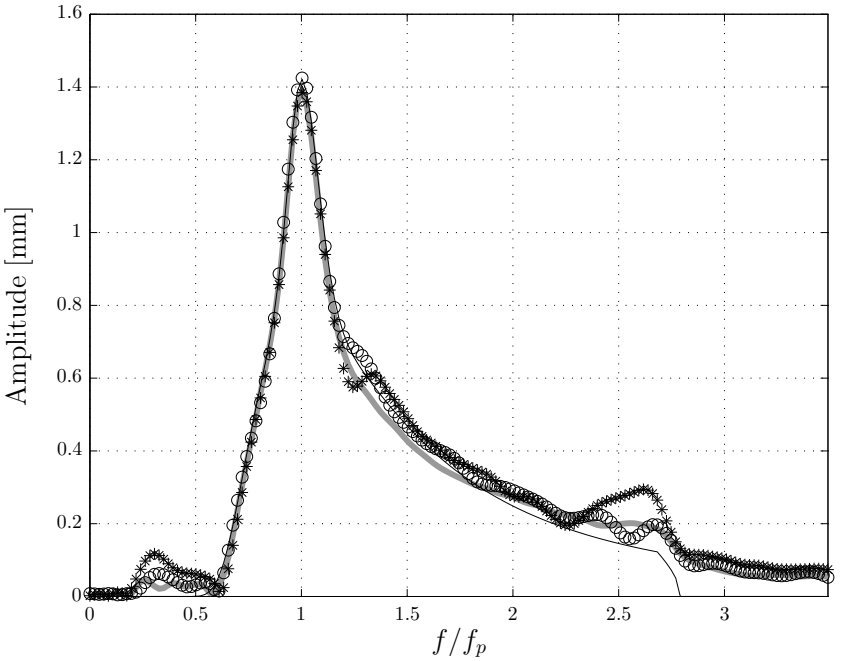
Having established the empirical magnitude and phase corrections for a small-amplitude focused wave group, this revised transfer function is now adopted for the generation of a large amplitude event with $A_{\text{sum}}k_p = 0.10$; all other parameters being identical to the small-amplitude wave group. Figure 5.17(a) illustrates the surface elevation for this wave group, and directly contrasts position control (symbol $\circ$) and force control (symbol $*$). For comparison, linear wave theory (black line) and the BEM computation for this event (grey line) are also shown.

Both of the experimentally generated surface profiles show maximum elevations significantly larger than those predicted by the BEM solution. In the case of position control (symbol $\circ$), the maximum surface elevation reaches $\eta_{\max}/A_{\text{sum}} = 1.18$ (5% over prediction). In force control, the maximum surface elevation is as high as $\eta_{\max}/A_{\text{sum}} = 1.28$ (13% over prediction). After careful comparison with the BEM solution, as well as previously established evidence on focused wave groups (Johannessen and Swan, 2001, 2003), it was concluded that these increased surface elevations are non-physical, and are not exclusively associated with nonlinear wave-wave interactions.

To demonstrate this, Figure 5.17(b) shows the corresponding spectral content, including all four solutions (linear, BEM, position control and force control). In considering Figure 5.17(b), it can be observed that there is an increase in the experimentally observed spectral content for $f/f_p > 1.25$, which is particularly pronounced in force control and for $f/f_p \approx 2.5$. The increase in spectral content



(a) Normalised surface elevation η/A_{sum}



(b) Spectral content

Figure 5.17: Focused event with $A_{\text{sum}}k_p = 0.10$, $k_p h = 1.4$ and $x_f = 7h$, showing —— linear wave theory —— BEM computation, ∘ position-control data and ∗ force-control data.

in the range $1.25 \leq f/f_p \leq 1.75$ is inconsistent with both the BEM solution and established observations, as nonlinear wave-wave interactions are expected to lead to an energy transfer towards the higher frequency components (a widening of the free wave regime).

The most likely explanation for this effect is believed to be associated with the mechanics of the wave generation apparatus. In undertaking the calibration outlined in §5.10.1, the generation of the small amplitude event leads to small wavemaker motions and forces. In force control, small additional auxiliary forces act on the load cell. For example, the force in the bearings of the sector carrier is sensed as an additional small force, which is due to mechanical friction, but also stiction if the motion is small. When the overall fluid (or hydrodynamic) force is small, these additional force components may become an important contribution to the total forcing. As a result, the calibrated transfer function (§5.10.1) also includes compensations for these auxiliary non-hydrodynamic forces.

As the wave amplitude increases, the auxiliary mechanical forces are likely to reduce in their overall forcing influence. For example, a bearing stiction force may be relevant to very small motions, but becomes less significant once the system undergoes larger amplitude motions. As a result, the empirical transfer function is now over-compensating for some force components, which ultimately leads to excessive wavemaker motions. These increased wavemaker motions, in turn, lead to an increase in the free-wave energy content observed in Figure 5.17(b).

The fact that this increase is more pronounced in force control is consistent with the fact that auxiliary mechanical forces are responsible for the over-prediction. If based on position control, an extra forcing introduced through, for example, a bearing is simply compensated by the motion controller applying an additional current to the drive train. However, even in position control, excessive spectral content is observed. This is most probably due to (small) imperfections in the motion controller when responding to high-frequency and small-amplitude demands. In considering the wave groups in Figure 5.17, neither of the two methods (force control or position control) is considered satisfactory. In fact, the empirically gen-

erated wave events are considered less representative than the events based upon the simple modified coefficient $c_0{}'$ (Figure 5.15).

At this stage, it should be noted that the present findings do not necessarily conflict with the conclusions by Masterton and Swan (2008), who established the empirical calibration technique, and found excellent agreement in large amplitude focused wave events. Their study concerned a laboratory investigation in a wide basin using flap-type wavemakers. These flap-type wavemakers are mechanically very different from the present sector-carrier wavemaker, with far fewer moving parts and bearings. As a result, the mechanical friction and stiction effects noted here are likely to be less significant to the work by Masterton and Swan (2008).

5.11 A displacement-based calibration

To overcome the issues associated with the generation of small-amplitude surface elevation-based calibrations, a novel calibration method was devised. Instead of relying on the recorded water surface elevation, the new method directly calibrates the wavemaker displacement. To achieve this, the wave generator is calibrated so that the measured wavemaker displacement exactly matches the desired or theoretical wavemaker motion. In the context of focused wave groups, this is considered appropriate, as the wave group at the wavemaker is relatively dispersed so that a low order calibration (first-order in this case) may be considered sufficiently accurate.

The new method effectively avoids the issue of the nonlinear behaviour due to auxiliary mechanical forces, as it compensates for any difference between the actual and theoretical wavemaker displacement. Furthermore, this method is likely to be more robust, as the wavemaker displacement can generally be measured with higher accuracy than the water surface elevation. In the present case, this corresponds to the difference between a high-precision laser sensor (Micro Epsilon 1402-600 of accuracy $\pm$0.08mm) and a resistance-based wave probe (probe accuracy of $\pm$0.5mm). Finally, unlike the method outlined in §5.10, the wavemaker

displacement-based method does not require the generation of a small-amplitude wave for the purpose of calibration.

The immediate drawback of the displacement-based calibration is that it relies on a theoretical pre-computed description of the wavemaker (to fluid) transfer function. In other words, even if the wavemaker displacement is known, this does not necessarily yield the desired information of the generated water surface elevation. At first order, the wavemaker transfer function is given by the progressive wave field coefficient c_0. In this context, §3.4.1 (regular waves) and §5.9.1 (focused wave groups) established that the modified coefficient $c_0' = 0.85c_0$ provides a more accurate description of the transfer function. With these arguments in mind, the displacement-based calibration was carried out as follows:

(i) For the purpose of a first iteration, a large-amplitude focused wave group ($A_{\text{sum}}k_p = 0.10$ and $k_p h = 1.4$) was generated based on an entirely theoretical description. The wavemaker displacement for this wave group was measured for the full repeat time T_r. The surface elevation was not recorded.

(ii) A DFT was applied to the recorded wavemaker displacement, and correction factors for both the magnitude and the phase of this displacement were derived. These correction factors were obtained by comparison of the experimentally observed data and first-order wavemaker theory. An iterative procedure was now applied, until the experimentally observed wavemaker displacement matches the theoretical demand. In position control, this is relatively straightforward. The wavemaker displacement is the actual control quantity, and only small correction terms are applied to compensate for any deficiencies in the motion controller. In force control, the aforementioned auxiliary force components also affect the motion response, so that an increased level of compensation was required. Generally speaking, 1-2 iterations were sufficient in position control, whilst 4-5 iterations were required for force control.

(iii) In undertaking step (ii) above, two different approaches for the wavemaker

transfer function were implemented:

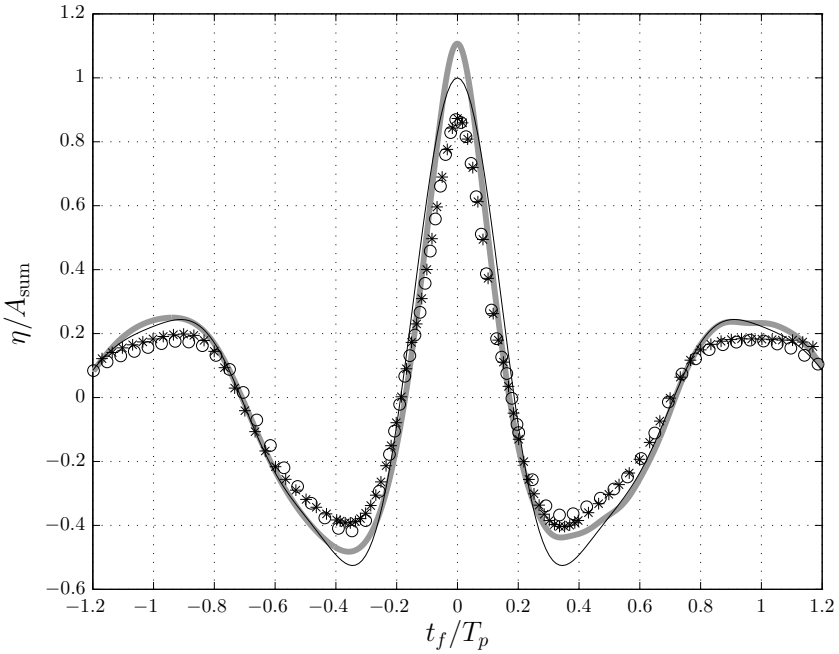
(a) The desired wavemaker displacement was calculated based on c_0

(b) The desired wavemaker displacement was calculated based on c_0'

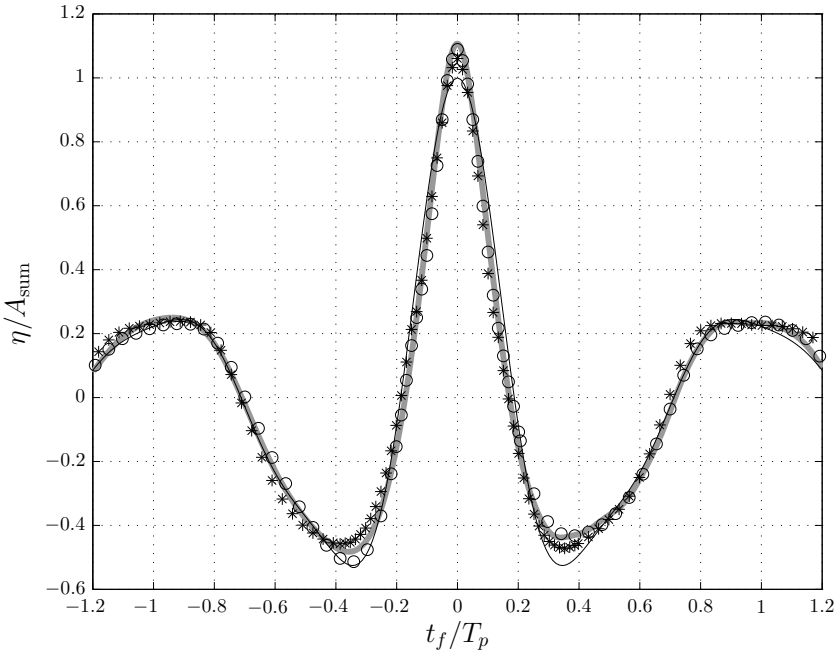
Figures 5.18(a) and 5.18(b) illustrate the water surface elevation following method (iii) (a) and (b) respectively. From Figure 5.18(a) it is clear that wave generation based on c_0 leads to a significant under-prediction of the focused wave event magnitude. This is, once again, consistent with the observation that c_0 is inadequate. However, Figure 5.18(a) partially confirms the success of the new methodology, in that the events under position control (symbol $\circ$) and force control (symbol $*$) are now very similar.

Figure 5.18(b), based on c_0', fully confirms the success of the method; the agreement between the BEM computation and the experimental observation being very good throughout. The maximum surface elevation under position control and force control are now $\eta_{\max}/A_{\text{sum}} = 1.11$ and $\eta_{\max}/A_{\text{sum}} = 1.09$ respectively; both being in close agreement to the BEM prediction of $\eta_{\max}/A_{\text{sum}} = 1.12$. Furthermore, the overall description of the event is reproduced closely in both cases. Taken as a whole, the new calibration methodology leads to a significant improvement when compared to either the direct theoretical generation (Figure 5.15) or the surface elevation-based calibration (Figure 5.17).

To demonstrate the success of the displacement-based calibration for a wider range of conditions, Figure 5.19 shows the surface elevation for (a) $A_{\text{sum}}k_p = 0.15$ and $k_p h = 1.1$ and (b) $A_{\text{sum}}k_p = 0.15$ and $k_p h = 1.4$. The figure considers both position control (symbol $\circ$) and force control (symbol $*$), and makes a direct comparison to the corresponding BEM computations. The excellent match between the experimental observations and the numerical predictions confirms that the calibration approach based on the wavemaker displacement is indeed suitable for an extended range of conditions. To quantify this, the maximum surface elevation in Figure 5.19(a) is $\eta_{\max}/A_{\text{sum}} = 1.2$, 1.23 and 1.22 for BEM computation, position control and force control respectively. In Figure 5.19(b) this corresponds to

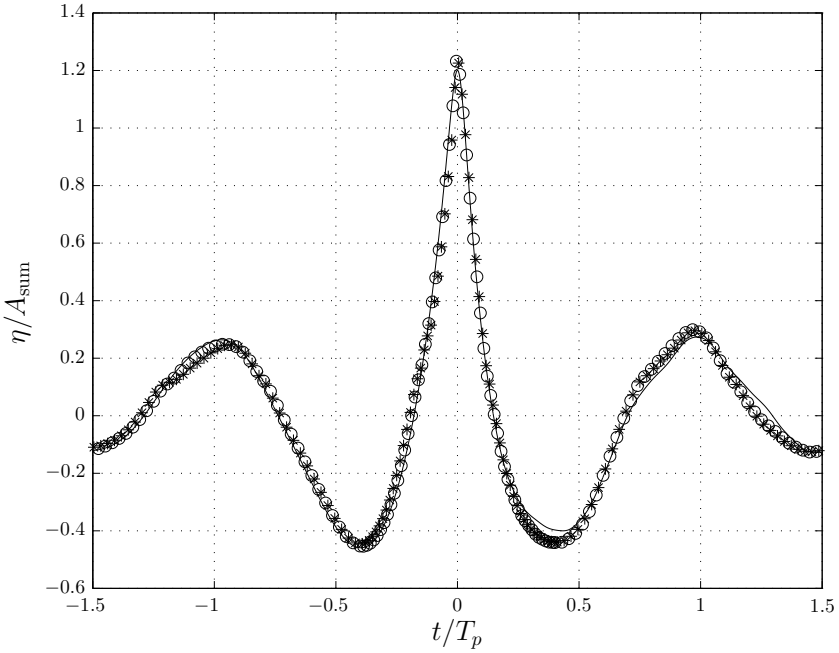


(a) Normalised surface elevation η/A_{sum} based on c_0

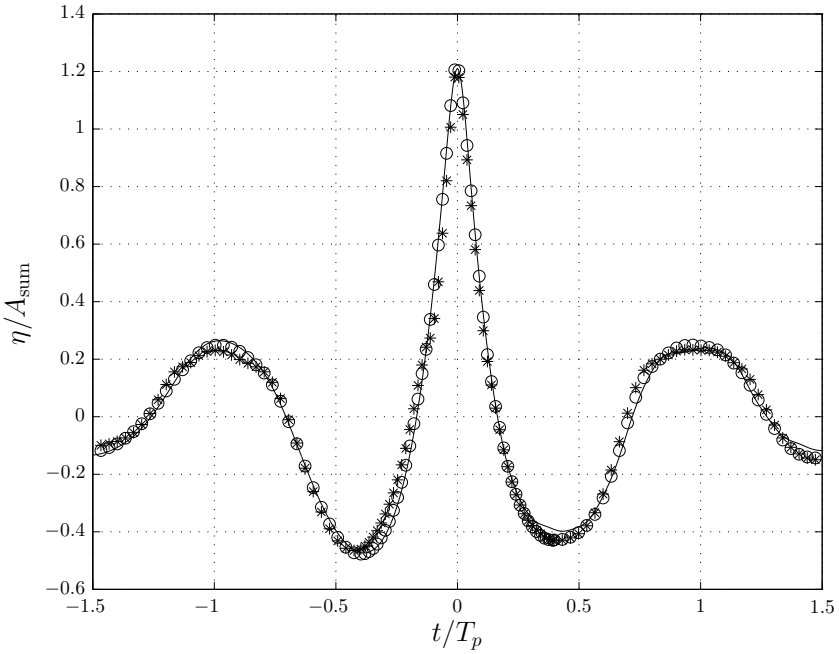


(b) Normalised surface elevation η/A_{sum} based on $c_0{}'$

Figure 5.18: Focused event with $A_{\mathrm{sum}}k_p = 0.10$, $k_p h = 1.4$ and $x_f = 7h$ showing —— linear wave theory —— BEM computation, ∘ position-control data and ∗ force-control data.



(a) Normalised surface elevation η/A_{sum} for $k_p h = 1.1$



(b) Normalised surface elevation η/A_{sum} for $k_p h = 1.4$

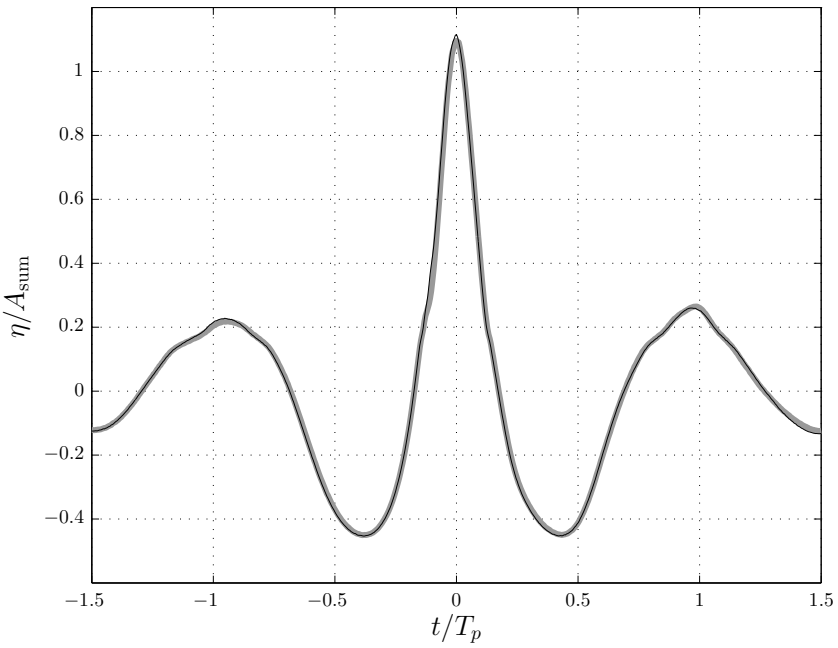
Figure 5.19: Focused events with $A_{\mathrm{sum}} k_p = 0.15$ showing ━━ BEM computation, ∘ position-control data and ∗ force-control data.

$\eta_{\max}/A_{\text{sum}} = 1.21$, 1.21 and 1.20. It should be noted once again that this relies on the calibration of the wavemaker displacement only, and that the wavemaker-to-fluid transfer function is calculated as $c_0{}' = 0.85c_0$ without any further adjustment or calibration.

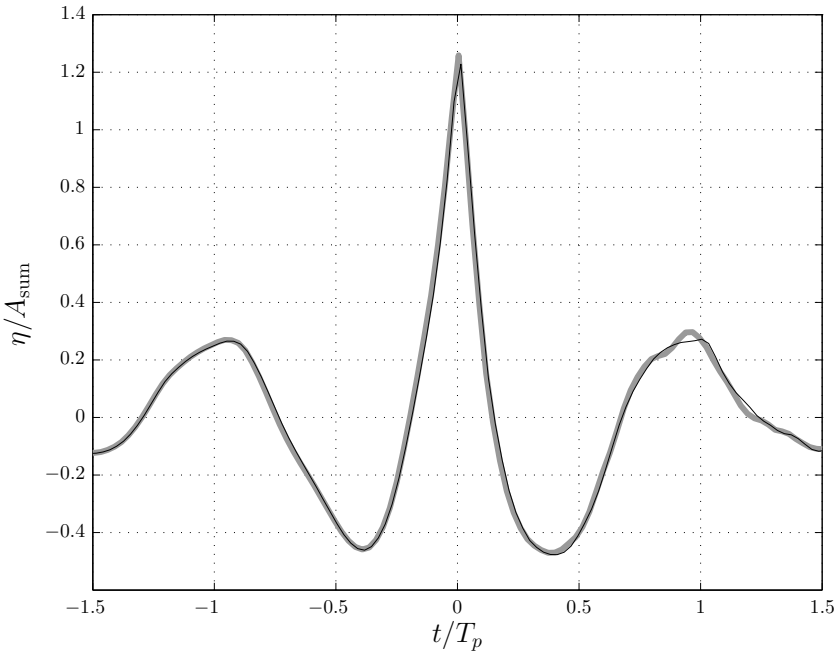
5.12 Wave generation in second-order control

The discussion in §5.11 highlighted that high-quality focused wave generation based on first-order control is possible. Indeed, the issues noted in the §5.9 - §5.11 are not related to the (first-order) demand signal, but rather to (i) inaccuracies in the progressive wave field coefficient c_0, (ii) imperfections in the motion controller in position control and (iii) small but important auxiliary mechanical forces in force control. If these issues are rectified, a first-order demand signal may be entirely adequate.

To demonstrate this further, Figure 5.20 shows the surface elevation for a focused wave group with $k_p h = 1.1$ and steepness (a) $A_{\text{sum}}k_p = 0.10$ and (b) $A_{\text{sum}}k_p = 0.15$. In both cases, data based on first-order force control (grey line) and second-order force control (black line) are included. As before, the events are based on the wavemaker-displacement calibration procedure. The two data sets are virtually indistinguishable for $A_{\text{sum}}k_p = 0.10$, and very similar for $A_{\text{sum}}k_p = 0.15$, confirming that the influence of the additional second-order demand input is small. This clearly demonstrates that the key to high-quality focused wave group generation lies in a number of practical considerations, but is not necessarily related to the order of the demand signal. Whilst some specific wave cases may require second-order control, due attention must first be paid to the largely dominating practical effects (i)-(iii) noted above.



(a) Normalised surface elevation η/A_{sum} for $A_{\text{sum}}k_p = 0.10$



(b) Normalised surface elevation η/A_{sum} for $A_{\text{sum}}k_p = 0.15$

Figure 5.20: Focused event with $k_p h = 1.1$ showing ▬ first-order force control and ▬ second-order force control.

5.13 Conclusions

A numerical investigation presented in Part I of the present chapter demonstrated that both the repeat time and the focus location have an influence on the quality of focused wave groups. Both of these may be adjusted to ensure that (i) all wave components have sufficient time to propagate to the focus location and (ii) their relative phasing does not lead to excessive wave-wave interactions at the input boundary. In terms of the focus location, events of moderate wave steepness should be focused 15-25 water depths downstream of the wavemaker to ensure that errors of $< 1\%$ are achieved in the maximum crest elevation and the RMS.

In contrast, the experimental work in Part II demonstrated that focusing at a location larger than 10 water depths can lead to significant energy dissipation at the flume glass side walls. Furthermore, focused wave group generation based on the analytical progressive wave field coefficient generally leads to a significant under-prediction of the maximum crest elevation. The errors observed are largely consistent with the findings in the context of regular waves, and lead to discrepancies in the order of 15% if focused within 10 water depths of the wavemaker. Adopting a simple modified wave field coefficient, these departures are reduced considerably, but some small inaccuracies remain.

To address these, an established calibration method based on the generation of a small-amplitude event was considered. This empirical approach indeed leads to an excellent agreement for the small-amplitude (or calibrated) event. Unfortunately, it does not lead to satisfactory performance when applied to the generation of large-amplitude wave groups. A number of potential sources of error were discussed, and these are primarily attributed to imperfections in the motion controller and small but important auxiliary forces.

A new calibration method was introduced, whereby the calibration is based on the displacement of the wavemaker and a pre-defined description of the wavemaker-to-fluid transfer function. This novel method yields the most accurate description of the experimentally observed focused wave groups. Given a number of practical

advantages, the method is also believed to provide a robust approach for future wave group calibrations.

A comparison between first- and second-order control established that the former may be entirely satisfactory. Whilst second-order control for focused wave groups could sometimes be required, this should also be based on a prior empirical calibration of the wavemaker displacement.

6

Irregular waves

6.1 Chapter overview

Realistic laboratory testing of any offshore or coastal structure must involve irregular sea testing. For irregular seas, the absorption performance of the wavemaker is of critical importance. With typical test durations at laboratory scale being in the order of 20-30 minutes, wave reflections arising at either the downstream beach or the test model may lead to the progressive built-up of wave energy in the tank. This built-up of energy ultimately leads to non-uniform wave statistics over the duration of the test. At the same time, the largest wave events arising in the sea state must also be modelled appropriately, which requires a nonlinear demand signal. As a result, an irregular sea state may be considered as the ultimate challenge for any high-quality absorbing wavemaker system. Given the importance of wave absorption in irregular seas, the present chapter focuses entirely on force-controlled operation.

The chapter commences with a brief theoretical description of the problem, outlining the difficulties associated with nonlinear control in irregular seas, §6.2. An introduction to the laboratory test parameters is then presented in §6.3. The role of wave absorption in long irregular sea simulations is discussed in §6.4. A quantification for the success of both linear and nonlinear force control is then

provided through a statistical analysis, whereby the experimentally observed crest elevations are compared to a set of reference solutions. This is first undertaken for a small amplitude sea state, §6.5, followed by steep sea states in both intermediate water depth (§6.6) and shallow water (§6.7). An alternative irregular wave generation approach, with the potential to overcome the shortcomings of second-order wavemaker theory in shallow water, is discussed in §6.8. Conclusions are drawn in §6.9.

6.2 Nonlinear control in irregular seas

6.2.1 Second-order control

Second-order control in irregular seas is a direct extension of the bi-chromatic wave case discussed in Chapter 4, §4.2. In the context of this earlier chapter, the interaction between two wave components (n, m) was shown to lead to both bound and free waves arising at superharmonics and subharmonics. In the case of irregular waves, these interactions must be summed over all N wave components composing the sea state. For a typical laboratory sea state, N may be in excess of 1000; this giving rise to a double sum of the form $\sum_{n=1}^{N}\sum_{m=n}^{N}$ for the computation of the second-order correction terms (Appendix A).

In addition, the interactions must also take into consideration J evanescent modes, where J is typically in the order of 50. The calculations hence require sums of the form $\sum_{n=1}^{N}\sum_{m=n}^{N}\sum_{j=0}^{J}\sum_{l=0}^{J}$, which lead to computation times in the order of several hours to calculate the second-order wavemaker correction for a 20 minutes sea state. For the purpose of the present second-order control evaluation (§6.6 and §6.7), all computations were undertaken using this direct approach. If computational cost is of concern, the asymptotic summation introduced by Schäffer (1993) may substantially reduce the number of terms involved. Setting aside the issue of long computations, the extension of the bi-chromatic case to irregular sea states is straightforward in terms of the second-order calculations.

6.2.2 Alternative nonlinear formulations

In the context of regular waves, a Stream-function based wavemaking theory proved highly versatile, particularly for low kh where the influence of the evanescent modes is small. The approach relied on a depth-averaged fluid velocity which was obtained from Stream-function wave theory and subjected to a set of operations to incorporate the departure of the wavemaker from its mean position (§2.3.6). This type of approach is general, and could potentially be extended to irregular seas. To gain any benefit over the second-order approach outlined in §6.2.1, this would require an evaluation of the irregular wave kinematics beyond second order.

Over the course of this PhD, numerous approaches of nonlinear kinematics computation were considered. This included methods such as the double Fourier technique (Lambrakos, 1981; Baldock and Swan, 1994), the BST model introduced by Bateman et al. (2003) or the local Fourier technique of Sobey (1992). Unfortunately, none of these approaches was found satisfactory in computing nonlinear kinematics in irregular seas. To demonstrate the underlying reasons for this, the following discussion outlines the mathematical formulation of the double Fourier methodology, and highlights the difficulties associated with irregular wave kinematics calculations.

In essence, the double Fourier approach provides an irregular wave extension to the Stream-function approach in that a least-squares fit to the free-surface boundary conditions is sought. In contrast to the Stream-function approach, the unsteadiness of the underlying wave solution leads to an optimisation involving both space and time. A general form of the velocity potential for an unsteady wave form is given by

$$\phi = \sum_{n=1}^{N} \sum_{m=1}^{M} -\cosh(k_n z) \left(A_{nm} \cos\left(\omega_m t - k_n x\right) + B_{nm} \sin\left(\omega_m t - k_n x\right) \right) \qquad (6.1)$$

which satisfies mass continuity, the bed boundary condition and the periodicity of

the wave solution. Within equation (6.1), the wave frequencies are given by $\omega_m = m\omega_1$, and the wavenumbers are defined as $k_n = nk_1$, where ω_1 is a fundamental wave frequency, k_1 is the corresponding wavenumber, and n and m are integers.

The Fourier coefficients A_{nm} and B_{nm} are unknowns of the solution. To obtain these coefficients, an iterative minimisation of the error in the free-surface boundary conditions is undertaken. The error in the dynamic free-surface boundary condition at location x_j and time t_i is defined as

$$E_{Dij} = \eta + \frac{1}{g}\frac{\partial \phi}{\partial t} + \frac{1}{2g}\left[\left(\frac{\partial \phi}{\partial x}\right)^2 + \left(\frac{\partial \phi}{\partial z}\right)^2\right] + Q \quad \text{on} \quad z = \eta(x_j, t_i), \tag{6.2}$$

where the Bernoulli constant Q is treated as an unknown. Similarly, the error in the kinematic free-surface boundary condition is given by

$$E_{Kij} = \frac{\partial \eta}{\partial t} + \frac{\partial \phi}{\partial x}\frac{\partial \eta}{\partial x} - \frac{\partial \phi}{\partial z} \quad \text{on} \quad z = \eta(x_j, t_i). \tag{6.3}$$

The optimisation procedure involves finding the minimum to the expression

$$E_T = \sum_{i=1}^{I}\sum_{j=1}^{J}\left[\left(E_{Dij}\frac{\omega_1^2}{g}\right)^2 + \left(E_{Kij}\frac{\omega_1}{g}\right)^2\right]. \tag{6.4}$$

Considering the above formulation, the inherent limitations of the double Fourier approach may be described as follows. The error minimisation is undertaken using equation (6.4), which in turn relies on equations (6.2) and (6.3) for the calculation of the error in the free-surface boundary conditions. These error descriptions must be based on a pre-defined surface elevation η and its derivatives $\partial\eta/\partial t$ and $\partial\eta/\partial x$. In the context of Lambrakos (1981) and Baldock and Swan (1994), the description of these quantities was obtained either from field data or laboratory measurements. In either case, this input data was only available for a localised (steep) event. For such a localised event, the double Fourier approach may be used to accurately compute the kinematics arising under a steep wave.

For a generalised irregular wavemaking approach, it is impractical to rely on

field data, as these are either not available or case specific. As a result, the highest accuracy description for η, $\partial\eta/\partial t$ and $\partial\eta/\partial x$ is given by the second-order irregular wave model by Sharma and Dean (1981). From equation (6.3), it is clear that the description by Sharma and Dean (1981) does not satisfy this fully-nonlinear free-surface boundary condition. Instead, this solution was developed by satisfying the second-order approximation of equation (6.3). In considering the above arguments, the double Fourier approach can lead to velocity computations beyond second order, but this only applies to a localised part of the sea state where the surface elevation and its derivatives are obtained through field or laboratory data. For an irregular sea state, second-order computations presently provide the most reliable description.

In considering the BST approach by Bateman et al. (2003), it was concluded that this type of solution suffers from the same limitations as the BEM formulation discussed in Chapter 5. In the context of the BST model, a time-marching procedure is adopted, which inherently relies on a set of initial conditions. If these initial conditions relate to a dispersed sea state free of steep wave events, then the time-marching towards the evolution of a large event offers improvements beyond second order. Unfortunately, this is not the case in an irregular sea, where large events may be present at any time and location. In the absence of a consistent kinematics solution beyond second order, the majority of the nonlinear control scenarios rely on a second-order model. An alternative *ad-hoc* approach, potentially overcoming some of the issues associated with second-order control in shallow water, is then introduced in §6.8.

6.3 Irregular sea laboratory testing

All experimental data presented in this chapter were once again obtained in the Coastal Wave Flume, with the water depth held constant at $h = 0.6$m. To achieve accurate wave generation, the irregular sea states were subjected to the same displacement-based calibration procedure as outlined in the context of focused

wave groups, Chapter 5. The irregular wave testing adopted a JONSWAP spectrum with spectral density function $S_{\eta\eta}$ as given in equation (5.1). In contrast to the focused wave investigation in Chapter 5, the phasing for each wave component was now selected as a uniformly distributed random number from the interval $[0,\ 2\pi]$. The peak enhancement factor was $\gamma = 3.3$ throughout.

Individual wave component magnitudes were scaled to achieve a particular or desired significant wave height H_s. The relative depth of each sea state was expressed as $k_p h$, where k_p is the wave number corresponding to the peak period of the spectrum, T_p. The nonlinearity of an irregular sea state may now be expressed by the non-dimensional product $\frac{1}{2}H_s k_p$, which may be understood as a wave steepness similar to Ak (regular waves) or $A_{\text{sum}}k_p$ (focused wave groups).

If statistical data is of concern, a large number of individual wave events must be realised. The present work considers sea state implementations with up to 10,000 individual waves. Whilst this could be undertaken as a single long continuous experiment, it is often more practical to limit the repeat time and amalgamate the data from individual runs. The difficulties associated with a single continuous experiment lie in the nature of the discretised form of $S_{\eta\eta}$. For long simulations, $S_{\eta\eta}$ is based upon a large number of very small individual wave components. The small component magnitude may lead to issues with numerical precision. Furthermore, a large number of individual wave components also leads to excessively long second-order computations as noted in §6.2.1.

To achieve a compromise between numerical accuracy and sufficiently long experimental runs, the present work adopts a repeat time of 1024s for all cases where statistical evidence is required. In cases where deterministic data are sought, a repeat time of 64s was considered sufficient.

6.4 Wave generation and absorption

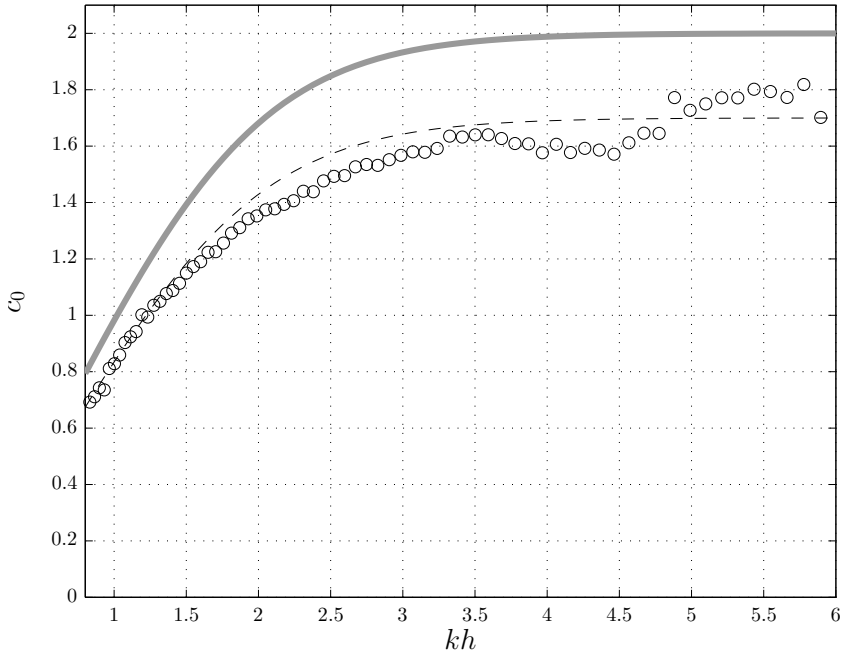
Throughout the present thesis, it has been established that the progressive wave field coefficient c_0 is generally over-predicted by potential flow theory. To confirm

this observation in the context of irregular seas, a small amplitude sea state with $\frac{1}{2}H_s k_p = 0.03$ and $k_p h = 1.4$ was considered. The surface elevation $\eta(t)$ was recorded by a single wave gauge located at $x = 7h$, and the wavemaker position was recorded using a high-precision laser displacement sensor. The progressive wave field coefficient may be obtained as $c_0 = A/X_a$, where A is the surface elevation magnitude, and X_a is the magnitude of the wavemaker displacement. To obtain these magnitudes for each of the components present within the sea state, an FFT was applied to a time window corresponding to the full repeat time of the spectrum, where $T_r = 64$s for this case.

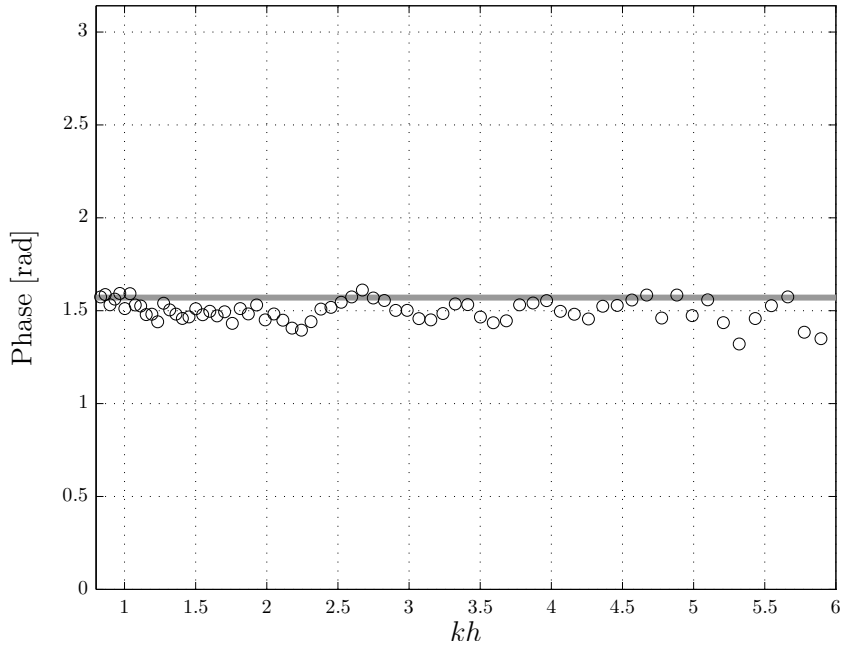
Figure 6.1 shows both the magnitude (part (a)) and the phase (part (b)) of c_0. The observations made in this figure are very similar to those reported in the context of regular waves (Figure 3.6) and focused wave groups (Figure 5.13). As before, the phasing is in generally good agreement, and the magnitude is over-predicted by approximately 15%. To visualise this departure, the modified coefficient $c_0{}' = 0.85c_0$ is included as the dashed line in Figure 6.1(a).

The variability of the data for $kh > 3.5$ is to be expected, as this relates to small component magnitudes towards the tail of the wave spectrum. Furthermore, it was previously shown (Figure 5.13) that these high frequency components are most affected by friction arising along the flume slide walls. Nevertheless, the agreement of the magnitude data with $c_0{}' = 0.85c_0$ is good, confirming that the progressive wave field coefficient exhibits strong similarities in regular, focused and irregular waves. As a result, the modified coefficient $c_0{}'$ is again adopted for the experimental comparisons to follow.

In addition to the accurate generation of a desired sea state, continuous and effective wave absorption is essential. To demonstrate the ability of the wave flume system (absorbing wavemaker and downstream beach) to sustain a given sea state over a long duration, Figure 6.2 shows the surface elevation $\eta(t)$ recorded at $x = 7h$ and corresponding to three time intervals: (i) $0.5 \leq t/T_r \leq 0.6$ (blue line), (ii) $1.5 \leq t/T_r \leq 1.6$ (red line) and (iii) $9.5 \leq t/T_r \leq 9.6$ (green line). To be entirely clear, the data shown in Figure 6.2 relate to one continuous experiment undertaken



(a) Magnitude of c_0



(b) Phase of c_0

Figure 6.1: Progressive wave field coefficient in an irregular sea state with $\frac{1}{2}H_s k_p = 0.03$ and $k_p h = 1.4$ showing ∘ experimental data ——— theoretical prediction of c_0 and — — adjusted coefficient $c_0{}' = 0.85 c_0$.

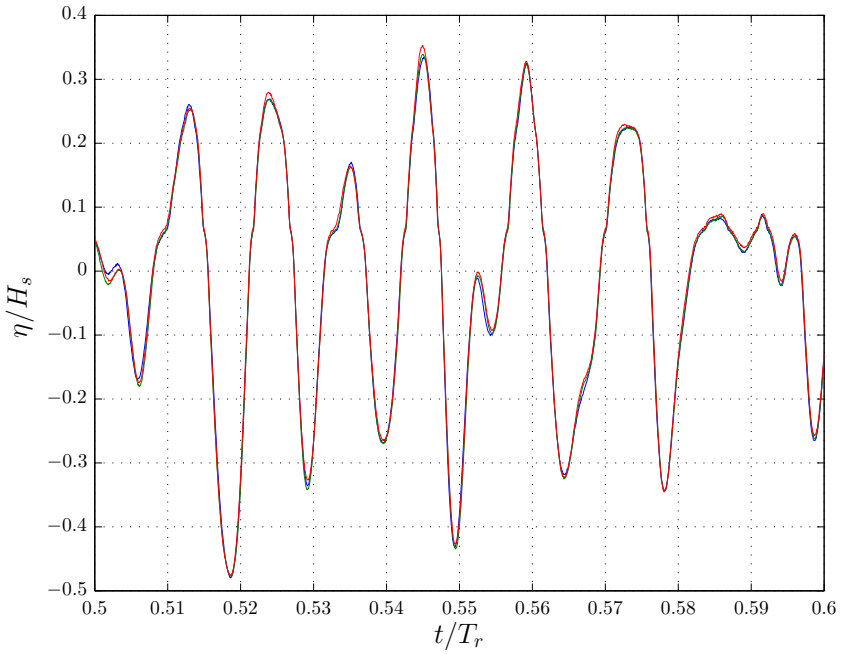


Figure 6.2: Water surface elevation $\eta(t)/H_s$ recorded in the time intervals $0.5 \leq t/T_r \leq 0.6$, $1.5 \leq t/T_r \leq 1.6$ and $9.5 \leq t/T_r \leq 9.6$. Note: The data shown relate to one continuous recording, where the latter two time intervals have been time-shifted to facilitate a comparison to the first repeat time.

for $0 \leq t/T_r \leq 10$. With the spectrum being periodic in T_r, the recordings at subsequent repeat times are expected to be identical if the sea state is free of wave reflections. To facilitate the comparison between data from intervals (i)-(iii), the recordings in intervals (ii) and (iii) were time-shifted by T_r and $9T_r$ respectively.

From Figure 6.2 it is clear that the surface elevations recorded within the three intervals are in excellent agreement. The first recording taken at $0.5 \leq t/T_r \leq 0.6$ is almost free from wave reflections, as the vast majority of wave components in the spectrum have had insufficient time to propagate to the downstream beach (located at $x = 35h$) and back to the wave probe at $x = 7h$. The surface elevation recorded in the interval $1.5 \leq t/T_r \leq 1.6$ shows some small departures from the initial interval, indicating that some beach reflections are now present. As the experiment progresses, the combination of an efficient beach and the absorbing wavemaker ensures that reflections do not build up, so that the recording at $9.5 \leq t/T_r \leq 9.6$ is in near-perfect agreement with the surface elevation at $1.5 \leq t/T_r \leq 1.6$.

Further analysis of this sea state showed that the beach performs very well for

the majority of the incident wave frequencies, with an average amplitude reflection coefficient of $< 3\%$. The largest wave reflections of up to 7% occurred at $kh \approx 1.0$. However, despite these wave reflections, the water surface elevation and spectral content (not shown herein) remain in excellent agreement with the desired content. The target significant wave height of $\frac{1}{2}H_s k_p = 0.03$ was achieved within 0.5% for all 10 repeat times, providing further evidence of the continuous nature of the experimental parameters.

6.5 Small amplitude sea states

In assessing the quality of a laboratory irregular sea state, a time-domain analysis or comparison often proves difficult; this approach being particularly limited when seeking to reveal the global nonlinearity of the sea state. In contrast, a statistical approach based upon crest elevations is often more appropriate, as this provides information relating to the entire sea state. A statistical approach commonly relies on the following procedure:

(1) An up-crossing analysis is applied to the time-domain surface elevation, $\eta(t)$, providing the crest elevations $\eta_{c1}...\eta_{cP}$, where P is the total number of crests recorded.

(2) The crest elevations η_{ci} are sorted in descending order, so that $\eta_{ci} > \eta_{cj}$ if $i < j$.

(3) The probability of exceedance $Q(\eta_{ci})$ is computed for each crest elevation η_{ci}, and is defined as $Q(\eta_{ci}) = i/P$.

If a wave crest elevation from an irregular sea state is considered, $Q(\eta_c)$ provides the probability of the crest elevation exceeding η_c. As the accuracy of the probability of exceedance mainly depends on the size of the sample, a sufficiently large number of crest elevations is required. Furthermore, it is commonly noted that the probability of exceedance Q provides an accurate measure one order of

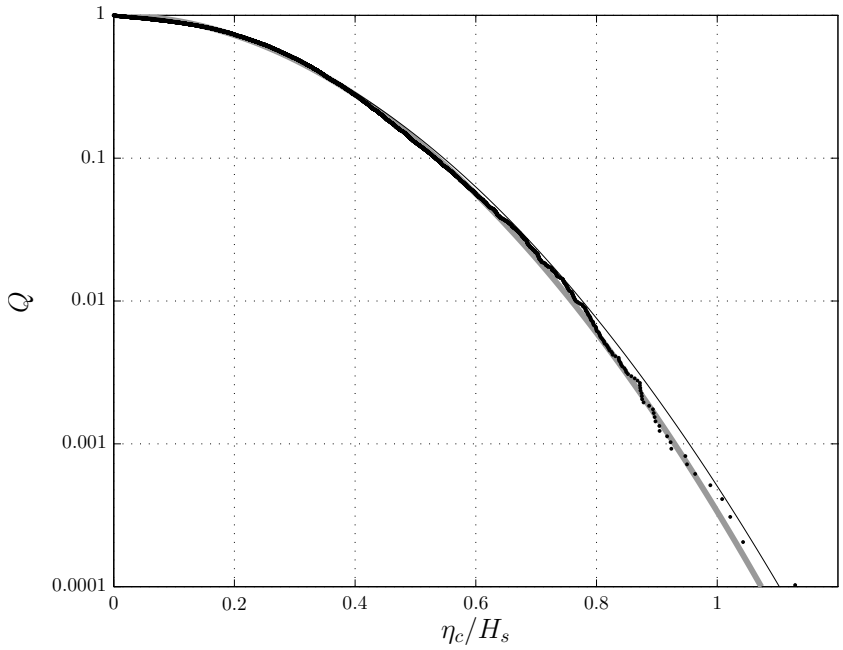


Figure 6.3: Probability of exceedance $Q(\eta_c/H_s)$ for a sea state with $\frac{1}{2}H_s k_p = 0.03$ and $k_p h = 1.4$ showing ——— linear Rayleigh distribution, ——— Forristall model and • experimental data

magnitude lower than the size of the sample. For example, if 10,000 crests are included, Q is considered accurate to a probability of approximately 10^{-3}. Following the work by Latheef and Swan (2013), up to 10,000 wave crests were realised for each irregular sea state. Based on a repeat time of $T_r = 1024$s (see §6.3), and given that 800-900 crests can be captured in 1024s, 11-12 experimental runs were carried out for each test case; the exact number depending on $k_p h$.

Figure 6.3 shows the probability of exceedance Q as a function of the normalised crest elevation η_c/H_s; the data representation chosen for the purpose of this figure being very similar to that in Latheef and Swan (2013). The discrete data points in Figure 6.3 relate to a small amplitude sea state with $\frac{1}{2}H_s k_p = 0.03$ and $k_p h = 1.4$. Indeed, all sea state parameters, except the repeat time, are identical to the sea state considered previously in §6.4. To obtain a theoretical comparison, Q may be computed based on time-domain surface elevation data provided by an analytical wave theory. The Rayleigh distribution provides theoretical crest statistics based on linear irregular wave theory. To include nonlinear effects, Forristall (2000) derived a distribution that relies on a large number of

second-order irregular wave simulations.

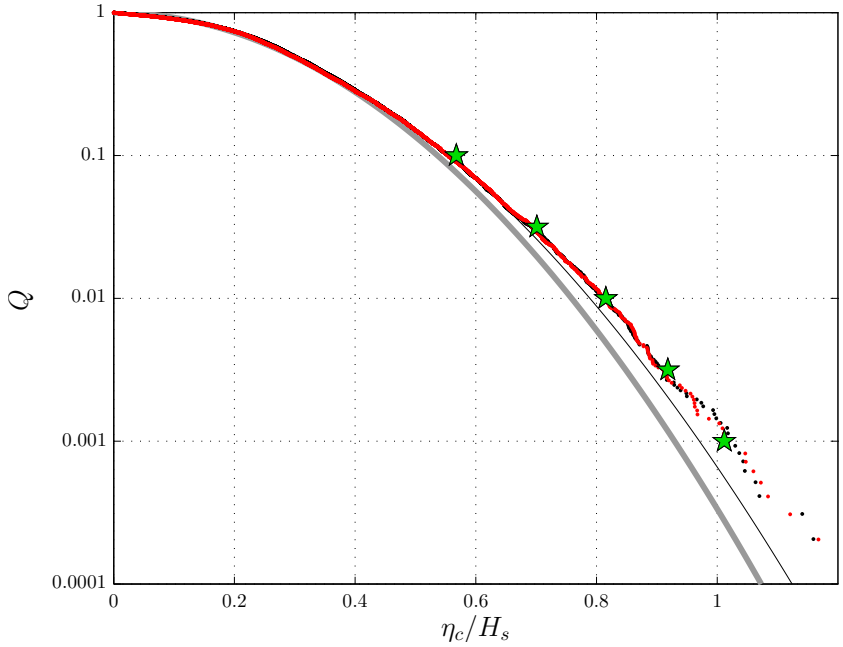
Figure 6.3 includes both the Rayleigh (grey line) and the Forristall (black line) distributions. Given the small sea state steepness, both distributions are in close agreement, with the experimental data lying between the two distributions. It may be argued that the experimental data lies somewhat closer to the Rayleigh distribution. However, given the small-amplitude nature of the sea state, the overall agreement between the three solutions (Rayleigh, Forristall and experimental data) is as expected.

6.6 Steep sea states in intermediate water depth

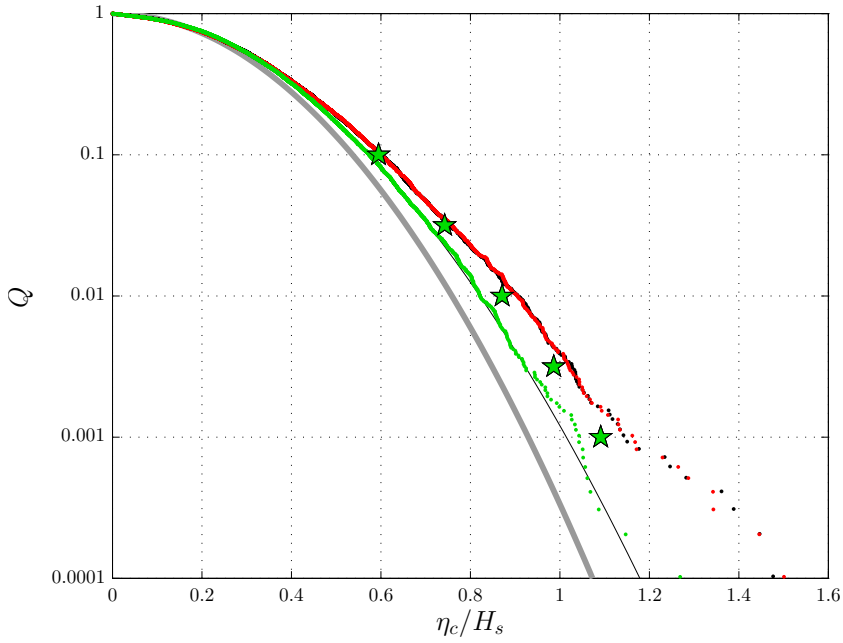
Figure 6.4 concerns a sea state with $k_p h = 1.4$ and (a) $\frac{1}{2} H_s k_p = 0.05$ and (b) $\frac{1}{2} H_s k_p = 0.10$; all other parameters being identical to the sea state considered in Figure 6.3. Having increased the sea state steepness, the difference between the linear Rayleigh distribution (grey line) and the Forristall model (black line) is apparent, indicating the importance of nonlinearity. Two experimental data sets are included, with the black symbols relating to first-order force control, and the red symbols relating to second-order force control.

Surprisingly, the order of control has little influence on the crest statistics for this sea state. At first sight, this behaviour is at odds with the importance of second-order wave-wave interactions, as evident by the marked difference between the Rayleigh and the Forristall distributions. However, from the discussion in previous chapters, it is clear that the second-order spurious free wave content is often significantly smaller than the bound wave content, particularly in intermediate water depth (see for example Figure 3.10).

To demonstrate this, it is instructive to consider the free wave correction term $A^{(23)\pm}$ introduced through second-order control. This free wave content is shown as the black lines in Figure 6.5 (solid line for superharmonics and dashed line for subharmonics), where the first-order amplitude spectrum $A^{(1)}$ (grey line) is included for reference. To set this into context, the computation of the first-



(a) Sea state with $\frac{1}{2}H_s k_p = 0.05$ and $k_p h = 1.4$



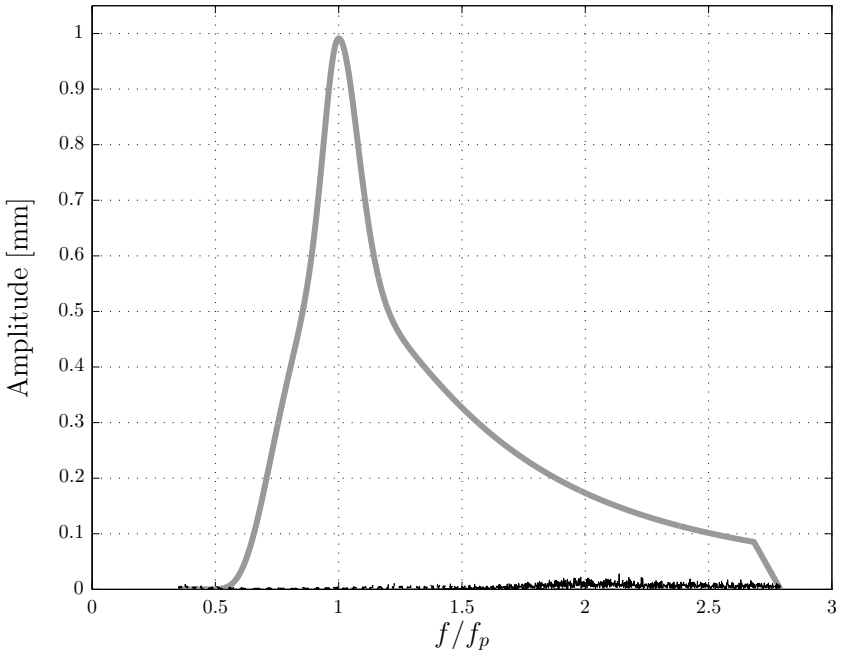
(b) Sea state with $\frac{1}{2}H_s k_p = 0.10$ and $k_p h = 1.4$

Figure 6.4: Probability of exceedance $Q(\eta_c/H_s)$ showing ▬ linear Rayleigh distribution, ▬ Forristall model, ● first-order control experimental data, ● second-order control experimental data, ● second-order computation including spurious free waves and ★ crest elevation from BEM computation.

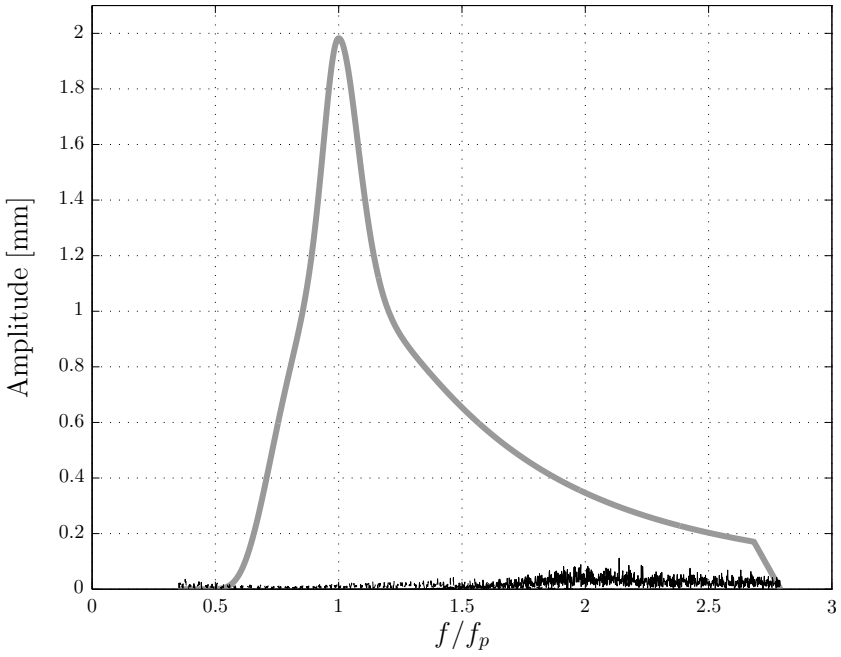
order demand signal is based upon $A^{(1)}$ alone, whilst second-order control relies on $A^{(1)} + A^{(23)\pm}$. For both wave steepnesses shown ($\frac{1}{2}H_s k_p = 0.05$ in part (a) and $\frac{1}{2}H_s k_p = 0.10$ in part (b)), the free wave correction term is substantially smaller than the first-order term. Indeed, the similarity between the first-order and the second-order demand signal is such that no noticeable effect on the wave crest statistics can be observed.

To confirm this observation further, the surface elevation for a sea state with $\frac{1}{2}H_s k_p = 0.10$ was simulated numerically, where the second-order expressions given in Chapter 2 and Appendix A were adopted. For the purpose of this simulation, the spurious free wave content was also included. An up-crossing analysis identical to that described above was applied to this numerical data, yielding the green data points in Figure 6.4(b). The close agreement between this spurious-wave contaminated sea state and the Forristall model confirms that the second-order free wave content only plays a minor role in the crest statistics pertaining to the present sea state.

Based upon the above discussion, the most likely explanation for the departures between the experimental data and the Forristall model lies in the importance of effects beyond second order. In seeking to obtain a description beyond second order, Latheef (2014) demonstrated that a fully-nonlinear BEM numerical model may be adopted to provide a reference solution for the crest elevations in steep irregular seas. Latheef (2014) suggests that a focused wave event, generated using a nonlinear numerical model, can produce an equivalent crest elevation when compared to a specific event arising in an irregular sea state. For this approach to succeed, two conditions must be met. First, the amplitude of the frequency components must be proportional to the energy spectrum, as shown in Tromans et al. (1991), and leading to so-called NewWave events. Second, it is essential that the linear amplitude sum A_{sum} is provided by the (linear) Rayleigh distribution for the same probability of exceedance Q. Latheef (2014) demonstrated the validity of these numerical computations in intermediate water conditions ($k_p h = 2$) and for steep irregular sea states (up to $\frac{1}{2}H_s k_p = 0.16$).



(a) Sea state with $\frac{1}{2}H_s k_p = 0.05$ and $k_p h = 1.4$



(b) Sea state with $\frac{1}{2}H_s k_p = 0.10$ and $k_p h = 1.4$

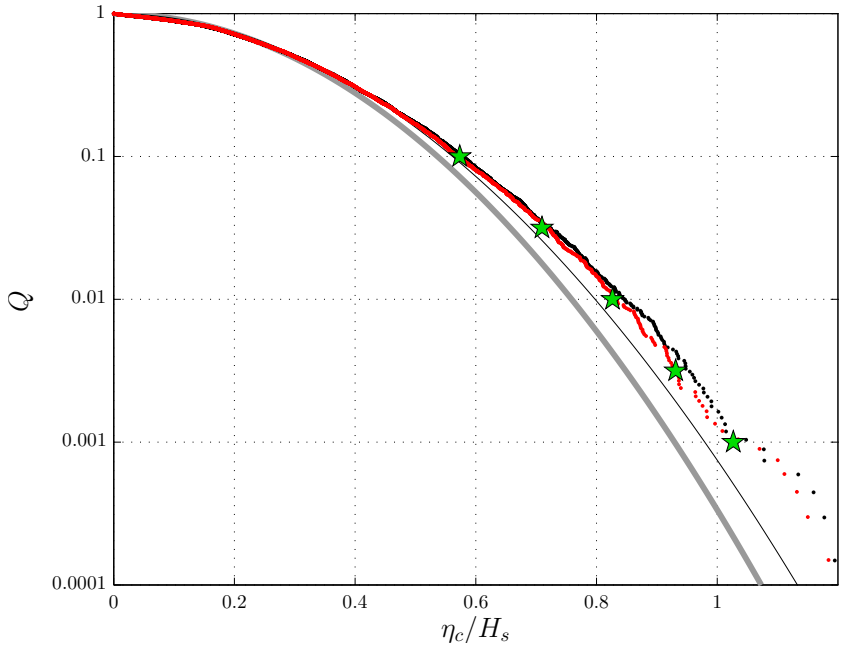
Figure 6.5: Wavemaker demand amplitude spectrum showing ——— first-order content $A^{(1)}$, ——— superharmonic correction amplitude $A^{(23)+}$ and – – – subharmonic correction amplitude $A^{(23)-}$.

Adopting a very similar approach to Latheef (2014), corresponding BEM computations were undertaken for both sea states considered herein ($k_ph = 1.4$ and $\frac{1}{2}H_sk_p = 0.05, 0.10$). The maximum crest elevation obtained from these computations are shown by the green stars in Figure 6.4. For the smaller amplitude sea state in Figure 6.4(a), the maximum crest elevations are in near-exact agreement with the corresponding irregular sea crest statistics. As a result, first-order control may be considered sufficiently accurate for this wave steepness with limited spurious free wave content. In contrast, the BEM crest elevations for $\frac{1}{2}H_sk_p = 0.10$ remain smaller than the experimental data. At present, the most likely explanation for this departure lies in the occurrence of spurious free wave content at third order and above. Before presenting any final conclusions concerning this important aspect of the irregular wave investigation, an additional sea state in shallow water is considered first.

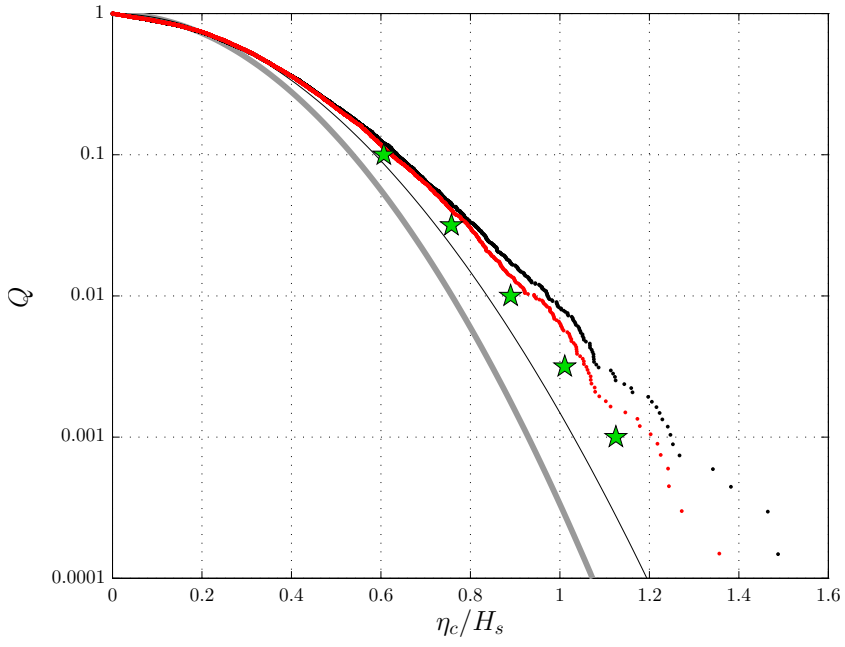
6.7 Steep sea states in shallow water

Figure 6.6 concerns a sea state with $k_ph = 0.8$ and (a) $\frac{1}{2}H_sk_p = 0.04$ and (b) $\frac{1}{2}H_sk_p = 0.08$. For this shallower water case, the maximum wave steepness was reduced to $\frac{1}{2}H_sk_p = 0.08$ to ensure that (i) the largest waves events do not break and (ii) the wavemaker stroke does not exceed its limitations. The data included in Figure 6.6 once again concern the Rayleigh distribution (grey line), the Forristall model (black line), first-order control (black points), second-order control (red points) and BEM computations (green stars).

For both sea state steepnesses, a clear difference between first-order and second-order control is observed. This is in marked contrast to the sea state with $k_ph = 1.4$ (Figure 6.4) and highlights the increased importance of nonlinear control in shallow water conditions. In both Figures 6.6 (a) and (b), second-order control reduces the maximum crest elevation. Considering the steeper sea state with $\frac{1}{2}H_sk_p = 0.08$, this reduction accounts for up to 8% at $Q = 10^{-2}$, and increases further as Q decreases.



(a) Sea state with $\frac{1}{2}H_s k_p = 0.04$ and $k_p h = 0.8$



(b) Sea state with $\frac{1}{2}H_s k_p = 0.08$ and $k_p h = 0.8$

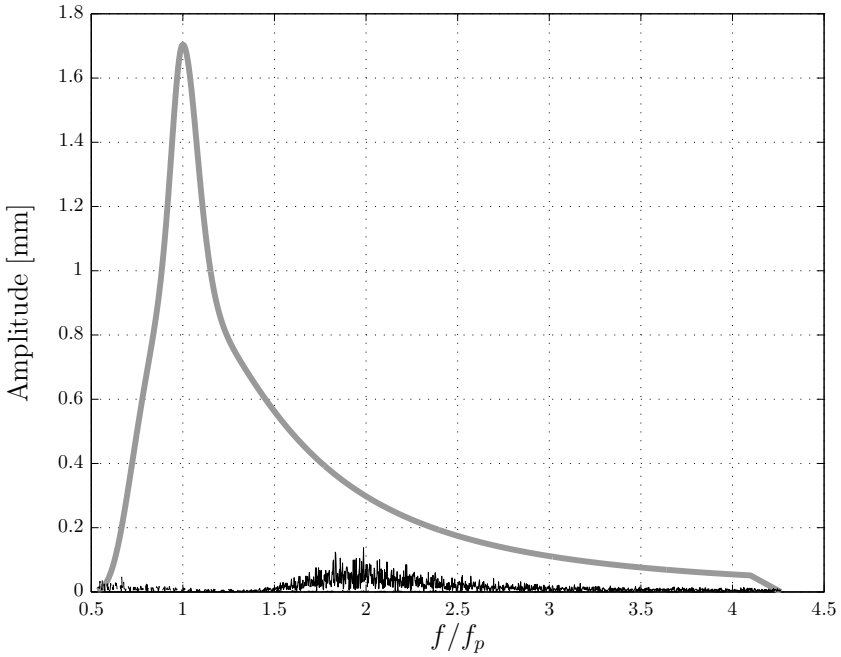
Figure 6.6: Probability of exceedance $Q(\eta_c/H_s)$ showing — linear Rayleigh distribution, — Forristall model, • first-order control experimental data, • second-order control experimental data, and ★ crest elevation from BEM computation.

The reasons for the difference between first-order and second-order control are further highlighted in Figure 6.7. In close similarity to Figure 6.5, the data presented relate to both the linear wave amplitude demand $A^{(1)}$ (grey line) and the second-order correction amplitude $A^{(23)\pm}$ (black lines). For this shallow water case with $k_p h = 0.8$, the spurious free wave content is significantly more pronounced, leading to a substantial correction term $A^{(23)\pm}$. The free wave content is primarily induced by wave-wave interactions arising between components in the vicinity of the spectral peak. Evidence of this is provided in Figure 6.7(b), where the maximum amplitude correction terms arise in the proximity of $f/f_p = 2$, corresponding to second-harmonic interaction terms produced by the spectral peak. The additional free wave components at higher wave frequencies are likely to lead to a steepening of the water surface, causing the large crest elevations observed in Figure 6.6. The second-order correction term $A^{(23)\pm}$ eliminates the spurious free wave content, which is seen to yield significant reductions in the crest elevations (red data points in Figure 6.6).

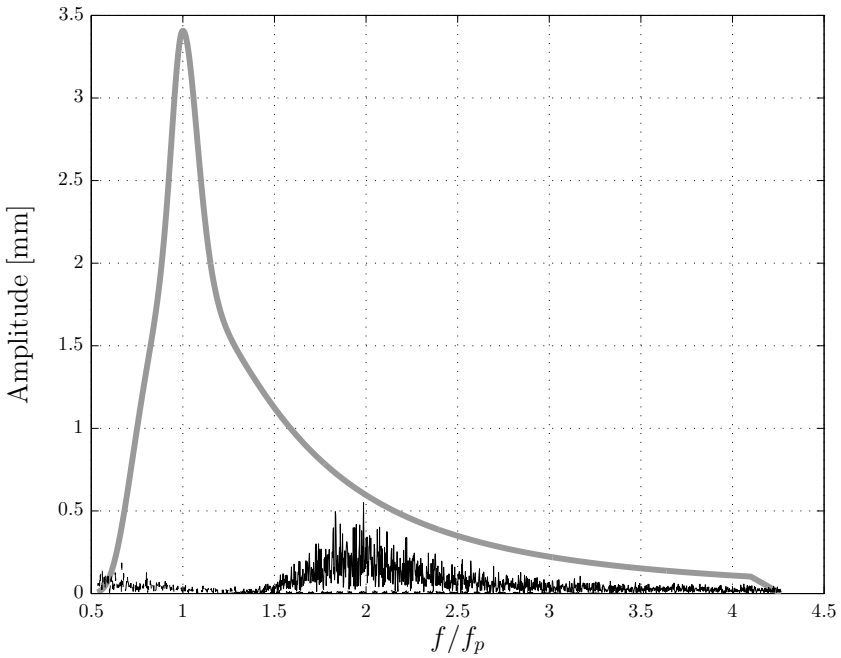
The focused wave computations (green stars), are in excellent agreement with the second-order control data for $\frac{1}{2}H_s k_p = 0.04$ (Figure 6.6(a)). For the steeper sea state with $\frac{1}{2}H_s k_p = 0.08$ in Figure 6.6(b), second-order control provides crest elevations in good agreement with the computations. However, some departures remain, and these may be attributed to at least two causes. First, third-order spurious free waves are likely to contaminate the wave field. In addition, the wave steepness and relative water depth of this sea state are such that the range of validity of second-order theory must be questioned. Once applied outside its range of validity, second-order wavemaker theory may introduce excessive nonlinear correction terms, and fail to compensate the actual free wave content.

6.8 An alternative wave generation approach

The above discussion highlighted that second-order control may not be entirely appropriate for the generation of steep sea states in shallow water. To address



(a) Sea state with $\frac{1}{2}H_s k_p = 0.04$ and $k_p h = 0.8$



(b) Sea state with $\frac{1}{2}H_s k_p = 0.08$ and $k_p h = 0.8$

Figure 6.7: Wavemaker demand amplitude spectrum showing ——— first-order content $A^{(1)}$, ——— superharmonic correction amplitude $A^{(23)+}$ and – – – subharmonic correction amplitude $A^{(23)-}$.

this, an alternative *ad-hoc* approach is introduced here. This approach is *ad-hoc* in the sense that it does not follow a consistent mathematical formulation, but rather seeks to eliminate the shortcomings associated with second-order control.

In essence, this *ad-hoc* approach relies on a very similar formulation as the Stream-function wavemaker theory introduced in Chapters 2 and 3. In formulating this latter theory, the boundary condition on the wavemaker imposed that the wavemaker velocity must match the horizontal depth-averaged fluid velocity. In addition, the departure of the wavemaker from its mean position was accounted for through a simulation in the time domain (§2.3.6). To formulate a similar approach for irregular waves, the depth-averaged fluid velocities at the wavemaker are required at each moment in time.

If second-order theory was used to calculate these kinematics, at least three fundamental issues would arise. Firstly, the second-order expansion may over-predict the second-harmonic wave content in shallow water; this having been discussed in detail in Chapter 3. Secondly, the kinematics predictions associated with large wave crests may be inaccurate (Sobey et al. (1987)) so that some form of stretching method would have to be adopted. Finally, it is unlikely that this would lead to any improvement over the complete second-order theory by Schäffer (1996).

In the absence of a complete irregular wave model valid beyond second order, the following *ad-hoc* procedure is adopted:

(i) The sea state is simulated using a linear irregular wave theory.

(ii) An up-crossing analysis is applied to the entire record, yielding the wave height H and the wave period T for each up-crossing interval.

(iii) A fifth-order regular wave solution (Fenton, 1985) is fitted to each up-crossing interval, using $A = H/2$ and T as the input to the nonlinear solution.

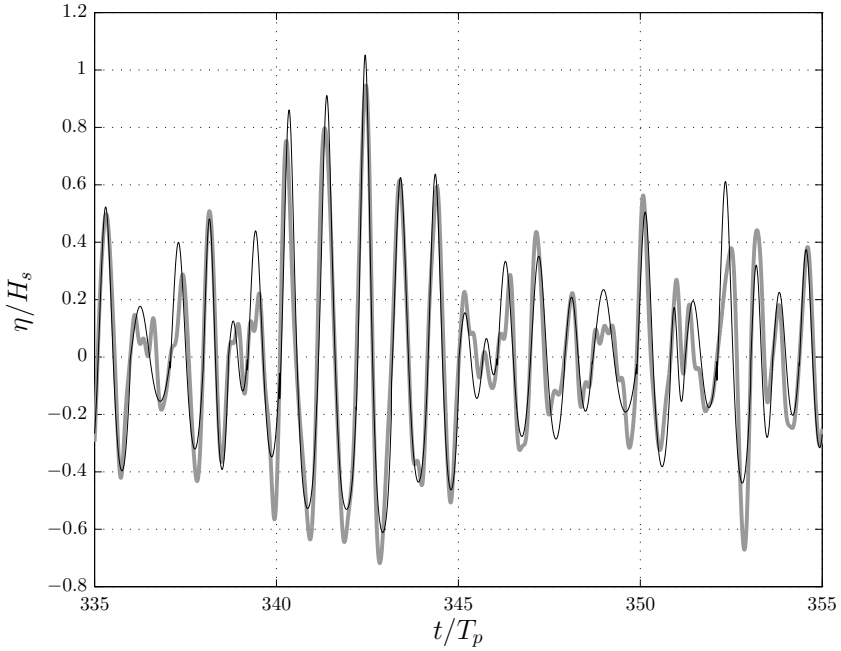
(iv) The horizontal fluid velocity is obtained from the fifth-order regular wave solution, and depth averaged at each moment in time.

(v) A series of steps equivalent to those described in §2.3.6 is used to obtain the wavemaker demand signal from the depth-averaged fluid velocity.

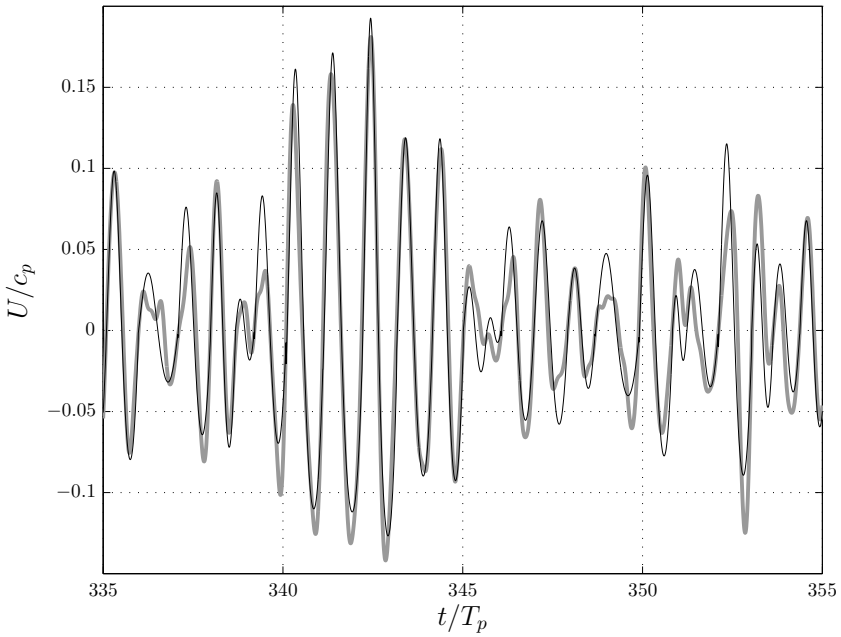
Figure 6.8(a) makes a comparison between the linearly calculated sea state (grey line) and the fifth-order solution (black line) fitted to each wave period. The corresponding depth-averaged horizontal fluid velocities, U/c_p, where c_p is the phase velocity corresponding to the peak period of the spectrum, T_p, are shown in Figure 6.8(b). From both parts of Figure 6.8 it is clear that significant differences exist between the two solutions, highlighting both the nonlinearity of the sea state and the distinct set of assumptions upon which each solution is based.

These differences are best illustrated as shown in Figure 6.9, providing the probability of exceedance of the normalised depth-averaged velocity U/c_p. The velocities calculated using the fifth-order regular wave solution (red data points) are significantly larger than the linearly calculated velocities (black data points). Unfortunately, in the absence of any complete theory beyond second order, it is difficult to judge which of the two descriptions is more accurate.

To test the *ad-hoc* approach in practice, the depth-averaged fluid velocities were used to compute the wavemaker demand signal in force control. Adopting this demand signal yields the crest elevations indicated by the blue data points in Figure 6.10. This figure also includes, for reference, all other previous solutions (Rayleigh, Forristall, linear force control, second-order force control and BEM computations). The blue data points in Figure 6.10 are in very good agreement with the maximum crest elevations taken from the numerical BEM computations. Most importantly, the match is improved substantially when compared to the second-order wavemaking case (red data points). The data corresponding to the *ad-hoc* approach and the second-order control case deviate from approximately $Q = 0.05$. Additional calculations have shown that these events ($Q < 0.05$) correspond to a wave nonlinearity parameter of $S > 0.8$, which may serve as a measure for the validity of second-order theory in irregular seas. Taken as a whole the data illustrate the potential of the *ad-hoc* approach in providing an



(a) Water surface elevation η/H_s



(b) Depth-averaged horizontal fluid velocity U/c_p

Figure 6.8: Time histories of (a) surface elevation and (b) depth-averaged horizontal velocity for a sea state with $k_p h = 0.8$ and $\frac{1}{2} H_s k_p = 0.08$ using ——— linear irregular wave calculation and ——— *ad-hoc* approach.

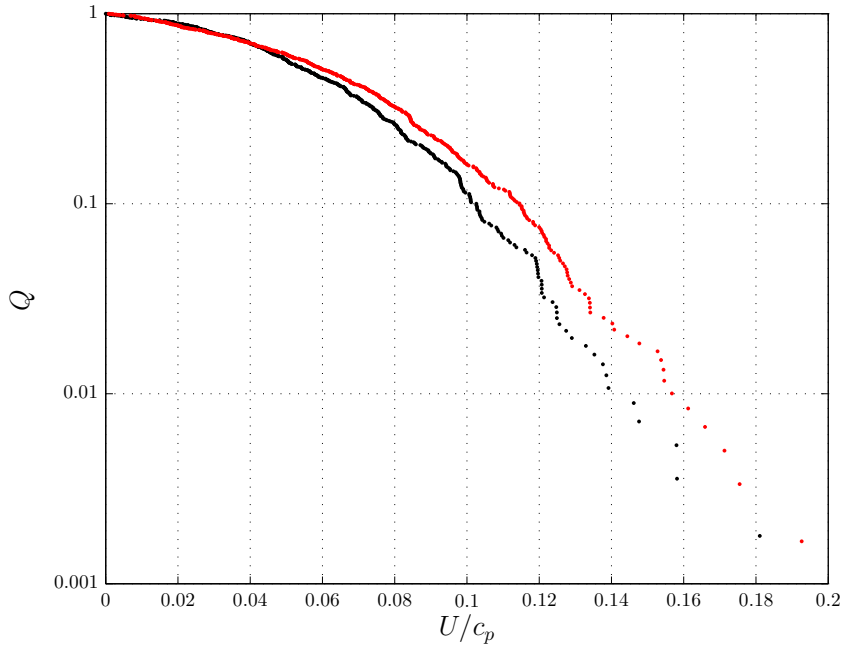


Figure 6.9: Probability of exceedance of depth-averaged horizontal fluid velocity for • linear irregular wave calculation and • *ad-hoc* approach.

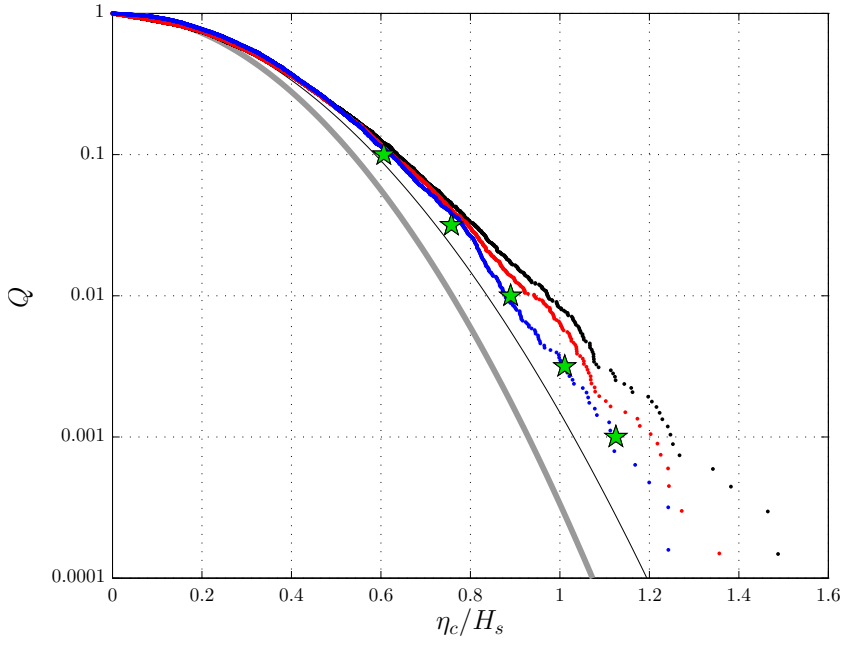


Figure 6.10: Probability of exceedance $Q(\eta_c/H_s)$ for sea state with $\frac{1}{2}H_s k_p = 0.08$ and $k_p h = 0.8$ showing ▬ linear Rayleigh distribution, ▬ Forristall model, • first-order control experimental data, • second-order control experimental data, ★ crest elevation from BEM computation and • *ad-hoc* approach.

improved technique for the generation of nonlinear irregular seas in shallow water. At present, this has only been confirmed for the single sea state shown in Figure 6.10; additional tests being recommended for future work.

6.9 Conclusions

The accurate generation and absorption of irregular seas in a shallow water environment is a challenging task. The chapter discussed a selection of alternative theoretical descriptions that capture the nonlinear interactions between multiple wave components. A number of these approaches have previously been shown to successfully model the nonlinearity associated with focused wave groups. Unfortunately, none of these approaches is readily extended to irregular sea simulations. As a result, second-order wavemaker theory provides the only consistent formulation.

If long irregular sea simulation are considered, active wave absorption is essential. The experimental data presented here demonstrate that the combination of an effective beach and an absorbing wavemaker enables the generation of stable long irregular sea simulations with high confidence. In seeking to match a desired significant wave height H_s, an empirical amplitude correction of 15% was found to lead to a match of H_s within 0.5%.

The generation of steep sea states in intermediate water depth showed that the influence of the order of control (first order or second order) is relatively limited; this being confirmed for two sea state steepnesses. The explanation for this lies in the fact that the second-order correction term is relatively small, such that first-order and second-order control lead to very similar wave crest statistics. A comparison to fully-nonlinear computations of individual wave events confirmed that (i) the crest statistics are clearly affected by interactions beyond second order and (ii) even a first-order control signal may lead to a good match between the experimental data and the numerical computations. Small remaining departures were attributed to spurious free waves arising at third order and beyond.

The generation of shallow water irregular waves highlighted the importance of second-order control. For the cases considered, the second-order correction term is sizeable, and clearly impacts upon the wave crest statistics. A comparison to selected nonlinear computations of individual events showed excellent agreement if the steepness of the sea states remains moderate. For the steepest sea state, second-order control leads to an over-prediction of the wave crest statistics. This was again attributed to spurious free waves at third order and beyond, but may also be associated with the limitations of second-order theory in shallow water. An *ad-hoc* approach, based upon a fit of a fifth-order regular wave solution to individual waves, was found to be in very good agreement with the selected nonlinear computations. At present, this *ad-hoc* approach was only tested for one sea state; additional verification being recommended as future work.

7

Conclusions

This PhD was motivated by the need to improve both the theoretical understanding and the practical success of shallow water wavemaking. Despite a significant body of work concerning this field, a number of shortcomings exist. Previous work primarily focused on the long-wave regime and the associated suppression of a subharmonic free wave. Very little evidence exists for the successful suppression of superharmonic free waves in shallow to intermediate water depth. Perhaps most importantly, there was also a severe lack of high-quality experimental data confirming the success of the established theories. This is exacerbated by the fact that very few previous studies addressed simultaneous nonlinear wave generation and active wave absorption. With the majority of modern laboratory wavemakers adopting some form of active wave absorption, this implies that their nonlinear generation performance is entirely uncertain at present. Based upon these shortcomings, the present PhD aimed to:

(i) Carefully assess the capabilities of existing wavemaker theories appropriate to shallow and intermediate water depth conditions.

(ii) Advance, as necessary, a recently developed wavemaker theory for actively-absorbing force-controlled operation, to ensure that this theory also meets the requirements of a shallow water environment.

(iii) Experimentally verify the success of the latest advances in nonlinear wavemaking, covering all practical requirements of modern laboratory testing, including regular waves, bi-chromatic waves, focused wave groups and irregular seas.

(iv) Make recommendations as to the range of validity of nonlinear, absorbing wavemaking techniques, and suggest avenues for their future development.

7.1 Principal achievements

With the above tasks in mind, the following principal achievements were made:

(1) Experimental evidence revealed that well-established linear wavemaker theory may be inaccurate if a piston-type wave generator is adopted. A consistent error of 15% was observed in the first-order wave amplitude; this being confirmed for a wide range of wave regimes. This result is of the upmost importance, as it has a major influence on any further development in the wavemaker control. At second order, any first-order error enters the analytical wavemaker expressions as the square, leading to 30% departures if left uncorrected. The first-order error is suspected to be caused by viscous effects, which questions the validity of the potential flow assumption in the wavemaking problem. In the absence of a viscous wavemaker theory, an empirical correction was carried forward.

(2) A new force-control Stream-function wavemaker theory was developed; this theory being expected to provide more accurate results than a second-order expansion. Perhaps surprisingly, experimental evidence showed that both second-order wavemaker theory and Stream-function wavemaker theory lead to comparable results in the generation of steep regular waves. This is partially due to the fact that the present wavemaker apparatus provides limited stroke, so that the wave amplitude for the most shallow water cases is limited. Nev-

ertheless, experimental evidence for both wavemaker theories confirmed that either is applicable for a standard-sized laboratory piston-type wavemaker.

(3) The most stringent accuracy requirements are commonly placed on the generation of focused wave groups. In this context, a novel wavemaker calibration approach was introduced. The new approach is based upon a calibration of the wavemaker displacement, which contrasts to previous calibration approaches based upon the surface elevation. The new technique was demonstrated to greatly improve the generation of both focused wave groups and irregular seas. The improvements were particularly evident in the case of focused wave groups, for which an exceptional match was obtained with reference data provided by a fully-nonlinear numerical method.

(4) The nonlinear generation of steep focused wave groups was considered in further detail. If based on the calibration approach noted under (3) above, an experimental assessment demonstrated that a linear wavemaker control signal is sufficiently accurate. This is facilitated by the effect of wave dispersion, which decreases the amount of nonlinear interactions in the vicinity of the wave generator. A second-order control signal was also tested, but this leads to insignificant difference over first-order control. As a result, the accuracy of the experimental apparatus is primarily driven by first-order effects, including the amplitude correction noted under (1) above. In comparing the experimental evidence to numerical data, some important differences in the wave generation approach were established. In a numerical computation, it is often advantageous to focus the wave event far downstream of the wavemaker, commonly in the order of 20-30 water depths. In contrast, this focus distance was kept to under 10 water depths in the experimental approach, as viscous dissipation along the flume's side walls was shown to affect the data if focused further downstream.

(5) Second-order force-control was applied, for the first time, to the generation of irregular sea states in shallow and intermediate water conditions. An im-

provement of the wave quality, expressed through the crest statistics of the sea state, was notable in shallow-water conditions. In contrast, the second-order correction was shown to have little influence on the generation of moderately steep sea states in intermediate water conditions. This highlights the fact that second-order interaction terms are significantly more pronounced in shallow water, where nonlinear control was found to be an essential part of the generation process.

(6) An *ad-hoc* approach was introduced for the generation of steep irregular sea states in shallow water. Based upon a fit of a regular fifth-order solution to individual waves within the sea state, this *ad-hoc* technique showed clear potential for the accurate prediction of wave crest statistics. At present, this has only been demonstrated for a single sea state, and additional verification is recommended.

(7) Taken as a whole, the experimental data presented in this PhD concern in excess of 1500 test cases, taken from more than 500 hours of laboratory testing. These data remain the principal source of evidence on which reliable wavemaker theories should be based and developed further.

A large number of laboratories world-wide have commissioned force-controlled wavemaking systems. Where these are flap-type devices, the findings of Spinneken and Swan (2009*a*,*b*) remain applicable, and linear control is likely to be sufficient. This thesis has clearly demonstrated that this is not the case for piston-type wavemakers, particularly in shallow water. In the piston case, a nonlinear control signal is absolutely essential to the successful operation in force control. If based on a linear demand signal, significant spurious free wave content must be expected. The main advance of the present work lies in the solutions that are offered to overcome the problem of spurious wave contamination. In regular waves, this may rely on a traditional second-order type control which was extended here to force-controlled piston-type wavemakers. For steep irregular waves, second-order

control was not found entirely adequate, and the *ad-hoc* approach outlined above offers the best available wavemaking solution to date.

7.2 Further work

The achievements noted above demonstrate the success of this PhD thesis in improving wave generation and absorption in shallow-water conditions. However, they also highlight areas in which the existing theories fail to make accurate predictions, which motivates the following recommendations for further work.

7.2.1 Modelling viscous effects

As discussed above, viscous effects are likely to cause first-order errors in the order of 15%. All wavemaker theories presently rely on the assumption of potential flow, where viscous effects are neglected. In the development of an alternative viscous wavemaker theory, a fundamental research question arises. This question relates to the source(s) of viscous energy dissipation, whereby it is presently unclear whether this is related to skin friction at the wavemaker front or flow separation at some of the wavemaker's sharp corners. Preliminary numerical CFD data not shown herein suggest that skin friction may account for a wave amplitude reduction in the order of 5%. This reduction is related to the no-slip condition on the wavemaker front face, which introduces large vertical velocity gradients and vorticity. However, based upon the present understanding, this skin friction effect is unlikely to account for the total error of approximately 15%. This is consistent with the established literature on drag, where flow separation (or form drag) is known to greatly outweigh the effect of skin friction. Given the present experimental setup, the only possibility for flow separation exists at the bottom corner of the wavemaker. It is hence recommended to focus any future work on the flow separation that may occur as this bottom corner traverses the fluid.

7.2.2 Irregular sea wave generation

The *ad-hoc* approach introduced in the context of irregular sea states, Chapter 6, showed clear potential to overcome some of the limitations associated with second-order theory in shallow water. To demonstrate this further, the technique should be tested for an extended range of sea states, varying both the non-dimensional water depth and the sea state steepness. The approach could potentially be extended to flap-type wavemakers. In the formulation of the appropriate wavemaker boundary condition, this extension would have to account for the fact that a flap motion is composed of both horizontal and (small) vertical displacement components.

7.2.3 Multi-directional wave generation

It is crucial to keep in mind that a realistic reproduction of sea states must account for directionality. Historically, much of the work on nonlinear wave generation was tested in laboratory wave flumes. Nonlinear directional wavemaker theories have been established for more than one decade, but these are yet to be validated. Indeed, there is a complete lack of experimental data concerning the application of nonlinear (say second order) directional wavemaking theories. In this context, the experience gained in this PhD has taught an important lesson. In considering the nonlinear wavemaking problem, it is easy to get 'carried away' with the development of ever more complex theoretical formulations. However, in the field of laboratory wavemaking, the only ultimate truth lies in the experimental data. It is hence recommended to undertake a systematic assessment of wavemaker theories in a directional wave basin. This should commence with the careful validation of linear wavemaker theory, specifically the progressive wave field coefficient. Subsequently, the full range of applicability of second-order theory should be explored; the unidirectional formulation of this theory having been found to be more applicable than generally anticipated.

7.3 Final remarks

In the development of this research, both theoretical formulations and empirical evidence have played essential roles. To quote Henri Poincaré, *'Science is built up of facts, as a house is with stones. But a collection of facts is no more a science than a heap of stones is a house.'* To set this into context, the success of the present work is defined by the effective linkage of theory and practice, and this PhD is hoped to have contributed to 'building the house' of practical laboratory wavemaking.

A

Second-order wavemaker theory

Any force-control wavemaking theory ultimately relies on the underlying hydrodynamic formulation appropriate to position control. Schäffer (1996) derived complete expressions for the potential Φ and the wave elevation η appropriate to the second-order irregular wavemaking problem. The notation and form of solution adopted herein closely follows that of Schäffer (1996). In contrast to Schäffer (1996), all formulation reported here have been simplified for a piston-type wavemaker.

A two-dimensional formulation in a Cartesian coordinate system (x, z) is adopted, where time is denoted as t. To obtain a second-order solution, a Taylor expansion of the fully-nonlinear quantities must be undertaken, where the truncation is made at second order. This yields the velocity potential Φ as

$$\Phi(x, z, t) = \Phi^{(1)}(x, z, t) + \Phi^{(2)}(x, z, t), \tag{A.1}$$

the free-surface elevation as

$$\eta(x, t) = \eta^{(1)}(x, t) + \eta^{(2)}(x, t) \tag{A.2}$$

and the wavemaker displacement as

$$X(t) = X^{(1)}(t) + X^{(2)}(t). \tag{A.3}$$

The first-order solution terms $\Phi^{(1)}$, $\eta^{(1)}$ and $X^{(1)}$ are provided in §2.3.4. The second-order term is further decomposed and given by

$$\begin{aligned}\Phi^{(2)}(x,z,t) = \Phi^{(21)+}(x,z,t) + \Phi^{(21)-}(x,z,t) + \Phi^{(22)+}(x,z,t) \\ + \Phi^{(22)-}(x,z,t) + \Phi^{(23)+}(x,z,t) + \Phi^{(23)-}(x,z,t).\end{aligned} \tag{A.4}$$

Within this formulation, $\Phi^{(21)}$ is the bound second-order term, $\Phi^{(22)}$ is a spurious free wave term, and $\Phi^{(23)}$ is required to provide a free wave suppression. The second-order bound wave potential is given by

$$\begin{aligned}\Phi^{(21)\pm}(x,z,t) = \mathbb{R}\left\{2\sum_{n=1}^{N}\sum_{m=n}^{N} i\delta_{nm} X_n X_m^{-*} \sum_{j=0}^{\infty}\sum_{l=0}^{\infty} c_{jn} c_{lm}^{-*} \frac{H^{\pm}_{jnlm}}{D^{\pm}_{jnlm}} \right. \\ \left. \frac{\cosh(k_{jn} \pm k_{lm}^{-*})(z+h)}{\cosh(k_{jn} \pm k_{lm}^{-*})h} e^{i(\omega_n t - k_{jn} x \pm (\omega_m t - k_{lm}^{-*} x))}\right\},\end{aligned} \tag{A.5}$$

where

$$\delta_{nm} = \begin{cases} 1 \text{ if n} \neq \text{m} \\ 0.5 \text{ if n} = \text{m}. \end{cases} \tag{A.6}$$

Furthermore

$$H^{\pm}_{jnlm} = (\omega_n \pm \omega_m)\left(\pm\omega_n\omega_m - \frac{g^2 k_{jn} k_{lm}^{-*}}{\omega_n \omega_m}\right) + \frac{\omega_n^3 \pm \omega_m^3}{2} - \frac{g^2}{2}\left(\frac{{k_{jn}}^2}{\omega_n} \pm \frac{{k_{lm}}^2}{\omega_m}\right) \tag{A.7}$$

and

$$D^{\pm}_{jnlm} = g(k_{jn} \pm {k_{lm}}^{-*}) \tanh{(k_{jn} \pm {k_{lm}}^{-*})h} - (\omega_n \pm \omega_m)^2 \tag{A.8}$$

where the superscript $^{-*}$ refers to the complex conjugate for subharmonics. The

spurious free wave potential is given by

$$\Phi^{(22)\pm}(x,z,t) = \mathbb{R}\left\{2\sum_{n=1}^{N}\sum_{m=n}^{N}\frac{igc_{0n}X_nc_{0m}X_m^{-*}}{h(\omega_n \pm \omega_m)} \sum_{p=0}^{\infty} c_p^{(22)\pm}\frac{\cosh K_p^{\pm}(z+h)}{\cosh K_p^{\pm}h}e^{i((\omega_n\pm\omega_m)t-K_p^{\pm}x)}\right\}, \quad \text{(A.9)}$$

where

$$c_p^{(22)\pm} = \frac{\delta_{nm}h(\omega_n \pm \omega_m)\cosh^2(K_p^{\pm}h)}{g^2c_{0n}c_{0m}\Lambda_2(K_p^{\pm})}\left\{-\sum_{j=0}^{\infty}\sum_{l=0}^{\infty}c_{jn}c_{lm}^{-*}\frac{k_{jn}\pm k_{lm}^{-*}}{(k_{jn}\pm k_{lm}^{-*})^2-(K_p^{\pm})^2}H_{jnlm}^{\pm} \pm\frac{g}{2\omega_n}\sum_{j=0}^{\infty}\frac{c_{jn}k_{jn}^2}{k_{jn}^2-(K_p^{\pm})^2}(\omega_n^2-(\omega_n\pm\omega_m)^2) \pm\frac{g}{2\omega_m}\sum_{l=0}^{\infty}\frac{c_{lm}^{-*}k_{lm}^2}{k_{lm}^2-(K_p^{\pm})^2}(\omega_m^2-(\omega_n\pm\omega_m)^2)\right\}, \quad \text{(A.10)}$$

$$\Lambda_2(K_p^{\pm}) = \frac{1}{2}\left\{K_p^{\pm}h + \sinh K_p^{\pm}h\cosh K_p^{\pm}h\right\} \quad \text{(A.11)}$$

and $K_p^{\pm}$ is the solution of

$$(\omega_n \pm \omega_m)^2 = K_p^{\pm}g\tanh K_p^{\pm}h. \quad \text{(A.12)}$$

The additional second-order required to cancel the spurious free wave is given by

$$\Phi^{(23)\pm}(x,z,t) = \mathbb{R}\left\{2\sum_{n=1}^{N}\sum_{m=n}^{N}\frac{igX_{nm}^{(2)\pm}}{(\omega_n\pm\omega_m)}\sum_{p=0}^{\infty}c_p^{(23)\pm}\frac{\cosh K_p^{\pm}(z+h)}{\cosh K_p^{\pm}h}e^{i((\omega_n\pm\omega_m)t-K_p^{\pm}x)}\right\} \quad \text{(A.13)}$$

where the second-order wavemaker displacement is

$$X_{nm}^{(2)\pm} = \mathscr{F}^{\pm}\frac{c_{0n}X_nc_{0m}X_m^{-*}}{h}, \quad \text{(A.14)}$$

the transfer function $\mathscr{F}^{\pm}$ is defined by

$$\mathscr{F}^{\pm} = -\frac{c_0^{(22)\pm}}{c_0^{(23)\pm}} \tag{A.15}$$

and

$$c_p^{(23)\pm} = \frac{2\sinh K_p^{\pm}h(\sinh K_p^{\pm}h - \sinh K_p^{\pm}d)}{K_p^{\pm}h + \sinh K_p^{\pm}h\cosh K_p^{\pm}h}. \tag{A.16}$$

The second-order wave elevation is given by the sum

$$\eta^{(2)}(x,t) = \eta^{(21)+}(x,t) + \eta^{(21)-}(x,t) + \eta^{(22)+}(x,t) + \eta^{(22)-}(x,t) + \eta^{(23)+}(x,t) + \eta^{(23)-}(x,t), \tag{A.17}$$

where the superscripts are defined as for the velocity potential above. The second-order bound wave elevation is given by

$$\eta^{(21)\pm}(x,t) = \mathbb{R}\left\{2\sum_{n=1}^{N}\sum_{m=n}^{N} X_n X_m^{-*} \sum_{j=0}^{\infty}\sum_{l=0}^{\infty} c_{jn}c_{lm}^{-*}G_{jnlm}^{\pm} e^{i(\omega_n t - k_{jn}x \pm (\omega_m t - k_{lm}^{-*}x))}\right\}, \tag{A.18}$$

where

$$G_{jnlm}^{\pm} = \frac{\delta_{nm}}{g}\left\{(\omega_n \pm \omega_m)\frac{H_{jnlm}^{\pm}}{D_{jnlm}^{\pm}} - L_{jnlm}^{\pm}\right\} \tag{A.19}$$

and

$$L_{jnlm}^{\pm} = \frac{1}{2}\left\{\frac{g^2 k_{jn}{k_{lm}}^{-*}}{\omega_n\omega_m} \mp \omega_n\omega_m - (\omega_n^2 \pm \omega_m^2)\right\}. \tag{A.20}$$

Finally the spurious free wave elevation is given by

$$\eta^{(22)\pm}(x,t) = \mathbb{R}\left\{2\sum_{n=1}^{N}\sum_{m=n}^{N}\frac{c_{0n}X_n c_{0m}X_m^{-*}}{h}\sum_{p=0}^{\infty} c_p^{(22)\pm} e^{i((\omega_n \pm \omega_m)t - K_p^{\pm}x)}\right\} \tag{A.21}$$

and the additional free wave, required to cancel $\eta^{(22)\pm}$, is defined as

$$\eta^{(23)\pm}(x,t) = \mathbb{R}\left\{2\sum_{n=1}^{N}\sum_{m=n}^{N} X_{nm}^{(2)\pm}\sum_{p=0}^{\infty} c_p^{(23)\pm} e^{i((\omega_n \pm \omega_m)t - K_p^{\pm}x)}\right\}. \tag{A.22}$$

B

Stream-function wavemaker theory

Zhang and Schäffer (2007) developed a Stream-function wavemaker theory in position control, based on an *ad-hoc* combination of linear fully-dispersive wavemaker theory and a methodology developed for nonlinear long-wave generation. This theory essentially relies on the two following concepts:

(i) The wavemaker displacement and the wave amplitude are related by $A(\omega) = ic_0 X_a(\omega)$, where $A(\omega)$ and $X_a(\omega)$ are the Fourier transforms of the wave elevation at the wavemaker, $\eta(t)$, and the wavemaker displacement, $X_{0s}(t)$.

(ii) The depth-averaged fluid velocity and the wave amplitude are related by $U_a(\omega) = \frac{\omega}{kh} A(\omega)$, where $U_a(\omega)$ is the Fourier transform of the depth-averaged fluid velocity at the wavemaker, k is the wavenumber and h the water depth. This relation is obtained by integrating the velocity divergence at the wavemaker between the bed and the free surface. For an incompressible fluid, this divergence must be zero.

Eliminating $A(\omega)$ in the two expressions above yields

$$i\omega X_a(\omega) = \Lambda(\omega) U_a(\omega), \tag{B.1}$$

where $\Lambda(\omega)$ is a dispersion correction provided by $\Lambda(\omega) = kh/c_0$. Introducing

the shallow-water wavemaker displacement as $X^{sw}(t)$, which excludes the effect of wave dispersion, equation (B.1) may be separated into

$$i\omega X_a^{sw}(\omega) = U_a(\omega) \tag{B.2}$$

and

$$X_a(\omega) = \Lambda(\omega) X_a^{sw}(\omega), \tag{B.3}$$

where $X_a^{sw}(\omega)$ is the Fourier transform of $X^{sw}(t)$. Applying an inverse Fourier transform to equations (B.2) and (B.3) gives the expressions in the time domain as

$$\frac{dX^{sw}(t)}{dt} = U(X^{sw}(t), t) \tag{B.4}$$

and

$$X_{0s}(t) = \int_{-t_0}^{t_0} X^{sw}(t-\tau)\lambda_d(\tau)d\tau, \tag{B.5}$$

where t_0 is the width of the convolution window and $\lambda_d(t)$ is the inverse Fourier transform of the dispersion correction term $\Lambda(\omega)$. The wavemaker displacement $X_{0s}(t)$ may now be formulated as the solution of the problem

$$\begin{cases} \frac{dX^{sw}(t)}{dt} + \omega_c X^{sw}(t) = U(X^{sw}(t), t), \\ X_{0s}(t) = \int_{-t_0}^{t_0} X^{sw}(t-\tau)\lambda_d(\tau)d\tau, \\ X^{sw}(0) = 0, \end{cases} \tag{B.6}$$

where the additional term $\omega_c X^{sw}(t)$ represents a first-order high-pass filter introduced to avoid any drift of the wavemaker. Assuming continuity, the depth-averaged horizontal velocity $U(x,t)$, required on the right hand side of equation (B.6), may be expressed as

$$U(x,t) = \frac{c\eta(x,t)}{h + \eta(x,t)}, \tag{B.7}$$

where c is the phase velocity and $\eta(x,t)$ is the water surface elevation. The water surface elevation may be obtained directly from Stream-function wave theory.

C

Force-control wavemaker theory

C.1 Added mass and radiation damping

The first-order hydrodynamic force $F^{(1)}$ acting on a piston-type wavemaker is expressed as the sum of a radiation damping term and an added mass term. While the radiation damping term is induced by the progressive wave field, the added mass term represents the forcing due to the evanescent wave field. If $X^{(1)}$ is the first-order wavemaker displacement, $F^{(1)}$ is given by

$$F^{(1)}(\omega) = d(\omega)\dot{X}^{(1)}(\omega) + m(\omega)\ddot{X}^{(1)}(\omega), \tag{C.1}$$

where the radiation damping $d(\omega)$ is defined by

$$d(\omega) = \frac{\rho g}{\omega}\frac{c_0}{k_0}\tanh k_0 h \tag{C.2}$$

and the added mass $m(\omega)$ is equal to

$$m(\omega) = -i\frac{\rho g}{\omega^2}\sum_{j=1}^{\infty}\frac{c_j}{k_j}\tanh k_j h. \tag{C.3}$$

A full derivation of these expressions can be found in Spinneken (2010).

C.2 Second-order wavemaker forces for a piston-type wavemaker

Following Spinneken (2010), the second-order hydrodynamic force $F_{\Phi}^{(2)}$ acting upon a piston-type wavemaker may be expressed as

$$F_{\Phi}^{(2)} = F_{\Phi^{(1)}}^{(2)+} + F_{\Phi^{(1)}}^{(2)-} + F_{hydro}^{(2)+} + F_{hydro}^{(2)-} + F_{u^2}^{(2)+} + F_{u^2}^{(2)-} + F_{w^2}^{(2)+} + F_{w^2}^{(2)-} + F_{\Phi^{(21)}}^{(2)+} + F_{\Phi^{(21)}}^{(2)-} + F_{\Phi^{(22)}}^{(2)+} + F_{\Phi^{(22)}}^{(2)-}. \quad \text{(C.4)}$$

where the subscripts make reference to the hydrodynamic solution provided in Appendix A. The full expressions required to obtain these forcing terms can be found in Spinneken (2010). For brevity, only the final results are included. The first-order unsteady wave acceleration integrated to the first-order free surface leads to

$$F_{\Phi^{(1)}}^{(2)\pm}(t) = \mathbb{R}\left\{\sum_{n=1}^{N}\sum_{m=n}^{N}\delta_{nm}\rho g X_n X_m^{-*}\sum_{j=0}^{\infty}\sum_{l=0}^{\infty}c_{jn}c_{lm}^{-*}e^{i(\omega_n\pm\omega_m)t}\right\}. \quad \text{(C.5)}$$

The changing effective wetted surface of the wavemaker induces the second-order force component

$$F_{hydro}^{(2)\pm}(t) = \mathbb{R}\left\{\sum_{n=1}^{N}\sum_{m=n}^{N}-\frac{\delta_{nm}\rho g X_n X_m^{-*}}{2}\sum_{j=0}^{\infty}\sum_{l=0}^{\infty}c_{jn}c_{lm}^{-*}e^{i(\omega_n\pm\omega_m)t}\right\} \quad \text{(C.6)}$$

which is equal to $-F_{\Phi^{(1)}}^{(2)\pm}/2$. The force associated with the horizontal velocity term is

$$F_{u^2}^{(2)\pm}(t) = \mathbb{R}\left\{\sum_{n=1}^{N}\sum_{m=n}^{N}\frac{\delta_{nm}\rho g^2 X_n X_m^{-*}}{2\omega_n\omega_m}\sum_{j=0}^{\infty}\sum_{l=0}^{\infty}\frac{c_{jn}k_{jn}c_{lm}^{-*}k_{lm}^{-*}}{\cosh k_{jn}h\cosh k_{lm}^{-*}h}\Gamma_{u^2}e^{i(\omega_n\pm\omega_m)t}\right\} \quad \text{(C.7)}$$

where

$$\Gamma_{u^2} = \begin{cases} \frac{-1}{2k_{jn}} \{\sinh k_{jn}h \cosh k_{jn}h - \sinh k_{jn}d \cosh k_{jn}d \\ +k_{jn}(h-d)\} \text{ for } n = m \text{ and } j = l \\ \frac{-1}{k_{jn}^2 - k_{lm}^{-*2}} \left\{k_{jn} \sinh k_{jn}h \cosh k_{lm}^{-*}h - k_{lm}^{-*} \cosh k_{jn}h \sinh k_{lm}^{-*}h \right. \\ \left. -k_{jn} \sinh k_{jn}d \cosh k_{lm}^{-*}d + k_{lm}^{-*} \cosh k_{jn}d \sinh k_{lm}^{-*}d\right\} \text{otherwise.} \end{cases} \tag{C.8}$$

Similarly, the force associated with the vertical velocity term is

$$F_{w^2}^{(2)\pm}(t) = \mathbb{R}\left\{\sum_{n=1}^{N}\sum_{m=n}^{N} \mp \frac{\delta_{nm}\rho g^2 X_n X_m^{-*}}{2\omega_n\omega_m} \sum_{j=0}^{\infty}\sum_{l=0}^{\infty} \frac{c_{jn}k_{jn}c_{lm}^{-*}k_{lm}^{-*}}{\cosh k_{jn}h \cosh k_{lm}^{-*}h} \sigma_l \Gamma_{w^2} e^{i(\omega_n \pm \omega_m)t}\right\} \tag{C.9}$$

where

$$\Gamma_{w^2} = \begin{cases} \frac{-1}{2k_{jn}} \{\sinh k_{jn}h \cosh k_{jn}h - \sinh k_{jn}d \cosh k_{jn}d \\ -k_{jn}(h-d)\} \text{ for } n = m \text{ and } j = l \\ \frac{-1}{k_{jn}^2 - k_{lm}^{-*2}} \left\{k_{jn} \cosh k_{jn}h \sinh k_{lm}^{-*}h - k_{lm}^{-*} \sinh k_{jn}h \cosh k_{lm}^{-*}h \right. \\ \left. -k_{jn} \cosh k_{jn}d \sinh k_{lm}^{-*}d + k_{lm}^{-*} \sinh k_{jn}d \cosh k_{lm}^{-*}d\right\} \text{otherwise} \end{cases} \tag{C.10}$$

and

$$\sigma_l = \begin{cases} \text{-1 if l} > 0 \text{ and for subharmonics} \\ \text{1 otherwise} \end{cases} \tag{C.11}$$

The force induced by the second-order bound wave potential is given by

$$F_{\Phi^{(21)}}^{(2)\pm}(t) = \mathbb{R}\left\{\sum_{n=1}^{N}\sum_{m=n}^{N} \delta_{nm}\rho(\omega_n \pm \omega_m) X_n X_m^{-*} \sum_{j=0}^{\infty}\sum_{l=0}^{\infty} \frac{H_{jnlm}^{\pm}}{D_{jnlm}^{\pm}} \frac{c_{jn}c_{lm}^{-*}}{k_{jn} \pm k_{lm}^{-*}} \Gamma_1 e^{i(\omega_n \pm \omega_m)t}\right\} \tag{C.12}$$

where

$$\Gamma_1 = \frac{\sinh(k_{jn} \pm k_{lm}^{-*})h - \sinh(k_{jn} \pm k_{lm}^{-*})d}{\cosh(k_{jn} \pm k_{lm}^{-*})h}. \tag{C.13}$$

Finally the force induced by the spurious free wave potential is

$$F_{\Phi^{(22)}}^{(2)\pm}(t) = \mathbb{R}\left\{\frac{\rho g c_{0n} X_n c_{0m} X_m^{-*}}{h} \sum_{p=0}^{\infty} \frac{c_p^{(22)\pm}}{(K_p^{\pm})^2} \Gamma_1 e^{i(\omega_n \pm \omega_m)t}\right\} \tag{C.14}$$

where

$$\Gamma_1 = \frac{\sinh\left(K_p^{\pm}h\right) - \sinh\left(K_p^{\pm}d\right)}{\cosh\left(K_p^{\pm}h\right)}. \tag{C.15}$$

D

Independent confirmation of progressive wave field coefficient

The results presented in this thesis demonstrate that both linear wavemaker theory and second-order wavemaker theory require empirical correction factors to succeed. To establish this conclusion further, an independent experimental assessment was conducted in the Sediment Flume at Plymouth University. The Sediment Flume at Plymouth University is very similar to the Coastal Flume at Imperial College London. Equipped with a similar piston-type wavemaker, the Sediment Flume is 0.6m wide, 35m long and operates at a water depth up to 0.8m.

This independent assessment is included to provide additional evidence of the effects shown in Chapter 3. To achieve this, a set of eight rod-type wave gauges was used to measure the water surface elevation, while the position of the piston-type wavemaker was recorded using a calibration-free shaft encoder provided as part of the wavemaking system.

A validation of the progressive wave field coefficient c_0, as shown in §3.4.1, was first conducted. Figure D.1 presents the magnitude of the coefficient c_0, with the corresponding Costal Flume data being presented in Figure 3.6(a). In close similarity to Figure 3.6(a), Figure D.1 confirms the error of 15% in the magnitude

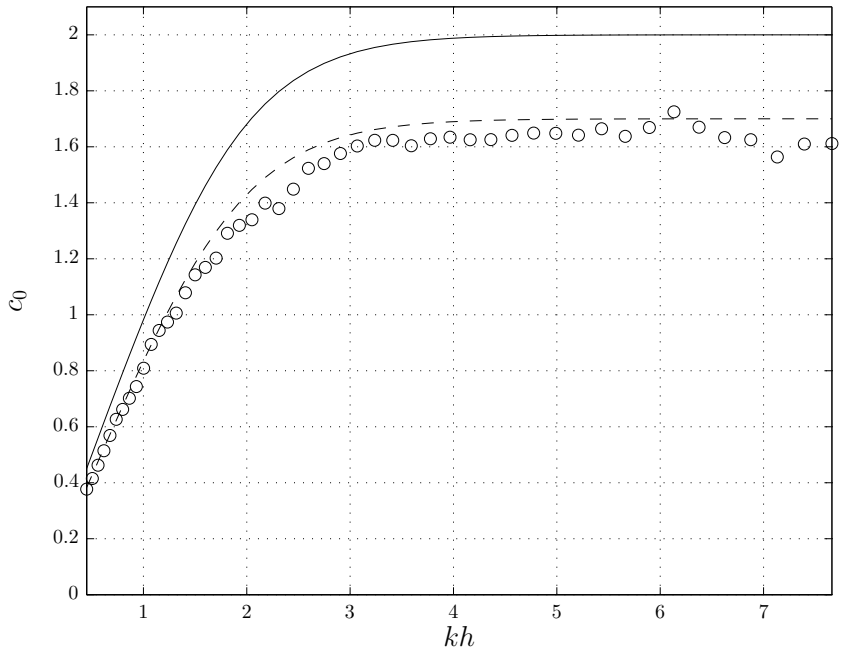


Figure D.1: Magnitude of progressive wave field coefficient with ∘ experimental measurement —— theoretical coefficient c_0 and — — adjusted coefficient $c_0{}' = 0.85c_0$.

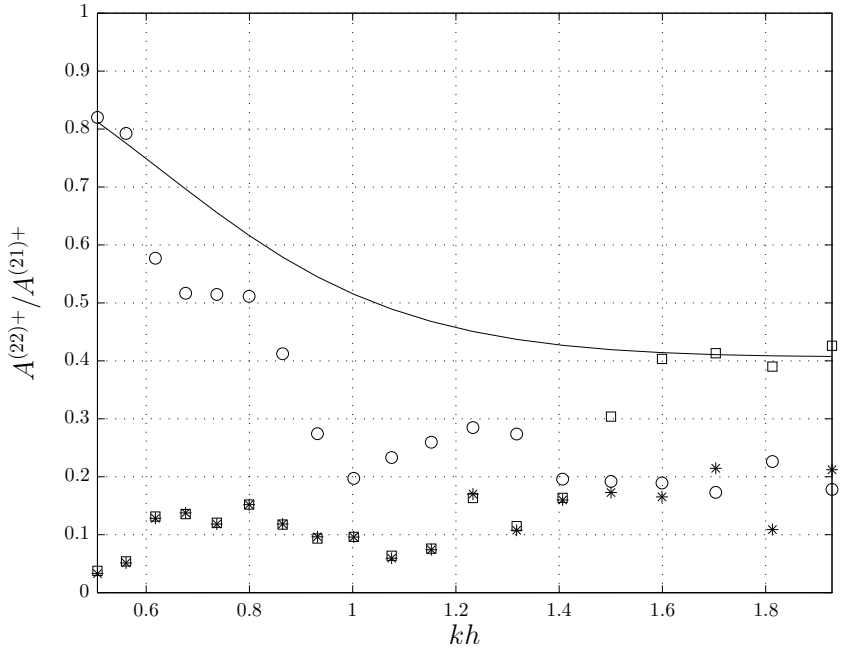


Figure D.2: Spurious free wave content in position control for —— theoretical linear wave-maker theory and experiment data based up ∘ linear control, □ second-order control, and ∗ second-order control including a phase correction.

of the progressive wave field coefficient; this error being only marginally larger in the Sediment Flume. As a result, the additional experimental data support the introduction of an adjusted coefficient $c_0{}' = 0.85c_0$ in §3.4.1.

An independent confirmation of the second-order correction in regular waves, introduced in §3.4.4, was also undertaken. Figure D.2 shows the spurious free-wave content obtained using (i) a linear control signal (symbol $\circ$), (ii) a direct second-order compensation (symbol $\square$) and (iii) a second-order compensation including an optimised phase correction (symbol $*$). The compensation of the second-order spurious free wave is effective in both cases up to $kh = 1.4$. In contrast, it can be observed that for water depths beyond $kh = 1.4$, a phase correction is required to reduce the spurious free wave content; this confirming the conclusions of §3.4.4.

Bibliography

Baldock, T. E. and Swan, C. (1994), 'Numerical calculations of large transient water waves.', *Applied Ocean Research* **16**, 101–112.

Bateman, W., Swan, C. and Taylor, P. H. (2001), 'On the efficient numerical simulation of directionally spread surface water waves', *Journal of Computational Physics* **174**, 277–305.

Bateman, W., Swan, C. and Taylor, P. H. (2003), 'On the calculation of the water particle kinematics arising in a directionally spread wavefield', *Journal of Computational Physics* **186**, 70–92.

Chaplin, J. (1980), 'Developments of stream-function wave theory', *Coastal Engineering* **3**, 179–205.

Chatry, G., Clement, A. H. and Gouraud, T. (1998), Self-adaptive control of a piston wave absorber, *in* 'Proceedings of the Eighth International Offshore and Polar Engineering Conference', Vol. 1, pp. 127–133.

Dean, R. (1972), Evaluation and development of water wave theories for engineering applications, Technical Report 14, Coastal and Oceanographic Engineering Laboratory.

Evans, D. (1976), 'A theory for wave-power absorption by oscillating bodies', *Journal of Fluid Mechanics* **77**, 1–25.

Falnes, J. (1980), 'Radiation impedances matrix and optimum power absorption for interacting oscillators in surface waves', *Applied Ocean Research* **2**(2), 75–80.

Falnes, J. (1993), Optimum control of oscillation of wave-energy converters, Wave energy converters: Generic technical evaluation study, DG XII Joule Wave Energy Initiative.

Fenton, J. (1979), 'A high-order cnoidal wave theory', *Journal of Fluid Mechanics* **94**, 129–161.

Fenton, J. (1985), 'Fifth-order stokes theory for steady waves.', *Journal of Waterway, Port, Coastal and Ocean Engineering* **111**(2), 216 – 234.

Fenton, J. (1988), 'The numerical solution of steady water wave problems', *Computers and Geosciences* **14**(3), 357 – 68.

Forristall, G. (2000), 'Wave crest distributions: observations and second-order theory', *Journal of Physical Oceanography* **30**(8), 1931 – 43.

Frigaard, P. and Christensen, M. (1994), An absorbing wave-maker based on digital filters, *in* '24th International Conference on Coastal Engineering', Vol. 1, pp. 169–180.

Goring, D. (1979), Tsunamis-the propagation of long waves onto a shelf., PhD Thesis, W.M. Keck Laboratory of Hydraulics and Water Resources.

Goring, D. and Raichlen, F. (1980), 'Generation of long waves in the laboratory.', *National Conference Publication - Institution of Engineers, Australia* (80/1), 304 – 306.

Hague, C. and Swan, C. (2009), 'A multiple flux boundary element method applied to the description of surface water waves', *Journal of Computational Physics* **228**(14), 5111 – 5128.

Havelock, T. (1929), 'Forced surface-wave on water', *Philosophical Magazine* **viii**, 569–576.

Isobe, M. (1985), 'Calculation and application of first-order cnoidal wave theory.', *Coastal Engineering* **9**, 309–325.

Johannessen, T. and Swan, C. (2001), 'A laboratory study of the focusing of transient and directionally spread surface water waves.', *Proc. Roy. Soc. Lond. A* **457**, 1–36.

Johannessen, T. and Swan, C. (2003), 'On the nonlinear dynamics of focused wave groups in two and three dimensions.', *Proc. Roy. Soc. Lond. A* **459**, 1021–1052.

Lambrakos, K. (1981), 'Extended velocity potential wave kinematics', *Journal of the Waterway Port Coastal and Ocean Division* **107**(3), 159 – 174.

Latheef, M. (2014), Surface wave statistics in directionally spread seas, PhD thesis, Imperial College London.

Latheef, M. and Swan, C. (2013), 'A laboratory study of wave crest statistics and the role of directional spreading', *Proceedings of the Royal Society A-Mathematical Physical and Engineering Sciences* **469**.

Lin, C.-Y. and Huang, C.-J. (2004), 'Decomposition of incident and reflected higher harmonic waves using four wave gauges', *Coastal Engineering* **51**(5-6), 395 – 406.

Longuet-Higgins, M. and Stewart, R. (1960), 'Changes in the form of short gravity waves on long waves and tidal currents', *Journal of Fluid Mechanics* **8**(4), 565 – 583.

Masterton, S. and Swan, C. (2008), 'On the accurate and efficient calibration of a 3D wave basin', *Ocean Engineering* **35**(8-9), 763–773.

Milgram, J. (1970), 'Active water-wave absorbers', *Journal of Fluid Mechanics* **43**, 845–859.

Naito, S. (2006), 'Wave generation and absorption in wave basins: Theory and applications', *International Journal of Offshore and Polar Engineering* **16**(2), 81–89.

Ottesen-Hansen, N.-E., Sand, S., Lundgren, H., Sorensen, T. and Gravesen, H. (1980), Correct reproduction of long group induced waves, *in* 'Proceedings of the 17th Coastal Engineering Conference, Sydney, Australia', pp. 784–800.

Salter, S. (1982), Absorbing wave-makers and wide tanks, *in* 'Directional Wave Spectra Applications', pp. 185–200.

Sand, S. E. and Donslund, B. (1985), 'Influence of the wave board type on bounded long waves', *Journal of Hydraulic Research* **23**, 147–163.

Schäffer, H. (1993), Second-order irregular wave generation in flumes: Computation of transfer functions by an asymptotic summation method, *in* '2nd International Symp. Ocean Wave Measurement and Analysis', New Orleans, USA.

Schäffer, H. (1996), 'Second-order wavemaker theory for irregular waves', *Ocean Engineering* **23**, 47–88.

Schäffer, H. and Jakobsen, K. (2003), Non-linear wave generation and active absorption in wave flumes, *in* 'Long Waves Symposium', pp. 69–77.

Schäffer, H. and Steenberg, C. (2003), 'Second-order wavemaker theory for multidirectional waves', *Ocean Engineering* **30**(10), 1203 – 1231.

Sharma, J. N. and Dean, R. G. (1981), 'Second-order directional seas and associated wave forces', *Society of Petroleum Engineering* **4**, 129–140.

Smith, S. and Swan, C. (2002), 'Extreme two-dimensional water waves: an assessment of potential design solutions', *Ocean Engineering* **29**, 387–416.

Sobey, R. (1992), 'A local fourier approximation method for irregular wave kinematics.', *Applied Ocean Research.* **14**, 93–105.

Sobey, R., Goodwin, P., Thieke, R. and Westberg, R. (1987), 'Application of stokes, cnoidal, and fourier wave theories.', *Journal of Waterway, Port, Coastal and Ocean Engineering.* **113**, 565–587.

Spinneken, J. (2010), Wave generation and absorption using force-feedback control, Phd thesis, Imperial College London.

Spinneken, J., Christou, M. and Swan, C. (2013), 'Force-controlled absorption in a fully-nonlinear numerical wavetank.', *Journal of Computational Physics* **272**, 127–148.

Spinneken, J. and Swan, C. (2009*a*), 'Second-order wave maker theory using force-feedback control. Part I: A new theory for regular wave generation', *Ocean Engineering* **36**(8), 539 – 548.

Spinneken, J. and Swan, C. (2009*b*), 'Second-order wave maker theory using force-feedback control. Part II: An experimental verification of regular wave generation', *Ocean Engineering* **36**(8), 549 – 555.

Spinneken, J. and Swan, C. (2009*c*), Wave generation and absorption using force-controlled wave machines, *in* 'Proceedings of the 19th International Offshore and Polar Engineering Conference', Vol. 3, pp. 397–404.

Spinneken, J. and Swan, C. (2011), 'Theoretical transfer function for force-controlled wave machines', *Internation Journal of Offshore and Polar Engineering* **21**, 160–177.

Stokes, G. (1847), 'On the theory of oscillatory waves.', *Transactions of the Cambridge Philosophical Society* **8**, 441–455.

Sulisz, W. and Hudspeth, R. T. (1993), 'Complete second-order solution for water waves generated in wave flumes', *Journal of Fluids and Structures* **7**, 253–268.

Tromans, P., Anaturk, A. and Hagemeijer, P. (1991), A new model for the kinematics of large ocean waves application as a design wave, *in* 'Proceedings of the 1st International Offshore and Polar Engineering Conference', Vol. 3, pp. 64–71.

Ursell, F., Dean, R. and Yu, Y. (1960), 'Forced small-amplitude water waves: a comparison of theory and experiment', *Journal of Fluid Mechanics* **7**, 33–52.

Zhang, H. and Schäffer, H. (2007), 'Approximate stream function wavemaker theory for highly non-linear waves in wave flumes', *Ocean Engineering* **34**(8-9), 1290–1302.